The Control of Grid-Connected Inverters in Microgrids

Thesis submitted in accordance with the requirements of

the University of Liverpool for the degree of Doctor in Philosophy

by

Jianguo Wang

May 2016

Department of Electrical Engineering and Electronics
The University of Liverpool

Acknowledgements

First and foremost, I would like to express my most sincere gratitude to my supervisor Dr. Joseph Yan, not only for insightfully guiding and financially supporting my research work, but also for giving me intellectual advice at academic and personal level. I also want to thank him for his valuable comments and questions on my writing, which have significantly improved the quality of my papers and thesis. His contribution to this work is therefore important.

Secondly, I wish to thank Dr. Lin Jiang, Prof. Jiyan Zou, and Dr. Xiaotian Zhang, for their helps in the work. They are always enthusiastic to share their expertise and help me solve problems. I expanded my knowledge through discussions with them. I would also like to thank Prof. Li Ran and Dr. Roberto Ferrero for their constructive advice in improving the thesis.

I also want to thank all my colleagues and friends for the good moments shared, as well as for their help during the last four years. I would especially like to thank Dr. Chuan Xiang for his useful advice in every aspects; he is more of a brother than a colleague.

The China Scholarship Council has provided me financial support on living expenses. I want to thank the relevant officials working for this.

And finally, without hesitation, I would like to thank my fiancee Ziming, my parents and sister for their support and encouragement. The last special thanks go to my family members.

Abstract

Microgrids based on renewable power generation are under increasing development all over the world. Grid-connected inverters form an indispensable interface between the microgrids and power grid, to deliver the renewable energy into the grid by controlling the injected current. Inductor-capacitor-inductor (*LCL*) filters have been widely adopted to attenuate the high-frequency harmonics generated by the inverters. However resonance of the *LCL* filters significantly affects the system control performance in terms of stability, transient response, grid synchronization, and power quality. This thesis carries out comprehensive stability analyses and proposes novel current control methods for studying and improving the performance of *LCL*-filtered grid-connected inverters.

Firstly, a systematic study is carried out on the relationship between the time delay and stability of single-loop controlled grid-connected inverters that employ inverter current feedback (ICF) or grid current feedback (GCF). The ranges of time delay for system stability are analyzed and deduced in the continuous *s*-domain and discrete *z*-domain. It is found that in the optimal range to achieve the maximum bandwidth and ensure adequate stability margins, the existence of a time delay weakens the stability of the ICF loop, whereas a proper time delay is required to maintain the stability of the GCF loop. The present work explains, for the first time, why different conclusions on the stability of ICF loop and GCF loop have been drawn in previous studies. To improve system stability, a linear predictor based time delay reduction method is proposed for ICF, while a time delay addition method is used for GCF. A controller design method is then presented that guarantees adequate stability margins. The study of the delay-dependent stability is validated by simulation and experiment.

Secondly, three current control methods (the single-loop control based on ICF, that based on GCF, and a dual-loop control with capacitor current feedback (CCF)

active damping) are compared by investigating their *LCL* resonance damping mechanism. The virtual impedance introduced by each method is identified, which comprises frequency-dependent resistance (positive or negative) and reactance (inductive or capacitive). The reactance shifts the *LCL* resonance frequency while a positive resistance provides damping to the resonance and hence stabilizes the system. Using the virtual impedance, the system stability is analyzed. The stable range of sampling frequency for the above methods is deduced, as well as the gain boundaries of the controllers. The simple and intuitive stability analysis approach by means of virtual impedance can be extended to other single- or dual-loop control methods. The study facilitates the analysis and design of control loops for grid-connected inverters with *LCL* filters, and it has been verified by experiment.

Thirdly, a pseudo-derivative-feedback (PDF) current control is, for the first time, applied to three-phase *LCL*-filtered grid-connected inverters, which significantly improves the transient response of the system to a step change in the reference input through the elimination of overshoot and oscillation. A complex vector method is applied to the modeling of three-phase *LCL*-filtered inverters in a synchronous rotating frame (SRF) by taking cross-couplings into consideration. Two PDF controllers with different terms in an inner feedback path are developed for an ICF system and a GCF system, respectively. For the ICF system, a simple PDF controller with a proportional term is used. Compared with a proportional-integral (PI) controller, which can only reduce the transient overshoot by decreasing controller gains, the PDF controller is able to eliminate the transient overshoot and oscillation over a wide range of controller parameters. For the GCF system, a PDF controller with a proportional term and a second-order derivative is developed. Active damping is achieved with only one feedback variable of the grid current, and simultaneously the system transient response is improved. Both theoretical analysis and experimental results verify the advantages of the PDF control over PI control methods.

Fourthly and finally, a direct grid current control method without phase-locked loop (PLL) is proposed to attenuate low-order current harmonics in three-phase *LCL*-filtered grid-connected inverters. In comparison with conventional indirect or direct controllers which need PLL and are difficult to achieve satisfactory harmonic attenuation performance, the proposed method is able to satisfactorily mitigate the harmonic distortion, and at the same time reduce control complexity and computation burden because PLL is avoided. It is found that the direct grid current control is necessary to effectively suppress the current harmonics caused by the distortion in grid voltage. Active damping is achieved with an inner ICF loop, which is found to be superior to the widely used CCF damping in improving system stability. A systematic controller design procedure is proposed to optimize the system performance. Experimental results confirm the improved harmonic attenuation ability of the proposed method in comparison to that of conventional control methods.

Contents

List of Figures

List of Tables

List of Abbreviations

ADC	analog-to-digital conversion
CCS	Code Composer Studio
CCF	capacitor current feedback
DAC	digital-to-analog converter
DG	distributed generation
DPGS	distributed power generation system
DSOGI	double second-order generalized integrator
DSP	digital signal processor
GCF	grid current feedback
GM	gain margin
HVDC	high voltage direct current
ICF	inverter current feedback
LCL	inductor-capacitor-inductor
LHP	left half-plane
LP	linear predictor
MIMO	multiple-input multiple-output
OP	optimized design
PCB	printed circuit board
PCC	point of common coupling
PDF	pseudo-derivative-feedback
PEI	power electronic interface
PF	power factor
PI	proportional-integral
PLL	phase-locked loop
PM	phase margin
PR	proportional-resonant

PWM	pulse-width-modulation
RESH	resonant harmonic
RHP	right half-plane
RMS	root-mean-square
SISO	single-input single-output
SO	symmetric optimum
SPI	serial peripheral interface
SPWM	sinusoidal pulse-width-modulation
SRF	synchronous rotating frame
THD	total harmonic distortion
VSI	voltage source inverter
ZOH	zero-order-hold

Chapter 1

Introduction

1.1 Microgrids

Conventional power system is facing the problems of depletion of fossil fuel resources and environmental pollution, which has led to a rising deployment of renewable energy worldwide over the past decade. According to the Renewables 2015 Global Status Report from the REN 21 (Renewable Energy Policy Network for the 21st Century), installed renewable power capacity increased from approximately 800 GW in 2004 to 1712 GW in 2014 [1]. By the end of 2014, renewables comprised an estimated 27.7% of the world's power generating capacity [1]. The growth in capacity and generation will continue to expand in the future [2]. Renewable energy (including hydropower) provided about 22.8% of the global final energy consumption in 2014, and the percentage is expected to reach 31% by 2035 [2, 3].

The development in renewables brings in a new trend of generating power locally at distribution voltage level using renewable energy (wind power, solar photovoltaic, geothermal power, biomass energy, ocean energy, etc.) and their integration into the utility distribution network [4]. This type of power generation is termed distributed generation (DG), which is devised to distinguish this concept of generation from centralized conventional generation [4].

Microgrids are local low-voltage electric power networks with the conglomerate of parallel distributed power generation systems (DPGSs) and a cluster of loads [4, 5]. The maximum capacity of per microgrid, according to IEEE recommendations, is normally restricted to 10 MVA [4, 5]. Microgrids give rise to significant technical

and economic advantages in terms of environmental and market issues, power quality, reliability, and flexibility [4].

Nevertheless, the development of microgrids based on renewable energy sources suffers from many challenges. For example, the intermittent nature (fluctuating wind speed, weather dependent illumination intensity, etc.) of the renewable energy source significantly challenges the power extraction. In addition, the steadily increased penetration and power ratings of renewable power generation play an important role in the operation and management of the power system, which has to be taken into account during its integration into the main grid.

As a consequence, microgrids have to be able to meet very high technical standards, such as voltage and frequency control, active and reactive power control, harmonics minimization etc. [4, 6]. From an operation point of view, the power sources are generally equipped with power electronic interfaces (PEIs) and proper controls to maintain specified power quality and power rating, in order to provide the necessary flexibility, security, and reliability for the operation of microgrids, and thus to ensure customer satisfaction [7, 8]. The PEIs are also essential to process the electricity generated from the renewable resources that may not be in the form needed by the public grid.

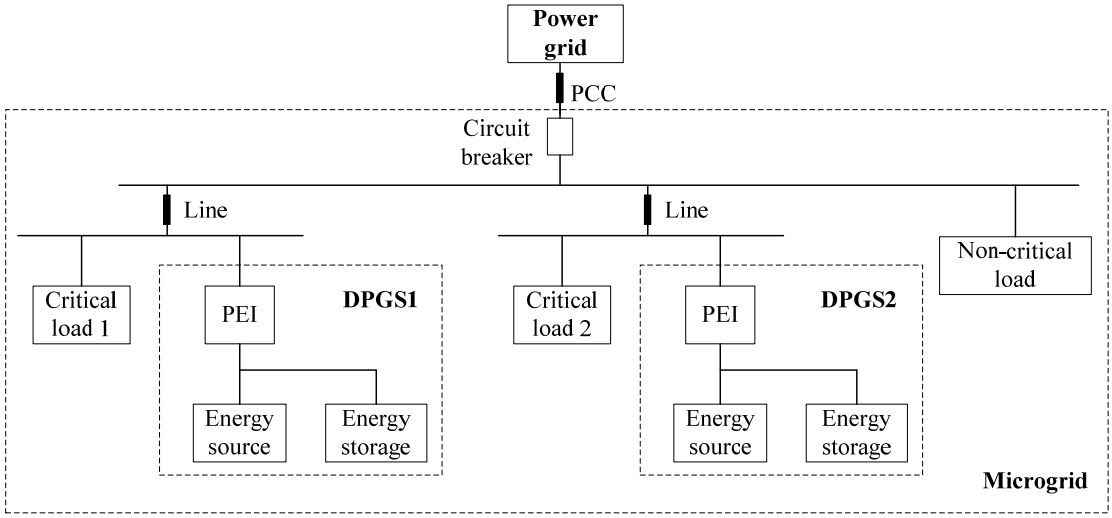

Figure 1.1: Structure of a simplified microgrid with two DPGSs.

A simplified microgrid with two power electronics interfaced DPGSs is illustrated in Figure 1.1. Each DPGS consists of an energy source, an energy storage system, and a PEI. The main function of the energy storage system is to balance the power and energy demand with generation [5, 9, 10]. The microgird is connected to the power grid through a circuit breaker at the point of common coupling (PCC). Microgrids are normally operated in a grid-connected mode, in which the microgrid imports from or exports power to the grid. On the other hand, especially in the case of disturbance in the grid, the microgrid can switch over to a stand-alone mode, in which it should at least feed power to critical loads which require a reliable power supply and good power quality [4].

1.2 DPGS Structure and Control

A general DPGS is illustrated in Figure 1.2 [11]. The input power is transformed into electricity through a power conversion unit which consists of an input-side converter and a grid-side converter [12]. Depending on the nature of input power (wind, solar, etc.), numerous hardware configurations for DPGS can be implemented [7, 8, 10, 13]. For solar energy, the input-side converter usually comprises a DC-DC converter. For wind power, a full-scale pulse-width-modulation (PWM) converter is nowadays becoming more and more attractive [14]. The grid-side converter is a power electronic inverter that transforms DC power into AC electricity. The generated electricity is delivered to the utility network and/or local loads.

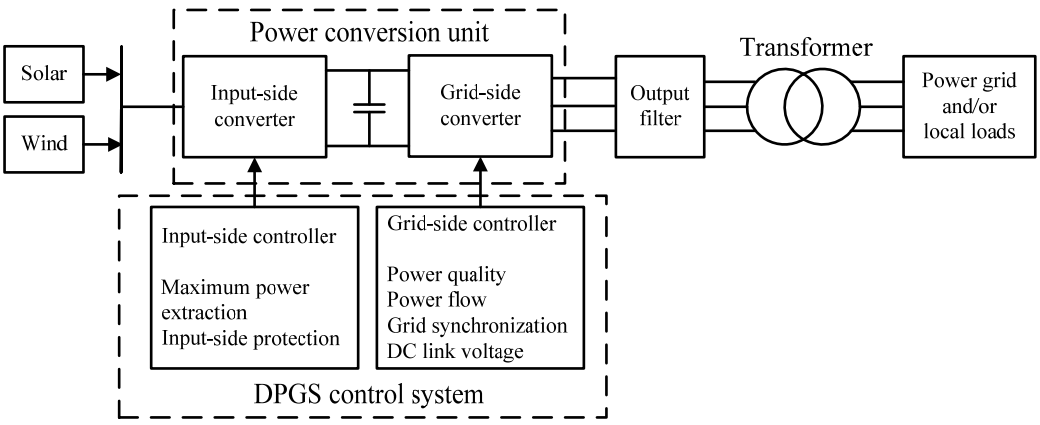

Figure 1.2: General structure of a DPGS with main control features.

The control of input- and grid-side power converters is an important part of the DPGS. The main task of the input-side controller is to extract maximum power from the source and transmit the information of available power to the grid-side controller [15, 16]. Naturally, the protection of input-sider converter should also be considered [12]. For wind turbine systems, the input-side controller has different tasks depending on the generator type used [7, 10, 11, 13]. The grid-side controller basically has the following tasks: power quality control, power flow including active and reactive power control, grid synchronization, and DC link voltage control [7]. Additionally, ancillary services like local voltage and frequency regulation might be requested by the operator [7, 12].

As introduced previously, power electronic inverters can work in grid-connected and stand-alone modes. Traditionally, in the grid-connected mode the inverters behave as a current source, since the grid voltage is generally not affected by the inverter operation [12]. In this case the injected current should be controlled, to deliver a scheduled amount of active and reactive power. By contrast, in the stand-alone mode, the inverters act as a voltage source which should maintain a stable voltage and frequency by performing active and reactive power control [17].

In the present work, two-level PWM voltage source inverters (VSIs) are used for interacting with the power grid, because at present this is the state-of-art topology employed by all manufacturers [7, 8, 12]. This structure of inverter allows the use of high switching frequencies and proper control strategies that provide flexibility in system design and control, making these converters suitable for the DPGS. Yet, more complicated three-level neutral-point-clamped VSI and multilevel converters are under development and can be used for high-power systems to avoid high voltage power devices [14, 18, 19]. The proposed methods and conclusions in this thesis are also applicable to the latter converter topologies.

1.3 Challenges in the Control of Grid-Connected Inverters

The work in this thesis focuses on the current control of grid-connected inverters in microgrids. Similar to a common control system, the current control of the inverter system should concern issues such as system stability and dynamic performance. Particularly, the main objective of the grid-tied converter is the interaction with the grid. Therefore other tasks including power quality control and grid synchronization should be achieved. In the following subsections, the main challenges in the current control of grid-connected inverters are introduced in details.

1.3.1 System Stability

Stability is the most important issue of a control system. A system should maintain stable operation with adequate stability margins before other requirements are fulfilled. For a linear time invariant analog system, the requirement for stability is that all poles of the closed-loop transfer function must be in the left half-plane (LHP) [20]. Hence stability analysis is to determine if there is any pole either on the imaginary axis or in the right half-plane (RHP). Stability analysis can be carried out in different approaches. Classical methods include Routh's stability criterion, root-locus analysis, frequency-response based Nyquist stability criterion, etc. [20-22].

With the increasing performance and decreasing price of digital signal processors (DSPs), nowadays there has been an increasing use of digital controllers for power converters. Compared with analog controllers, digital controllers have a number of advantages such as high flexibility and complexity in control algorithms, immunity to switching noises, lower sensitivity to variation of control parameters, and reduction of hardware components [23].

Ideally, signals are expected to be transmitted immediately in a control system. However, digital control introduces unavoidable time delay which will significantly affect the stability. The time delay consists of the time for analog-to-digital conver-

sion (ADC), computation, PWM, and signal transport [23]. The knowledge of digitally controlled power inverters is still developing. A few publications have focused on the study of the stability of grid-connected inverters. However, there are still confusions in conclusions and findings relevant to the stability analysis [23-34]. Therefore, a thorough theoretical study is needed to investigate the relationship between time delay and stability of digitally controlled grid-connected inverters.

1.3.2 Transient Performance

When the delivered power into the power grid needs to be adjusted, there is usually a step change in the reference current, which results in a transient response in the system. Requirements regarding the transient response are becoming more and more restrictive [22, 35-37]. Specifically, characteristics such as rise time, settling time, overshoot and oscillation damping are all required to be satisfactory [20]. For example, overshoot is often limited by the converter current rating, and the situation is more stringent in high power applications [33]. Un-damped oscillations would deteriorate the power quality and create objectionable flicker [38].

Conventionally, proportional-integral (PI) and proportional-resonant (PR) controllers are employed for grid-connected inverters, and they needs to be carefully tuned in order to achieve reasonable dynamic performance [33, 35-37, 39]. However, it is difficult to obtain satisfactory system performance in all aspects. For example, when the rise time and resonance damping meet requirements, overshoot would occur [33]. A common method to reduce overshoot is to decrease controller gains, which however leads to degraded bandwidth and disturbance rejection capability [25, 36, 40]. Several other current control techniques, including hysteresis, deadbeat, and nonlinear controllers, have been reported to achieve an improved transient response [35, 41-48]. Nonetheless, these methods are more complicated than the conventional PI and PR controllers.

In view of the limitations of existing controllers in optimizing the transient response, it is of great interest to study and propose a simple yet effective control

method for grid-connected inverters to achieve satisfactory transient performance with fast response but without overshoot or oscillation.

1.3.3 Grid Synchronization

The delivered current from the inverter into the power grid has to be synchronized with the grid voltage [12]. For the purpose of grid synchronization, the phase angle used for the grid-connected inverters to generate the reference current should be a clean signal and be synchronized with the grid voltage. Grid synchronization algorithms play an important role for the inverter to accurately detect the phase signal of the positive sequence component of the grid voltage [12, 49].

A comparison of the main techniques used for detecting the phase angle on different grid conditions can be found in [50]. Among the different strategies including zero crossing methods and filter algorithms, phase-locked loop (PLL) is most widely used [12, 50]. For balanced three-phase grid voltage, a synchronous reference frame (SRF) PLL is able to achieve satisfactory performance [51]. On the other hand, under non-ideal grid conditions, for example with unbalanced grid faults and/or harmonic distortions, improvements to the SRF-PLL are necessary [52-54].

It is apparent that the use of PLL increases the complexity and computation burden in the control algorithm, especially for sophisticated PLLs. PLL will also affect the output admittance and even trigger low-frequency instability [55, 56]. Therefore simple and satisfactory grid synchronization method without the use of a PLL, which is able to reduce the control complexity and alleviate the computation burden, is attractive in view that the resource of DSP is limited.

1.3.4 Power Quality

One of the demands for a grid-connected inverter system is the quality of the power injected to the grid. More and more attention has been paid on the control of power quality as a result of the increased use of power electronic equipment (nonlinear loads) which is a significant source of current harmonics. The harmonics can

cause harmonic distortion to the grid voltage and result in extra losses or even in disturbances with other customers. Therefore it is necessary to suppress harmonics and to prevent power quality degradation. According to the standards in this field, the limit for the total harmonic distortion (THD) of the delivered current is set to 5% [12, 38, 49]. A detailed limitation of the harmonic distortion with regard to each harmonic component is summarized in Table 1.1.

Table 1.1: Distortion limits for grid-connected inverters

Odd harmonics	Distortion limit
$3^{rd} – 9^{th}$	< 4.0%
$11^{th} – 15^{th}$	< 2.0%
$17^{th} – 21^{st}$	< 1.5%
$23^{rd} – 33^{rd}$	< 0.6%

In order to comply with these requirements, different control and harmonics compensation methods can be employed, especially for low-order harmonics that normally have a high content in the power system. Different current controllers implemented in different reference frames provide the system with different harmonic attenuation capability [26, 57-60].

High-order harmonics, mainly caused by PWM switching, are small in magnitude and can be mitigated by a low-pass filter that is connected as an interface between the inverter and power grid. An inductor (*L*-filter) is conventionally adopted. It however requires a large inductance and high switching frequency in order to satisfactorily attenuate the PWM harmonics [22, 45, 61]. To address the problem, inductor-capacitor-inductor (*LCL*) filters have been widely applied, which have better attenuating ability and require lower inductance inductors leading to cost-effective solutions [23, 62-65]. The *LCL* filter is thus employed in the work of the thesis and will be introduced in more details in Section 2.2.

Despite the above advantages, additional resonance effects are brought in by the third-order *LCL* filters, which create a pair of open-loop poles located on the

closed-loop stability boundary and thus cause stability problems [66-69]. The *LCL* resonance will also degrade system dynamics leading to undesired overshoot and oscillation [33, 40, 42, 45]. Furthermore, because of the high-order of the filter, complexity and difficulty are dramatically increased in the modeling of the system as well as in the control of grid synchronization and power quality [25, 26, 55, 56, 70].

1.4 Objectives, Overview, and Achievements of the Thesis

1.4.1 Objectives

The objective of the thesis is to address the aforementioned issues in the current control of grid-connected inverters with *LCL* filters, by performing comprehensive system stability analyses and proposing novel current control methods. Specific objectives are summarized below.

The first is to systematically study the relationship between time delay and stability of single-loop controlled grid-connected inverters, in order to clarify the confusions among different conclusions and findings in existing work relevant to stability and to provide a unified explanation.

The second is to study the *LCL* resonance damping mechanism of different control methods, and to propose a simple and intuitive approach to analyze system stability and predict controller gain boundaries.

The third is to apply a pseudo-derivative-feedback (PDF) method, as an advantageous strategy over the PI control, to improve the transient response of three-phase *LCL*-filtered grid-connected inverters to a step change in the reference input via eliminating overshoot and oscillation.

The last objective is to propose a simple and effective current control method for power quality improvement and grid synchronization without the use of PLL, with the aim to effectively attenuate low-order current harmonics and significantly reduce control complexity and computation burden.

1.4.2 Thesis Overview

This thesis contains seven chapters. In addition to Chapter 1 on the background and introduction of the work, the other chapters are organized as follows:

In Chapter 2, a number of fundamental aspects that are involved in the control of grid-connected inverters are introduced in detail. First of all the resonance problem of an *LCL* filter is presented. Then the principle of a basic PLL is introduced, as well as signal transformations among three different reference frames: natural frame, stationary frame, and synchronous rotating frame (SRF). In addition, different control schemes in these frames are introduced. This is followed by a description of different PWM strategies. Furthermore, a single-loop control system is provided to exemplify the modeling of digitally controlled grid-connected inverters. Finally, the design and development of the experimental system that is used to carry out real-time experiments are described.

Chapter 3 carries out a thorough theoretical study on the relationship between time delay and stability of single-loop controlled grid-connected inverters with *LCL* filters. Stable ranges of the time delay are derived in the continuous *s*-domain as well as in the discrete *z*-domain. Following this, time delay compensation methods are proposed for improving the stability of the single-loop systems. This is followed by a simple PI tuning method, without simplification, to ensure adequate stability margins. In the end, simulated and experimental results are provided to validate and verify the delay-dependent stability study.

Chapter 4 compares three current control methods by investigating their virtual impedances, which are used to study system stabilities. It is found that the virtual impedance achieves a potential damping to the *LCL* resonance. Based on this finding, the requirements on sampling frequency are identified by the analysis of damping characteristics. Furthermore, the gain boundaries of the controllers for different cases are deduced in an intuitive manner, which are then confirmed by root loci. Experimental results validate the stability analysis by means of virtual impedance.

Chapter 5 applies the PDF current control method to improve the transient response to a step change in the reference input through the elimination of overshoot and oscillation. This chapter begins with an introduction of a generalized PDF control system. Then a complex vector method is applied to the modeling of a three-phase *LCL*-filtered system in the SRF, with cross-couplings being taken into account. Two PDF controllers are then developed for an inverter current feedback (ICF) and a grid current feedback (GCF) system, respectively. Having designed the PDF controllers, experimental results are finally presented to verify their improved transient performance compared to conventional PI control methods.

Chapter 6 proposes a novel current control method for three-phase grid-connected inverters, which generates the reference current directly from the grid voltage and effectively suppresses the low-order harmonic distortions. It is demonstrated that the conventional current control methods are difficult to achieve satisfactory harmonic attenuation performance because of an indirect control and/or PLL. The interaction between active damping methods and resonant harmonic (RESH) compensators is discussed. Then a systematic controller design method is proposed to optimize the control performance. The improved harmonic attenuation ability of the proposed method in comparison to that of conventional control methods is confirmed by experimental results.

Finally, conclusions are summarized and possible future work is proposed in Chapter 7.

1.4.3 Major Achievements

A. Delay-dependent stability of single-loop controlled grid-connected inverters with *LCL* filters

A systematical study is carried out on the relationship between time delay and stability of single-loop controlled grid-connected inverters that employ ICF or GCF. It is found that the time delay is a key factor that affects the system stability. The

study has, for the first time, explained why different conclusions on the stability of the single-loop control systems were drawn in different publications.

- Stable ranges of the time delay are derived in the continuous *s*-domain and discrete *z*-domain. Optimal delay range is also identified. The procedure can be extended to analyze the influence of time delay on other control methods including active damping.
- It is found that the existence of a time delay weakens the stability of the ICF loop, whereas a proper time delay is required for the GCF loop.
- Time delay compensation methods are proposed to improve the stability and the allowed sampling frequency ranges of the single-loop control systems.
- A simple PI tuning method without simplification is proposed, by which adequate stability margins can be guaranteed.

B. Damping investigation of *LCL*-filtered grid-connected inverters

The damping mechanism of three different control methods to the *LCL* resonance has been investigated by identifying their closed-loop virtual impedances, in this way a simple and intuitive approach by means of the virtual impedance is proposed that is able to analyze system stability and predict controller gain boundaries.

- The virtual impedances of three control methods including single- and dual-loop strategies are identified, and the stability of these methods are explicitly compared.
- Requirements on the sampling frequency of single-loop controllers have been deduced, different cases of the dual-loop controller have been identified.
- Controller gain boundaries are intuitively and easily derived by means of the virtual impedance.

C. Pseudo-derivative-feedback current control for three-phase grid-connected inverters with *LCL* filters

The PDF current control is, for the first time, applied to three-phase *LCL*-filtered grid-connected inverters, which significantly improves the transient response of the system to a step change in the reference input through the elimination of overshoot and oscillation. Compared with the PI control, which can only reduce the transient overshoot by decreasing controller gains, the PDF control completely eliminates the overshoot and oscillation over a wide range of controller parameters.

- Complex vector continuous and discrete models of the three-phase inverter in the SRF are derived, with cross-couplings being accurately taken into account.
- A simple PDF controller with the structure similar to PI controller is designed for an ICF system. A complete comparison between the transient performance of the PDF and PI controllers is presented.
- A PDF controller with an additional second-order derivative term is developed for a GCF loop. Active damping is achieved with only one feedback signal, and simultaneously the transient response is improved.
- Controller tuning procedures are proposed to optimize system performance.

D. Attenuation of low-order current harmonics in three-phase *LCL*-filtered grid-connected inverters

A direct grid current control method is proposed that omits the use of PLL and effectively mitigates the low-order current harmonics in digitally controlled three-phase *LCL* filtered inverters. In comparison to conventional control methods, the proposed strategy obtains a much higher power quality and reduces the control complexity and computation burden.

- It is found that the conventional current control methods are difficult to achieve a satisfactory harmonic attenuation performance because of an indirect control and/or PLL.

- The interaction between active damping methods and RESH compensators is studied, and it is found an ICF damping is superior to a widely used capacitor current feedback (CCF) damping in improving system stability.
- A controller design procedure is presented that guarantees adequate stability margins and ensures satisfactory power factor (PF) when the grid frequency varies.

1.5 List of Publications

Journal papers

1. J. Wang, J. Yan, L. Jiang, and J. Zou, "Delay-dependent stability of single-loop controlled grid-connected inverters with LCL filters," *IEEE Transactions on Power Electron*ics, 31(01): 743-757, Jan. 2016.
2. J. Wang, J. Yan, and L. Jiang, "Pseudo-derivative-feedback current control for three-phase grid-connected inverters with LCL filters," *IEEE Transactions on Power Electron*ics, 31(05): 3898-3912, May. 2016.
3. J. Wang, J. Yan, and J. Zou, "Complex vector modeling and control of three-phase LCL-filtered grid-connected inverters," *IEEE Transactions on Industrial Electron*ics, under review.
4. J. Wang, J. Yan, and J. Zou, "Damping investigation of LCL-filtered grid-connected inverters: An overview," A manuscript will be submitted to *IEEE Transactions on Power Electron*ics.

Conference papers

1. J. Wang and J. Yan, "Using virtual impedance to analyze the stability of LCL-filtered grid-connected inverters", in *16th IEEE International Conference on Industrial Technology*, ICIT 2015, Seville, Spain, pages 1220-1225, Mar. 2015.

2. J. Wang, J. Yan, L. Jiang, and J. Zou, “Attenuation of low-order current harmonics in three-phase LCL-filtered grid-connected inverters” In *41st Annual Conference of the IEEE Industrial Electronics Society*, IECON 2015, Yokohama, Japan, pages 1982-1987, Nov. 2015.
3. J. Wang, J. Yan, and J. Zou, “Inherent damping of single-loop digitally controlled voltage source converters with LCL filters,” in *25th IEEE International Symposium on Industrial Electronics*, ISIE 2016, Santa Clara, USA, pages 487-492, Jun. 2016.

Chapter 2

Fundamental Aspects in the Control of Grid-Connected Inverters

2.1 Introduction

Grid-connected inverters form an indispensable interface between the DPGS and power grid. The inverter normally acts as a voltage controlled current source and its operation and control play a crucial role upon the quality of power injected to the grid [12]. The operation and control of grid-connected inverters involve a number of fundamental aspects.

The first one is the *LCL* filter that is widely adopted to attenuate the high-frequency harmonics generated from PWM switching. The *LCL* filter has a wonderful harmonic suppression capability but introduces resonance problems that considerably challenge the control design [25, 40, 71, 72]. Damping strategies to the *LCL* resonance are usually used to improve control performances.

The second is PLL that is commonly adopted to detect the accurate phase information of the grid voltage, for the purpose of grid synchronization. A basic PLL system is implemented in the SRF, known as SRF-PLL [51]. Signal transformations among three different reference frames are needed to design the PLL. The three frames are: natural frame, stationary frame, and SRF [11, 12, 73]. Different signal types are obtained by the transformations.

The transformations enable the control of three-phase grid-connected inverters to be implemented in these three different reference frames. In the frames, different

circuit models are obtained, and different control schemes and compensators are employed.

PWM strategies are necessary to generate pulses for driving switching transistors (IGBTs are used) in the inverters, in this way to transfer modulation signals produced by controllers into inverter voltage [74]. Different PWM methods are available, and the most used carrier-based bipolar sinusoidal PWM (SPWM) is adopted in the work.

The analysis and design of a digitally controlled system can be performed in the discrete *z*-domain as well as in the continuous *s*-domain [21, 23]. In order to complete the control design, models of the PWM and control system should be obtained.

In this chapter, the above issues in the control of grid-connected inverters are introduced in detail. This chapter is closed by an introduction of the design and development of the experimental system that is used to carry out real-time experiments. Hardware components and functions are described, as well as the software environment. The system has a complete hardware and software protection design to prevent hazards from errors. All findings and conclusions in the work have been validated and verified by experimental results from the system.

2.2 *LCL* Filter

The PWM inverter with a typical switching frequency between 2–15 kHz produces high-order harmonics around the switching frequency that can disturb sensitive equipment and cause power losses. Conventionally, an inductance with high value is used to reduce the harmonics. However, it becomes rather expensive to realize high value inductor when applications are above several kilowatts. *LCL* filter is an attractive alternative to solve this problem, which allows the range of power levels up to hundreds of kilovoltamperes while using quite small values of inductors and capacitors, thus leading to cost-effective solutions.

The *LCL*-filtered grid-connected inverter is shown in Figure 2.1, where the inverter is supplied with a constant DC voltage V_{dc}. The inverter-side inductor L_i and

its parasitic resistor R_i, grid-side inductor L_g and its parasitic resistor R_g, and capacitor C are the components of the LCL filter (parameters used in the work are given in Table 2.2). v_i is the inverter voltage generated by the inverter, v_c is the voltage across the capacitor, and v_g is the grid voltage; i_i is the inverter current, i_c is the capacitor current, and i_g is the grid current that is injected into the grid.

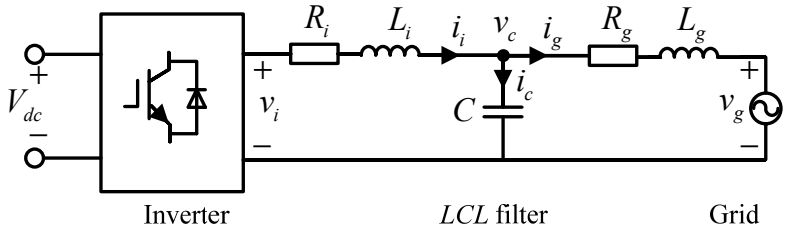

Figure 2.1: LCL-filtered grid-connected inverter.

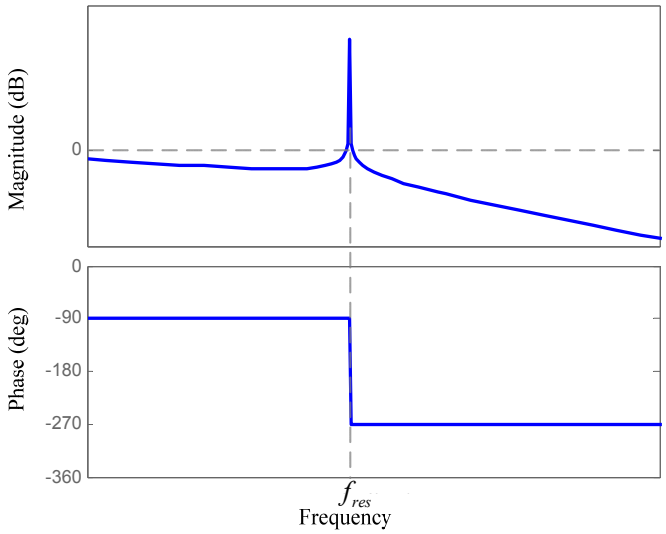

Figure 2.2: Bode diagram of the transfer function from v_i to i_g.

The transfer function from v_i to i_g is given as (considering the grid as a short circuit):

$$G_{i_g v_i}(s) = \frac{i_g(s)}{v_i(s)} = \frac{1}{s^3 C L_i L_g + s^2 C\left(R_i L_g + L_i R_g\right) + s(C R_i R_g + L_i + L_g) + R_i + R_g}. \quad (2.1)$$

The Bode diagram of (2.1), when the small parasitic resistances are ignored, is shown in Figure 2.2, where $f_{res} = \sqrt{(L_i + L_g)/L_i L_g C}/2\pi$ is the LCL resonance frequency. As can be seen, the third-order filter has a pair of poles at the resonance frequency, at which a ripple in the magnitude and a –180° fall in the phase are generated

[30]. The resonance will cause stability problems which considerably challenge the control design for the system [25, 40, 71, 72]. The small parasitic resistances can slightly alleviate the resonance problem, but the damping is far from sufficiency and thus can be neglected [24, 30].

A step-by-step procedure to design an *LCL* filter has been proposed in [62], which aims to optimize the current ripple attenuation passing from i_i to i_g, the voltage drop across the inductors, and the decrease of power factor caused by the capacitor, etc. In particular, the resonance frequency f_{res} should be in a range between ten times the grid frequency and one-half of the switching frequency, in order to avoid resonance problems in the lower and upper parts of the harmonic spectrum [62]. Note that the switching frequency can be adjusted to fulfill this requirement when the resonance frequency is set.

A direct way to damp the resonance is adding a passive resistor to be in series or parallel with the capacitor or inductors. This method, called passive damping, is easy to be implemented but will bring in power losses [68]. To avoid the power loss, active damping methods are widely researched by designing proper controller schemes [75-78]. Active damping methods can be classified into two main classes: multiloop- and filter-based active damping. The filter-based damping is using a high order controller to cancel the resonance poles, and it can be seen as a filter [25, 79, 80]. The drawback of this active damping method is its complex design algorithms. The multiloop-based active damping is realized by employing an inner damping loop with the feedback of variables such as the inverter current, capacitor voltage, and capacitor current [23, 58, 76, 81]. This type of active damping is the most popular method to improve the stability of *LCL*-filtered grid-connected inverters. Nonetheless, it requires the feedback of more than one signal, which increases the number of sensors.

Besides the methods incorporating active damping techniques, simple but effective single-loop control methods without additional damping have been proposed and researched for the *LCL*-filtered grid-connected inverters, employing inverter current

feedback (ICF) or grid current feedback (GCF) [23-34]. It has been proved that both the ICF and GCF loops can be made stable because of their inherent damping characteristics [24, 28, 29].

Apart from being used as the grid-connected inverter in microgrids, the converter structure in Figure 2.1 can be used in other applications, e.g., active power filters and rectifiers in power systems [62, 82], AC drives for electric machines [36], and power converters in high-voltage DC (HVDC) transmission systems [83, 84], etc. Current control is also essential in these applications. Therefore the work in this thesis can also contribute to these applications.

2.3 PLL and Frame Transformations

The injected current from the grid-connected inverters should be synchronized with the grid voltage. For grid synchronization, PLLs are commonly adopted to detect the accurate phase information of the grid voltage, and thus is an important part of the DPGS.

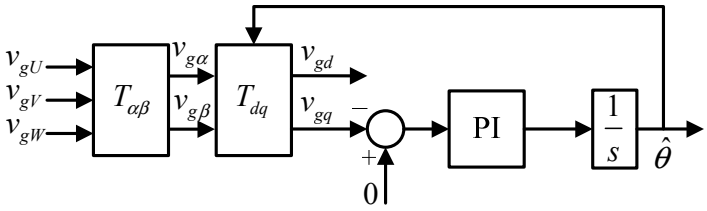

Figure 2.3: Structure of the SRF-PLL.

A basic PLL system is implemented in the SRF, known as SRF-PLL [51]. The structure of the SRF-PLL is shown in Figure 2.3. The three-phase grid voltage in the natural *abc* frame is firstly transformed into the stationary $\alpha\beta$ frame using the Clarke transformation (2.2) [53] (the inverse Clarke transformation is given in (2.3)). Then the $\alpha\beta$ signals are transformed into the SRF using the Park transformation (2.4) with the detected phase signal $\hat{\theta}$(the inverse Park transformation is given in (2.5)).

$$\begin{bmatrix} x_\alpha \\ x_\beta \end{bmatrix} = T_{\alpha\beta} \begin{bmatrix} x_a \\ x_b \\ x_c \end{bmatrix} = \frac{2}{3} \begin{bmatrix} 1 & -\frac{1}{2} & -\frac{1}{2} \\ 0 & \frac{\sqrt{3}}{2} & -\frac{\sqrt{3}}{2} \end{bmatrix} \begin{bmatrix} x_a \\ x_b \\ x_c \end{bmatrix} \tag{2.2}$$

$$\begin{bmatrix} x_a \\ x_b \\ x_c \end{bmatrix} = T_{\alpha\beta}^{-1} \begin{bmatrix} x_\alpha \\ x_\beta \end{bmatrix} = \begin{bmatrix} 1 & 0 \\ -\frac{1}{2} & \frac{\sqrt{3}}{2} \\ -\frac{1}{2} & -\frac{\sqrt{3}}{2} \end{bmatrix} \begin{bmatrix} x_\alpha \\ x_\beta \end{bmatrix} \tag{2.3}$$

$$\begin{bmatrix} x_d \\ x_q \end{bmatrix} = T_{dq} \begin{bmatrix} x_\alpha \\ x_\beta \end{bmatrix} = \begin{bmatrix} \cos\hat{\theta} & \sin\hat{\theta} \\ -\sin\hat{\theta} & \cos\hat{\theta} \end{bmatrix} \begin{bmatrix} x_\alpha \\ x_\beta \end{bmatrix} \tag{2.4}$$

$$\begin{bmatrix} x_\alpha \\ x_\beta \end{bmatrix} = T_{dq}^{-1} \begin{bmatrix} x_d \\ x_q \end{bmatrix} = \begin{bmatrix} \cos\hat{\theta} & -\sin\hat{\theta} \\ \sin\hat{\theta} & \cos\hat{\theta} \end{bmatrix} \begin{bmatrix} x_d \\ x_q \end{bmatrix} \tag{2.5}$$

A balanced three-phase grid voltage is represented as (2.6), where V_m is the amplitude and $\theta_g = \omega_n t$, with ω_n being the fundamental grid frequency. The $\alpha\beta$ and dq signals are then yielded as (2.7) and (2.8), respectively. As can be seen, the $\alpha\beta$ signals are AC while the dq signals are DC if the detected phase $\hat{\theta}$ is identical to θ_g [73].

$$\begin{bmatrix} v_{gU} \\ v_{gV} \\ v_{gW} \end{bmatrix} = V_m \begin{bmatrix} \cos\theta_g \\ \cos(\theta_g - \frac{2}{3}\pi) \\ \cos(\theta_g + \frac{2}{3}\pi) \end{bmatrix} \tag{2.6}$$

$$\begin{bmatrix} v_{g\alpha} \\ v_{g\beta} \end{bmatrix} = T_{\alpha\beta} \begin{bmatrix} v_{gU} \\ v_{gV} \\ v_{gW} \end{bmatrix} = V_m \begin{bmatrix} \cos\theta_g \\ \sin\theta_g \end{bmatrix} \tag{2.7}$$

$$\begin{bmatrix} v_{gd} \\ v_{gq} \end{bmatrix} = T_{dq} \begin{bmatrix} v_{g\alpha} \\ v_{g\beta} \end{bmatrix} = V_m \begin{bmatrix} \cos(\theta_g - \hat{\theta}) \\ \sin(\theta_g - \hat{\theta}) \end{bmatrix} \tag{2.8}$$

The linearized model of Figure 2.3 is demonstrated in Figure 2.4, where the PI controller is employed [51, 52]:

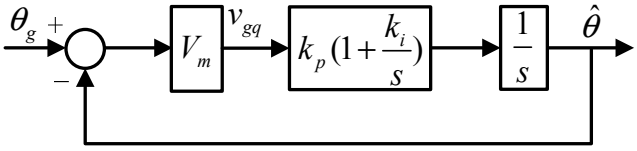

Figure 2.4: Linearized control loop of SRF-PLL.

$$G_{PI}(s) = k_p(1+\frac{k_i}{s}). \tag{2.9}$$

It is obvious that the system is type 2 which is able to track the ramp phase signal with zero steady-state error, i.e., $\hat{\theta} = \theta_g$. Therefore the grid synchronization is achieved.

When the grid voltage is unbalanced and/or with harmonic distortions, the phase signal detected by the SRF-PLL would be distorted. In this case, sophisticated PLLs such as a decoupled double SRF-PLL and double second-order generalized integrator (DSOGI) based PLL can achieve a satisfactory performance [52, 53].

2.4 Control Schemes for Grid-Connected Inverters

As introduced above, different signal types are obtained by the frame transformations. As a result, for three-phase grid-connected inverters, the current control can be performed in the three reference frames [11, 12]. In this section, control schemes in these frames are introduced.

2.4.1 Natural Frame Control

The control scheme in the natural frame is shown in Figure 2.5. The idea of the scheme is to have an individual controller for each phase. The inverter current i_i, grid current i_g, and/or capacitor current i_c are usually sensed as the feedback variables, to form a single- or dual-loop current control system. The current controller can be linear and nonlinear. Typical linear controllers include PI and PR controllers. Representative nonlinear controllers include hysteresis and deadbeat controllers [35, 41, 48]. m_U, m_V, and m_W are modulation signals generated from the controller. The refer-

ence current is produced from the reference i_{dq}^{*} in the SRF, to deliver controllable active/reactive power (see Section 2.4.3) [12, 85].

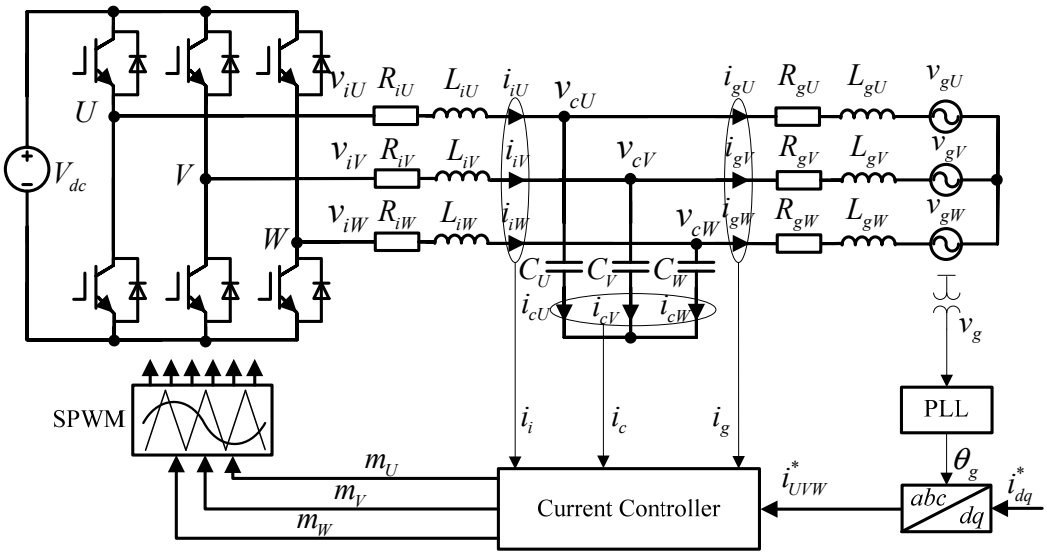

Figure 2.5: Control scheme in the natural frame.

In the situation of an isolated neutral transformer being used as grid interface, only two of the three-phase grid current needs be independently measured, because according to the Kirchhoff's current law the third one is the negative sum of the other two [12]. It means that only two controllers are necessary.

The circuit and electrical variables are considered as balanced throughout the thesis. Differential equations of the circuit in the natural frame are given as:

$$\begin{cases} L_i \dfrac{d}{dt}\begin{bmatrix} i_{iU} \\ i_{iV} \\ i_{iW} \end{bmatrix} + R_i \begin{bmatrix} i_{iU} \\ i_{iV} \\ i_{iW} \end{bmatrix} = \begin{bmatrix} v_{iU} \\ v_{iV} \\ v_{iW} \end{bmatrix} - \begin{bmatrix} v_{cU} \\ v_{cV} \\ v_{cW} \end{bmatrix} \\ C \dfrac{d}{dt}\begin{bmatrix} v_{cU} \\ v_{cV} \\ v_{cW} \end{bmatrix} = \begin{bmatrix} i_{iU} \\ i_{iV} \\ i_{iW} \end{bmatrix} - \begin{bmatrix} i_{gU} \\ i_{gV} \\ i_{gW} \end{bmatrix} \\ L_g \dfrac{d}{dt}\begin{bmatrix} i_{gU} \\ i_{gV} \\ i_{gW} \end{bmatrix} + R_g \begin{bmatrix} i_{gU} \\ i_{gV} \\ i_{gW} \end{bmatrix} = \begin{bmatrix} v_{cU} \\ v_{cV} \\ v_{cW} \end{bmatrix} - \begin{bmatrix} v_{gU} \\ v_{gV} \\ v_{gW} \end{bmatrix} \end{cases} \tag{2.10}$$

2.4.2 Stationary Frame Control

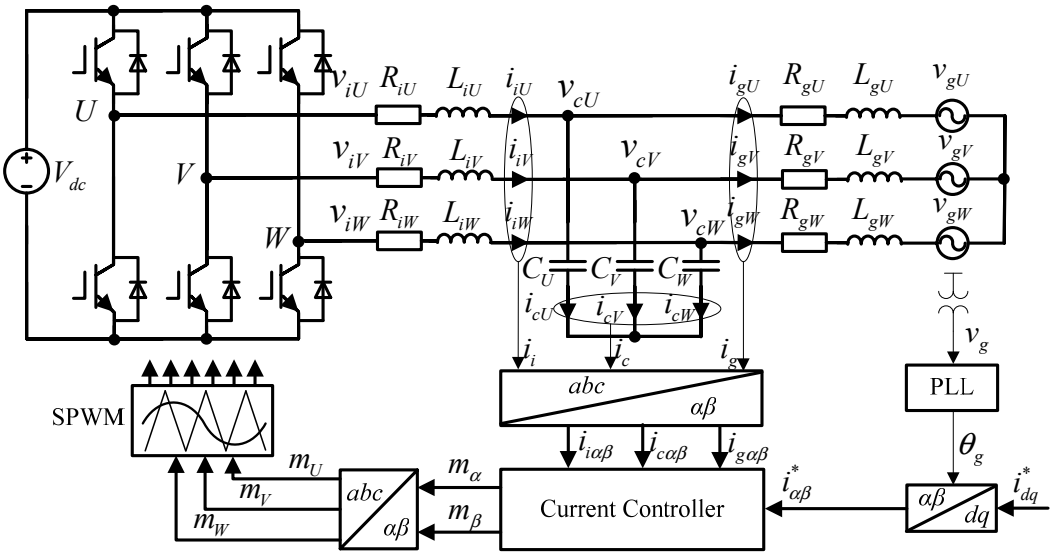

Figure 2.6: Control scheme in the stationary frame.

The control scheme is shown in Figure 2.6. The same as in the natural frame, the control variables in the stationary frame are sinusoidal, leading to difficulties in regulating the fundamental frequency and rejecting harmonic distortions. The PR regulator, expressed as (2.11) where k_p is the proportional gain and k_r the resonant gain and ω_0 the resonant frequency (fundamental or harmonics frequency), is able to achieve a zero steady-state error because of the infinite at the resonant frequency [37, 86, 87]. Therefore the PR controller is usually employed in the stationary frame and natural frame [22, 26, 75, 86]. More details about the PR controller can be found in Chapter 6.

$$G_{PR}(s) = k_p\left(1 + \frac{k_r s}{s^2 + \omega_0^2}\right) \tag{2.11}$$

Differential equations of the circuit in the stationary frame are deduced as:

$$\begin{cases} L_i \dfrac{d}{dt}\begin{bmatrix} i_{i\alpha} \\ i_{i\beta} \end{bmatrix} + R_i \begin{bmatrix} i_{i\alpha} \\ i_{i\beta} \end{bmatrix} = \begin{bmatrix} v_{i\alpha} \\ v_{i\beta} \end{bmatrix} - \begin{bmatrix} v_{c\alpha} \\ v_{c\beta} \end{bmatrix} \\ C \dfrac{d}{dt}\begin{bmatrix} v_{c\alpha} \\ v_{c\beta} \end{bmatrix} = \begin{bmatrix} i_{i\alpha} \\ i_{i\beta} \end{bmatrix} - \begin{bmatrix} i_{g\alpha} \\ i_{g\beta} \end{bmatrix} \\ L_g \dfrac{d}{dt}\begin{bmatrix} i_{g\alpha} \\ i_{g\beta} \end{bmatrix} + R_g \begin{bmatrix} i_{g\alpha} \\ i_{g\beta} \end{bmatrix} = \begin{bmatrix} v_{c\alpha} \\ v_{c\beta} \end{bmatrix} - \begin{bmatrix} v_{g\alpha} \\ v_{g\beta} \end{bmatrix} \end{cases} \tag{2.12}$$

It can be seen that α- and β-axis variables are independently from each other. In addition, the structure and parameters of the two-axis system are identical to that of the original three-phase system (2.10) [73, 87]. Consequently, the design of current controllers in this frame can be done exactly as on a single-phase inverter [73].

2.4.3 Synchronous Rotating Frame Control

As introduced previously, three-phase sinusoidal variables can be transformed into two DC signals in the SRF that synchronously rotates with the frequency of the grid voltage [11, 12, 73, 88]. From the control point of view, the control in the SRF with DC signals is advantageous and is thus widely used [12, 35, 36].

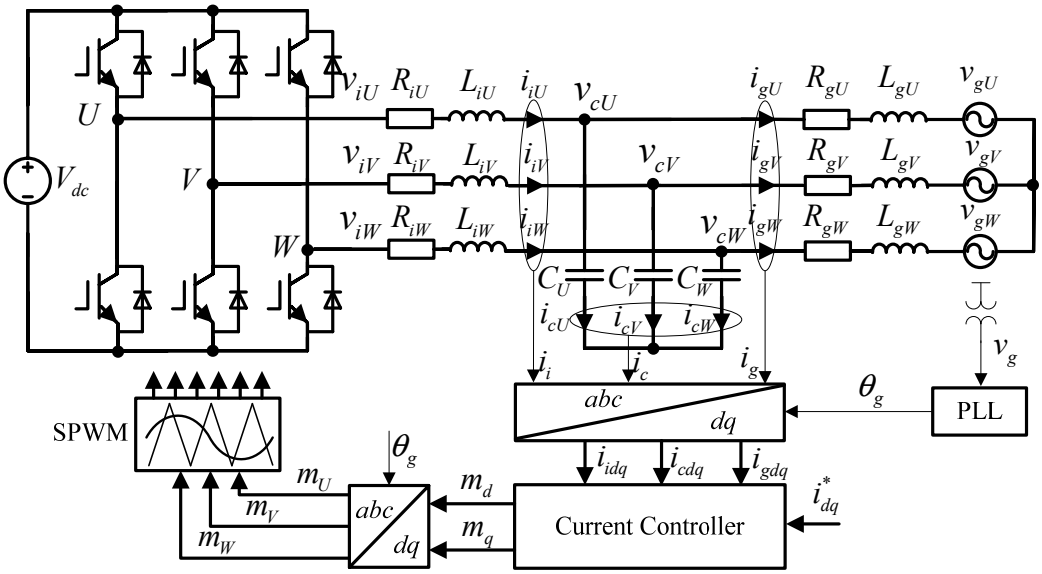

Figure 2.7: Control scheme in the SRF.

The control scheme in the SRF is shown in Figure 2.7. The instantaneous active (P) and reactive (Q) powers injected into the power grid are given as (2.13) [89, 90]. Normally, PI controllers are associated with this control structure [34, 35, 61].

$$\begin{cases} P = \dfrac{3}{2}(v_{gd}i_{gd} + v_{gq}i_{gq}) \\ Q = \dfrac{3}{2}(v_{gq}i_{gd} - v_{gd}i_{gq}) \end{cases} \tag{2.13}$$

Differential equations of the circuit in the SRF are yielded as:

$$\begin{cases} L_i \dfrac{d}{dt}\begin{bmatrix} i_{id} \\ i_{iq} \end{bmatrix} + \begin{bmatrix} R_i & -\omega_n L_i \\ \omega_n L_i & R_i \end{bmatrix}\begin{bmatrix} i_{id} \\ i_{iq} \end{bmatrix} = \begin{bmatrix} v_{id} \\ v_{iq} \end{bmatrix} - \begin{bmatrix} v_{cd} \\ v_{cq} \end{bmatrix} \\ C \dfrac{d}{dt}\begin{bmatrix} v_{cd} \\ v_{cq} \end{bmatrix} + \begin{bmatrix} 0 & -\omega_n C \\ \omega_n C & 0 \end{bmatrix}\begin{bmatrix} v_{cd} \\ v_{cq} \end{bmatrix} = \begin{bmatrix} i_{id} \\ i_{iq} \end{bmatrix} - \begin{bmatrix} i_{gd} \\ i_{gq} \end{bmatrix} \\ L_g \dfrac{d}{dt}\begin{bmatrix} i_{gd} \\ i_{gq} \end{bmatrix} + \begin{bmatrix} R_g & -\omega_n L_g \\ \omega_n L_g & R_g \end{bmatrix}\begin{bmatrix} i_{gd} \\ i_{gq} \end{bmatrix} = \begin{bmatrix} v_{cd} \\ v_{cq} \end{bmatrix} - \begin{bmatrix} v_{gd} \\ v_{gq} \end{bmatrix} \end{cases} \tag{2.14}$$

It can be observed from (2.14) that the Park transformation creates cross-couplings between *d*- and *q*-axis variables, i.e., the two variables are not independent from each other [35, 36, 91]. In comparison to an *L*-filter in which the coupling is only produced by the inductor, the *LCL* system has much more complicated couplings generated by both the *LCL* inductors and capacitor [44, 45, 92]. The couplings significantly increase the difficulty in the modeling and decoupling of the system, especially when the time delay in the control loop is considered [42, 44, 45, 93, 94]. Furthermore, the couplings would cause stability problems when a low sampling to operating frequency ratio is used [35, 95-97]. More details regarding the couplings, modeling, and control of the *LCL*-filtered system in the SRF are presented in Chapter 5.

2.5 PWM and Control Modeling

2.5.1 PWM

Different PWM methods, such as carrier-based PWM and space vector PWM, can be applied to generate pulses to drive the IGBTs [7, 73, 98]. In the thesis, the carrier-based bipolar SPWM is adopted, which is achieved by comparing three modulating waveforms ($-1 \leq m_U, m_V, m_W \leq 1$) with a carrier waveform [7, 98]. The modulations are defined as naturally sampled and uniformly sampled PWM for analog and digital implementation, respectively [73].

As introduced previously, DSP based digital controllers are more and more used in switching converters instead of analog controllers. The modulation signals are generated from digital controllers. Different types of uniformly sampled PWMs can

be obtained depending on the shape of the carrier waveform (sawtooth or triangular) and on the relationship between the sampling frequency f_s and switching frequency f_{sw} ($f_s = f_{sw}$: single-update mode; $f_s = 2f_{sw}$: double-update mode) [74]. The most used single-update-mode triangular-carrier modulator can be further classified into two types: symmetric-on-time type if variables are sampled when the DSP PWM counter reaches the peak value, and symmetric-off-time type at the zero value [74].

The symmetric-on-time triangular PWM is shown in Figure 2.8(a). A discrete modulation signal m is firstly processed by a zero-order-hold (ZOH) which is given as:

$$G_{PWM}(s) = G_{ZOH}(s) = \frac{1 - e^{-sT_s}}{s}. \tag{2.15}$$

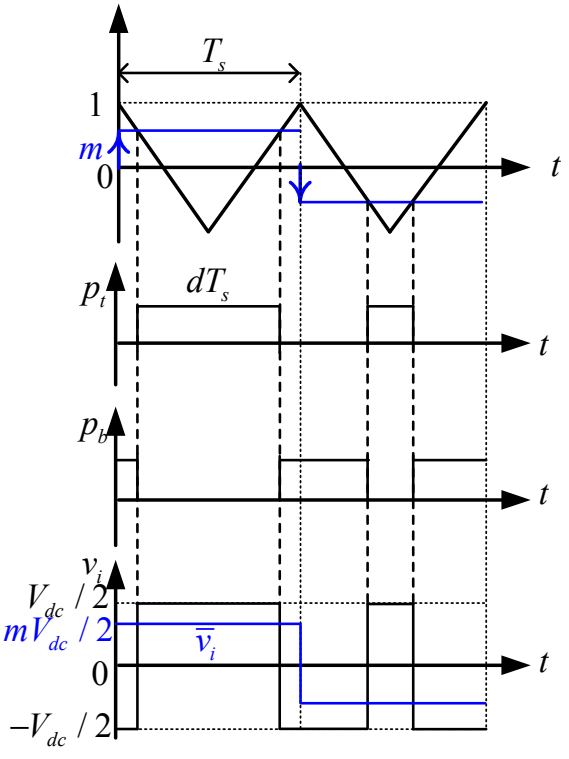

(a)

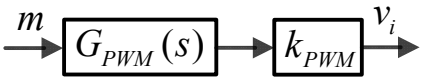

(b)

Figure 2.8: Uniformly sampled symmetric-on-time PWM. (a) Modulation process. (b) Model.

Then the processed modulation signal is compared with the triangular-carrier waveform, resulting in a pulse p_t with a duty-ratio of d (= $\frac{m+1}{2}$) and a pulse p_b with a duty-ratio of (1– d). The former is used to drive the top IGBT in a leg while the latter to the bottom IGBT. The duty ratio, in turn, is transferred into the inverter voltage v_i waveform, which is square and thus contains high-frequency harmonics [73].

The model of the PWM can be derived by averaging the filter input voltage (v_i) in a sampling period T_s [21, 23]. The average value of v_i is calculated as

$$\begin{aligned}\overline{v}_i &= \frac{1}{T_s}\left[dT_s\frac{V_{dc}}{2} - (1-d)T_s\frac{V_{dc}}{2}\right] \\ &= V_{dc}\left(d-\frac{1}{2}\right) \\ &= \frac{m}{2}V_{dc}\end{aligned} \tag{2.16}$$

It can be seen from (2.16) that the gain of the PWM, k_{PWM}, is equal to V_{dc} / 2. As a result, the model of the PWM is illustrated in Figure 2.8(b).

2.5.2 Control Modeling

Taking a single-loop digitally controlled GCF system for example, according to previous discussions and analyses, the single-phase control block diagram is shown in Figure 2.9(a). $e^{-s\lambda T_s}$ is the processing delay time for ADC, computation, and duty-ratio update, and generally $\lambda = 1$ [23, 74, 99] (λ is assumed to be a random value in Chapter 3 in order to deduce stable ranges of time delay, while $\lambda = 1$ is adopted in other chapters to form a general case). $G_c(z)$ is the digital controller. The classical PI (2.9) and PR controllers (2.11) can be digitalized using the Tustin's method (or called bilinear transform), with the Laplace operator s being replaced by:

$$s = \frac{2}{T_s}\frac{z-1}{z+1} \tag{2.17}$$

Therefore, the discrete closed-loop transfer function of the system is yielded as

$$G_{cl}(z)=\frac{i_g(z)}{i_g^*(z)}=\frac{G_c(z)G_g(z)}{1+G_c(z)G_g(z)}, \tag{2.18}$$

where $G_g(z)=Z\{e^{-s\lambda T_s}G_{PWM}(s)k_{PWM}G_{i_g v_i}(s)\}$.

The equivalent continuous *s*-domain system can be obtained as Figure 2.9(b), with $G_d(s) = e^{-sT_d}$ being the total time delay in the control loop that includes the processing delay and an equivalent half sampling period delay of the ZOH ($T_d = (\lambda + 0.5)T_s$) [23, 71].

More details regarding the time delay will be presented in Chapter 3. Using the method in this section, the modeling of systems with different feedback variables, single- or multi-loop controlled, will be further discussed in the following chapters that concern different control structures.

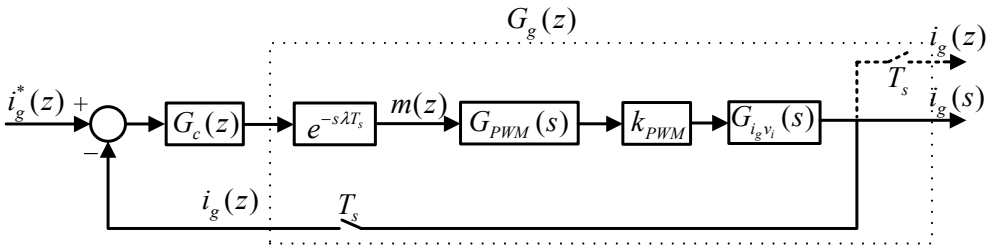

(a)

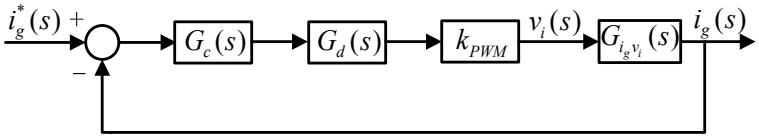

(b)

Figure 2.9: Block diagram of a single-loop controlled grid-connected inverter with GCF. (a) Discrete *z*-domain. (b) Continuous *s*-domain.

The bode diagrams of a proportional gain k_p, PI controller, and PR controller are shown in Figure 2.10. In frequencies sufficiently larger than ω_0, the PR (2.11) gradually returns to the PI (2.9) when $k_r = k_i$ [39]. At a frequency $\omega_L = 10k_i$, the phases of the PI and PR are approximately equal to –5°, and simultaneously the magnitudes approximately equal k_p [39]. Therefore, when ω_L is set to be sufficiently smaller than

the crossover frequency of an open-loop system, the integral or resonant term has a negligible influence on the system stability. In this case, the PI or PR controller can be simplified as a proportional gain k_p when studying the stability of the system [25, 39].

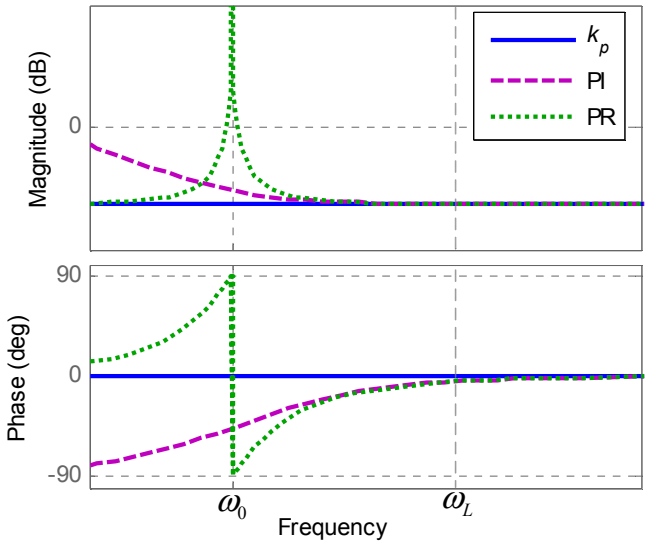

Figure 2.10: Bode diagrams of proportional, PI, and PR controllers.

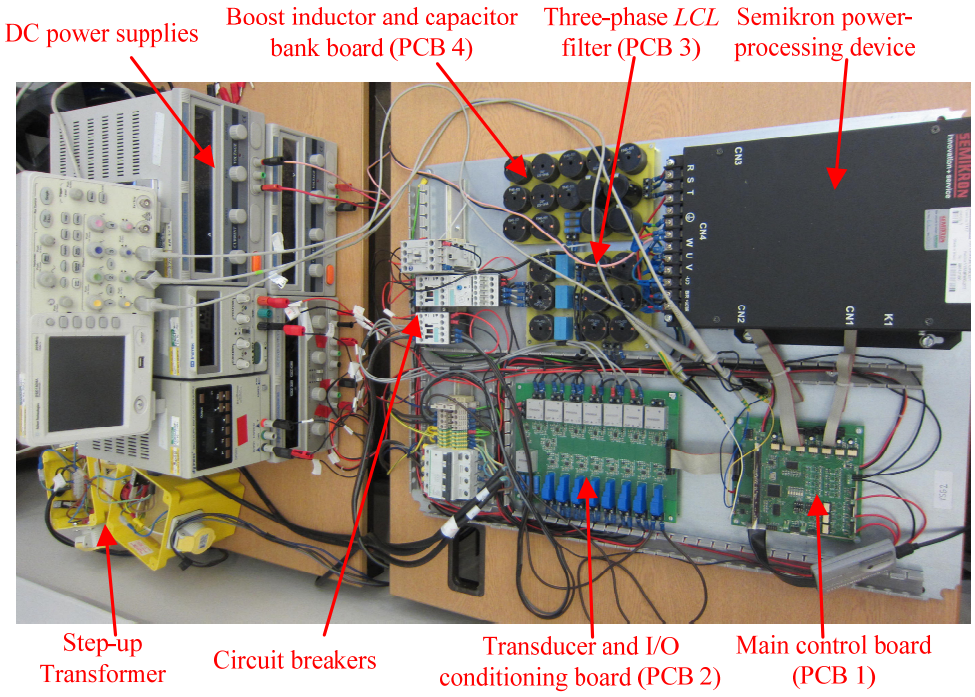

Figure 2.11: Experimental grid-connected inverter system.

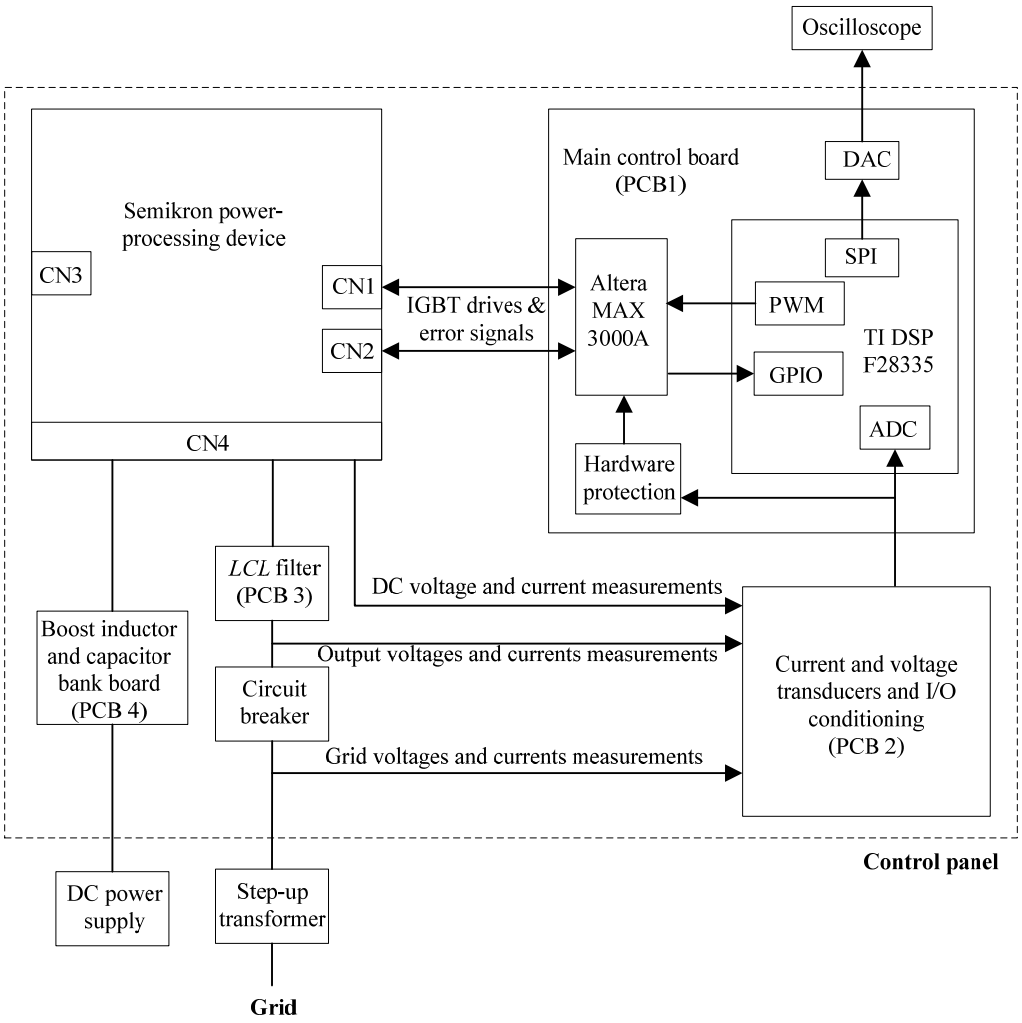

Figure 2.12: Hardware block scheme.

2.6 Experimental Setup

In this section, the design and development of the experimental system which is used to carry out real-time experiments, as shown in Figure 2.11, are described.

2.6.1 Hardware Design

The hardware block scheme of this system is shown in Figure 2.12. It consists of a Semikron power-processing device, a main control printed circuit board (PCB 1) including Texas Instrument (TI) DSP TMS320F28335, voltage and current transducers (PCB 2), a three-phase *LCL* filter (PCB 3), a boost inductor and capacitor bank board (PCB 4), circuit breakers, DC power supplies, and an isolated three-phase

step-up transformer. The system has a complete hardware and software protection design. A short description of all major components follows.

2.6.1.1 Semikron Power-Processing Device

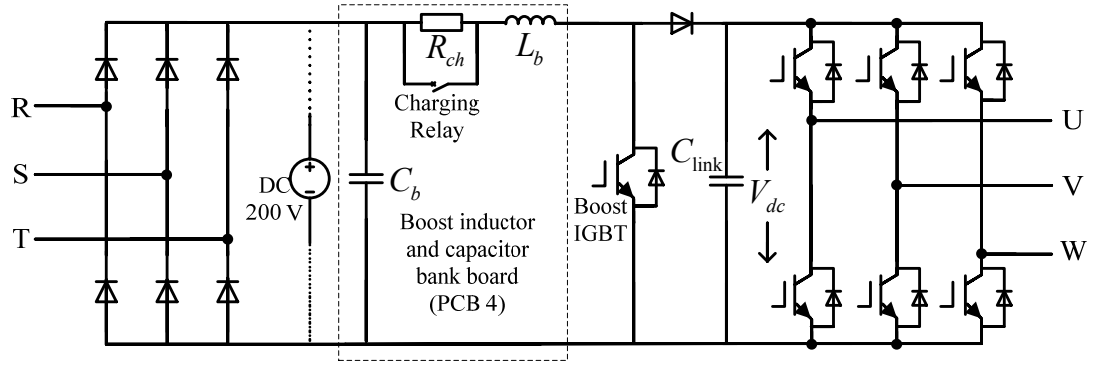

Figure 2.13: Semikron power-processing device.

The Semikron device, as shown in Figure 2.13, is an off-the-shelf power-processing device (the boost inductor and capacitor bank board PCB 4 including the charging resistor R_{ch} will be introduced later in Section 2.6.1.5). It consists of a three-phase uncontrolled bridge rectifier (not used, a 200 V DC power supply is used for power source, see Section 2.6.1.8), a boost converter, and a three-phase IGBT inverter. The device is equipped with IGBT drivers for the booster and inverter. As the voltage and frequency of the Semistack input can vary, the boost converter is to be utilized to control DC current to follow the optimized current reference for maximum power point operation. Since an energy storage system is not to be included, the three-phase inverter is to be responsible for grid synchronization and power flow control by regulating DC link voltage [100].

Semistack specification: Maximum rated root-mean-square (RMS) current: 22 A, rated RMS voltage: 380 V, maximum rated DC voltage applied to the capacitor bank: 750 V, maximum collector-emitter DC voltage: 1200 V, maximum switching frequency: 15 kHz.

2.6.1.2 Main Control Board (PCB 1)

As shown in Figure 2.12, the main control board (PCB 1) consists of DSP, digital-to-analog converter (DAC), hardware protection circuit including Altera programmable logic device (PLD), and digital I/O (PWM, DO, and DI) conditioning.

TI DSP TMS320F28335

The 32-bit floating-point DSP TMS320F28335 is fixed on the top of the main control board. The operating speed is 150 MHz (30 MHz input clock). The integrated peripherals of the TMS320F28335 device used in the experiments are: 16 input channels with 12-bit ADC, 6 enhanced PWM modules (ePWM), 16 digital general purposed I/O (GPIO) and 1 serial peripheral interface (SPI) module.

The ADC module comprises a 12-bit ADC with a built-in sample-and-hold circuit and provides flexible interface to peripherals with a fast conversion rate of up to 80 ns at 25 MHz ADC clock. The ADC module has 16 channels, configurable as two independent 8-channel modules.

An ePWM module represents one complete PWM channel composed of two PWM outputs. ePWM modules are chained together via a clock synchronization scheme that allows them to operate as a single system when required. For three-phase inverters, six IGBTs can be controlled using three ePWM modules, one for each leg. Each leg must switch at the same frequency and the three legs must be synchronized. Dead time can be properly set in the ePWM module. Moreover, PWM switching has to be synchronized with ADC sampling. Each ePWM module has two ADC start of conversion signals (one for each sequencer). Any ePWM module can trigger a start of conversion for either sequencer. Which event triggers the start of conversion is configured in the Event-Trigger submodule.

The GPIO multiplexing registers are used to select the operation of shared pins. These pins can be individually selected to operate as digital I/O, referred to as GPIO, or connected to one of up to three peripheral I/O signals. If selected for GPIO, registers are provided to configure the direction of the pin as either input or output.

DAC

TLV5614 is a quadruple 12-bit voltage output DAC with a flexible 4-wire serial interface. The 4-wire serial interface allows interface to TI DSP serial port. The TLV5614 is programmed with a 16-bit serial word, which is comprised of a 4-bit DAC address and a 12-bit DAC value. The DAC communicates with TI DSP via SPI-A and it is used to display and record up to eight variables from DSP.

Hardware protection circuit and Altera programmable logic

The protection circuit consists of an Alter PLD MAX 3000A, error signals from the DSP and Semikron device (IGBT switching errors), and analog inputs (DC link voltage and current). The PLD is a high-performance, low-cost CMOS EEPROM based programmable logic built on a MAX architecture. The user-configurable MAX 3000A architecture accommodates a variety of independent combinatorial and sequential logic functions. The device can be reprogrammed for quick and efficient iterations during design development and debugging cycles.

Table 2.1: Protection functions of the experimental prototype

Parameter	Value
Maximum AC inverter output current	7 A
Maximum DC link voltage (Software)	600 V
Maximum DC link voltage (Hardware)	750 V
Maximum DC link current (Software)	10 A
Maximum DC link current (Hardware)	10 A
Error output signals from Semikron (U, V, W and boost converter)	DI

The protection functions are summarized in Table 2.1. In case that any of these inputs is activated or in case of DSP failure, the protection logic from the PLD will disable all PWM outputs, digital outputs, and circuit breakers using SN74ABT541B octal buffers integrated circuit on PCB 1. The particular error is then visualized by different LED diodes on PCB 1. All outputs are disabled until a reset signal is sent.

Digital I/O conditioning

PWM, DI and DO signals are processed via opto-couplers with 3.3 V on the controller side and 15 V on the device side. The 15 V CMOS signal are necessary to control PWM outputs and to process error input signals from the Semikron device. For DO's purposes, four high current MOSFET's transistors are used to control contractors and relays (circuit breaker, Semistack fan etc.). Semikron PWM control signals, error outputs and supply voltages (± 15 V and GND) are processed from PCB 1 via two ribbon cables.

2.6.1.3 Transducer and I/O Conditioning Board (PCB 2)

The transducer and I/O conditioning board (PCB 2) is employed like an interface between voltage and current measurements and the DSP. It consists of 8 current (HY 10-P) and 8 voltage (LV 28-P) LEM transducers with instantaneous voltage or current outputs respectively. Both transducer types have galvanic isolation between the primary circuit (high power) and the secondary circuit (electronic circuit). Signals from transducers are further processed via conditioning circuits. As the DSP uses 3.3V voltage level signals, the transducers outputs are scaled and shifted using two operational amplifiers from approximately ± 3 V to 0 – 3 V.

2.6.1.4 Three-Phase *LCL* Filter (PCB 3)

The three-phase *LCL* filter, as introduced previously, is used to remove high-order frequency PWM harmonics generated by the inverter. The filter board is equipped with several terminals to allow current and voltage measurements. Parameters of the *LCL* filter, chosen using the method in [62], are given in Table 2.2.

2.6.1.5 Boost Inductor and Capacitor Bank Board (PCB 4)

The inductor for the boost converter and the capacitor bank between the rectifier and boost converter are not part of the Semikron device, they are added according to design requirements. The board is equipped with a circuit to allow safe charging of the DC link capacitor C_{link} (see Figure 2.13) via a parallel combination of three charging resistors. Once DC link capacitors are charged, the resistors can be by-

passed using a relay. Parameters of the boost inductor L_b and capacitor bank C_b are given in Table 2.2, where R_b is boost inductor winding resistance and R_{ch} is parallel combination of the charging resistors.

Table 2.2: Parameters of the experimental setup

Parameter	Value	Rating	Parameter	Value	Rating
L_i	4.4 mH	4 A	R_i	0.988 Ω	4 A
L_g	2.2 mH	4 A	R_g	0.494 Ω	4 A
C	10 µF	305 V	C_b	680 µF	800 V
L_b	8.2 mH	7.2 A	R_b	1.54 Ω	7.2 A
R_{ch}	73 Ω	15 W	V_{dc}	450 V	750 V
v_i	110 V_{RMS}	380 V_{RMS}	v_g	230 V_{RMS}	-

2.6.1.6 Circuit Breakers

Circuit breakers are used to protect the devices from damage caused by short circuit. For this purpose they are equipped with over-current protections. Circuit breakers status (open/close) is part of the hardware protection.

2.6.1.7 Step-up Transformer

The three-phase (three single-phase isolating transformers) step-up transformer is used to transform 110 V_{RMS} voltages generated by the inverter to 230 V_{RMS} for utility grid connection. The step-up transformer is also used for safety reasons and to allow better accommodate low power local resistive load. Transformer specification: Three-phase Y–Y connection, primary voltage: 230 V_{RMS} (line to neutral) 50/60 Hz, secondary voltage: 110 V_{RMS} (line to neutral), power rating: 2250 VA.

2.6.1.8 DC Power Supplies

The experimental prototype is powered from DC bench power supplies. Table 2.3 shows voltage levels and minimum currents necessary to provide supply for the prototype. Two 100 V / 10 A power supplies are connected in series, which are then boosted to 450 V DC link voltage (V_{dc}) via the boost converter.

Because of the large capacitance of the DC link capacitor (1360 μF) and fast response of the booster controller, in the work of the thesis, the DC link voltage 450 V that is boosted from the 200 V DC supply is assumed to be constant for the purpose of simplification in the analysis of the operation of the inverter.

Table 2.3: DC power supplies

Voltage level [V]	Minimum current [A]	Equipment
5	0.7	PCB 1 (TI DSP, Altera PLD)
± 15	± 0.5	PCB 2 (Transducers and measurements conditioning)
15	1.1	PCB 1 and Semikron devices (PWM and relay control)
24	1.2	Circuit breakers and charging relay

2.6.2 Software Environment

2.6.2.1 TI DSP

MATLAB software packages, including Simulink, SimPower, and Target Support Package TC2, are used to simulate and implement control strategies to the TI DSP. The Simulink, integrated with MATLAB, is an environment for simulation and model-based design for dynamic and embedded systems. It provides an interactive graphical environment and a set of block libraries that allow design, simulation, and implementation of a variety of time-varying systems.

For TMS320F28335 programming, the Target Support Package TC2 is used. The package integrates MATLAB and Simulink with TI's eXpressDSP tool Code Composer Studio (CCS). Using the TC2 package a C-language real-time implementation of the Simulink model is generated and automatically compiled, and the generated code is downloaded to DSP board. Onboard DSP peripherals are directly supported. A Blackhawk USB2000 controller is used to communicate with TI DSP via a 14-pin header mounted on PCB 1.

CCS is the integrated development environment for TI DSPs. It includes a suite of tools used to develop and debug embedded applications. It includes compilers for each of TI's device families, source code editor, project build environment, debugger, profiler, simulators, and many other features.

For simulation purpose, the SimPower toolbox and PLECS have been used. The SimPower toolbox extends the Simulink software with tools for modeling and simulating electrical circuits and power systems. PLECS is efficient simulation software for circuit and control design, and it can be embedded in the Matlab/Simulink.

2.6.2.2 Altera PLD

The Quartus II development software has been used to implement hardware protection features to the Altera PLD. The Quartus II software provides a complete environment for easy design entry to programmable logic, and ensures fast processing and straightforward device programming. The USB-Blaster cable is used to send configuration data from a host computer to a standard 10-pin header connected to the PLD.

Chapter 3

Delay-Dependent Stability of Single-Loop Controlled Grid-Connected Inverters with *LCL* Filters

3.1 Introduction

LCL filters have been widely adopted to mitigate switching harmonics generated by the grid-connected inverters. However the inherent resonance of *LCL* filters has the tendency to destabilize the inverter systems [34, 62, 78]. Different passive and active damping methods can be adopted to improve system stability [67, 68, 78]. The passive damping strategy increases the power loss. The active damping methods, multi-loop or filter based, are complex in the realization and design of the controller [68, 79, 101, 102].

Simple but effective single-loop current control methods without additional damping have been proposed and researched for the *LCL*-filtered grid-connected inverters, employing ICF or GCF [23-34]. It has been proved that both the ICF loop and GCF loop can be made stable because of their inherent damping characteristics [24, 28, 29].

However, the stability of the ICF and GCF loops has not been fully studied so far, especially when the time delay is taken into account. The time delay roots from the time for ADC, computation, duty-ratio update, and PWM generation [23, 67, 99].

Much work has been devoted to the choice of the feedback current and different conclusions on the stability of ICF loop and GCF loop have been drawn, leading to much confusion. Without considering any time delay, Tang *et al.* [24] found that the ICF loop is stable due to its inherent damping characteristics, while the GCF loop is unstable. Similar findings were demonstrated in [25] and [26] where the grid current is indirectly controlled by the inverter current. Active damping methods are needed if the grid current is to be controlled directly [58, 66]. Considering time delay, Zhang *et al.* [23] and Bierhoff *et al.* [69] found that the ICF is still more advantageous than the GCF. Again, damping methods are necessary if the grid current is to be controlled directly [75, 103]. In contrast, Dannehl *et al.* [34] found that GCF is superior to ICF based on stability evaluation using root loci. Similar conclusions were drawn in [27-29] which showed that the GCF loop can maintain stability without any additional damping method.

A number of publications have been devoted to the identification of the factors that influence the stability of the single-loop control systems. Dannehl *et al.* [34, 104] indicated that the stability is closely related to the ratio of sampling frequency to the *LCL* resonance frequency, but the nature of this relationship is not known. Yin *et al.* [29] presented the damping characteristic of the time delay in the GCF loop, and Park *et al.* [30] found that the GCF loop can be stable if the resonance frequency is smaller than $1/6$ of the sampling frequency. However only the GCF with a total delay of $1.5T_s$ (T_s is the sampling period) is studied. Rui *et al.* [31] implied that the GCF loop is stable when the time delay is between $0.53T_s$ and $1.33T_s$, but this range is only valid for the controller parameters used by the authors. Zou *et al.* [32] proposed a method to obtain the stable ranges of time delay for ICF and GCF loops. However the method is not based on precise derivations, and the deduced stable ranges, which are different to the result in [31], are only for specified *LCL* and controller parameters.

In this chapter, a thorough theoretical study is carried out on the relationship between the time delay and stability of single-loop controlled grid-connected inverters with *LCL* filters. It is found that the time delay is a key factor that affects the system stability. The main contributions of the present work are summarized below.

Firstly, stable ranges of the time delay (the ranges of time delay within which the system can be made stable) are deduced in the continuous *s*-domain as well as in the discrete *z*-domain, applicable to any given *LCL* parameters. The present study explains why different conclusions on the stability of the single-loop control systems are drawn in previous studies, i.e., the time delay in these cases falls into different ranges. Furthermore, it can be deduced that the stable ranges of time delay for the loop with a CCF are the same as those of the ICF loop. Therefore the study can also facilitate the analysis of the active damping methods which employ an inner ICF or CCF loop.

Secondly, to improve the stability of the single-loop control systems, time delay compensation methods are proposed. For ICF, a linear predictor (LP) based time delay reduction is used [105, 106]. For GCF, a proper time delay is added. By employing the proposed time delay compensators, the allowed sampling frequency ranges can be increased while still maintaining system stability.

Thirdly, a simple PI tuning method without simplification is proposed. To design the controller, the *LCL* filter is often simplified as an *L* filter [30, 33, 39]; this approach however is not accurate enough since the *LCL* resonance frequency significantly impacts stability margins. By using the proposed design method, adequate stability margins can be guaranteed.

Simulation and experimental results have been obtained to validate and verify the delay-dependent stability study.

3.2 Single-Loop Controlled Three-Phase Grid-Connected Inverters with *LCL* Filters

3.2.1 System Description

In order to represent the worst case in stability, the parasitic resistance associated with the inductors is neglected [24, 30]. The circuit diagram of the three-phase grid-connected inverter is shown in Figure 3.1.

The inverter current i_i or grid current i_g can be sensed as the feedback variable to form a single-loop ICF system or GCF system, respectively. The transfer functions from the inverter voltage v_i to i_i and to i_g are given as (3.1) and (3.2) respectively, where $\omega_r = \sqrt{1/L_g C}$ and $\omega_{res} = \sqrt{(L_i + L_g)/L_i L_g C}$ $(\omega_{res} > \omega_r)$.

$$G_{i_i v_i}(s) = \frac{i_i(s)}{v_i(s)} = \frac{s^2 + \omega_r^2}{sL_i(s^2 + \omega_{res}^2)} \tag{3.1}$$

$$G_{i_g v_i}(s) = \frac{i_g(s)}{v_i(s)} = \frac{\omega_r^2}{sL_i(s^2 + \omega_{res}^2)} \tag{3.2}$$

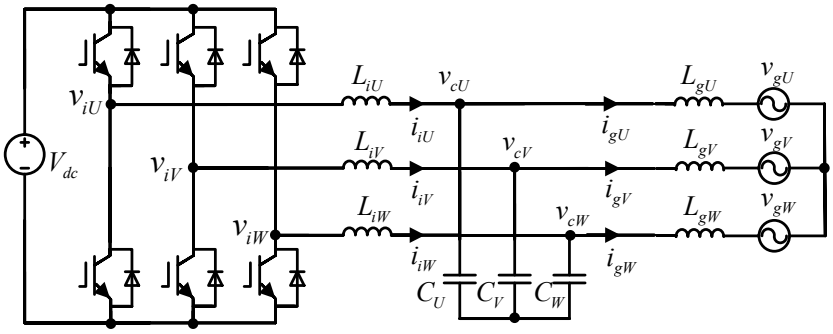

Figure 3.1: Three-phase grid-connected inverter with *LCL* filters.

3.2.2 Time Delay in the Control Loop

To acquire the average value of a current in a switching period and to avoid switching noises, the synchronous sampling method is commonly adopted. The currents are sampled at the beginning or the middle of a switching period [74].

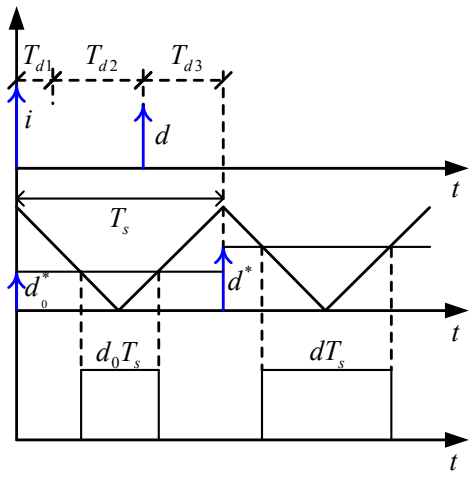

Figure 3.2: Time delays in the digital control of a grid-connected inverter system.

Taking the symmetric-on-time modulator as an example, the digital control process is shown in Figure 3.2. A current is sampled when the PWM counter reaches the peak value, resulting in a sampled quantity i. T_{d1} represents the time for ADC. With a digital controller, the duty-ratio d (the shadow compare register value) is calculated, and T_{d2} is the time for computation. In a DSP, d is generally updated to the compare register (with a value of d^*, equal to d) when the counter reaches zero and/or the period value, leading to a duty-ratio update delay T_{d3}. The total processing delay is expressed in terms of T_s as $T_{d1} + T_{d2} + T_{d3} = \lambda T_s$. Normally, λT_s is not larger than one sampling period T_s, and its typical values in real operation are $0.5T_s$ and T_s [23, 74]. In addition to the processing delay, there is a delay T_{d4} due to the PWM, and equivalently $T_{d4} = 0.5T_s$ [105]. Therefore the total time delay in the control loop is $T_d = T_{d1} + T_{d2} + T_{d3} + T_{d4} = (\lambda + 0.5)T_s$ [99]. In the following analysis to deduce the stable ranges of time delay, λ is assumed to be a random value (Note that $\lambda = 1$ is adopted in other chapters to form a general case).

3.3 Analysis of the Delay-Dependent Stability in Continuous *s*-Domain

The block diagrams of the single-loop controlled grid-connected inverters are shown in Figure 3.3. The total time delay is expressed as $G_d(s) = e^{-sT_d}$. $G_c(s)$ is the

controller, and a PI is used:

$$G_c(s) = k_p(1 + \frac{k_i}{s}). \tag{3.3}$$

The loop gains of the ICF and GCF are $T_i(s) = k_{PWM} G_c(s) G_d(s) G_{i_i v_i}(s)$ and $T_g(s) = k_{PWM} G_c(s) G_d(s) G_{i_g v_i}(s)$, respectively. The stability analysis can be carried out using the Nyquist stability criterion. In the open-loop Bode diagram, only the frequency ranges with magnitudes above 0 dB are considered. For the phase plot in these ranges, a $\pm (2k + 1)\pi$ crossing in the direction of phase rising is defined as a positive crossing, while a crossing in the direction of phase falling is defined as a negative crossing. The numbers of the positive and negative crossings are denoted as N_+ and N_-, respectively [21]. According to the Nyquist stability criterion, the number of the open-loop unstable poles P must equal $2(N_+ - N_-)$ to ensure system stability, i.e., $P = 2(N_+ - N_-)$. As can be seen from (3.1) – (3.3), $P = 0$, hence $N_+ - N_- = 0$ is required for both of the ICF and GCF systems.

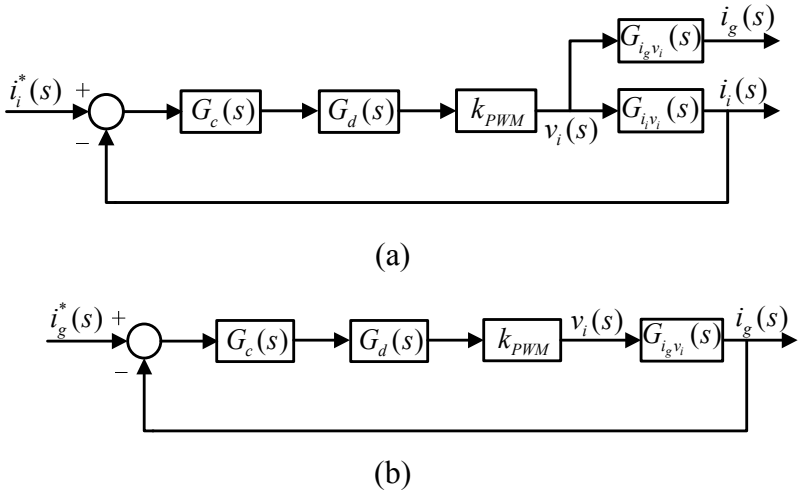

Figure 3.3: *s*-domain block diagrams of the single-loop controlled grid-connected inverters. (a) ICF. (b) GCF.

3.3.1 Inverter Current Feedback

The magnitude (in decibels) and phase of $T_i(s)$ with $G_c(s) = k_p$ (the integral term $k_p k_i / s$ can be designed to have a negligible influence on system stability [25]) are given in (3.4) and (3.5), respectively.

$$20\lg\left|T_i(s)\right|_{s=j\omega}\left| = 20\lg\right|k_p k_{PWM} e^{-j\omega T_d}\frac{-\omega^2+\omega_r^2}{j\omega L_i(-\omega^2+\omega_{res}^2)}\Bigg|$$

$$= \begin{cases} 20\lg[k_p k_{PWM}\dfrac{\omega_r^2-\omega^2}{\omega L_i(\omega_{res}^2-\omega^2)}], (\omega<\omega_r) \\ -\infty, (\omega=\omega_r) \\ 20\lg[k_p k_{PWM}\dfrac{\omega^2-\omega_r^2}{\omega L_i(\omega_{res}^2-\omega^2)}], (\omega_r<\omega<\omega_{res}) \\ +\infty, (\omega=\omega_{res}) \\ 20\lg[k_p k_{PWM}\dfrac{\omega_r^2-\omega^2}{\omega L_i(\omega_{res}^2-\omega^2)}], (\omega>\omega_{res}) \end{cases} \tag{3.4}$$

$$\angle T_i(s)\Big|_{s=j\omega} = \angle k_p k_{PWM} e^{-j\omega T_d}\frac{-\omega^2+\omega_r^2}{j\omega L_i(-\omega^2+\omega_{res}^2)}$$

$$= \begin{cases} -\dfrac{\pi}{2}-\omega T_d, (\omega<\omega_r) \\ \dfrac{\pi}{2}-\omega T_d, (\omega_r<\omega<\omega_{res}) \\ -\dfrac{\pi}{2}-\omega T_d, (\omega>\omega_{res}) \end{cases} \tag{3.5}$$

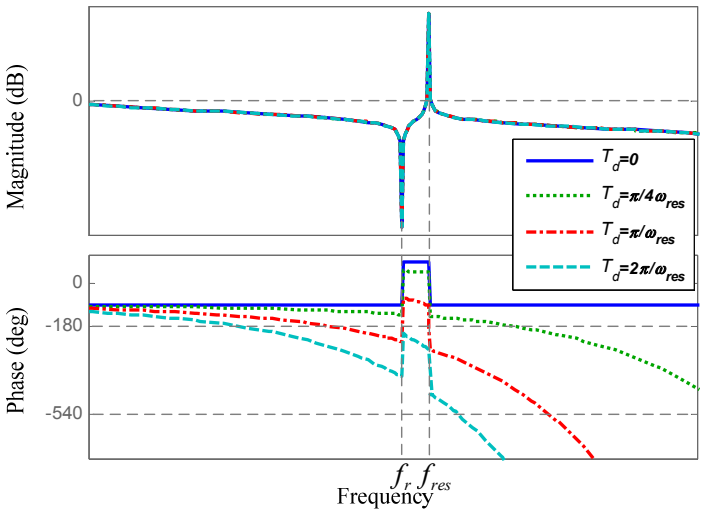

Figure 3.4: Bode diagrams of the ICF loop gain with different time delays.

The Bode diagrams of $T_i(s)$ with several different time delays are shown in Figure 3.4. The magnitude at f_r (= $\omega_r/2\pi$) is definitely below 0 dB although there is a +180° jump in the phase, hence $N_+ = 0$. $N_- = 0$ is thus required for system stability. Using a sufficiently small k_p, the magnitude of $T_i(s)$ can be set below 0 dB to avoid

negative crossing, except at the resonance frequency f_{res} (= $\omega_{res}/2\pi$) where the magnitude is positive infinite and there is a fall of 180° in the phase. Therefore, assuming k_p is adjustable, the system can be made stable only if the phase at f_{res} does not cross over ± (2k + 1)π. Otherwise there will be a negative crossing at f_{res} whatever k_p is, i.e., $N_- \neq 0$ and thus the system is unstable. Without any time delay, the phase at f_{res} falls from 90° to –90° and no negative crossing is generated, so the system is stable, in agreement with the findings in [24].With a finite time delay, the phase lag increases. To avoid any ± (2k + 1)π crossing at f_{res}, it can be derived from (3.5) that the time delay should fall into one of the following ranges:

$$\begin{cases} T_d < \dfrac{\pi}{2\omega_{res}}, (k=0) \\ \dfrac{(4k-1)\pi}{2\omega_{res}} < T_d < \dfrac{(4k+1)\pi}{2\omega_{res}}, (k=1,2,3...) \end{cases} \tag{3.6}$$

3.3.2 Grid Current Feedback

The magnitude (in decibels) and phase of $T_g(s)$ with $G_c(s) = k_p$ are given as (3.7) and (3.8), respectively.

$$\begin{aligned} 20\lg\left|T_g(s)\right|_{s=j\omega}\left| = 20\lg\right|k_p k_{PWM} e^{-j\omega T_d} \frac{\omega_r^2}{j\omega L_i(-\omega^2+\omega_{res}^2)}\Big| \\ = \begin{cases} 20\lg[k_p k_{PWM} \dfrac{\omega_r^2}{\omega L_i(\omega_{res}^2-\omega^2)}], (\omega<\omega_{res}) \\ +\infty, (\omega=\omega_{res}) \\ 20\lg[k_p k_{PWM} \dfrac{\omega_r^2}{\omega L_i(\omega^2-\omega_{res}^2)}], (\omega>\omega_{res}) \end{cases} \end{aligned} \tag{3.7}$$

$$\begin{aligned} \angle T_g(s)\Big|_{s=j\omega} = \angle k_p k_{PWM} e^{-j\omega T_d} \frac{\omega_r^2}{j\omega L_i(-\omega^2+\omega_{res}^2)} \\ = \begin{cases} -\dfrac{\pi}{2} - \omega T_d, (\omega<\omega_{res}) \\ -\dfrac{3\pi}{2} - \omega T_d, (\omega>\omega_{res}) \end{cases} \end{aligned} \tag{3.8}$$

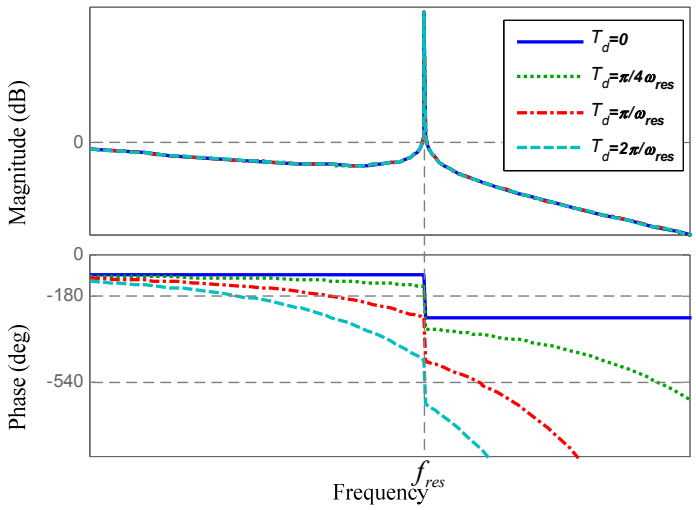

Figure 3.5: Bode diagrams of the GCF loop gain with different time delays.

The Bode diagrams of $T_g(s)$ with different time delays are shown in Figure 3.5. Similar to the ICF loop, the GCF loop can be made stable if there is no negative crossing at f_{res}, i.e., the phase at f_{res} does not cross over $\pm(2k+1)\pi$. Without any time delay, the phase at f_{res} falls from –90° to –270° and a negative crossing exists, the system is thus unstable. To avoid any potential negative crossing at f_{res}, it can be deduced from (3.8) that the time delay should be in the following ranges:

$$\frac{(4k+1)\pi}{2\omega_{res}} < T_d < \frac{(4k+3)\pi}{2\omega_{res}}, (k = 0,1,2,\ldots). \tag{3.9}$$

The result indicates that a proper time delay is required for the stability of GCF loop.

3.4 Analysis of the Delay-Dependent Stability in Discrete *z*-Domain

In this section, the delay-dependent stability of the single-loop controlled grid-connected inverters with *LCL* filters is studied in the discrete *z*-domain. The proportional gain k_p is assumed to be adjustable. Then the stable ranges of the time delay for ICF and GCF loops are deduced, based on the requirement that when the time delay is in the stable ranges all discrete closed-loop poles should be inside the unit circle when an infinitely small k_p is used. On the contrary, if the time delay is

outside the stable ranges, there will be unstable closed-loop poles outside the unit circle whatever k_p is.

3.4.1 Discrete Models

To obtain the discrete models, the processing delay and PWM are analyzed separately. The processing delay is expressed as $e^{-s\lambda T_s}$. The PWM is usually modeled as ZOH [107], that is

$$G_{PWM}(s) = \frac{1-e^{-sT_s}}{s}. \tag{3.10}$$

A more precise PWM model has been proposed in [23] and [74] and is given as

$$G'_{PWM}(s) = \frac{T_s}{2}(e^{-s\frac{T_s}{4}} + e^{-s\frac{3T_s}{4}}). \tag{3.11}$$

The frequency domain models of (3.10) and (3.11) are denoted as

$$G_{PWM}(j\omega) = \frac{1-e^{-j\omega T_s}}{j\omega} = \frac{\sin\frac{\omega T_s}{4}\cos\frac{\omega T_s}{4}}{\frac{\omega}{4}} e^{-j\omega\frac{T_s}{2}} \tag{3.12}$$

and

$$G'_{PWM}(j\omega) = \frac{T_s}{2}(e^{-j\omega\frac{T_s}{4}} + e^{-j\omega\frac{3T_s}{4}}) = T_s\cos\frac{\omega T_s}{4} e^{-j\omega\frac{T_s}{2}}, \tag{3.13}$$

respectively. It can be seen that the time delays of these two PWM models are identical ($0.5T_s$), and their magnitude gains are almost the same because a small T_s is commonly used. Therefore the ZOH model (3.10) is adequate for the discrete analysis [107].

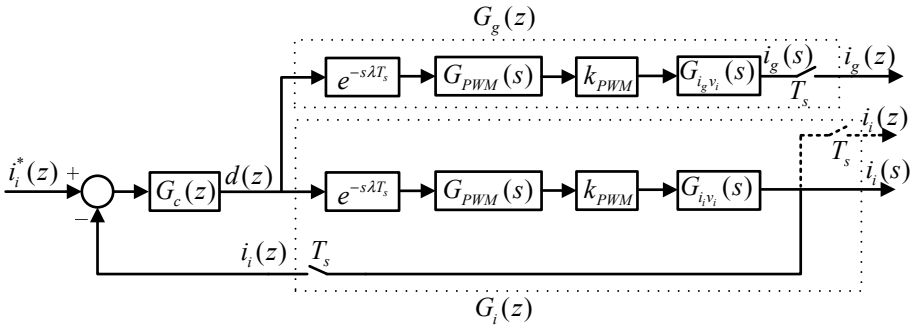

(a)

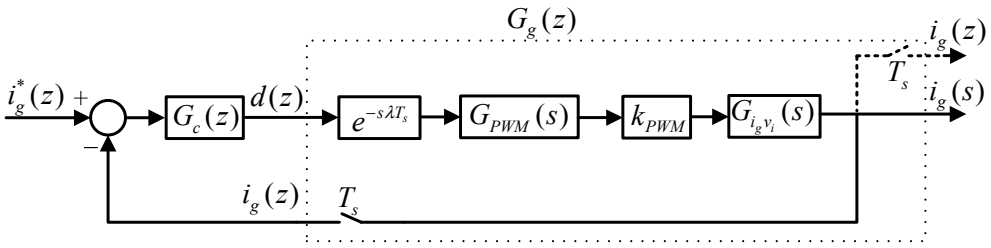

(b)

Figure 3.6: Block diagrams of the single-loop digitally controlled grid-connected inverters. (a) ICF. (b) GCF.

The block diagrams of the single-loop digitally controlled grid-connected inverters are shown in Figure 3.6, where $G_c(z)$ is the discrete equivalent of $G_c(s)$ [74]. To obtain the closed-loop discrete transfer functions of the two control systems, the discrete transfer function from $d(z)$ to $i_i(z)$ and to $i_g(z)$ should be obtained first. Therefore z-transform is used to obtain the discrete transfer functions of the paths which contain the processing delay, PWM, and the plant transfer functions $G_{i_i v_i}(s)$ and $G_{i_g v_i}(s)$ followed by ideal samplers. For a plant transfer function $G(s)$, the discrete transfer function is expressed as [23, 74]

$$\begin{aligned} G(z) &= Z\{e^{-s\lambda T_s} G_{PWM}(s) k_{PWM} G(s)\} \\ &= k_{PWM} \frac{z-1}{z^{\ell+1}} Z\left\{\frac{G(s)}{s} e^{smT_s}\right\}, \end{aligned} \tag{3.14}$$

where ℓ is an integer, $0 \le m < 1$, and $\lambda = \ell - m$. $Z\left\{\frac{G(s)}{s} e^{smT_s}\right\}$ in (3.14) can be obtained using the following property [107]:

$$Z\left\{\frac{G(s)}{s} e^{smT_s}\right\} = \sum_{i=1}^{n} \text{Res}\left[\frac{zG(s)e^{smT_s}}{s(z-e^{sT_s})}\right]_{s=p_i}, \tag{3.15}$$

where p_i ($i = 1, 2, \ldots, n$) are the poles of $G(s)/s$, and Res denotes the residue.

Substituting $G_{i_i v_i}(s)$ and $G_{i_g v_i}(s)$ for $G(s)$ in (3.14) and (3.15), discrete transfer functions from $d(z)$ to $i_i(z)$ and to $i_g(z)$ are obtained as (3.16) and (3.17), respectively.

$$G_i(z) = \frac{k_{PWM}(z-1)}{(L_i + L_g)z^{\ell}} \left[\frac{mz+1-m}{(z-1)^2} T_s + \frac{L_g}{L_i \omega_{res}} \frac{z \sin m\omega_{res} T_s + \sin(1-m)\omega_{res} T_s}{z^2 - 2z\cos\omega_{res} T_s + 1} \right] \tag{3.16}$$

$$G_g(z)=\frac{k_{PWM}(z-1)}{(L_i+L_g)z^{\ell}}\left[\frac{mz+1-m}{(z-1)^2}T_s-\frac{1}{\omega_{res}}\frac{z\sin m\omega_{res}T_s+\sin(1-m)\omega_{res}T_s}{z^2-2z\cos\omega_{res}T_s+1}\right] \quad (3.17)$$

Therefore, the closed-loop transfer functions of the control loops with ICF and GCF are given as (3.18) and (3.19), respectively.

$$G_{icl}(z)=\frac{i_g(z)}{i_i^*(z)}=\frac{G_c(z)G_g(z)}{1+G_c(z)G_i(z)} \quad (3.18)$$

$$G_{gcl}(z)=\frac{i_g(z)}{i_g^*(z)}=\frac{G_c(z)G_g(z)}{1+G_c(z)G_g(z)} \quad (3.19)$$

A discrete closed-loop is stable if all closed-loop poles are inside the unit circle. From (3.16) and (3.17) it can be seen that the ICF and GCF have identical open-loop poles, and three are on the unit circle ($z_1 = 1$, $z_{2,3} = \cos\omega_{res}T_s \pm j\sin\omega_{res}T_s$). Thus, with $G_c(z) = k_p$, for a possible stable operation, i.e. the time delay being in the stable ranges, all closed-loop poles should be inside the unit circle when an infinitely small k_p is used. On the other hand, if the time delay is outside the stable ranges, there will be unstable closed-loop poles outside the unit circle whatever k_p is.

The w-transform $z = (w + 1)/(w - 1)$ is used to map the area inside the unit circle in the z-plane into the LHP of the w-plane, such that the Routh's stability criterion can be used [21]. The stable ranges of the time delay can be derived based on the requirement that the roots of $D_i(w) = 1 + k_pG_i(w) = 0$ and $D_g(w) = 1 + k_pG_g(w) = 0$ should be in the LHP when an infinitely small k_p is used. An exemplary derivation for the GCF with the case of $0 < \lambda \leq 1$, i.e., $\ell = 1$ and $0 \leq m < 1$, is provided in Appendix A. The stable ranges of GCF with other cases of λ can be derived using the same method, as well as those of the ICF.

3.4.2 Inverter Current Feedback

Using the method in Appendix A, the general requirement for the stability of the ICF loop can be obtained as

$$\begin{aligned}&\sin[(\ell+1-m)\omega_{res}T_s]>\sin[(\ell-m)\omega_{res}T_s]\\&\Rightarrow\sin[(\lambda+1)\omega_{res}T_s]>\sin(\lambda\omega_{res}T_s),\end{aligned} \quad (3.20)$$

which results in $(\lambda+\frac{1}{2})T_s<\frac{\pi}{2\omega_{res}}$ $(k=0)$, $\frac{(4k-1)\pi}{2\omega_{res}}<(\lambda+\frac{1}{2})T_s<\frac{(4k+1)\pi}{2\omega_{res}}$ $(k=1,2,3...)$, the same as (3.6) that was deduced in the *s*-domain. However for controllability, f_{res} should be smaller than half the sampling frequency ($f_s/2$, the Nyquist frequency), i.e., $\omega_{res}T_s<\pi$ [21, 108]. Considering this restriction, the stable ranges of the time delay are obtained as:

$$\begin{cases}(\lambda+\frac{1}{2})T_s<\frac{\pi}{2\omega_{res}},(\lambda\geq k,k=0)\\ \frac{(4k-1)\pi}{2\omega_{res}}<(\lambda+\frac{1}{2})T_s<(\lambda+\frac{1}{2})\frac{\pi}{\omega_{res}},(2k-1<\lambda\leq 2k,k=1,2,3,...)\\ \frac{(4k-1)\pi}{2\omega_{res}}<(\lambda+\frac{1}{2})T_s<\frac{(4k+1)\pi}{2\omega_{res}},(\lambda>2k,k=1,2,3,...)\end{cases} \tag{3.21}$$

It is interesting from (3.21) that for a given T_s, the system can be stabilized by modifying the value of λ, and vice versa. Moreover, there are many optional ranges for λ and T_s. Taking $\lambda = 3$ for example, the available values of k are 0 and 1; therefore the resultant condition is $T_s \in (0, \pi/7\omega_{res}) \cup (3\pi/7\omega_{res}, 5\pi/7\omega_{res})$. The root loci of the closed-loop system with T_s in different ranges are shown in Figure 3.7, which demonstrate that there are at least two unstable poles outside the unit circle if the condition is not met.

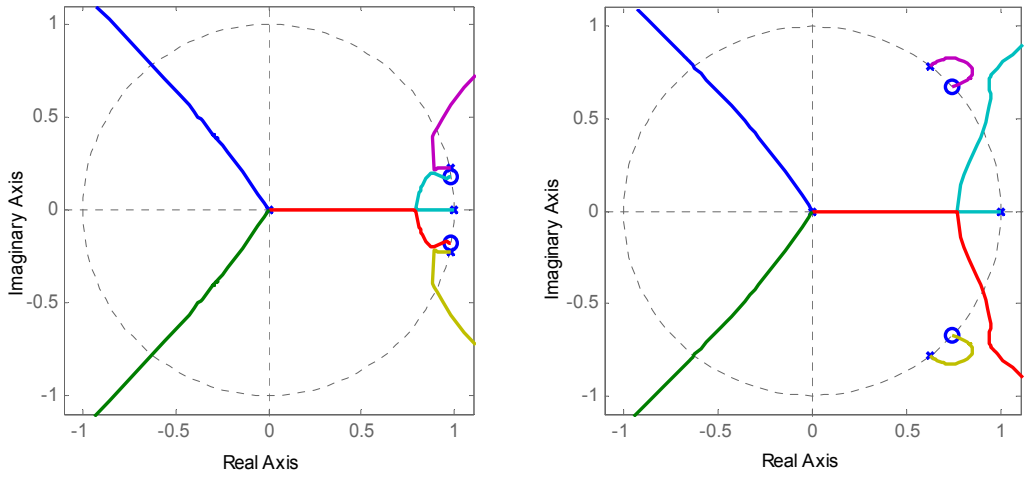

(a) (b)

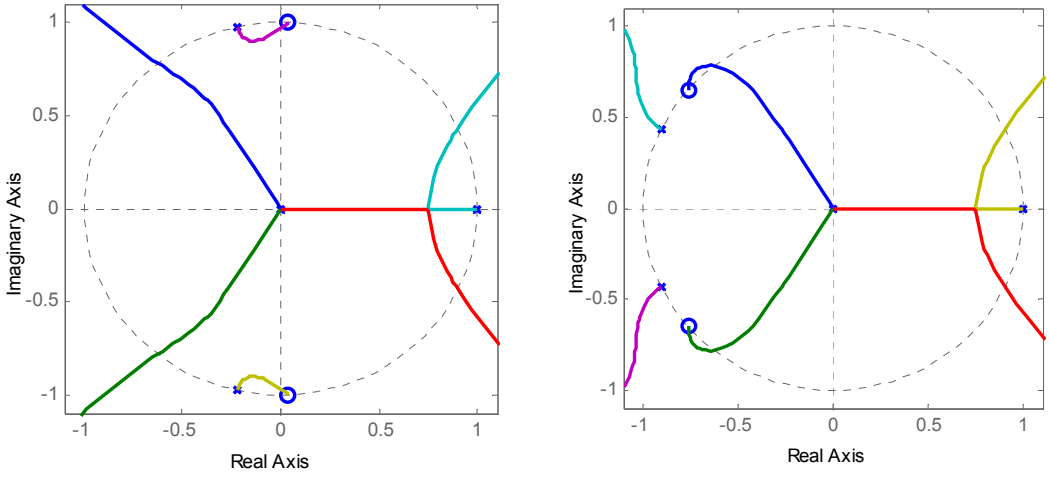

(c) (d)

Figure 3.7: Root loci of the ICF loop when $\lambda = 3$ and with T_s in different ranges. (a) $T_s \in (0, \pi/7\omega_{res})$. (b) $T_s \in (\pi/7\omega_{res}, 3\pi/7\omega_{res})$. (c) $T_s \in (3\pi/7\omega_{res}, 5\pi/7\omega_{res})$. (d) $T_s \in (5\pi/7\omega_{res}, \pi/\omega_{res})$.

3.4.3 Grid Current Feedback

Using the method in Appendix A, the following stable condition can be obtained for the GCF loop:

$$\begin{aligned} &\sin[(\ell+1-m)\omega_{res}T_s] < \sin[(\ell-m)\omega_{res}T_s] \\ &\Rightarrow \sin[(\lambda+1)\omega_{res}T_s] < \sin(\lambda\omega_{res}T_s), \end{aligned} \tag{3.22}$$

which results in $\frac{(4k+1)\pi}{2\omega_{res}} < (\lambda+\frac{1}{2})T_s < \frac{(4k+3)\pi}{2\omega_{res}}$ $(k = 0,1,2,...)$, the same as (3.9) that was derived in the *s*-domain. Also considering the restriction $\omega_{res}T_s < \pi$, the stable ranges of the time delay are yielded as:

$$\begin{cases} \frac{(4k+1)\pi}{2\omega_{res}} < (\lambda+\frac{1}{2})T_s < (\lambda+\frac{1}{2})\frac{\pi}{\omega_{res}}, (2k < \lambda \le 2k+1, k = 0,1,2,...) \\ \frac{(4k+1)\pi}{2\omega_{res}} < (\lambda+\frac{1}{2})T_s < \frac{(4k+3)\pi}{2\omega_{res}}, (\lambda > 2k+1, k = 0,1,2,...) \end{cases} \tag{3.23}$$

Like ICF, the GCF loop can also be stabilized by adjusting the value of λ or T_s. For example, for the case of $\lambda = 3$, the available values of k are 0 and 1, thus the stable ranges of T_s are $(\pi/7\omega_{res}, 3\pi/7\omega_{res}) \cup (5\pi/7\omega_{res}, \pi/\omega_{res})$. The root loci of the closed-loop system with T_s in different ranges are shown in Figure 3.8. As seen if T_s

is outside the stable ranges, there are at least two unstable poles whatever the proportional gain k_p is.

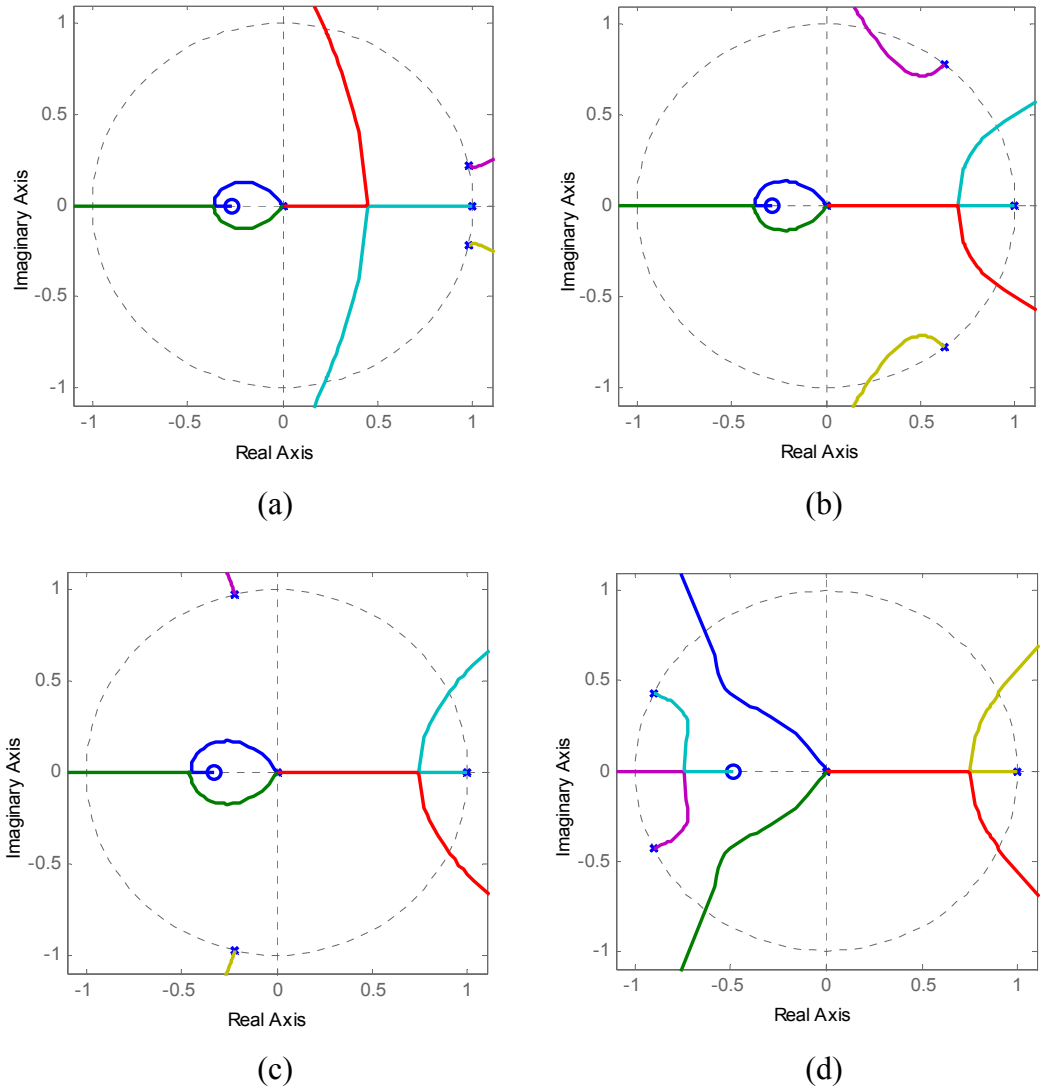

Figure 3.8: Root loci of the GCF loop when $\lambda = 3$ and with T_s in different ranges. (a) $T_s \in (0, \pi/7\omega_{res})$. (b) $T_s \in (\pi/7\omega_{res}, 3\pi/7\omega_{res})$. (c) $T_s \in (3\pi/7\omega_{res}, 5\pi/7\omega_{res})$. (d) $T_s \in (5\pi/7\omega_{res}, \pi/\omega_{res})$.

It can be observed from (3.6) and (3.9), (3.21) and (3.23) that the stable ranges of the time delay for ICF and GCF are complementary. It means that with a given time delay, only one of the two single-loop controlled systems can be made stable if no time delay compensator is applied.

3.5 Optimal Range of Time Delay and Compensators

In this section the optimal range of the time delay is discussed and identified, to achieve the maximum bandwidth and ensure adequate stability margins. It is found that in the optimal range, the existence of a time delay degrades the stability of the ICF loop, whereas a proper time delay is needed for the GCF loop. To improve stability, a LP based time delay reduction method is proposed for ICF, while a proper time delay can be added to GCF.

3.5.1 Reasonable Time Delay Range

The stable ranges (3.21) and (3.23) indicate that there are many available ranges for the time delay. However, for a large k, the phase lag due to the time delay is significant. In this case, small controller gains have to be used to guarantee stability, leading to a low bandwidth. It is apparent that $k = 0$ is the case for achieving the highest bandwidth. The reasonable time delay ranges of ICF and GCF are thus given as (3.24) and (3.25), respectively.

$$(\lambda+\frac{1}{2})T_s < \frac{\pi}{2\omega_{res}}, (\lambda \geq 0) \tag{3.24}$$

$$\begin{cases} \frac{\pi}{2\omega_{res}} < (\lambda+\frac{1}{2})T_s < (\lambda+\frac{1}{2})\frac{\pi}{\omega_{res}}, (0<\lambda\leq 1) \\ \frac{\pi}{2\omega_{res}} < (\lambda+\frac{1}{2})T_s < \frac{3\pi}{2\omega_{res}}, (\lambda>1) \end{cases} \tag{3.25}$$

From (3.24) it can be seen that an increase in time delay degrades the stability of the ICF loop. By contrast, (3.25) indicates that a proper time delay is required for the stability of the GCF loop. And furthermore, in the scale of $0 < \lambda \leq 1$, $\lambda = 1$ is the best option to get the largest available range for the sampling period T_s.

For a given λ, requirements (3.24) and (3.25) can also be used to calculate the stable range of f_s. Taking $\lambda = 0.5$ and $\lambda = 1$ for example, the stable ranges of f_s are summarized in Table 3.1. Note that the requirement of GCF for $\lambda = 1$ is in agreement with the findings in [30].

Table 3.1: Stable and optimal ranges of the sampling frequency

method	λ	stable range	optimal range
ICF	0.5	$f_s > 4f_{res}$	$f_s > 6f_{res}$
	1	$f_s > 6f_{res}$	$f_s > 9f_{res}$
GCF	0.5	$2f_{res} < f_s < 4f_{res}$	$2f_{res} < f_s < 3f_{res}$
	1	$2f_{res} < f_s < 6f_{res}$	$9f_{res}/4 < f_s < 9f_{res}/2$

3.5.2 Optimal Time Delay Range

A system can be made stable when the time delay falls into the stable ranges. However, the possible stable operation is not enough, adequate stability margins including phase margin (PM) and gain margin (GM) should also be guaranteed.

For the ICF, when the time delay is within the stable range (3.24), the Bode diagram of the loop gain is shown in Figure 3.9. There are three crossover frequencies: ω_{i1}, ω_{i2}, and ω_{i3} ($\omega_{i1} < \omega_r$, $\omega_r < \omega_{i2} < \omega_{res}$, $\omega_{i3} > \omega_{res}$). It is apparent that the PM of ϕ_i at ω_{i3} is the smallest one. For a predetermined PM of φ ($\varphi < \pi/2$), to ensure a possibility for $\phi_i \geq \varphi$, the phase lag of the time delay at ω_{res} should be smaller than $\pi/2 - \varphi$, that is

$$(\lambda + \frac{1}{2})T_s < \frac{\pi/2 - \varphi}{\omega_{res}}. \tag{3.26}$$

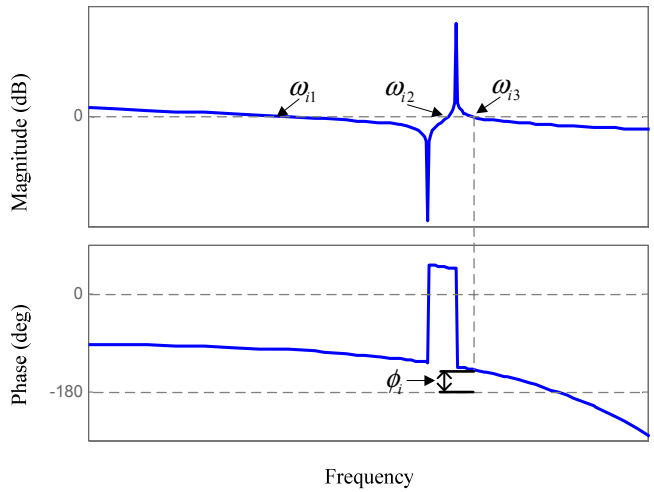

Figure 3.9: Bode diagram of the ICF loop gain with time delay in the optimal range.

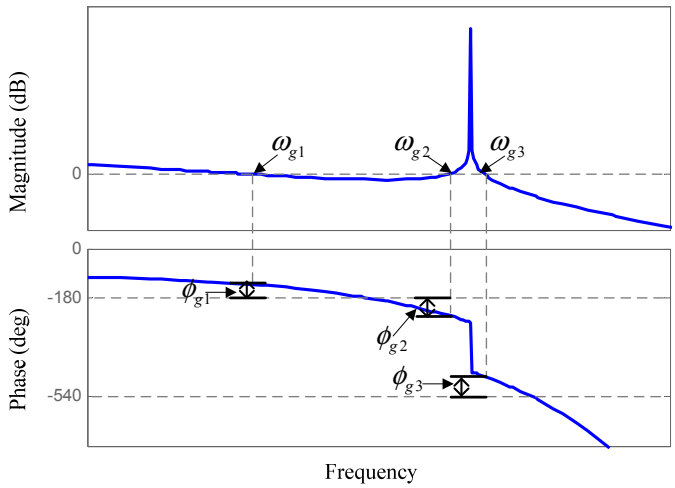

Figure 3.10: Bode diagram of the GCF loop gain with time delay in the optimal range.

For the GCF, based on (3.25), the Bode diagram of the loop gain is shown in Figure 3.10. There are also three crossover frequencies: ω_{g1}, ω_{g2}, and ω_{g3}. ϕ_{g1} can be modified to be larger than φ by adjusting k_p. To make it possible for $\phi_{g2} \geq \varphi$ and $\phi_{g3} \geq \varphi$, the following optimal range of the time delay can be yielded:

$$\begin{cases} \dfrac{\pi/2+\varphi}{\omega_{res}} < (\lambda+\dfrac{1}{2})T_s < (\lambda+\dfrac{1}{2})\dfrac{\pi}{\omega_{res}}, (\dfrac{\varphi}{\pi} < \lambda \leq 1-\dfrac{\varphi}{\pi}) \\ \dfrac{\pi/2+\varphi}{\omega_{res}} < (\lambda+\dfrac{1}{2})T_s < \dfrac{3\pi/2-\varphi}{\omega_{res}}, (\lambda > 1-\dfrac{\varphi}{\pi}) \end{cases} \tag{3.27}$$

To sum up, in order to make it is possible for PM to be larger than φ, the time delay of the ICF and GCF must fall into the optimal range (3.26) and (3.27), respectively. For a given λ, the optimal range of f_s can also be deduced. Taking $\varphi = \pi/6$ (30°) for instance, the optimal range of f_s for $\lambda = 0.5$ and $\lambda = 1$ are also summarized in Table 3.1.

3.5.3 Time Delay Compensators

As stated previously, a time delay weakens the stability of the ICF loop. Therefore, time delay reduction methods should be adopted if (3.26) is not met. Numerous compensators have been studied, such as the state observers [103] and shifting of

sampling instants [21, 107]. However, the state observers are sensitive to parameter variations, and the shifting of the sampling instants is limited by aliasing and switching noises [21]. A LP as described in [105] is adopted in the present work due to its effectiveness and ease of realization. Its discrete transfer function is given as

$$G_{LP}(z) = 1 + \frac{T_d}{T_s} - \frac{T_d}{T_s} z^{-1} = \lambda + \frac{3}{2} - (\lambda + \frac{1}{2}) z^{-1} . \tag{3.28}$$

The compensated block diagram is shown in Figure 3.11, where the LP is in the feedback loop [99]. Taking $\lambda = 1$ for example, Table 3.1 indicates that $f_s = 6f_{res}$ is the critical sampling frequency. However, with the adoption of the LP, the PM is increased significantly as shown in Figure 3.12, thus the stability is improved.

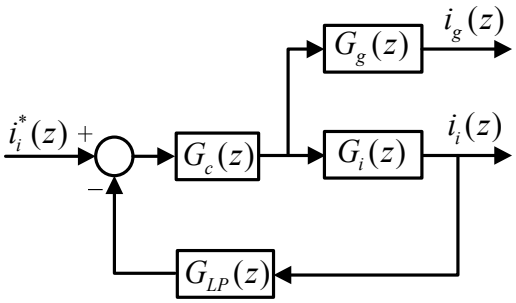

Figure 3.11: Block diagram of the ICF loop with a LP.

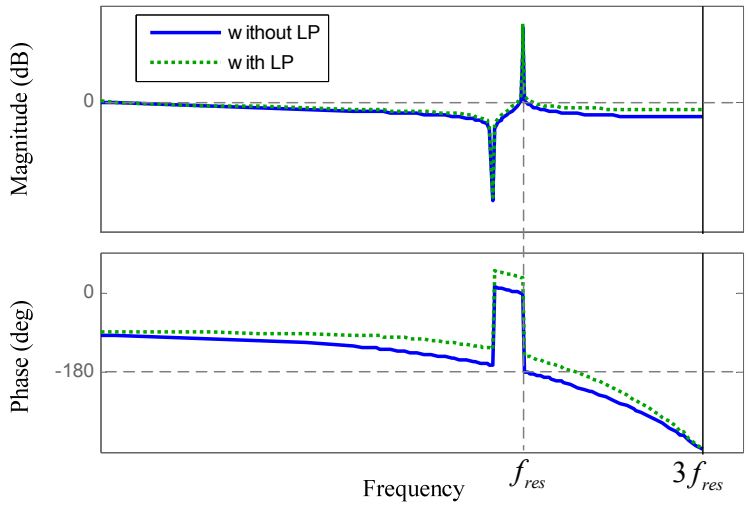

Figure 3.12: Bode diagrams of the loop gain of ICF when $\lambda = 1$ and $f_s = 6f_{res}$, with or without the LP.

Using the previous procedure, it can be deduced that the stable ranges of time delay for the loop with CCF, which is usually adopted as an inner active damping loop [104], are same as those of the ICF loop. This is why time delay reduction methods are employed to eliminate a potential non-minimum phase behavior of the inner loop, and thus to improve the overall system stability [21, 75]. Therefore, the present work can also facilitate the analysis of the active damping methods with an inner loop using CCF or ICF [78].

For the GCF, with a given $f_s > 2f_{res}$, if (3.27) is not fulfilled, λ should generally be increased properly. The available range of λ can be yielded as

$$(\frac{1}{4}+\frac{\varphi}{2\pi})\frac{f_s}{f_{res}}-\frac{1}{2}<\lambda<(\frac{3}{4}-\frac{\varphi}{2\pi})\frac{f_s}{f_{res}}-\frac{1}{2}. \tag{3.29}$$

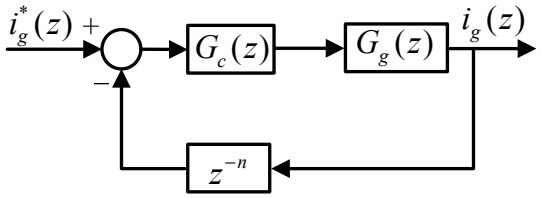

Figure 3.13: Block diagram of the GCF loop with an addition of time delay.

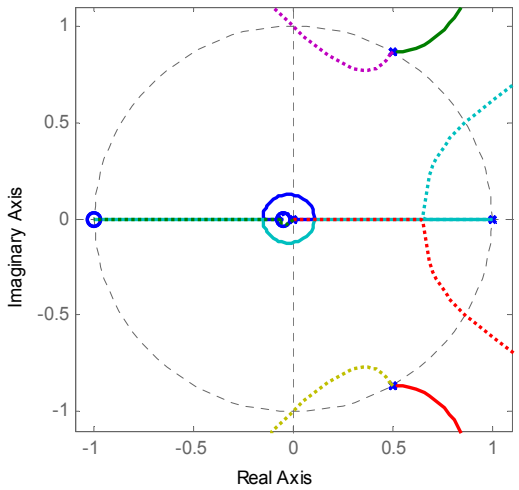

Figure 3.14: Root loci of the GCF loop when $f_s = 6f_{res}$, with $\lambda = 0.5$ (solid lines) and $\lambda = 2.5$ (dotted lines).

The corresponding compensated GCF is shown in Figure 3.13, where a delay z^{-n} is added so that the processing time delay fulfills (3.29). In the real operation, λ is an integer multiple of 0.5 [23], this should be considered when using (3.29).

Taking $\lambda = 0.5$ and $f_s = 6f_{res}$ for example, Table 3.1 and the root loci in Figure 3.14 indicate this is an unstable case. According to (3.29), the optimal range for $\varphi = 30°$ is $1.5 < \lambda < 3.5$. The root loci of the system with a compromised value $\lambda = 2.5$ ($n = 2$) are shown in Figure 3.14. It can be seen that the system can be stabilized by adding a proper time delay.

3.5.4 Discussion on the Choice of the Feedback Current

Confusions exist in conclusions and findings relevant to the stability of the single-loop control systems from different previous work. The analysis in the present work is able to clarify the confusions and provide a unified explanation.

Without considering any time delay, the ICF loop can be made stable while the GCF loop can never be stabilized without other measures. This is why the inverter current was chosen as the control variable in [24-26, 49]. The GCF has only been used with additional active damping methods [58, 78, 101, 102].

In previous studies, the total time delay is predominantly considered to be $T_d = 1.5T_s$ ($\lambda = 1$). In this case, as indicated in Table 3.1, the ICF loop can be made stable when $f_s > 6f_{res}$, while the requirement for GCF is $2f_{res} < f_s < 6f_{res}$. In [23], $f_{res} = 1756.5$ Hz and $f_s = 20000$ Hz gives $f_s/f_{res} = 11.3863$, then it found the ICF is superior to the GCF. Similar results were given in [69] ($f_{res} = 726.44$ Hz and $f_s = 5000$ Hz, $f_s/f_{res} = 6.8829$) and [103] ($f_{res} = 1136.8$ Hz and $f_s = 10000$Hz, $f_s/f_{res} = 8.7966$), and it is shown that active damping is required if the grid current is to be controlled directly [75].

In contrast, in [34], $f_{res} = 1224.1$ Hz and $f_s \in$ (3500 Hz, 7000 Hz) thus $f_s/f_{res} \in$ (2.8592, 5.7185), then it concluded that the GCF loop is stable whereas the ICF loop is unstable. Similar conclusions were drawn in [28] ($f_{res} = 2219.3$ Hz and $f_s = 8000$ Hz, $f_s/f_{res} = 3.6047$) and [29] ($f_{res} \in$ (2905.8 Hz, 5058.3 Hz) and $f_s = 16000$ Hz, $f_s/f_{res} \in$ (3.1631, 5.5062)) which used the grid current as the feedback variable.

From aforementioned analyses, the choice of the feedback current should be made based on the *LCL* parameters. For a low *LCL* resonance frequency, it is better

to choose the inverter current to obtain a large stable range of sampling frequency. For a high *LCL* resonance frequency, the grid current can be used to avoid a too high sampling frequency. In some cases, both of these two currents can be adopted with the proposed time delay compensators being applied.

In a real circuit, the parasitic resistance of the inductors improves the stability of both single-loop control systems, which will lead to different stable time delay ranges. Taking the resistance into consideration, the magnitude at the resonance frequency f_{res} (see Figures 3.4 and 3.5) is not infinite, and it will be smaller than 0 dB when a sufficiently small k_p is used. Thus the negative crossing at f_{res} can be avoided and the systems can be made stable irrespective of the time delay. However, the resistance does not make significant difference on system stability, because it is generally small (see Table 2.2). If the time delay is outside the stable ranges deduced in the previous sections, systems with the resistance would be unstable even when a small controller gain is used. Therefore the case without the resistance is actually the worst one.

Finally, the robustness of the single-loop control systems against the grid inductance variation is discussed. The addition of a grid inductance is equivalent to an increase in L_g, hence leading to a lower ω_{res}. For the ICF, it can be seen from (3.24) and (3.26) that the available time delay range is increased. The ICF is therefore robust to the grid inductance variation. For the GCF, (3.25) and (3.27) indicate that the decreased ω_{res} shifts the available time delay range. The time delay in the system would not be covered by the shifted stable range. Therefore, the GCF is susceptible to the grid inductance variation.

3.6 Design of the Controller

Now that a single-loop control system can be stabilized if the time delay is in the stable ranges, and the optimal range makes it is possible for the PM to be larger than a predetermined value, the PI controller has to be designed to guarantee adequate stability margins.

The design of PI controller for an *LCL*-filtered inverter is usually implemented by simplifying the *LCL* as an *L*-filter [30, 33, 101]. However from previous analysis, the *LCL* resonance affects the stability margins significantly, this approximation is thus not accurate enough. In this section, a simple tuning procedure is proposed.

3.6.1 Inverter Current Feedback

Firstly, the proportional gain k_p is discussed. There are three main values, k_{p1} to achieve a PM of φ, k_{p2} to ensure a GM of 3 dB [49], and the maximum value $k_{p\max}$ to ensure stability.

For a predetermined PM of φ, according to (3.5) the crossover frequency ω_{i3} in Figure 3.9 can be yielded as

$$\varphi = \pi - \frac{\pi}{2} - (\lambda + \frac{1}{2})\omega_{i3}T_s \Rightarrow \omega_{i3} = \frac{\pi - 2\varphi}{(2\lambda + 1)T_s}. \tag{3.30}$$

k_{p1} is then set to achieve unity loop gain at ω_{i3}:

$$k_{p1} = \frac{\omega_{i3}L_i(\omega_{i3}^2 - \omega_{res}^2)}{k_{PWM}(\omega_{i3}^2 - \omega_r^2)}. \tag{3.31}$$

The frequency ω_m at which the phase of the open-loop transfer function crosses over –180° is given as

$$(\lambda + \frac{1}{2})\omega_m T_s = \frac{\pi}{2} \Rightarrow \omega_m = \frac{\omega_s}{2(2\lambda + 1)}, \tag{3.32}$$

where $\omega_s = 2\pi f_s$. $k_{p\max}$ is then set to achieve unity at ω_m, derived as

$$k_{p\max} = \frac{\omega_s L_i[\omega_s^2 - 4(2\lambda + 1)^2\omega_{res}^2]}{k_{PWM}[2(2\lambda + 1)\omega_s^2 - 8(2\lambda + 1)^3\omega_r^2]}. \tag{3.33}$$

k_{p2} to ensure a GM of 3 dB is therefore expressed as

$$k_{p2} = \frac{\sqrt{2}}{2}\frac{\omega_s L_i[\omega_s^2 - 4(2\lambda + 1)^2\omega_{res}^2]}{k_{PWM}[2(2\lambda + 1)\omega_s^2 - 8(2\lambda + 1)^3\omega_r^2]}. \tag{3.34}$$

As a result, k_p is chosen to be the smaller one of k_{p1} and k_{p2}.

Finally the integral term k_i can be tuned to make a small phase contribution at $\omega_{res}/2$, given as [24, 39]

$$k_i = \frac{\omega_{res}}{20}. \tag{3.35}$$

When a LP is applied to enhance the stability, the parameters should be modified. The magnitude and phase of the loop gain becomes $|T_i(z)|=|k_{PWM}G_c(z)G_{LP}(z)G_i(z)|$ and $\angle T_i(z)=\angle k_{PWM}G_c(z)G_{LP}(z)G_i(z)$, respectively. The magnitude and phase of the LP are

$$\begin{cases} \left|G_{LP}(\omega)\right| = \dfrac{\sqrt{8\lambda^2+16\lambda+10-(8\lambda^2+16\lambda+6)\cos\omega T_s}}{2}, \\ \theta_{LP}(\omega) = \arctan\dfrac{(2\lambda+3)\sin\omega T_s}{(2\lambda+3)\cos\omega T_s-(2\lambda+1)} - \omega T_s + \pi. \end{cases} \tag{3.36}$$

Therefore following the same tuning procedure above, k_{p1} and k_{p2} can be calculated as

$$\begin{cases} k_{p1} = \dfrac{\omega_{i3}L_i(\omega_{i3}^2-\omega_{res}^2)}{k_{PWM}(\omega_{i3}^2-\omega_r^2)\left|G_{LP}(\omega_{i3})\right|} \\ k_{p2} = \dfrac{\sqrt{2}}{2}\dfrac{\omega_m L_i(\omega_m^2-\omega_{res}^2)}{k_{PWM}(\omega_m^2-\omega_r^2)\left|G_{LP}(\omega_{i3})\right|}, \end{cases} \tag{3.37}$$

where ω_{i3} and ω_m are modified to

$$\omega_{i3} = \frac{\pi-2\varphi+2\theta_{LP}(\omega_{i3})}{(2\lambda+1)T_s}, \omega_m = \frac{\pi+2\theta_{LP}(\omega_m)}{(2\lambda+1)T_s}. \tag{3.38}$$

The integral term k_i is still given by (3.35).

3.6.2 Grid Current Feedback

On the basis of (3.27), to achieve a PM of φ, the crossover frequencies ω_{g1}, ω_{g2}, and ω_{g3} are obtained from (3.8) as

$$\omega_{g1} = \frac{\pi-2\varphi}{(2\lambda+1)T_s}, \omega_{g2} = \frac{\pi+2\varphi}{(2\lambda+1)T_s}, \omega_{g3} = \frac{3\pi-2\varphi}{(2\lambda+1)T_s}. \tag{3.39}$$

The corresponding proportional gains are then derived from (3.7) as

$$\begin{cases} k_{p1} = \dfrac{\omega_{g1}L_i(\omega_{res}^2-\omega_{g1}^2)}{k_{PWM}\omega_r^2}, \\ k_{p2} = \dfrac{\omega_{g2}L_i(\omega_{res}^2-\omega_{g2}^2)}{k_{PWM}\omega_r^2}, \\ k_{p3} = \dfrac{\omega_{g3}L_i(\omega_{g3}^2-\omega_{res}^2)}{k_{PWM}\omega_r^2}. \end{cases} \tag{3.40}$$

The frequency ω_m at which the phase of the open-loop transfer function crosses over –180° is the same as (3.32). The maximum value $k_{p\max}$, and k_{p4} to give a GM of 3 dB are then written as

$$\begin{cases} k_{p\max} = \dfrac{\omega_s L_i[4(2\lambda+1)^2\omega_{res}^2 - \omega_s^2]}{8k_{PWM}(2\lambda+1)^3\omega_r^2}, \\ k_{p4} = \dfrac{\sqrt{2}\omega_s L_i[4(2\lambda+1)^2\omega_{res}^2 - \omega_s^2]}{16k_{PWM}\omega_r^2(2\lambda+1)^3}. \end{cases} \tag{3.41}$$

Then k_p is chosen to be the smallest value among k_{p1}, k_{p2}, k_{p3}, and k_{p4}.

Finally, the integral term k_i is tuned to have a small influence on the phase at ω_{g1}:

$$k_i = \frac{\omega_{g1}}{10} = \frac{\pi - 2\varphi}{10(2\lambda+1)T_s}. \tag{3.42}$$

Table 3.2: Parameters of the circuit

Symbol	Quantity	Value
V_{dc}	DC input voltage amplitude	450 V
V_g	Single-phase grid voltage amplitude	155 V
f_n	Fundamental frequency	50 Hz
ω_n	Fundamental angular frequency	2π·50 rad/s
L_i	Inverter side inductor	4.4 mH
L_g	Grid side inductor	2.2 mH
C	Capacitor of *LCL* filter	10 μF
ω_r	Resonant angular frequency between L_g and C	6742 rad/s
f_r	Resonant frequency between L_g and C	1073 Hz
ω_{res}	*LCL* resonance angular frequency	8257.2 rad/s
f_{res}	*LCL* resonance frequency	1314.2 Hz

3.7 Results

Simulation and experiment were implemented to verify the delay-dependent stability of the single-loop controlled grid-connected inverters with *LCL* filters. Parameters of the circuit described in Section 2.6 are summarized in Table 3.2; note that the secondary voltage of the step-up transformer is looked as the grid voltage hencefor-

ward. The control is implemented in the SRF. The transient response as the amplitude of the grid current stepping from 1 to 4 A is examined to evaluate the system stability. Therefore it is achieved by stepping the reference *d*-axis current from 1 to 4 A. For GCF, the reference *q*-axis current is set to 0. For ICF, as the grid current is indirectly controlled, the reference *q*-axis current is set to $\omega_n C V_g$ instead of 0 to achieve the unity PF [24].

3.7.1 Simulation Results

Simulations in MATLAB/PLECS were used to verify the stable ranges of the time delay obtained previously. Taking $f_s = 6f_{res}$ for example, $\omega_{res}T_s < \pi$ is fulfilled, therefore the stable ranges (3.6) and (3.21) of the ICF are identical, as well as the stable ranges (3.9) and (3.23) of the GCF.

The reference *d*-axis current steps from 1 to 4 A at 0.02 s. For ICF, the transient responses when $T_d < \pi/2\omega_{res}$ ($k = 0$), $3\pi/2\omega_{res} < T_d < 5\pi/2\omega_{res}$ ($k = 1$), and $7\pi/2\omega_{res} < T_d < 9\pi/2\omega_{res}$ ($k = 2$) are shown in Figure 3.15, the lags in the responses are due to the time delay in the forward-loop. It can be seen that when the time delay is within these ranges, the ICF loop can be made stable. The instabilities when T_d is outside the stable ranges are also illustrated in Figure 3.15, where the range of T_d changes at 0.08 s. For $k \geq 3$ in (3.6), although not shown here, the loop can also be made stable. However, as can be seen from Figure 3.15, for a larger *k*, a slower transient response is produced because of the lower bandwidth.

For GCF, the stable transient responses when $\pi/2\omega_{res} < T_d < 3\pi/2\omega_{res}$ ($k = 0$), $5\pi/2\omega_{res} < T_d < 7\pi/2\omega_{res}$ ($k = 1$), and $9\pi/2\omega_{res} < T_d < 11\pi/2\omega_{res}$ ($k = 2$) and the unstable responses when T_d is outside the stable ranges are presented in Figure 3.16. For $k \geq 3$ in (3.9), the GCF loop can also be stabilized with well-designed controller parameters. If the time delay is not within the stable ranges, the system can never be stabilized with any controller gains.

These simulated results verify the stable ranges of time delay derived in Section 3.3 and 3.4.

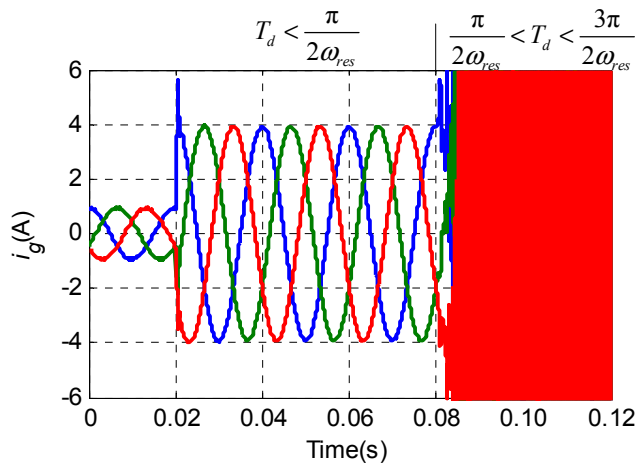

(a)

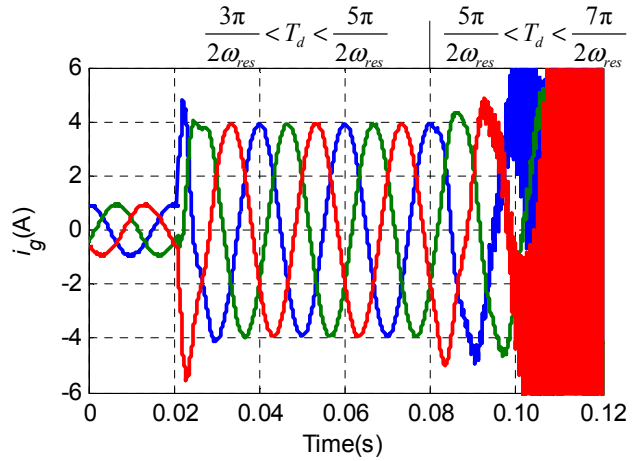

(b)

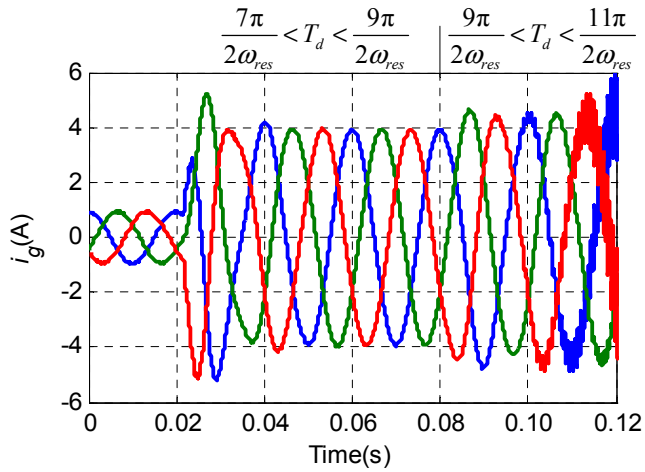

(c)

Figure 3.15: Simulated transient responses of ICF when T_d is in different ranges. (a) $T_d < \pi/2\omega_{res}$, $\pi/2\omega_{res} < T_d < 3\pi/2\omega_{res}$. (b) $3\pi/2\omega_{res} < T_d < 5\pi/2\omega_{res}$, $5\pi/2\omega_{res} < T_d < 7\pi/2\omega_{res}$ (c) $7\pi/2\omega_{res} < T_d < 9\pi/2\omega_{res}$, $9\pi/2\omega_{res} < T_d < 11\pi/2\omega_{res}$.

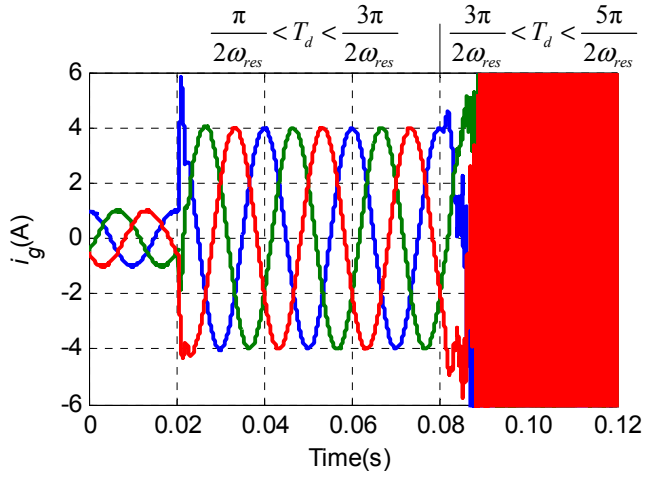

(a)

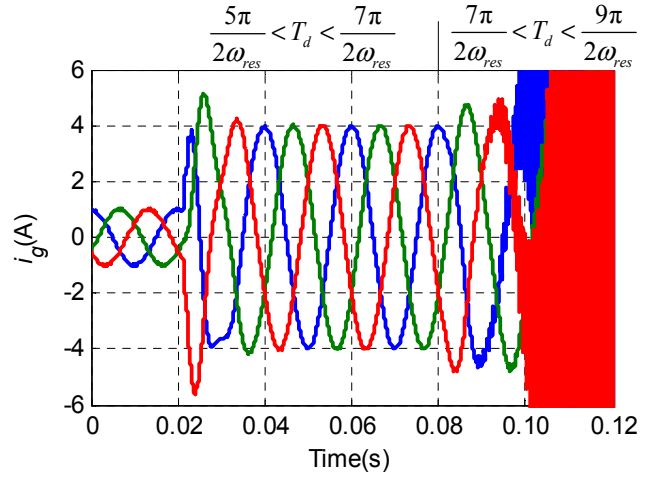

(b)

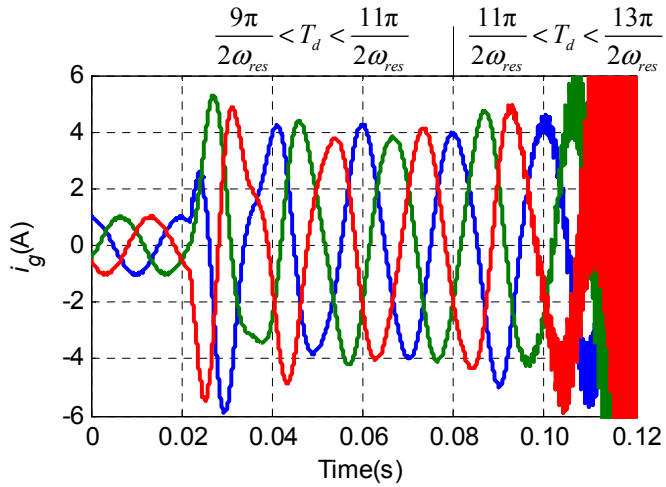

(c)

Figure 3.16: Simulated transient responses of GCF when T_d is in different ranges. (a) $\pi/2\omega_{res} < T_d < 3\pi/2\omega_{res}$, $3\pi/2\omega_{res} < T_d < 5\pi/2\omega_{res}$. (b) $5\pi/2\omega_{res} < T_d < 7\pi/2\omega_{res}$, $7\pi/2\omega_{res} < T_d < 9\pi/2\omega_{res}$. (c) $9\pi/2\omega_{res} < T_d < 11\pi/2\omega_{res}$, $11\pi/2\omega_{res} < T_d < 13\pi/2\omega_{res}$.

3.7.2 Experimental Results

Because in the real operation the normal values of λ are 0.5 and 1, experiments are implemented to verify the stable range of f_s in Table 3.1, and to validate the time delay compensators and PI design method. The uniformly sampled symmetric-on-time triangle PWM is applied. Samplings are conducted when the PWM counter reaches the period value. $\lambda = 0.5$ is achieved by updating the duty ratio to the compare register when the counter reaches zero, while $\lambda = 1$ is realized by updating the compare register when the counter reaches the period value [23]. For the cases with time delay in the optimal range, controller parameters are designed using the method in Section 3.6. For other cases, compromised parameters are used to validate the stable ranges.

3.7.2.1 Inverter Current Feedback

Figure 3.17(a) shows the one-phase grid voltage and current. As can be seen the grid current can be synchronized with the grid voltage when it is controlled indirectly by the inverter current.

For $\lambda = 0.5$, as shown in Table 3.1 $f_s = 4f_{res}$ is the critical value, below which the system is unable to be stabilized. When $f_s = 6f_{res}$, the transient response is shown in Figure 3.17(b), which indicates the stable operation. When $f_s = 4f_{res}$, the system is marginally stable, as presented in Figure 3.17(c), where the steady-state oscillation appears. Although not shown here, when $f_s < 4f_{res}$ the system is more likely to be unstable. When a LP is used when $f_s = 4f_{res}$, the transient response is shown in Figure 3.17(d). It can be seen that the LP stabilizes the system, thus the stable range of the sampling frequency is increased.

For $\lambda = 1$, $f_s > 6f_{res}$ is required for stability. When $f_s = 6f_{res}$, the transient response is shown in Figure 3.17(e), the current ripples imply the weak stability. In comparison to the case of $\lambda = 0.5$, the increase in the time delay degrades the stability of the ICF system. However, with the adoption of the LP, the system is stabilized, as shown

in Figure 3.17(f). When $f_s = 10f_{res}$, the response in Figure 3.17(g) indicates a stable system.

These experimental results verify the stable ranges of the sampling frequency deduced previously from the stable ranges of time delay. The stability improvement due to the LP has also been confirmed.

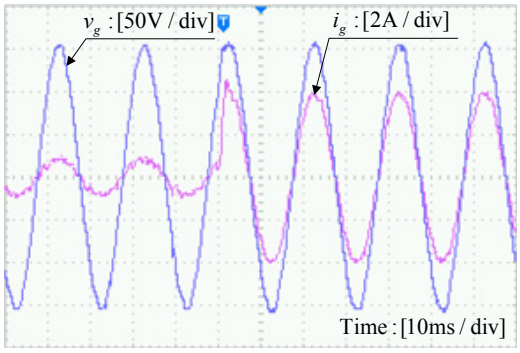

(a)

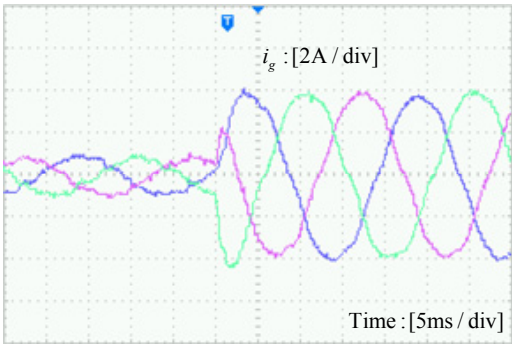

(b)

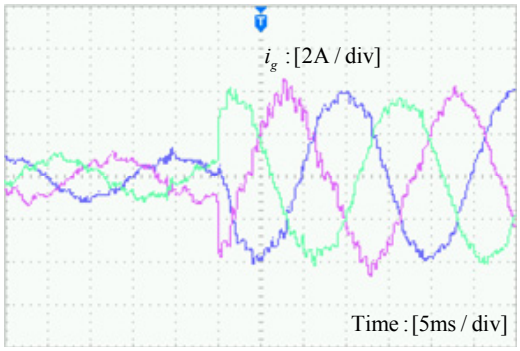

(c)

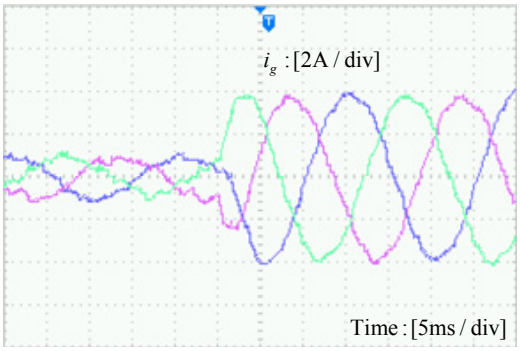

(d)

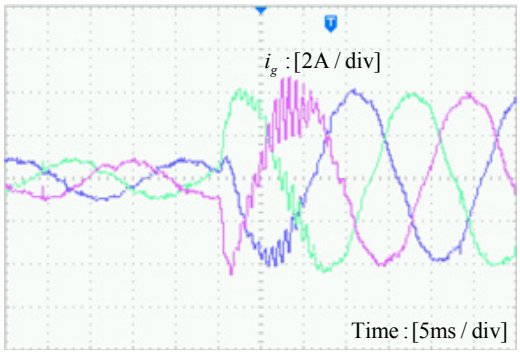

(e)

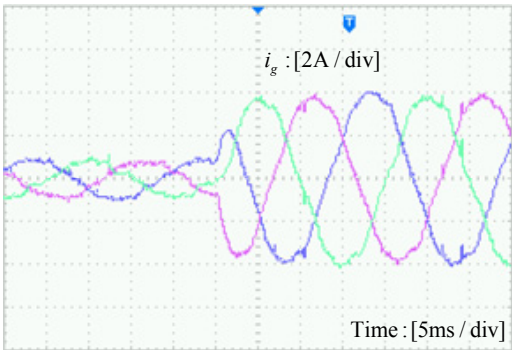

(f)

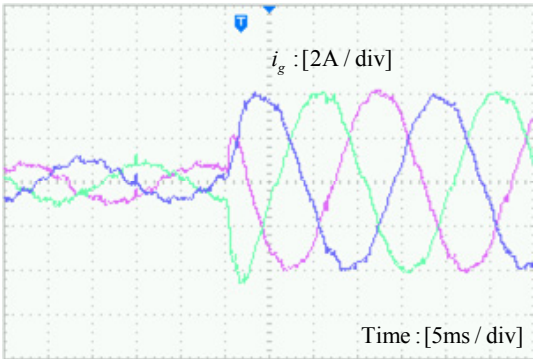

(g)

Figure 3.17: Experimental transient responses of ICF. (a) One-phase grid voltage and grid current of ICF with $\lambda = 0.5, f_s = 7f_{res}$. (b) Grid current with $\lambda = 0.5, f_s = 6f_{res}$. (c) $\lambda = 0.5, f_s = 4f_{res}$. (d) $\lambda = 0.5, f_s = 4f_{res}$, with LP. (e) $\lambda = 1, f_s = 6f_{res}$. (f) $\lambda = 1, f_s = 6f_{res}$, with LP. (g) $\lambda = 1, f_s = 10f_{res}$.

3.7.2.2 Grid Current Feedback

For $\lambda = 0.5$, $2f_{res} < f_s < 4f_{res}$ is required for stability. When $f_s = 4f_{res}$, the transient response shown in Figure 3.18(a) indicates the critical stability. The system is unstable when $f_s > 4f_{res}$ irrespective of the controller parameters. To improve the stability when a high sampling frequency is used, a proper time delay should be added. Taking $f_s = 6f_{res}$ for example, by adding a delay of $2T_s$, the system is stabilized, as shown in Figure 3.18(b).

For $\lambda = 1$, $2f_{res} < f_s < 6f_{res}$ is the stable range. When $f_s = 4f_{res}$ the transient response in Figure 3.18(c) shows a stable operation. Compared with that of $\lambda = 0.5$, it is obvious that the time delay improves the stability and increases the stable range of the sampling frequency. The transient response when $f_s = 6f_{res}$ is shown in Figure 3.18(d). In this case the system is obvious unstable, and circuit breaks are opened due to the overcurrent. To enhance the stability, a proper time delay should be added. Taking $f_s = 7f_{res}$ for instance, an additional delay of $2T_s$ is used. The transient response is given in Figure 3.18(e), which shows the improvement on stability due to the time delay addition.

The above results validate the stable ranges of sampling frequency in Table 3.1 which are deduced from the study of time delay requirements. It is also verified that the stability of the GCF system can be enhanced by using the delay addition method when a high sampling frequency is used.

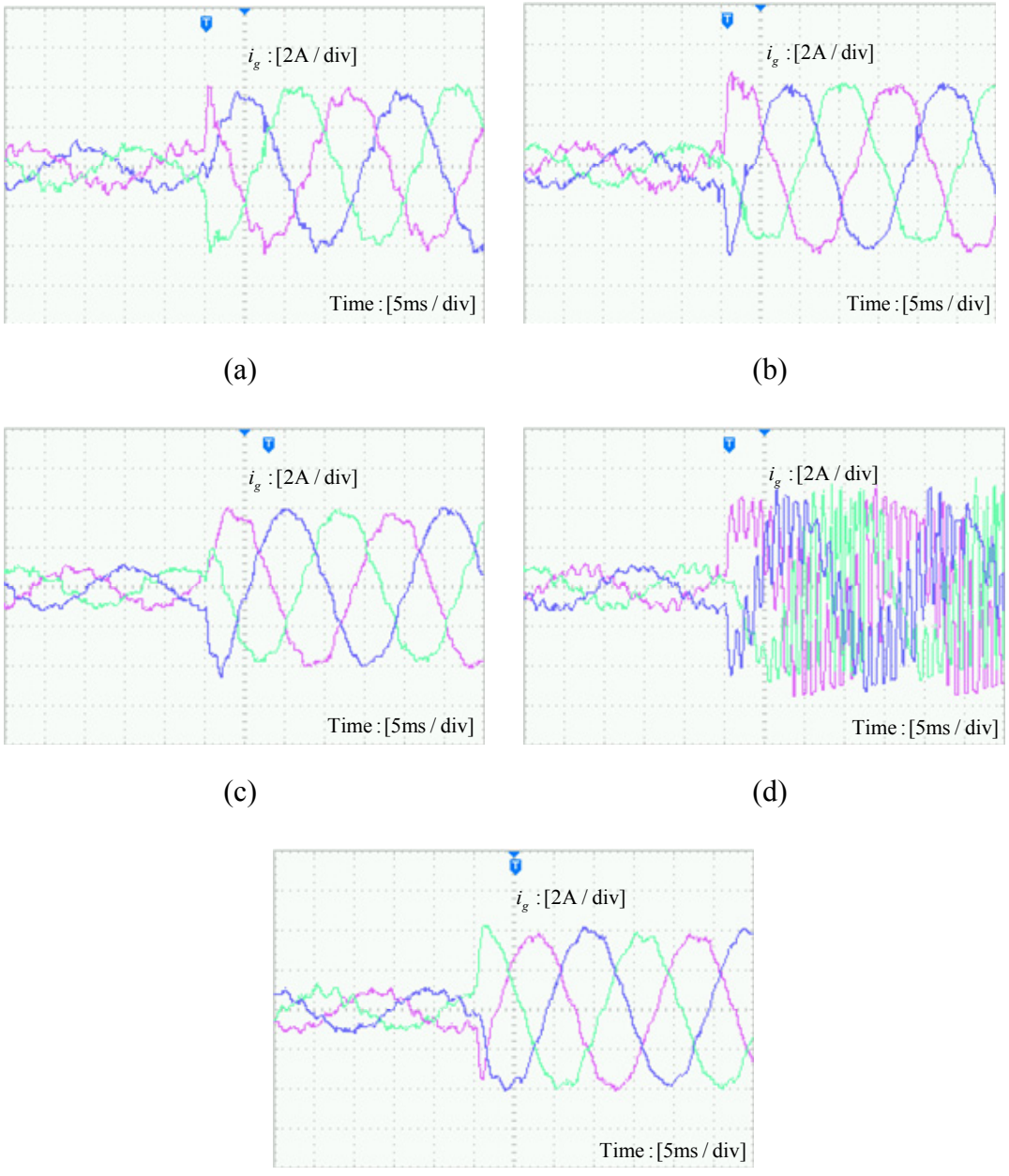

Figure 3.18: Experimental transient responses of the grid current in GCF. (a) $\lambda = 0.5$, $f_s = 4f_{res}$. (b) $\lambda = 0.5$, $f_s = 6f_{res}$, a delay of $2T_s$ added. (c) $\lambda = 1$, $f_s = 4f_{res}$. (d) $\lambda = 1$, $f_s = 6f_{res}$. (e) $\lambda = 1$, $f_s = 7f_{res}$, a delay of $2T_s$ added.

3.8 Conclusion

A systematic study of the relationship between time delay and stability of single-loop controlled grid-connected inverters with *LCL* filters has been carried out. The stable ranges of time delay for the ICF loop and GCF loop are obtained, in the continuous *s*-domain and also in the discrete *z*-domain. The optimal range of the time delay is also discussed. To improve system stability, a LP based time delay reduction method is proposed for the ICF, whereas a proper time delay is added to the GCF. The available sampling frequency ranges are therefore increased. Furthermore, a simple PI controller design method has been presented, by which adequate stability margins can be guaranteed. Simulation and experimental results have validated the study of the delay-dependent stability. This study has, for the first time, explained why different conclusions on the stability of the single-loop control systems were drawn in different studies. Moreover, the procedure can be extended to analyze the influence of time delay on the stability of *LCL*-filtered grid-connected inverters controlled by other methods including active damping.

Chapter 4

Damping Investigation of *LCL*-Filtered Grid-Connected Inverters

4.1 Introduction

In view of the inherent resonance of *LCL* filters which is harmful to the stability of grid-connected inverter systems, a function of resonance damping is essential for current control methods that are applied to the system [62, 104].

There are numerous current control strategies that can be used for *LCL*-filtered grid-connected inverters, which can be basically divided into single- and dual-loop methods [23, 30, 71, 76]. For single-loop control, as introduced in the previous chapter, the inverter current or grid current can be sensed as the feedback variable. For dual-loop control, an outer GCF loop plus an inner capacitor current proportional feedback active damping loop is usually applied [58, 75].

For the single-loop control with ICF, Tang *et al.* [24] found that it provides an inherent damping to the *LCL* resonance. However the time delay is ignored, and the nature of the inherent damping is vague. And it is indicated that the single-loop system with GCF is unstable [23, 24, 26]. On the contrary, the GCF has been adopted in [27-29, 34], and it is implied that the system can maintain stability. It is found in [34] that the stability is closely related to the ratio of the sampling frequency to resonance frequency, but the nature of this relationship is unknown. Yin *et al.* [29] presented the damping effect due to the time delay in the control loop, but the reason of the damping is also not clear.

To introduce a damping intentionally, the dual-loop control with CCF (capacitor current feedback) active damping is widely used [78, 101, 109]. It has been indicated that the inner CCF loop is equivalent to a virtual impedance that is connected in parallel with the capacitor, thus a damping is achieved [21, 55]. Nevertheless, only the inner loop has been analyzed, rather than the whole control system. As a result, the outer loop has to be considered separately, leading to a complex controller tuning procedure [101, 102].

These three control methods have been adopted in different articles. However, no comparison among them has been presented, for instance in which condition one can be used. The reason of their damping effect is not clear either. Furthermore, there is not a simple but accurate method to predict the gain boundary of the controllers.

In Chapter 3, the stability of the single-loop control methods has proved to be delay-dependent by means of classical stability analysis methods, they are Nyquist stability criterion and root locus. The study finds that the single-loop control systems can be stable if the time delay falls into their stable ranges. Yet the inherent damping mechanism of the systems has not been revealed, and thus should be studied using a method that is different to the classical ones.

In this chapter, these three control methods are compared, through investigating the damping due to their virtual impedances. It will be revealed that the single-loop control with ICF results in a virtual impedance connected in series with the inverter side inductor, while the other two methods introduce a virtual impedance connected in parallel with the capacitor. In all cases, the virtual reactance, inductive or capacitive, shifts the resonance frequency, while a positive virtual resistance at the virtual resonance frequency provides the necessary damping to stabilize the system.

Based on the analysis of the virtual impedance, it is found that the single-loop control systems can be stable if the sampling frequency falls into their respective stable range. The results agree with those obtained in the former chapter through meticulous derivations [71]. On the other hand, it is found that the stability requirement for

the dual-loop control method varies when different sampling frequencies are used. The gain boundaries of the controllers are then deduced, and are verified by means of root locus. Finally, experimental results validate the stability analysis using the virtual impedance.

4.2 Control Strategies for *LCL*-Filtered Grid-Connected Inverters

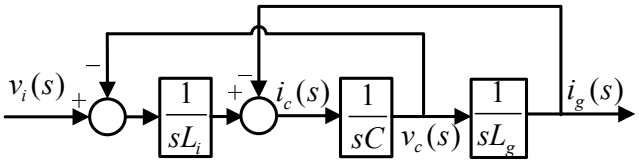

Figure 4.1: Plant model of the *LCL*-filtered grid-connected inverter.

The circuit diagram of the *LCL*-filtered grid-connected inverter was shown in Figure 3.1. The plant model is demonstrated in Figure 4.1. The grid voltage is not included because it is considered as the disturbance [61]. The inverter current i_i, grid current i_g, and/or capacitor current i_c are usually sensed as the feedback variables, to form a single- or dual-loop current control system. The transfer functions from the inverter voltage v_i to i_i, i_g, and i_c are given in (3.1), (3.2), and (4.1), respectively.

$$G_{i_c v_i}(s) = \frac{i_c(s)}{v_i(s)} = \frac{s}{L_i(s^2 + \omega_{res}^2)} \tag{4.1}$$

There are many alternative current control strategies for the *LCL*-filtered grid-connected inverter, mainly including single-loop controllers and dual-loop controllers. For the single-loop control, i_i or i_g can be chosen as the feedback variable. For the dual-loop control, an outer GCF loop plus an inner active damping loop with CCF is usually adopted [58].

The *s*-domain block diagrams of the single-loop control methods were given in Figure 3.3 (with λ = 1), while the dual-loop systems is shown in Figure 4.2(a). A compensator $G_c(s)$ is used, generally a PI in the SRF or a PR in the stationary frames

[11]. k_d is the proportional gain of the inner damping loop, and $G_d(s) = e^{-1.5sT_s}$ is the time delay due to computation (T_s) and PWM generation ($0.5T_s$) [75]. Note that in this chapter, the general case with a total time delay of $1.5T_s$ is discussed, the other cases with different delays or even random values as presented in Chapter 3 can also be studied using the same method proposed in this chapter.

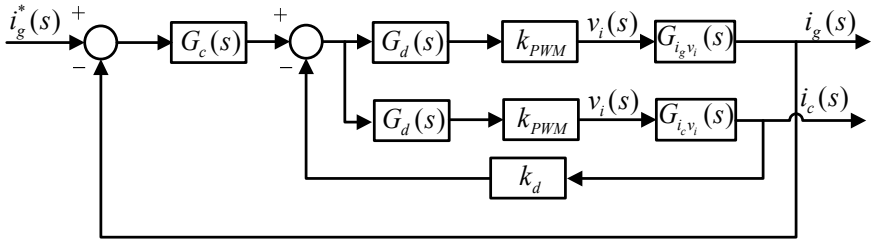

(a)

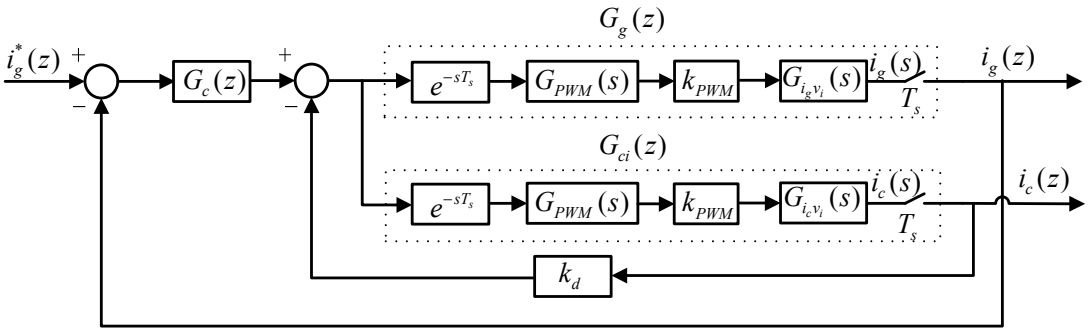

(b)

Figure 4.2: Block diagram of the dual-loop control loop with CCF active damping. (a) Continuous *s*-domain. (b) Discrete *z*-domain.

The *z*-domain block diagrams of the single-loop control methods were given in Figure 3.6, and the corresponding closed-loop transfer functions were given in (3.18) and (3.19). The dual-loop system is shown in Figure 4.2(b). The discrete transfer function $G_{ci}(z)$ can be obtained using the digitization method in Section 3.4.1, i.e. applying the ZOH transform to (4.1) together with k_{PWM} and the processing delay, as expressed in (4.2). The discrete closed-loop transfer function is then yielded as (4.3), where $G_c(z)$ is the discrete equivalent of $G_c(s)$, and $G_g(z)$ was given in (3.17) with $\ell = 1$ and $m = 0$.

$$\begin{aligned} G_{ci}(z) &= Z\{e^{-sT_s} G_{PWM}(s) k_{PWM} G(s)\} \\ &= \frac{k_{PWM} \sin \omega_{res} T_s}{\omega_{res} L_i} \frac{z-1}{z(z^2 - 2z\cos \omega_{res} T_s + 1)} \end{aligned} \tag{4.2}$$

$$G_{ccl}(z)=\frac{i_g(z)}{i_g^*(z)}=\frac{G_c(z)G_g(z)}{1+k_dG_{ci}(z)+G_c(z)G_g(z)} \tag{4.3}$$

Although these controllers have been adopted in different publications, there is neither a general research to clarify in which condition these controllers can be used, nor a simple but accurate method to predict the gain boundary of the compensators. In the following sections, these issues are addressed using the virtual impedance introduced by these control methods.

4.3 Virtual Impedance and Stability Analysis of Single-Loop Control Methods

In this section, the virtual impedance of the single-loop control methods is analyzed. The system can be stable if the virtual resistance is positive at a virtual resonance frequency [21, 75]. As a result, the stable range of sampling frequency for each controller is derived, as well as the gain boundaries, which are validated by means of root locus.

$G_c(s)$ is simplified as a proportional gain k_p, because either the integral term in a PI or the resonant term in a PR can be designed to have a negligible influence on system stability [23, 39].

4.3.1 Single-Loop Control with ICF

4.3.1.1 Virtual Impedance

To illustrate the damping due to the virtual impedance introduced by the control strategy, the equivalent block diagram is drawn in Figure 4.3(a). It can be seen that a virtual impedance Z_{vi} expressed in (4.4) is connected in series with L_i.

$$Z_{vi}(s)=k_pk_{PWM}G_d(s) \tag{4.4}$$

When the delay is ignored, i.e., $G_d(s) = 1$, (4.4) results in a resistance of k_pk_{PWM}, implying that the closed-loop is always stable because of the damping to the *LCL* resonance [24].

On the other hand, in the frequency domain, (4.4) becomes (4.5) after incorporating the delay.

$$Z_{vi}(j\omega) = k_p k_{PWM} \cos 1.5\omega T_s + j\omega\left(\frac{-k_p k_{PWM} \sin 1.5\omega T_s}{\omega}\right) \\ = R_{vi}(\omega) + j\omega L_{vi}(\omega) \tag{4.5}$$

It is apparent that the time delay leads to a resistor R_{vi} and an inductor L_{vi}, the value of both are frequency-dependent. The equivalent circuit is shown in Figure 4.3(b).

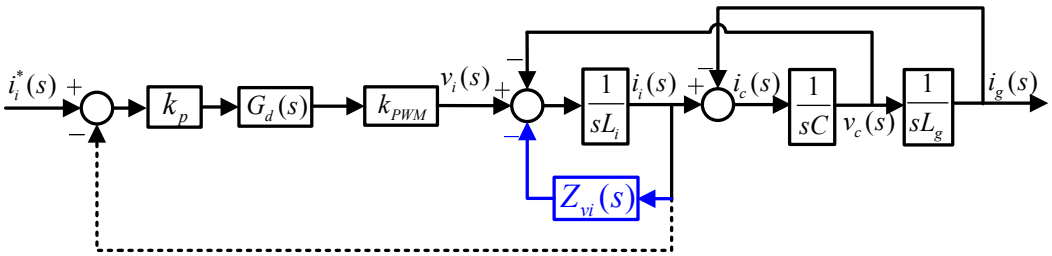

(a)

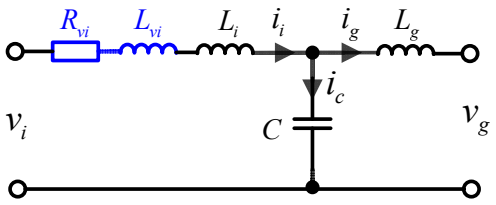

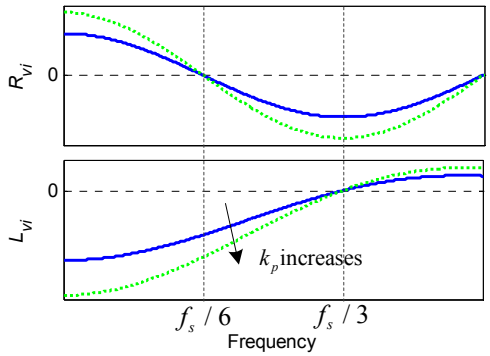

(b) (c)

Figure 4.3: Single-loop control with ICF (a) Equivalent block diagram. (b) Equivalent circuit. (c) Plots of R_{vi} (ω)and L_{vi}(ω).

4.3.1.2 Stability Analysis

The plots of $R_{vi}(\omega)$ and $L_{vi}(\omega)$ are shown in Figure 4.3(c). As can be seen, the frequency boundary for R_{vi} to be positive and negative is f_s / 6. For stability, R_{vi} should be positive at the resonant frequency f_{res} [72, 75]. Therefore the stability requirement on f_s is given as

$$f_s > 6 f_{res}\,. \tag{4.6}$$

The result matches the frequency stable range derived in Chapter 3 for the case with

$\lambda = 1$ (see Table 3.1).

However, the existence of L_{vi} causes the virtual resonance frequency $f_{res}^{'}$ to deviate from f_{res}. The frequency boundary for L_{vi} to be positive and negative is $f_s/3$. In the range below $f_s/3$, an increase of k_p leads to larger negative inductance, thus a higher $f_{res}^{'}$. To ensure stability, $f_{res}^{'}$ is required to be smaller than $f_s/6$, such that the damping resistance R_{vi} at $f_{res}^{'}$ is positive [109]. The maximum of k_p is therefore the value which yields $f_{res}^{'} = f_s/6$ (i.e., a virtual resonance angular frequency $\omega_v = 2\pi f_{res}^{'} = \omega_s/6$, with $\omega_s = 2\pi f_s$). According to $\omega_v = \sqrt{(L_i + L_v + L_g)/[(L_i + L_v)L_g C]}$, $k_{p\max}$ is derived as:

$$\sqrt{\frac{L_i - \dfrac{k_{p\max}k_{PWM}}{\omega_v} + L_g}{(L_i - \dfrac{k_{p\max}k_{PWM}}{\omega_v})L_g C}} = \omega_v = \frac{\omega_s}{6}$$
$$\Rightarrow k_{p\max} = \frac{L_i\omega_s(\omega_s^2 - 36\omega_{res}^2)}{k_{PWM}(6\omega_s^2 - 216\omega_r^2)}. \tag{4.7}$$

For the circuit parameters in Table 3.2, using f_s = 12 kHz ($f_s > 6f_{res}$), the root loci are shown in Figure 4.4. It can be seen that the natural resonance frequency is increased when k_p rises. From (4.7), $k_{p\max} = 0.1961$, which is identical to the boundary in Figure 4.4, validating the previous analysis.

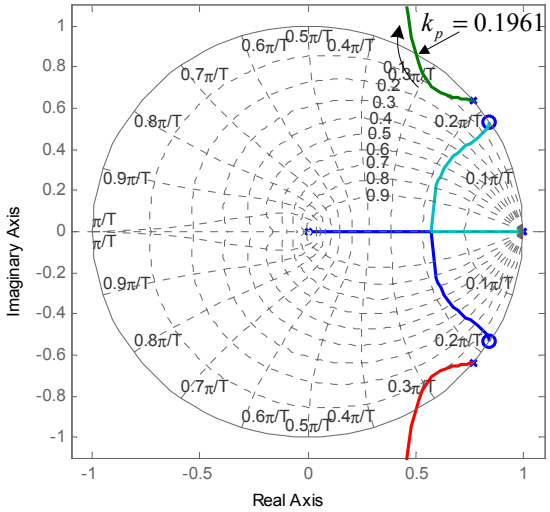

Figure 4.4: Root loci of single-loop control with ICF.

4.3.2 Single-Loop Control with GCF

4.3.2.1 Virtual Impedance

The equivalent block diagram is shown in Figure 4.5(a), it is obvious that equivalently a virtual impedance Z_{vg} is connected in parallel with the capacitor:

$$Z_{vg}(s) = \frac{s^2 L_i L_g}{k_p k_{PWM} G_d(s)} \tag{4.8}$$

Without considering the time delay, the frequency domain expression of (4.8) is written as

$$Z_{vg}(j\omega) = \frac{-L_i L_g}{k_p k_{PWM}} \omega^2 . \tag{4.9}$$

Obviously, a negative resistance is added in the circuit, indicating an ineffective damping without delay.

Taking the time delay into account, (4.8) is denoted as

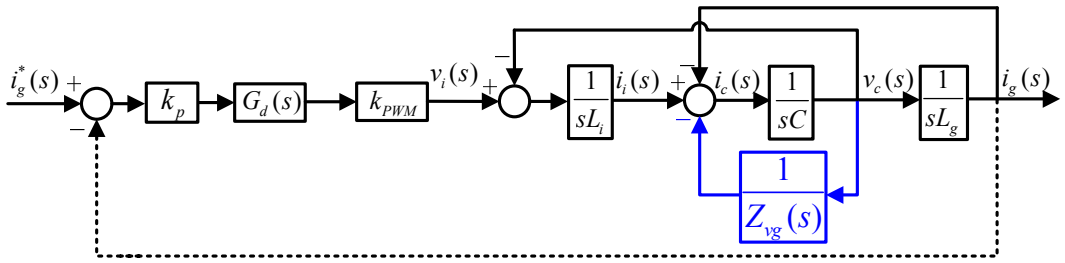

(a)

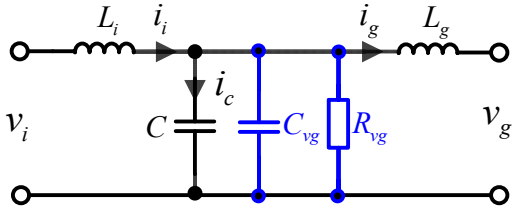

(b)

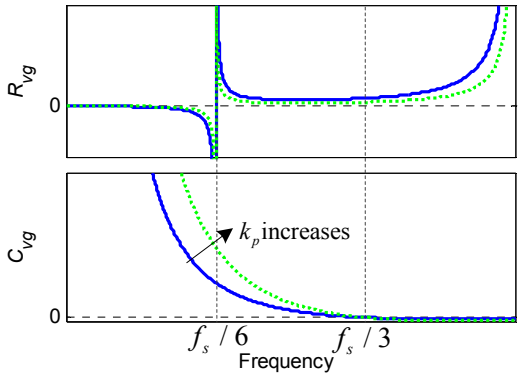

(c)

Figure 4.5: Single-loop control with GCF. (a) Equivalent block diagram. (b) Equivalent circuit. (c) Plots of $R_{vg}(\omega)$ and $C_{vg}(\omega)$.

$$
\begin{aligned}
Z_{vg}(j\omega) &= \frac{-L_i L_g}{k_p k_{PWM}} \omega^2 (\cos 1.5\omega T_s + j \sin 1.5\omega T_s) \\
&= R_{vg}(\omega) \,||\, \frac{1}{j\omega C_{vg}(\omega)},
\end{aligned}
\tag{4.10}
$$

where

$$
R_{vg}(\omega) = \frac{-L_i L_g \omega^2}{k_p k_{PWM} \cos 1.5\omega T_s}, C_{vg}(\omega) = \frac{k_p k_{PWM} \sin 1.5\omega T_s}{L_i L_g \omega^3}. \tag{4.11}
$$

It is revealed that a virtual resistor R_{vg} and capacitor C_{vg} are in parallel with the capacitor, as shown in Figure 4.5(b). Thanks to the time delay, R_{vg} is positive in a certain frequency range, which provides a potential damping. This is why it is indicated in [29] that the time delay in GCF loop generates an inherent damping.

4.3.2.2 Stability Analysis

The plots of $R_{vg}(\omega)$ and $C_{vg}(\omega)$ are shown in Figure 4.5(c). R_{vg} is positive above $f_s / 6$, f_{res} is therefore required to be in this range. The basic stability requirement is given in (4.12), which also matches the result in Table 3.1. ($f_s > 2f_{res}$ is necessary for controllability according to the Nyquist criterion [108].)

$$
2f_{res} < f_s < 6f_{res} \tag{4.12}
$$

In the frequency range above $f_s/3$, the negative C_{vg} leads to $f_{res}^{'} > f_{res}$, but it will not trigger instability because of the positive resistance in this range. By contrast, a positive C_{vg} is generated below $f_s / 3$, which decreases $f_{res}^{'}$. Furthermore, $f_{res}^{'}$ reduces with a larger k_p. Hence, the gain boundary of k_p is the value which renders $f_{res}^{'} = f_s / 6$, given as

$$
\begin{aligned}
&\sqrt{\frac{L_i + L_g}{L_i L_g (C + \frac{k_{p\max} k_{PWM}}{L_i L_g \omega_v^3})}} = \omega_v \\
&\Rightarrow k_{p\max} = \frac{L_i \omega_s (36\omega_{res}^2 - \omega_s^2)}{216 k_{PWM} \omega_r^2}.
\end{aligned}
\tag{4.13}
$$

Using f_s = 5 kHz ($f_s < 6f_{res}$), the root loci are shown in Figure 4.6. It can be seen

that the resonance frequency decreases when k_p rises. Based on (4.13), $k_{p\max} = 0.0918$, which coincides with the gain boundary in Figure 4.6.

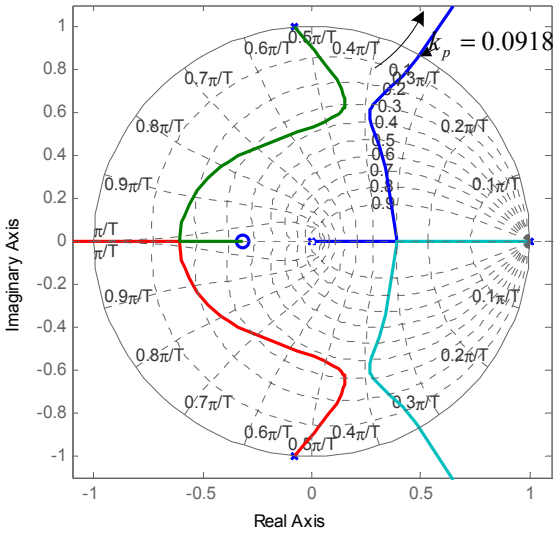

Figure 4.6: Root loci of single-loop control with GCF.

4.4 Analysis of Dual-Loop Control with CCF Active Damping

4.4.1 Virtual Impedance

The equivalent block diagram is shown in Figure 4.7(a). As can be seen, both the outer GCF and inner CCF produce a virtual impedance that is connected in parallel with the capacitor, denoted as Z_{vg} and Z_{vc} respectively:

$$Z_{vg}(s) = \frac{s^2 L_i L_g}{k_p k_{PWM} G_d(s)}, Z_{vc}(s) = \frac{L_i}{k_d k_{PWM} C G_d(s)}. \tag{4.14}$$

Therefore, a total virtual impedance Z_{vAD} is obtained as

$$Z_{vAD}(s) = Z_{vg}(s) \| Z_{vc}(s) = \frac{s^2 L_i L_g}{(s^2 L_g k_d k_{PWM} C + k_p k_{PWM}) G_d(s)}. \tag{4.15}$$

The frequency domain expression of (4.15) is given as

$$Z_{vAD}(j\omega) = R_{vAD}(\omega) \| \frac{1}{j\omega C_{vAD}(\omega)}, \tag{4.16}$$

where $R_{vAD}(\omega)$ and $C_{vAD}(\omega)$ are written as

$$\begin{cases} R_{vAD}(\omega) = \dfrac{L_i L_g \omega^2}{(k_d k_{PWM} L_g C\omega^2 - k_p k_{PWM})\cos 1.5\omega T_s} \\ C_{vAD}(\omega) = \dfrac{(k_p k_{PWM} - k_d k_{PWM} L_g C\omega^2)\sin 1.5\omega T_s}{L_i L_g \omega^3}. \end{cases} \tag{4.17}$$

The equivalent circuit is shown in Figure 4.7(b), where the virtual resistor R_{vAD} and capacitor C_{vAD} are inserted.

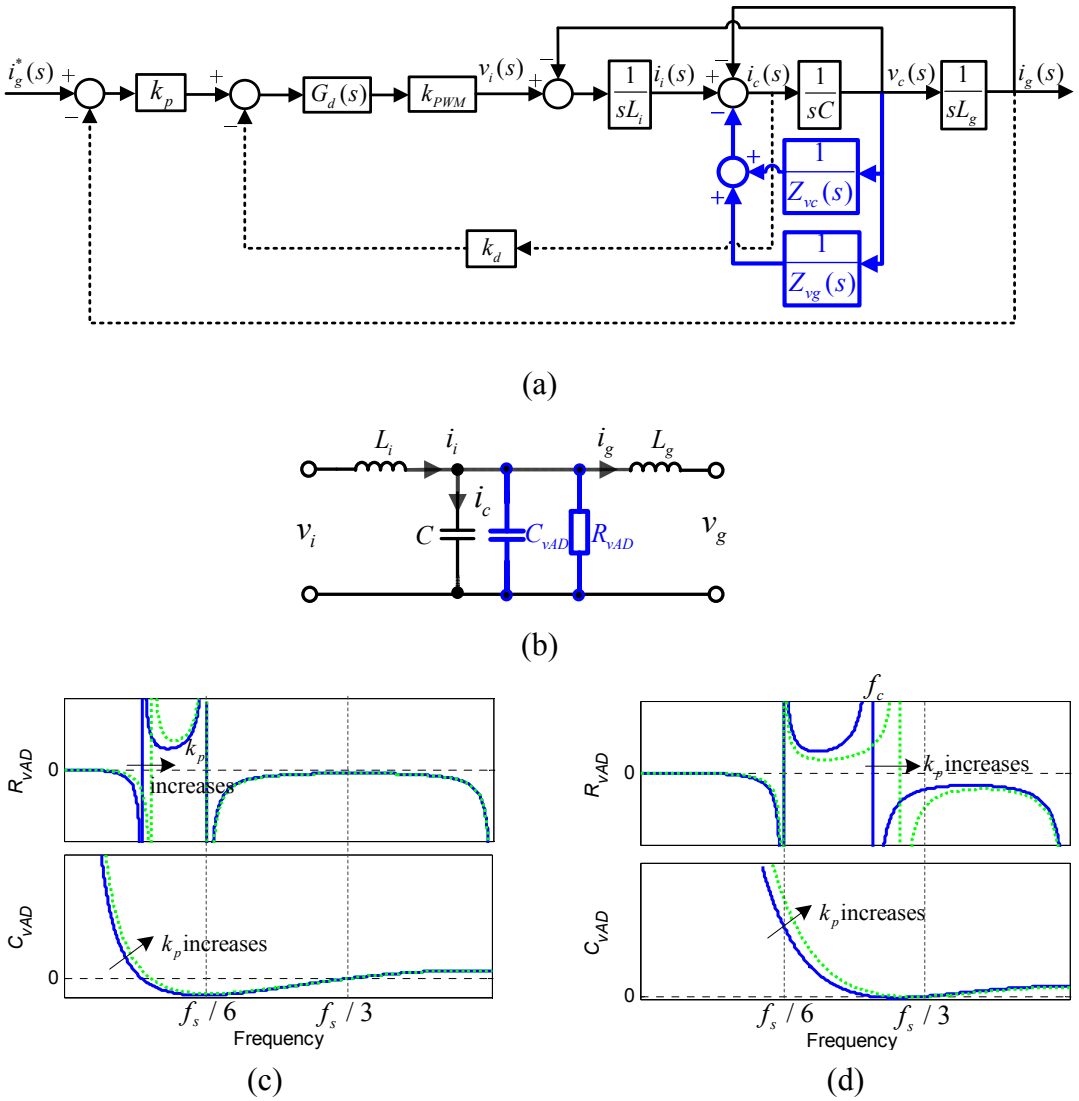

Figure 4.7: Dual-loop control with CCF active damping (a) Equivalent block diagram. (b) Equivalent circuit. (c) R_{vAD} and C_{vAD} of case I. (d) R_{vAD} and C_{vAD} of case II.

4.4.2 Stability Analysis

R_{vAD} and C_{vAD} in (4.17) are also frequency-dependent. However, unlike the sin-

gle-loop controllers in which the damping resistance is only positive below $f_s/6$ or above $f_s/6$, R_{vAD} can be positive in both ranges by tuning k_p and k_d. The element $\cos(1.5\omega T_s)$ in (4.17) is positive below $f_s/6$ while negative above $f_s/6$. Therefore, there are two cases for the requirement of the controller parameters: case I for $f_{res} < f_s/6$, and case II for $f_{res} > f_s/6$.

4.4.2.1 Case I: $f_{res} < f_s/6$

The same as the single-loop controllers, the basic requirement for system stability is that R_{vAD} is positive at f_{res}. $\cos(1.5\omega T_s)$ in (4.17) at f_{res} is positive, thus k_p and k_d should meet the following condition:

$$k_p < k_d L_g C \omega_{res}^2 . \tag{4.18}$$

The curves of $R_{vAD}(\omega)$ and $C_{vAD}(\omega)$ are shown in Figure 4.7(c). In the frequency range between f_{res} and $f_s/3$, C_{vAD} is negative which increases the virtual resonance frequency $f_{res}^{'}$. However, for a given k_d, an increase in k_p decreases $f_{res}^{'}$. Since the critical frequency for R_{vAD} changing from positive to negative is $f_s/6$, the requirement on the controller parameters falls into two situations: assuming $k_p = 0$, $f_{res}^{'} < f_s/6$ or $f_{res}^{'} > f_s/6$ with the inner CCF only.

The value of k_d to obtain $f_{res}^{'} = f_s/6$ is denoted as

$$\begin{aligned} &\sqrt{\frac{L_i + L_g}{L_i L_g C(1 - \frac{k_{dc} k_{PWM}}{\omega_v L_i})}} = \omega_v \\ &\Rightarrow k_{dc} = \frac{L_i}{k_{PWM}}(\frac{\omega_s}{6} - \frac{6\omega_{res}^2}{\omega_s}). \end{aligned} \tag{4.19}$$

If $k_d < k_{dc}$, this is $f_{res}^{'} < f_s/6$, increasing k_p will reduce $f_{res}^{'}$, until the maximum value determined by (4.18). If $k_d > k_{dc}$, this is $f_{res}^{'} > f_s/6$ with the inner CCF only, it is necessary for k_p to ensure $f_{res}^{'} < f_s/6$, the minimum k_p is therefore obtained as

$$\sqrt{\frac{L_i+L_g}{L_iL_g[C+\frac{(k_{p\min}k_{PWM}-k_dk_{PWM}L_gC\omega_v^2)}{L_iL_g\omega_v^3}]}}=\omega_v$$
$$\Rightarrow k_{p\min}=\frac{(L_i+L_g)\omega_s}{6k_{PWM}}+\frac{k_dL_gC\omega_s^2}{36}-\frac{L_iL_gC\omega_s^3}{216k_{PWM}}. \tag{4.20}$$

To sum up, for the case I with $f_s > 6f_{res}$, the requirements on k_p and k_d are given as (4.21) or in another situation (4.22).

$$\begin{cases} k_d < \dfrac{L_i}{k_{PWM}}\left(\dfrac{\omega_s}{6}-\dfrac{6\omega_{res}^2}{\omega_s}\right) \\ k_p < k_dL_gC\omega_{res}^2 \end{cases} \tag{4.21}$$

$$\begin{cases} \dfrac{L_i}{k_{PWM}}\left(\dfrac{\omega_s}{6}-\dfrac{6\omega_{res}^2}{\omega_s}\right) < k_d < \dfrac{L_iL_gC\omega_s^3-36(L_i+L_g)\omega_s}{6k_{PWM}(L_gC\omega_s^2-36L_gC\omega_{res}^2)} \\ \dfrac{(L_i+L_g)\omega_s}{6k_{PWM}}+\dfrac{k_dL_gC\omega_s^2}{36}-\dfrac{L_iL_gC\omega_s^3}{216k_{PWM}} < k_p < k_dL_gC\omega_{res}^2 \end{cases} \tag{4.22}$$

For the circuit parameters in Table 3.2, using f_s = 12 kHz ($f_s > 6f_{res}$), k_{dc} in (4.19) is 0.1396. When $k_d < k_{dc}$, k_p is required to meet (4.21). Choosing k_d = 0.07, k_p < 0.105 is obtained, which is identical to the maximum gain in the root loci shown in Figure 4.8(a). When $k_d > k_{dc}$, (4.22) results in 0.1396 < k_d < 0.2457. Choosing k_d = 0.19, it is drawn from (4.22) that 0.175 < k_p < 0.285. The root loci are illustrated in Figure 4.8(b), from which the same gain boundaries can be observed.

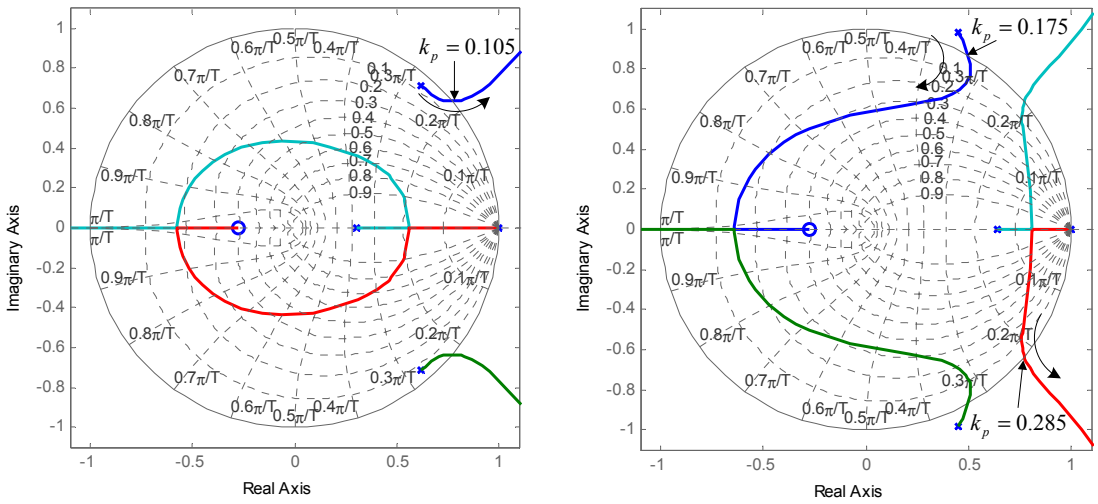

(a) (b)

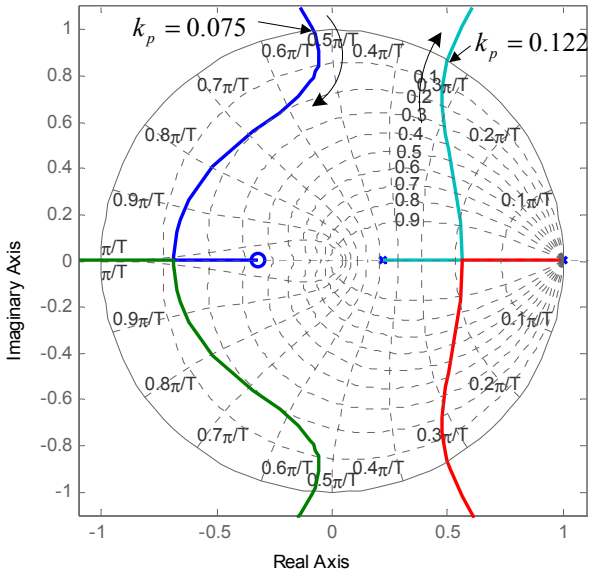

(c)

Figure 4.8: Root loci of dual-loop control with CCF active damping. (a) Case I: f_s = 12 kHz > $6f_{res}$ and $k_d < k_{dc}$. (b) Case I: f_s = 12 kHz > $6f_{res}$ and $k_d > k_{dc}$. (c) Case II: f_s = 5 kHz < $6f_{res}$.

4.4.2.2 Case II: $f_{res} > f_s / 6$

Likewise, the basic requirement is that the damping resistance R_{vAD} is positive at f_{res}. $\cos(1.5\omega T_s)$ in (4.17) at f_{res} is negative, hence k_p and k_d should meet the following condition:

$$k_p > k_d L_g C \omega_{res}^2 . \tag{4.23}$$

The curves of $R_{vAD}(\omega)$ and $C_{vAD}(\omega)$ are shown in Figure 4.7(d). There is a frequency ($f_c = \sqrt{k_p / k_d L_g C} / 2\pi > f_{res}$) determined by k_p and k_d that shifts R_{vAD} from positive to negative, and below which C_{vAD} is positive leading to a smaller $f_{res}^{'}$. Furthermore, an increase of k_p results in a larger positive C_{vAD}, causing $f_{res}^{'}$ to fall. Therefore the design of k_p and k_d should guarantee that $f_{res}^{'} > f_s / 6$. The maximum value of k_p can be obtained using the same procedure that deduces (4.20), and then the following is yielded:

$$\begin{cases} k_d < \dfrac{36(L_i + L_g)\omega_s - L_i L_g C\omega_s^3}{6k_{PWM}(36L_g C\omega_{res}^2 - L_g C\omega_s^2)} \\ k_d L_g C\omega_{res}^2 < k_p < \dfrac{k_d L_g C\omega_s^2}{36} + \dfrac{(L_i + L_g)\omega_s}{6k_{PWM}} - \dfrac{L_i L_g C\omega_s^3}{216k_{PWM}} \end{cases} \tag{4.24}$$

With f_s = 5 kHz ($f_s < 6f_{res}$), from (4.24) we can get $k_d < 0.1024$. Using $k_d = 0.05$, $0.075 < k_p < 0.122$ is gained from (4.24). The root loci when k_p changes are shown in Figure 4.8(c), it can be seen that the range of k_p is the same as that deduced using (4.24). The matched result validates the stability analysis using the virtual impedance.

4.5 Experimental Results

The control is implemented in the SRF; hence the PI controller is applied. k_p is chosen as half of the gain boundaries derived from Section 4.3 and 4.4.

For the single-loop control with ICF, $f_s > 6f_{res}$ is required for stability. As the grid current is indirectly controlled, the reference q-axis current is set to $\omega_n CV_g$ instead of 0 to achieve the unity PF [24]. Using f_s = 12 kHz, the steady-state one-phase grid voltage and current (4 A) are shown in Figure 4.9(a), which shows that the grid current is in phase with the grid voltage. The transient response with i_g stepping from 1 to 4 A is shown in Figure 4.9(b), which indicates the stability as well as good transient performance.

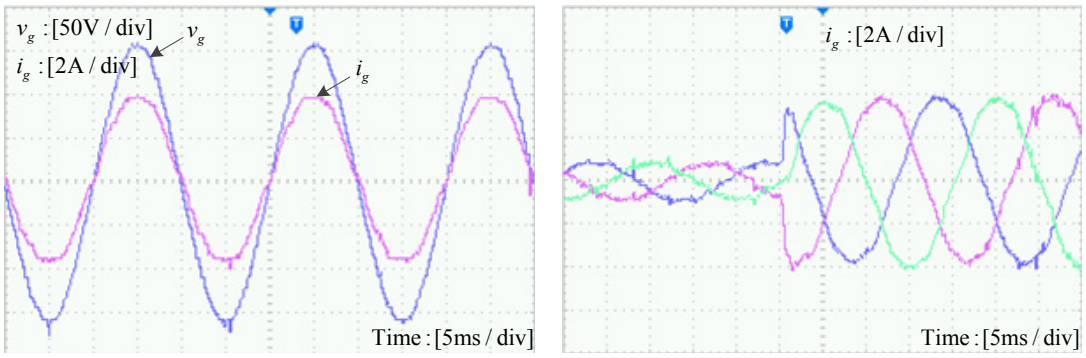

(a) (b)

Figure 4.9: Experimental results of single-loop control with ICF. (a) Steady-state one-phase v_g and i_g. (b) Transient response.

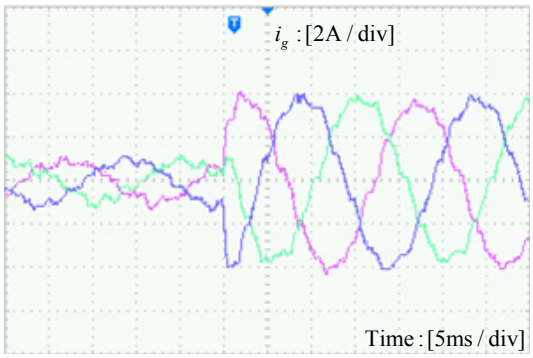

Figure 4.10: Experimental transient response of single-loop control with GCF.

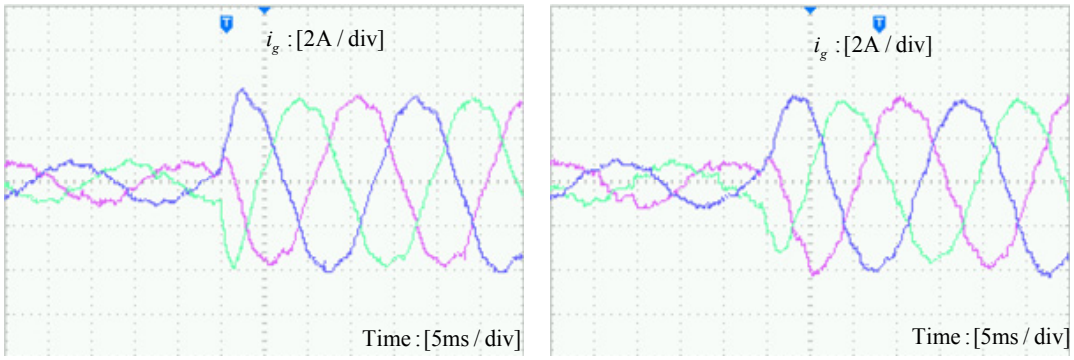

(a) (b)

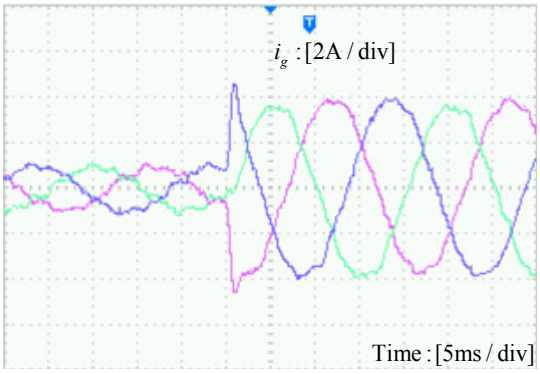

(c)

Figure 4.11: Experimental transient responses of dual-loop control with CCF active damping. (a) Case I: $f_s = 12$ kHz > $6f_{res}$ and $k_d < k_{dc}$. (b) Case I: $f_s = 12$ kHz > $6f_{res}$ and $k_d > k_{dc}$. (c) Case II: $f_s = 5$ kHz < $6f_{res}$.

For the single-loop control with GCF, $f_s < 6f_{res}$ is required and $f_s = 5$ kHz is used. The reference q-axis current is set to 0 because i_g is controlled directly. The stable transient response when i_g changes from 1 to 4 A is shown in Figure 4.10.

Finally, the dual-loop control with CCF active damping is tested. For f_s = 12 kHz, when k_d = 0.07, the transient response is demonstrated in Figure 4.11(a). When k_d = 0.19, the experimental result is given in Figure 4.11(b). For f_s = 5 kHz, the transient response with i_g stepping from 1 to 4 A is shown in Figure 4.11(c). All the stable results verify the damping investigation using the virtual impedance in this chapter.

4.6 Conclusion

This chapter has studied the virtual impedance of three different control methods for *LCL*-filtered grid-connected inverters. It has been shown that the virtual impedance achieves a potential damping to the *LCL* resonance. Based on the fact that a positive virtual resistance at the virtual resonance frequency is required for system stability, the requirement on the sampling frequency has been obtained for the single-loop control methods, and different cases of the dual-loop control method have been discussed. Furthermore, the gain boundaries of these controllers have been deduced in an intuitive manner, which facilitates the design of the control loop. The stability analysis using the virtual impedance has been verified by experiments. The stable frequency range of the single-loop control methods matches the results that were derived in Chapter 3 using classical methods including Nyquist stability criterion and root locus. In comparison to these methods, the virtual impedance approach is more general and intuitive, which can be extended to the cases with a different time delay and to other control methods.

Chapter 5

Pseudo-Derivative-Feedback Current Control for Three-Phase Grid-Connected Inverters with *LCL* Filters

5.1 Introduction

The operation and control of grid-connected inverters play a crucial role upon the quality of power injected from the DPGSs into the power grid [12]. Requirements for steady-state and transient response are becoming more and more restrictive [11, 33, 38]. Specifically, in the case of current reference changes, transient response characteristics such as rise time, settling time, overshoot and oscillation damping are all required to be satisfactory. For example, the overshoot is often limited by the converter current rating, and it is more stringent to limit the overshoot in high power applications [33]. Un-damped oscillations would deteriorate the power quality and create objectionable flicker [38].

LCL filters tend to cause stability problems due to the resonance, and the stability of different current control methods have been studied in previous two chapters. Apart from the stability problems, the *LCL* resonance will degrade the transient response, particularly leading to oscillations and overshoots.

Numerous control strategies can be applied to control the current of grid-connected inverters [34, 80]. Traditionally, a PI controller is employed in the SRF [33, 37, 110], and a PR or damped PR controller in the stationary frame [26, 78,

86]. Most of previous publications concerned system stability [71, 72, 80], the robustness against grid impedance variations [25, 75], and/or harmonic rejection [26, 59, 75]. The transient response in these studies contains overshoot and oscillation and has not been considered at the design stage, while only examined at simulation or experiment stages. Several other current control techniques, including hysteresis, deadbeat, and nonlinear controllers etc., have been reported to achieve an improved transient response [35, 41-48, 111]. Nonetheless, these methods are more complicated than the conventional PI and PR controllers.

The PI controller in the SRF is widely used because the control variables become DC signals, which is advantageous from the control point of view, although the transformation creates cross-couplings between *d*- and *q*-axis currents, i.e., the two currents are not independent from each other [61, 95, 112]. A number of methods have been proposed with an attempt to improve the transient performance of PI controlled *LCL*-filtered grid-connected inverters. Different tuning methods such as technical optimum, symmetric optimum (SO), and optimized design (OP) have been reported but cannot eliminate the transient overshoot and oscillation [33, 34, 36]. A common method to reduce the overshoot is decreasing controller gains, which however leads to degraded bandwidth and disturbance rejection capability [25]. A PI state space current control was presented in [33] to improve the rise time and resonance damping, but overshoot still occurs. In [22], controller parameters were optimized using discrete pole-zero plots to achieve a short settling time only.

Another effective alternative strategy is to introduce an additional damping to the *LCL* resonance. Multi-loop based active damping methods have been researched widely to form a damping term [40, 72, 81, 104]. However, they require the feedback of more than one signal, which complicates the controller design. Furthermore, most of the controllers are designed for good performance in stability, disturbance rejection, or robustness against grid impedance variations, resulting in transient responses with overshoot and/or oscillation [21, 58, 78, 104]. To obtain an improved transient

performance, controller parameters should be redesigned, which would degrade other performances. A second-order derivative method implemented as a high-pass filter has been used in [63, 66, 113] to provide active damping for the grid current. However, there are also significant overshoots and oscillations in the transient response.

In this chapter, the PDF control method [114-116] is applied, as an advantageous strategy over the PI control in the SRF, to improve the transient response of three-phase grid-connected inverters with *LCL* filters to a step change in the reference input via eliminating overshoot and oscillation.

Firstly, a generalized PDF controller is introduced. And a complex vector method is fully applied to modeling the *LCL*-filtered system in the SRF, which simplifies the system from multiple-input multiple-output (MIMO) to single-input single-output (SISO) while takes the cross-couplings into account [117, 118].

Then a simple PDF controller with a proportional feedback is designed for an ICF system. A complete comparison between the performance of PDF and PI controllers is presented. The main merit of the PDF controller is the removal of the additional zero of the closed-loop transfer function and the resultant impact of the transient response from the zero. Compared with the PI controller which can only reduce the overshoot by decreasing the controller gains, the PDF controller completely eliminates the overshoot and oscillation over a wide range of controller parameters.

To directly control the grid current, a PDF controller with a proportional plus a second-order derivative feedback is developed for a GCF system. The practical implementation of the PDF controller is discussed using the Nyquist stability criterion. The stable condition for the controller parameters is derived. Adequate stability margins are ensured by a controller design procedure. The analysis regarding the high-pass filter and system stability is more explicit than that in [63, 66, 113]. Compared with common active damping methods which require more than one feedback signal, the PDF controller provides damping with the GCF only, and simultaneously improves the transient response.

Having designed the PDF controllers, experimental results are finally presented to verify their improved performance compared to conventional PI control methods.

5.2 PDF Control and Complex Vector Modeling

5.2.1 PDF Control

A generalized PDF control system is shown in Figure 5.1(a). The generalized PDF controller comprises two parts: an integral term k_i / s in the forward path, and the superposition of a proportional term k_{d1} and selective derivative terms $k_{dn}s^{n-1}$ ($n >$ 1) in the inner feedback path [114].

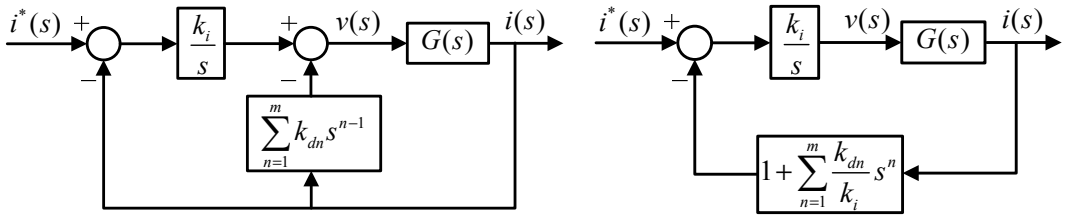

(a) (b)

Figure 5.1: Generalized PDF control system. (a) System block diagram. (b) Equivalent block diagram.

The equivalent block diagram is shown in Figure 5.1(b) where the second part of the PDF controller is moved to the feedback path which is used to be compared with the reference. It can be seen that the orders of the pseudo-derivative terms are increased by 1, and the proportional term becomes a first-order pseudo-derivative term. This is why the method is called PDF control [114]. The highest order m of the pseudo-derivative terms is not larger than the order of the plant $G(s)$ [114].

5.2.2 Three-Phase Grid-Connected Inverter with *LCL* Filters

Several methods have been used to model three-phase grid-connected inverters with *LCL* filters in the SRF, but they all have limitations. In numerous studies, all cross-couplings from the *LCL* inductors and capacitor were ignored for the sake of simplicity, i.e., the plant model in the SRF is identical to that in the stationary frame

[24, 34, 58, 62, 110, 113]. This simplification is obviously not accurate because of the dynamic dependency between *d*- and *q*-axis currents, see Section 2.4.3. The other approximation is only dismissing the coupling caused by the capacitor, since the *LCL* filter is similar to an *L*-filter in low frequency ranges [33, 40, 59, 61, 119, 120]. It is not precise either because the capacitor introduces resonance problems and non-ignorable coupling in high frequency ranges. State-space modeling has been used as an improved method which takes all couplings into account [44, 45, 48, 121]. However, it results in a MIMO system, and the state transition matrix computation brings complex work, especially when time delays are accounted for [23].

Complex vector based complex transfer functions have been proved to be useful in the modeling of three-phase systems, because the MIMO system is simplified to a SISO system while the couplings are included [117, 118, 122, 123]. The complex vector has been widely used in the current regulation of three-phase systems with *RL*-type loads (ac machines [95-97, 112, 124]) or *L*-filters (grid-tied converters [61, 125]). Several attempts have been made at applying the complex vector to *LCL*-filtered systems. In [41, 126, 127], the complex vector was used in state-space models. Again, the state-space form increases the complexity in derivations and computations. Complex transfer functions were concerned in [56, 92, 128, 129] for the analysis and design of power converters with *LCL* filters. However, complex vector models, especially discrete ones, have not been fully derived.

In this section, a thorough study is carried out on the application of complex vector to the modeling of a three-phase *LCL*-filtered grid-connected inverter (see Figure 3.1) in the SRF, in the continuous *s*-domain as well as in the discrete *z*-domain.

5.2.2.1 Stationary Frame Models

In the stationary frame, the differential equations of the *LCL* filter were given as (2.12) (In this chapter, the minor parasitic series resistors R_i and R_g associated with the inductors are neglected in the modeling, control design, and simulations, in order

to represent a worst case in stability and transient response). Using complex vector notation $\boldsymbol{f}_{\alpha\beta} = f_\alpha + jf_\beta$, the complex vector state equation is expressed as

$$\begin{cases} sL_i \boldsymbol{i}_{i\alpha\beta}(s) = \boldsymbol{v}_{i\alpha\beta}(s) - \boldsymbol{v}_{c\alpha\beta}(s) \\ sC\boldsymbol{v}_{c\alpha\beta}(s) = \boldsymbol{i}_{i\alpha\beta}(s) - \boldsymbol{i}_{g\alpha\beta}(s) \\ sL_g \boldsymbol{i}_{g\alpha\beta}(s) = \boldsymbol{v}_{c\alpha\beta}(s) - \boldsymbol{v}_{g\alpha\beta}(s) \end{cases} \tag{5.1}$$

As a result, transfer functions from $\boldsymbol{v}_{i\alpha\beta}$ to $\boldsymbol{i}_{i\alpha\beta}$ and to $\boldsymbol{i}_{g\alpha\beta}$ are obtained as (5.2), and those from $\boldsymbol{v}_{g\alpha\beta}$ to $\boldsymbol{i}_{i\alpha\beta}$ and to $\boldsymbol{i}_{g\alpha\beta}$ are given as (5.3).

$$G^s_{i_i v_i}(s) = \frac{\boldsymbol{i}_{i\alpha\beta}(s)}{\boldsymbol{v}_{i\alpha\beta}(s)} = \frac{s^2 + \omega_r^2}{sL_i(s^2 + \omega_{res}^2)}, G^s_{i_g v_i}(s) = \frac{\boldsymbol{i}_{g\alpha\beta}(s)}{\boldsymbol{v}_{i\alpha\beta}(s)} = \frac{\omega_r^2}{sL_i(s^2 + \omega_{res}^2)}. \tag{5.2}$$

$$G^s_{i_i v_g}(s) = \frac{\boldsymbol{i}_{i\alpha\beta}(s)}{\boldsymbol{v}_{g\alpha\beta}(s)} = -\frac{\omega_r^2}{sL_i(s^2 + \omega_{res}^2)}, G^s_{i_g v_g}(s) = \frac{\boldsymbol{i}_{g\alpha\beta}(s)}{\boldsymbol{v}_{g\alpha\beta}(s)} = -\frac{s^2 L_i C + 1}{sL_i L_g C(s^2 + \omega_{res}^2)}. \tag{5.3}$$

The *s*-domain model of the grid-connected inverter is shown in Figure 5.2(a). $\boldsymbol{m}_{\alpha\beta}$ ($-1 \le m_\alpha, m_\beta \le 1$) is the modulation signal generated from controllers which will be discussed later. The total time delay is $G_d(s) = e^{-s1.5T_s}$ [63, 77].

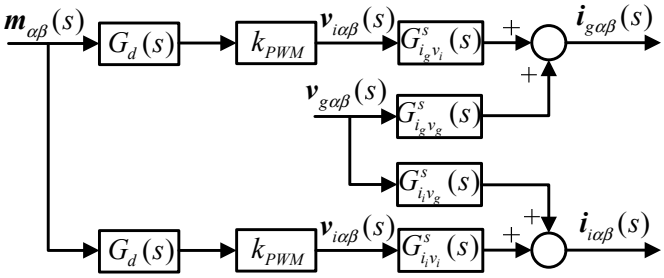

(a)

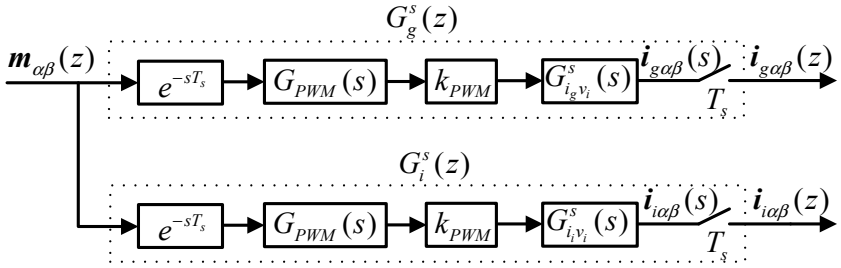

(b)

Figure 5.2: Stationary frame models. (a) Continuous *s*-domain. (b) Discrete *z*-domain.

The digital model is shown in Figure 5.2(b). The grid voltage is not presented because it is considered as disturbance [61]. The processing delay is described as e^{-sT_s} and $G_{PWM}(s) = (1 - e^{-sT_s}) / s$. Using (3.14) – (3.17), the transfer function from $\boldsymbol{m}_{\alpha\beta}(z)$ to $\boldsymbol{i}_{i\alpha\beta}(z)$ and to $\boldsymbol{i}_{g\alpha\beta}(z)$ are derived as (5.4) and (5.5), respectively:

$$\begin{aligned} G_i^s(z) &= Z\{e^{-sT_s}G_{PWM}(s)k_{PWM}G_{i_iv_i}^s(s)\} \\ &= \frac{k_{PWM}}{(L_i+L_g)z}\left(\frac{T_s}{z-1}+\frac{L_g\sin\omega_{res}T_s}{L_i\omega_{res}}\frac{z-1}{z^2-2z\cos\omega_{res}T_s+1}\right) \end{aligned} \tag{5.4}$$

$$\begin{aligned} G_g^s(z) &= Z\{e^{-sT_s}G_{PWM}(s)k_{PWM}G_{i_gv_i}^s(s)\} \\ &= \frac{k_{PWM}}{(L_i+L_g)z}\left(\frac{T_s}{z-1}-\frac{\sin\omega_{res}T_s}{\omega_{res}}\frac{z-1}{z^2-2z\cos\omega_{res}T_s+1}\right). \end{aligned} \tag{5.5}$$

The real transfer functions reveal the independence between α- and β-axis currents.

5.2.2.2 SRF Complex Vector Models

The differential equations in the SRF were denoted in (2.14) (ignoring R_i and R_g). Using complex vectors $\boldsymbol{f}_{dq} = f_d + jf_q$, which gives $\boldsymbol{f}_{dq} = \boldsymbol{f}_{\alpha\beta}e^{-j\hat{\theta}}$ ($\hat{\theta} = \omega_n t + \theta_0$, ω_n is the fundamental angular frequency, θ_0 is initial phase angle), the complex vector state equation is yielded as:

$$\begin{cases} (s+j\omega_n)L_i\boldsymbol{i}_{idq}(s) = \boldsymbol{v}_{idq}(s) - \boldsymbol{v}_{cdq}(s) \\ (s+j\omega_n)C\boldsymbol{v}_{cdq}(s) = \boldsymbol{i}_{idq}(s) - \boldsymbol{i}_{gdq}(s) \\ (s+j\omega_n)L_g\boldsymbol{i}_{gdq}(s) = \boldsymbol{v}_{cdq}(s) - \boldsymbol{v}_{gdq}(s) \end{cases} \tag{5.6}$$

Complex transfer functions in the SRF, including the time delay $\boldsymbol{G}_d(s) = e^{-(s+j\omega_n)1.5T_s}$, can be obtained by replacing the Laplace operator, s, in the stationary frame with $s + j\omega_n$ [87, 117, 118, 123]. The frequency shift property can also be observed by comparing (5.1) and (5.6). Thus, complex transfer functions from $\boldsymbol{v}_{idq}$ to $\boldsymbol{i}_{idq}$ and to $\boldsymbol{i}_{gdq}$ are yielded as (5.7), and those from $\boldsymbol{v}_{gdq}$ to $\boldsymbol{i}_{idq}$ and to $\boldsymbol{i}_{gdq}$ are written as (5.8).

$$\begin{cases} \boldsymbol{G}_{i_iv_i}(s) = \dfrac{\boldsymbol{i}_{idq}(s)}{\boldsymbol{v}_{idq}(s)} = \dfrac{(s+j\omega_n)^2+\omega_r^2}{L_i(s+j\omega_n)[(s+j\omega_n)^2+\omega_{res}^2]}, \\ \boldsymbol{G}_{i_gv_i}(s) = \dfrac{\boldsymbol{i}_{gdq}(s)}{\boldsymbol{v}_{idq}(s)} = \dfrac{\omega_r^2}{L_i(s+j\omega_n)[(s+j\omega_n)^2+\omega_{res}^2]}. \end{cases} \tag{5.7}$$

$$\begin{cases} \boldsymbol{G}_{i_i v_g}(s) = \dfrac{\boldsymbol{i}_{idq}(s)}{\boldsymbol{v}_{gdq}(s)} = -\dfrac{\omega_r^2}{L_i(s+j\omega_n)[(s+j\omega_n)^2+\omega_{res}^2]}, \\ \boldsymbol{G}_{i_g v_g}(s) = \dfrac{\boldsymbol{i}_{gdq}(s)}{\boldsymbol{v}_{gdq}(s)} = -\dfrac{(s+j\omega_n)^2 L_i C+1}{L_i L_g C(s+j\omega_n)[(s+j\omega_n)^2+\omega_{res}^2]}. \end{cases} \tag{5.8}$$

The poles of (5.7) and (5.8) are $s_1 = -j\omega_n$, $s_{2,3} = j(\pm\,\omega_{res} - \omega_n)$, which are asymmetric about the real axis [41, 117]. These transfer functions are denoted in boldface since they are complex.

The s-domain SRF complex vector model of the grid-connected inverter is shown in Figure 5.3(a). The digital complex vector model is shown in Figure 5.3(b). The relationship between discrete complex transfer functions in the stationary frame and in the SRF is derived in Appendix B, i.e., $\boldsymbol{G}(z) = \boldsymbol{G}^s(ze^{j\omega_n T_s})$. Therefore, the z-domain complex vector models in the SRF can be obtained by substituting $ze^{j\omega_n T_s}$ to z in (5.4) and (5.5), given as (5.9) and (5.10), respectively, where $\varphi = \omega_n T_s$ and $\theta = \omega_{res} T_s$.

$$\boldsymbol{G}_i(z) = \frac{k_{PWM} T_s}{(L_i + L_g) z e^{j\varphi}} \left(\frac{1}{z e^{j\varphi} - 1} + \frac{L_g \sin\theta}{L_i \theta} \frac{z e^{j\varphi} - 1}{z^2 e^{j2\varphi} - 2 z e^{j\varphi} \cos\theta + 1} \right), \tag{5.9}$$

$$\boldsymbol{G}_g(z) = \frac{k_{PWM} T_s}{(L_i + L_g) z e^{j\varphi}} \left(\frac{1}{z e^{j\varphi} - 1} - \frac{\sin\theta}{\theta} \frac{z e^{j\varphi} - 1}{z^2 e^{j2\varphi} - 2 z e^{j\varphi} \cos\theta + 1} \right). \tag{5.10}$$

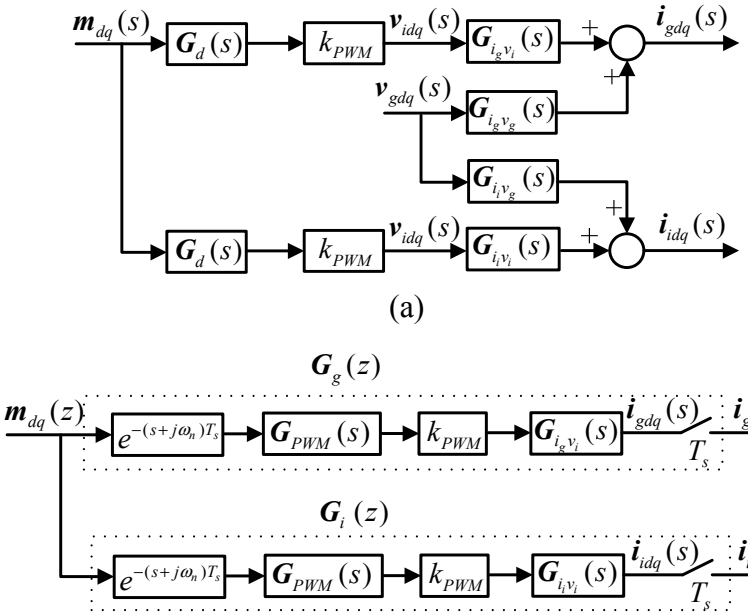

(a)

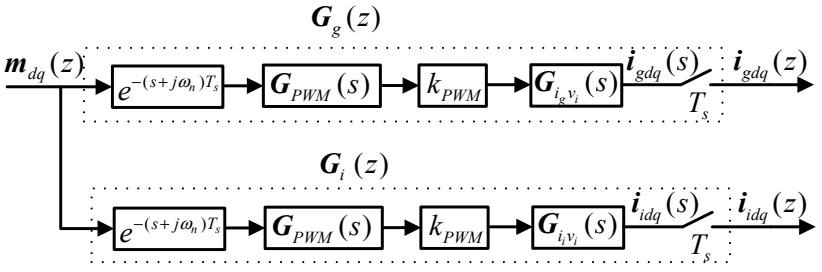

(b)

Figure 5.3: SRF models. (a) Continuous s-domain. (b) Discrete z-domain.

The complex transfer function (5.10) can be expressed in different forms, derived and presented in Appendix C. Different expressions of (5.9) can also be yielded by the method.

To control the grid current i_g to deliver power to the grid, either the inverter current i_i or grid current i_g can be used as the feedback signal [71]. The diagram of a generalized PDF controlled three-phase grid-connected inverter is shown in Figure 5.4. Since the *LCL*-filtered inverter is a third-order plant, the highest order m of the pseudo-derivative term is set to 3. The grid voltage feed-forward is used to improve the harmonic attenuation ability (see more details in Section 6.3.2) [56, 130].

In the following sections, two PDF controllers with different terms in the inner feedback path will be developed for an ICF and a GCF system, respectively.

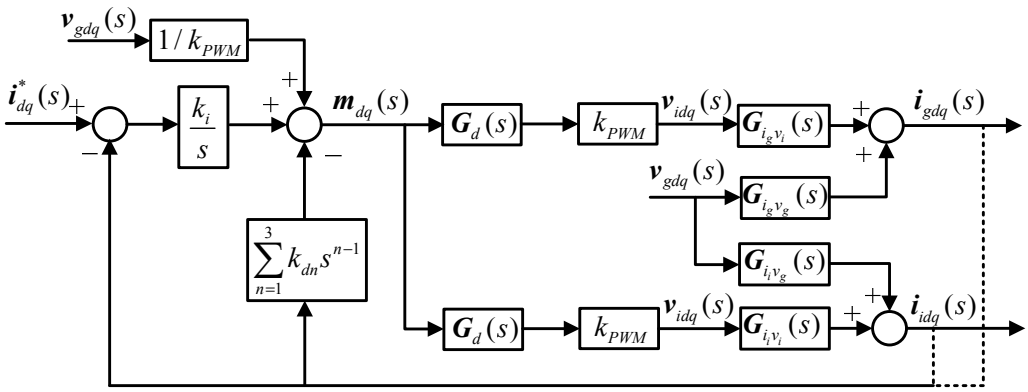

Figure 5.4: PDF controlled three-phase grid-connected inverter in the SRF.

5.3 PDF for Inverter Current Feedback System

The inverter current can be used as the feedback variable to indirectly control the grid current based on the following two reasons. Firstly, the inverter current is usually used to protect the power circuits in industrial applications [62]. Secondly, it can utilize the inherent damping characteristics of the *LCL* filter to neutralize its resonance to enhance system stability [24]. As presented in Chapter 3 and 4, a single-loop controlled ICF system can be made stable on condition that f_s is larger than $6f_{res}$ (for the general case with a total time delay of $1.5T_s$) [71, 72, 76]. Using f_s =

15000 Hz, the ratio of f_s to f_{res} is 11.4, which meets the stability condition with adequate margins (a ratio larger than 9 for a PM of 30°) [71].

In this section, a simple PDF controller with the inner feedback path employing only a proportional term is designed for the ICF system. In terms of structure, the difference between the PDF controller and PI controller rests with the change of the position for the proportional term. However, overshoot and oscillation in the transient response caused by reference changes, which are unavoidable for the PI controller, can be easily eliminated by the PDF controller.

5.3.1 Control Loops

The *s*-domain block diagram of an ICF system controlled by the simple PDF controller is shown in Figure 5.5. The block diagram of a PI controlled ICF system is shown in Figure 5.6. It can be seen that the difference between the PDF controller and PI controller is the change of the position of k_p.

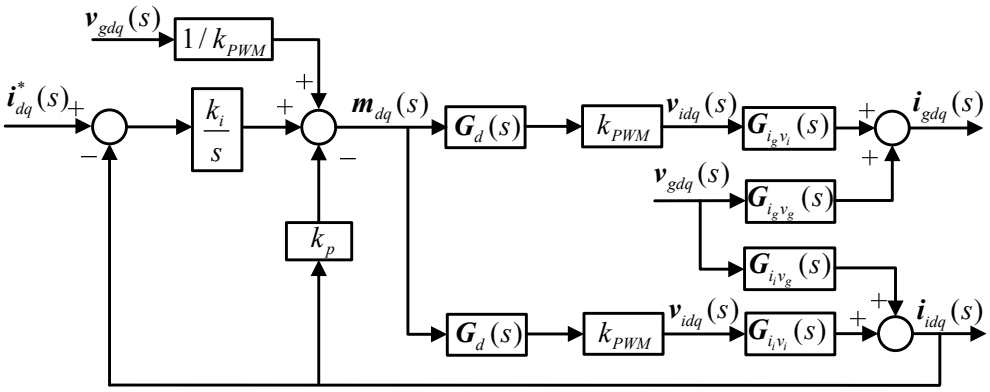

Figure 5.5: Block diagram of the PDF controlled ICF system.

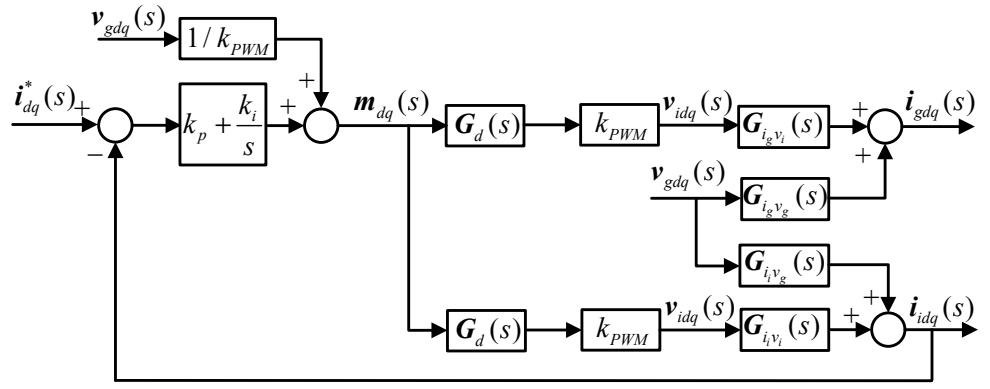

Figure 5.6: Block diagram of the PI controlled ICF system.

The closed-loop transfer function of the PDF control system is yielded as

$$\boldsymbol{G}_{clPDF}(s)=\frac{\boldsymbol{i}_{gdq}(s)}{\boldsymbol{i}^{*}_{dq}(s)}=\frac{k_i\boldsymbol{G}_d(s)k_{PWM}\boldsymbol{G}_{i_gv_i}(s)}{(sk_p+k_i)\boldsymbol{G}_d(s)k_{PWM}\boldsymbol{G}_{i_iv_i}(s)+s}, \tag{5.11}$$

while that of the PI control system is expressed as

$$\boldsymbol{G}_{clPI}(s)=\frac{\boldsymbol{i}_{gdq}(s)}{\boldsymbol{i}^{*}_{dq}(s)}=\frac{(sk_p+k_i)\boldsymbol{G}_d(s)k_{PWM}\boldsymbol{G}_{i_gv_i}(s)}{(sk_p+k_i)\boldsymbol{G}_d(s)k_{PWM}\boldsymbol{G}_{i_iv_i}(s)+s}. \tag{5.12}$$

As can be seen the PI system has one more closed-loop zero ($s = -K = -k_i/k_p$) than that of the PDF system. Yet their loop gains are identical provided that identical controller parameters are used, thus the same stability characteristics.

It can be derived from Figure 5.5 and 5.6 that the PDF and PI systems have an identical closed-loop transfer function from the grid voltage to grid current, given as

$$\boldsymbol{G}_{gd}(s)=\frac{\boldsymbol{i}_{gdq}(s)}{\boldsymbol{v}_{gdq}(s)}=\frac{s-(sk_p+k_i)k_{PWM}\boldsymbol{G}_{i_iv_g}(s)}{(sk_p+k_i)\boldsymbol{G}_d(s)k_{PWM}\boldsymbol{G}_{i_iv_i}(s)+s}\boldsymbol{G}_d(s)\boldsymbol{G}_{i_gv_i}(s)+\boldsymbol{G}_{i_gv_g}, \tag{5.13}$$

which implies that their disturbance rejection abilities for grid voltage harmonics are identical when identical controller parameters are used.

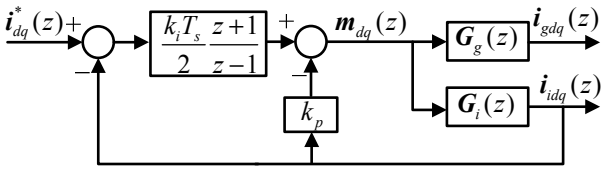

Figure 5.7: Block diagram of the PDF control system in the *z*-domain.

The *z*-domain block diagram of the PDF controlled grid-connected inverter is shown in Figure 5.7. The integral term is discretized using the Tustin's method [131]. Discrete closed-loop transfer functions of the PDF and PI systems are expressed as

$$\boldsymbol{G}_{clPDF}(z)=\frac{\boldsymbol{i}_{gdq}(z)}{\boldsymbol{i}^{*}_{dq}(z)}=\frac{(z+1)k_iT_s\boldsymbol{G}_g(z)}{2z-2+\left[z(2k_p+k_iT_s)-2k_p+k_iT_s\right]\boldsymbol{G}_i(z)} \tag{5.14}$$

and

$$\boldsymbol{G}_{clPI}(z)=\frac{\boldsymbol{i}_{gdq}(z)}{\boldsymbol{i}^{*}_{dq}(z)}=\frac{\left[z(2k_p+k_iT_s)-2k_p+k_iT_s\right]\boldsymbol{G}_g(z)}{2z-2+\left[z(2k_p+k_iT_s)-2k_p+k_iT_s\right]\boldsymbol{G}_i(z)}, \tag{5.15}$$

respectively. As seen in the z-domain the difference between the PDF and PI systems is the modification of one closed-loop zero ($z = -1$ for PDF and $(2k_p - k_iT_s) / (2k_p + k_iT_s)$ for PI).

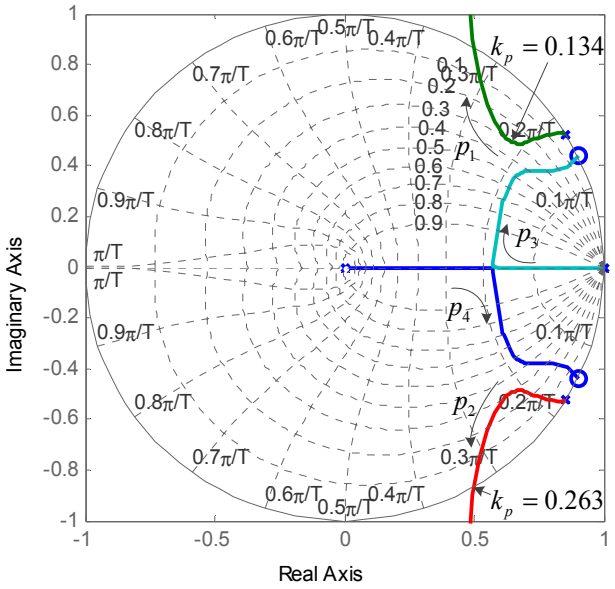

Figure 5.8: Root loci of ICF system controlled by a proportional compensator, shown in the stationary frame.

5.3.2 Transient Responses

Same as the PI control system, the stability of the PDF system is mainly determined by the proportional gain k_p [25], hence the stability boundary of k_p is investigated first. Moreover, the frequency shift between transfer functions in the stationary frame and SRF will not alter the stability, hence k_p can be evaluated in the stationary frame in which the transfer function is real [117] (This is also why the stability study in previous two chapters conducted in the stationary frame can be verified in the SRF). Parameters of the circuit are given in Table 3.2. The root loci of an ICF loop in the stationary frame with a proportional compensator are shown in Figure 5.8, where the arrows indicate the changing directions of four poles (p_1–p_4) when k_p increases. p_1 and p_2 are caused by the LCL resonance and are generally the dominant poles, p_3 is due to the inductors and p_4 due to the time delay [33]. The stable boundary of k_p is 0.263, which can also be calculated using (4.7). To guarantee a GM of 3 dB, k_p should be set to a value smaller than 0.186. When $k_p = 0.134$, the system would have

the fastest step response, since the dominant poles p_1 and p_2 are farthest away from the unit circle boundary.

Because the grid current i_g is indirectly controlled by the inverter current i_i, i_q^* is set to $\omega_n C V_g$ instead of 0 to achieve the unity PF [24]. With a unit step change in i_d^*, the simulated step responses of the PDF system with $k_p = 0.134$ and different values of K are shown in Figure 5.9(a), while those of the PI system are shown in Figure 5.9(b). As can be seen, in the PI control systems obvious couplings exist, whereas the coupling in PDF systems is much milder and even negligible. Concerning the response in the d-axis current, it is apparent that there are overshoots (60% – 100%) and oscillations in the PI system, and the overshoot increases when K rises. By contrast, much smoother responses are obtained by the PDF controller, in spite that mild overshoot also appears when a large K is used. Although the rise time of the PDF system is longer than that of the PI system, its settling time is relatively shorter than that of the latter when K is large ($K = 1400$: $t_{sPDF} = 2.24$ ms, $t_{sPI} = 2.51$ ms; $K = 2000$: $t_{sPDF} = 1.83$ ms, $t_{sPI} = 2.75$ ms. A tolerance band of 1% is defined for the settling time [36]). The slower response of the PDF system with a small K will be discussed later in Section 5.3.3. It can be seen that $k_p = 0.134$ and $K = 1400$ are suitable parameters for the PDF controller to give a satisfactory transient response, with a fast response and no overshoot or oscillation.

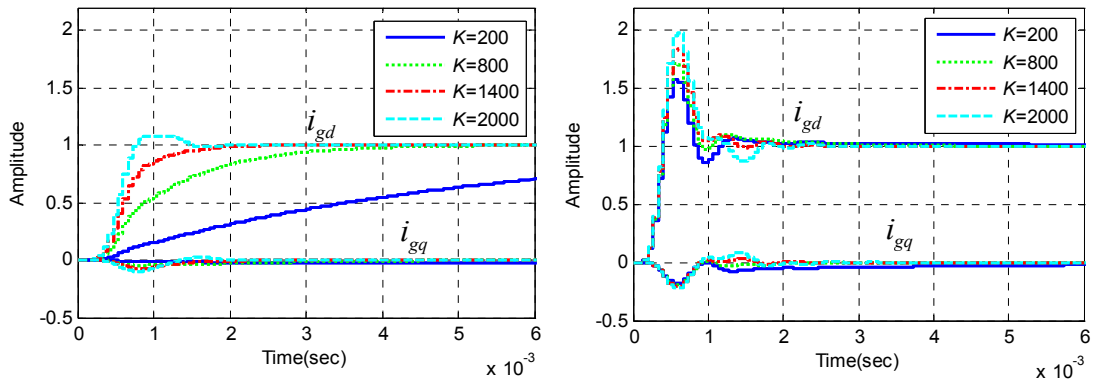

Figure 5.9: Step responses for $k_p = 0.134$ with different values of K (k_i / k_p). (a) PDF control system. (b) PI control system.

There are many parameter optimization methods for the PI controller to optimize its performance, such as the SO [34] and OP [39]. Parameters of SO and OP are tuned to have the values

$$k_p = \frac{L_i + L_g}{3k_{PWM}T_s}, K = \frac{1}{9T_s} \tag{5.16}$$

and

$$k_p = \frac{\omega_c(L_i + L_g)}{k_{PWM}}, K = \frac{\omega_c}{10}, \tag{5.17}$$

respectively, ω_c in (5.17) is the crossover frequency that can be chosen as $\omega_c = 0.3\omega_{res}$ [24]. The step responses of the PI system with the optimized parameters, and those of the PI and PDF systems with $k_p = 0.134$ and $K = 1400$ are shown in Figure 5.10(a). It can be seen that the PI controller always gives overshoot and oscillation. Particularly the settling time of the PI system with OP is much longer than that of the PDF system. The advantage of the PDF controller over PI controller in the transient response is obvious.

When the PI controller is tuned to give an identical rise time as the PDF controller (0.96 ms, from 10% to 90%), the step responses are presented in Figure 5.10(b), which shows that the PI controller ($k_p = 0.035$, $K = 150$) still produces overshoot and oscillation. Furthermore, the settling time of the PI system (18 ms) is about eight times that of the PDF system (2.24 ms).

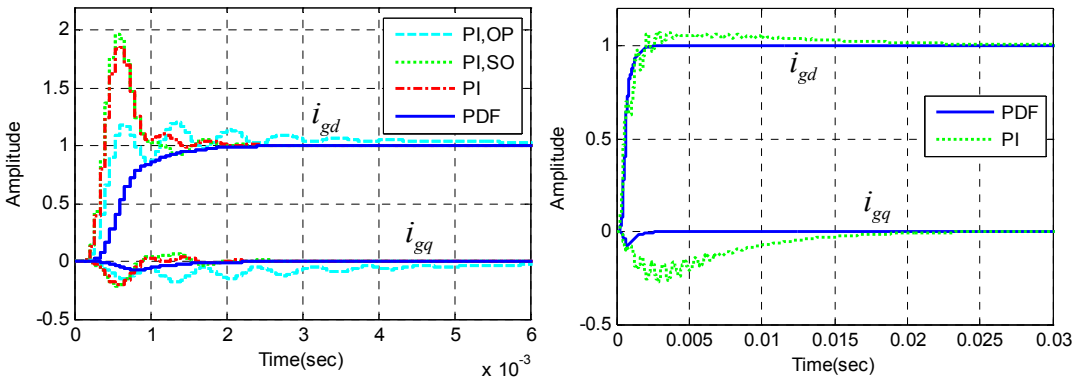

(a) (b)

Figure 5.10: Step responses of the PDF control system and PI system with different parameters. (a) By different design methods. (b) With same rise time.

In fact, there are unavoidable overshoots in the PI system, whereas the PDF controller can achieve an over-damping transient easily. Overshoots of the PI and PDF system with varied k_p and K values are shown in Figure 5.11(a) and (b), respectively. As seen, the overshoot generated by the PI controller ranges from 20% to 110%. To reduce the overshoot, smaller controller gains have to be used, resulting in a lower bandwidth and disturbance rejection ability [36, 40]. In contrast, no overshoot exists in the PDF system over a wide range of controller parameters. Although overshoot appears when the PDF controller employs a small k_p and large K, it is much smaller than that of the PI system. Therefore the PDF controller can achieve a better transient performance without degrading the bandwidth and disturbance rejection ability.

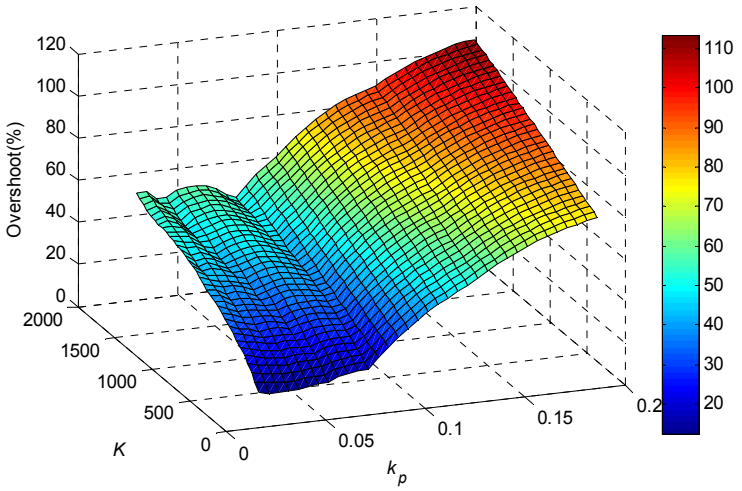

(a)

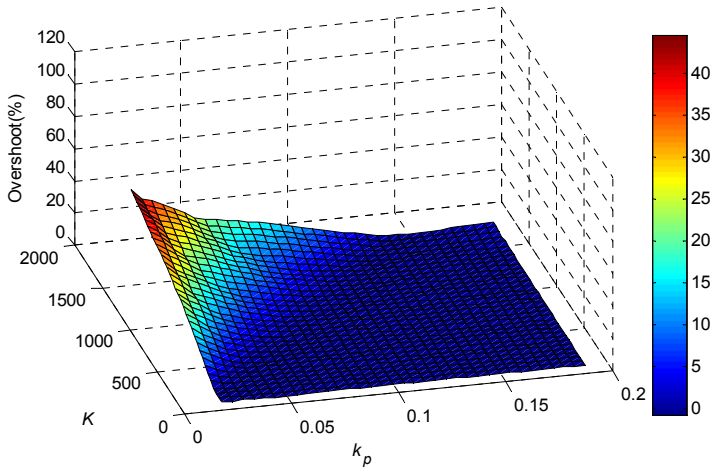

(b)

Figure 5.11: Overshoots of PI and PDF control systems with varied controller parameters. (a) PI controller. (b) PDF controller.

5.3.3 Discussion of Influence of Controller Parameters on the Transient Response

Corresponding to the transient responses of the PDF and PI systems in Figure 5.9, the closed-loop pole-zero maps are shown in Figure 5.12 (a complex zero outside the unit circle is omitted for a better view), where the arrows indicate the changing directions of poles and zeroes when K increases. Note that the poles and also zeros are asymmetric about the real axis because of the complex transfer functions [41, 95]. In comparison with Figure 5.8, the additional pole p_5, zeroes z_0 and z_1 are introduced by controllers. The difference between the PDF and PI systems, as demonstrated in (5.14) and (5.15), is that the zero $z_0 = -1$ is affiliated only to the PDF system whereas $z_1 = (2k_p - k_iT_s) / (2k_p + k_iT_s)$ is only to the PI system. With a small K value of 200, in the PI system, p_5 and z_1 are canceled by each other, but in the PDF system, p_5 is the dominant pole which is near the unit circle, leading to a slow transient response (see Figure 5.9(a)). When K increases, the dynamics of the PDF system becomes faster since p_5 moves more inside of the unit circle. Meanwhile, for the PI system, p_5 is not canceled by z_1, and thus the PI and PDF systems have identical closed-loop poles. Therefore, the times for the two systems to reach their steady-state values are approximately identical. When K is sufficiently large (= 2000), p_1 and p_2 are less damped, leading to mild overshoot and oscillation in the PDF system.

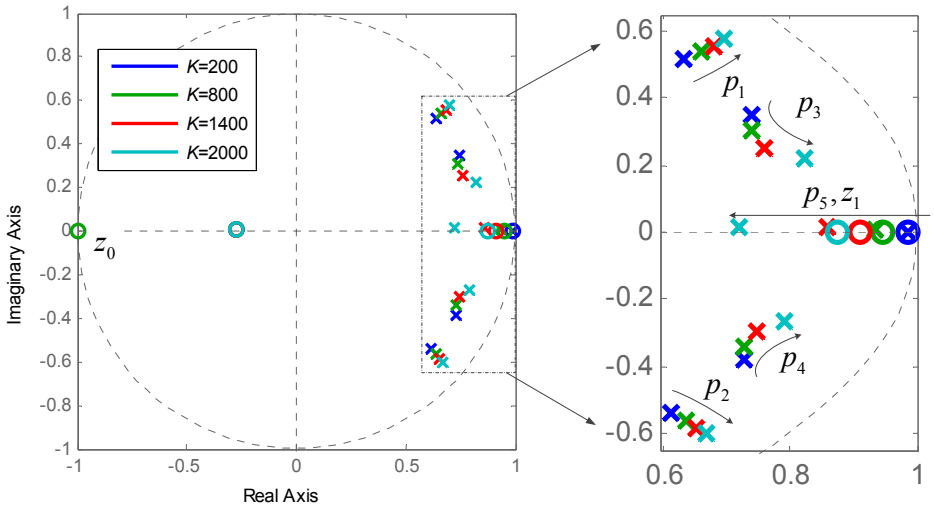

Figure 5.12: Pole-zero map of the PI and PDF systems with $k_p = 0.134$ and different values of K.

5.4 PDF for Grid Current Feedback System

As deduced in Chapters 3 and 4, a single-loop PI controller can stabilize a GCF system if $2f_{res} < f_s < 6f_{res}$ [30, 71], and in this case a simple PDF controller can be adopted to improve the transient response. However, this region is not attractive because the grid impedance variation in weak grids may shift f_{res} in a wide spectrum across the point of f_s / 6, which would trigger instability [75]. Instead, an additional inner active damping feedback loop is needed, but more than one signal is to be sensed [40, 72, 104]. A second-order derivative method implemented as a high-pass filter has been used in [63, 66, 113] to provide active damping for the grid current. However, the time delay is not considered in [66], thus the analysis of the control loop can potentially be unreliable [96, 97]. In [113], the design of the outer current controller is conducted before that of the inner loop, which would lead to inadequate stability margins or even an unstable system. In [63], the critical value for the cutoff frequency to ensure a positive virtual resistance has been discussed, but the relationship between the filter's cutoff frequency and gain to guarantee a stable inner active damping loop was not studied. Moreover, the so-called co-design flow for control parameters and the stability analysis of the overall system are vague. In all cases, it is difficult for the PI plus active damping methods to eliminate the transient overshoot and oscillation [21, 40, 58, 104, 113].

In this section, a PDF controller with a proportional gain and a second-order derivative in the inner feedback path is developed for a GCF system. Active damping is achieved with the GCF only. In addition to giving a stable operation, the PDF controller can also respond without overshoot to a step change in the reference input. A controller design procedure is proposed to ensure adequate stability margins and satisfactory transient performance.

5.4.1 Control Loops

The block diagram of the PDF controlled GCF system is shown in Figure 5.13.

In comparison to the simple PDF controller for the ICF system, a second-order derivative term $k_d s^2$ is added in the inner feedback path. It is actually a single-loop control system rather than a multi-loop one, because there is only one controller and one feedback signal [114]. Nonetheless, the second-order derivative feedback loop can be treated as an inner loop, for the purpose of damping analysis.

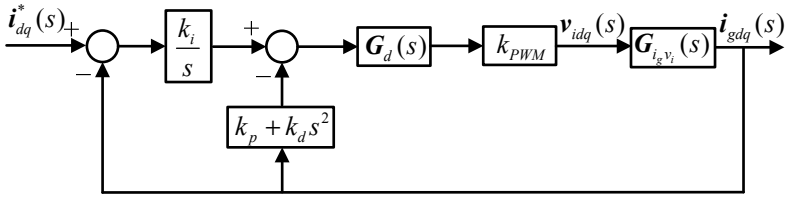

Figure 5.13: Block diagram of the PDF controlled GCF system.

It has been proved in [63, 66, 113] that the second-order derivative is able to provide damping because it is equivalent to a proportional k_d feedback of the capacitor current, which is a common active damping method as discussed in Chapter 4. However, the derivative term will dramatically amplify noise disturbances, which would lead to unreasonable consequences [113]. Therefore, the practical implementation of $k_d s^2$ should be developed. A high-pass filter with a negative gain can achieve this target and avoid the influence of noises [63, 66, 113], with the transfer function given as

$$G_{hp}(s) = -\frac{sk_{hp}}{s+\omega_{hp}}, \tag{5.18}$$

where ω_{hp} is the cut-off angular frequency (should be in the range of (0, $0.5\omega_s$], $\omega_s = 2\pi f_s$ [63]).

Nevertheless, the high-pass filter is proposed for the control in the stationary frame. For controllability, (5.18) should be transformed into the SRF, resulting in a complex high-pass filter, given as

$$\boldsymbol{G}_{hp}(s) = -\frac{(s+j\omega_n)k_{hp}}{s+j\omega_n+\omega_{hp}}, \tag{5.19}$$

Consequently the stability analysis can be carried out in the stationary frame, in which transfer functions are real [112, 117]. Hence only the positive frequency range needs to be concerned when using the Nyquist stability criterion [117, 118]. The Bode diagram of the loop gain in the stationary frame, i.e., $T_i^s(s) = G_d(s)k_{PWM}$ $G_{i_g v_i}^s(s)G_{hp}(s)$ is shown in Figure 5.14. As can be seen no $\pm(2k+1)\pi$ crossing exists at the resonance frequency, thus the inner loop can be tuned to be stable.

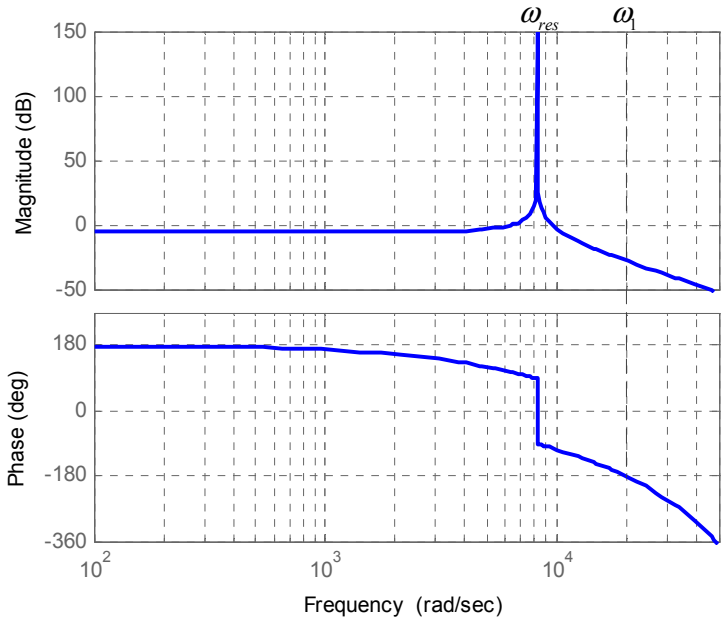

Figure 5.14: Bode diagram of the high-pass filter active damping loop gain, shown in the stationary frame.

5.4.2 Tuning of Controller Parameters

5.4.2.1 Inner Active Damping Loop

The magnitude (in decibels) and phase of $T_i^s(s)$ are given as

$$\begin{cases} 20\lg\left|T_i^s(s)\right|_{s=j\omega}\Big| = 20\lg\left|e^{-j\omega 1.5T_s}k_{PWM}\frac{\omega_r^2}{L_i(\omega_{res}^2-\omega^2)}\frac{-k_{hp}}{j\omega+\omega_{hp}}\right| = 20\lg\left(\frac{k_{PWM}\omega_r^2}{L_i\left|\omega_{res}^2-\omega^2\right|}\frac{k_{hp}}{\sqrt{\omega^2+\omega_{hp}^2}}\right), \\ \angle T_i^s(s)\Big|_{s=j\omega} = \angle e^{-j\omega 1.5T_s}k_{PWM}\frac{\omega_r^2}{L_i(\omega_{res}^2-\omega^2)}\frac{-k_{hp}}{j\omega+\omega_{hp}} = \begin{cases} -\frac{3\omega T_s}{2}+\pi-\arctan\frac{\omega}{\omega_{hp}}, \omega<\omega_{res} \\ -\frac{3\omega T_s}{2}-\arctan\frac{\omega}{\omega_{hp}}, \omega>\omega_{res}. \end{cases} \end{cases}$$

(5.20)

The phase starts from 180° at $\omega = 0$, and crosses over –180° at a frequency ω_1. The frequency ω_1, which should be larger than ω_{res} to avoid the negative crossing at ω_{res} (i.e., the phase does not cross over –180° at ω_{res}), can be obtained by solving the following equation:

$$\frac{3\pi\omega_1}{\omega_s} + \arctan\frac{\omega_1}{\omega_{hp}} = \pi . \tag{5.21}$$

It is interesting to note that ω_1 from (5.21) is identical to the 'critical frequency' in [63], below which a positive virtual resistance is achieved. The requirement on ω_{hp} can be deduced to ensure $\omega_1 > \omega_{res}$ (i.e., a positive virtual resistance at ω_{res} [76]), whereby the inner loop is possible to be stable [63]. Yet, the possible stability is not enough; the stable condition for k_{hp} should also be derived. According to the Nyquist stability criterion, if the magnitude in (5.20) is tuned to be below 0 dB at $\omega = 0$ (the phase crosses 180°) and ω_1 (the phase crosses –180°), no negative crossing exists, and the inner loop is stabilized. Therefore, with a given ω_s and a proper ω_{hp}, the two gain boundaries for k_{hp} are deduced as (5.22), and the smaller one of k_{hp0} and k_{hp1} is the critical value.

$$\begin{cases} k_{hp0} = \dfrac{(L_i + L_g)\omega_{hp}}{k_{PWM}}, \\ k_{hp1} = \dfrac{L_i(\omega_1^2 - \omega_{res}^2)\sqrt{\omega_1^2 + \omega_{hp}^2}}{k_{PWM}\omega_r^2}. \end{cases} \tag{5.22}$$

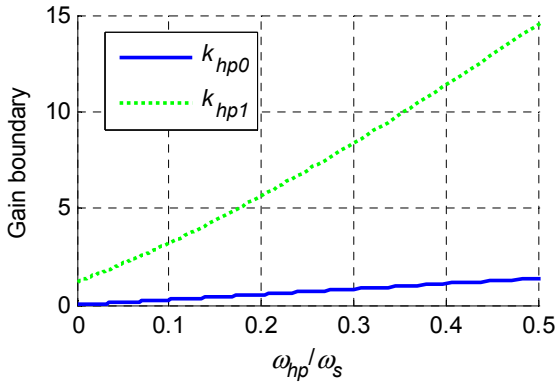

Figure 5.15: Gain boundaries k_{hp0} and k_{hp1} as a function of ω_{hp}/ω_s for the case with f_s = 15000 Hz.

With a high f_s = 15000 Hz = 11.4ω_{res}, it is indicated in (5.21) that a positive ω_{hp} is adequate for the possible stability. In this case, the curves of the two gain boundaries in (5.22) as a function of ω_{hp}/ω_s are shown in Figure 5.15. It can be seen that k_{hp0} is always smaller than k_{hp1}, hence k_{hp} can be chosen as $k_{hp} = k_{hp0}/2 = (L_i + L_g)\omega_{hp}/2k_{PWM}$. ω_{hp} is to be tuned later to obtain adequate stability margins for the whole loop.

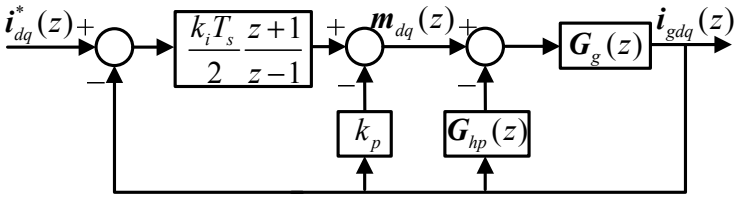

Figure 5.16: Discrete block diagram of the PDF controlled GCF system.

The z-domain block diagram of the grid-connected inverter with the PDF controller is shown in Figure 5.16, where $\boldsymbol{G}_{hp}(z)$ is the Tustin's discrete equivalent of $G_{hp}(s)$, $G_{hp}(z)$, with z being replaced by $z = e^{-j\omega_n T_s}$, given as

$$\boldsymbol{G}_{hp}(z) = -\frac{2k_{hp}(ze^{j\varphi} - 1)}{(\omega_{hp}T_s + 2)ze^{j\varphi} + \omega_{hp}T_s - 2}. \tag{5.23}$$

The discrete inner loop gain in the stationary frame $T_i^s(s) = G_g^s(z)G_{hp}(z)$ is given as:

$$T_i^s(z) = -\frac{2k_{PWM}k_{hp}}{(L_i + L_g)\omega_{res}} \cdot \frac{z^2(\omega_{res}T_s - \sin\omega_{res}T_s) + z(2\sin\omega_{res}T_s - 2\omega_{res}T_s\cos\omega_{res}T_s) + \omega_{res}T_s - \sin\omega_{res}T_s}{[(\omega_{hp}T_s + 2)z + \omega_{hp}T_s - 2](z^3 - z^2 2\cos\omega_{res}T_s + z)} \tag{5.24}$$

Therefore, in the stationary frame, the closed-loop transfer function of the inner loop is expressed as

$$G_{cli}^s(z) = \frac{i_{g\alpha\beta}(z)}{m_{\alpha\beta}(z)} = \frac{G_g^s(z)}{1 + T_i^s(z)}. \tag{5.25}$$

In the frequency range below ω_{res}, $G_g^s(z)$ is similar to an L-filter with an inductance of $L_i + L_g$ [24, 101]. The discrete transfer function of the L-filter is given as

$$G_L(z) = Z\left\{\frac{e^{-sT_s}G_{PWM}(s)k_{PWM}}{s(L_i+L_g)}\right\} = \frac{k_{PWM}T_s}{(L_i+L_g)z^2-(L_i+L_g)z} \tag{5.26}$$

With $k_{hp} = (L_i + L_g)\omega_{hp} / 2k_{PWM}$, $T_i^s(z) \approx -1/2$, hence $G_{cli}^s(z) = 2G_g^s(z) \approx 2G_L(z)$. It means that in the frequency range below ω_{res}, the inner loop approximately behaves as an L-filter with an inductance of $(L_i + L_g)/2$.

5.4.2.2 Outer Loop

Since the loop from $\boldsymbol{m}_{dq}(z)$ to $\boldsymbol{i}_{gdq}(z)$ has been treated as an inner loop, there is an outer loop with a simple PDF controller that was used in the ICF system. As discussed in Section 5.3, the loop gain of the outer loop with a simple PDF controller is identical to that with a PI controller.

Because $G_{cli}^s(z)$ is similar to an L-filter with an inductance of $(L_i + L_g)/2$ below ω_{res}, the simple outer PDF controller can be designed based on the OP method in (5.17). It is suggested in [24, 30] that ω_c equal to or be larger than $0.3\omega_{res}$. In the present work $\omega_c = 0.4\omega_{res}$ is used to obtain adequate stability margins and a larger bandwidth so that a better transient response is achieved. Consequently k_p and k_i are tuned to

$$k_p = \frac{\omega_{res}(L_i+L_g)}{5k_{PWM}}, k_i = \frac{k_p\omega_{res}}{25}. \tag{5.27}$$

With (5.27), the integral term has a negligible influence on the stability margins. Therefore, the outer loop can be discussed in the stationary frame by treating the PI as a proportional gain k_p. To pick a satisfactory ω_{hp}, the relationship between stability margins and the term ω_{hp}/ω_s is illustrated in Figure 5.17. It can be seen that $\omega_{hp} = \omega_{res}$ ($\omega_{hp}/\omega_s = 0.0876$) is a good option, with which GM = 5.53 dB and PM = 44.07°.

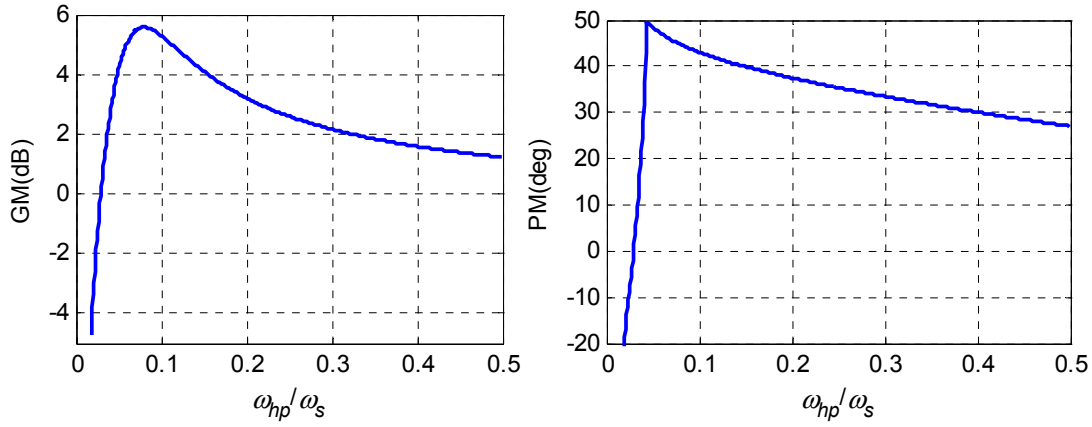

(a) (b)

Figure 5.17: Relationship between stability margins and ω_{hp}/ω_s. (a) GM. (b) PM.

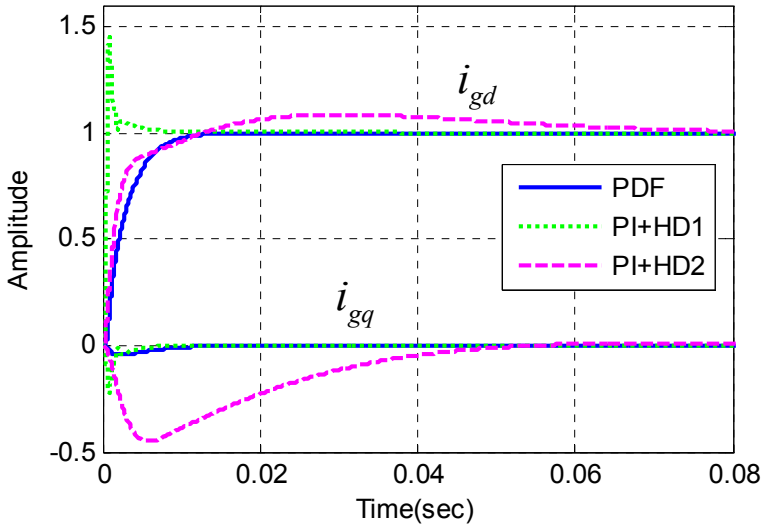

Figure 5.18: Step responses of the PDF system and PI plus high-pass filter active damping control system, with f_s = 15000 Hz.

As the grid current i_g is controlled directly, i_q^* is set to 0. With a unit step change in i_d^*, the step response of the PDF controlled GCF system is shown in Figure 5.18. Apparently, a smooth transient without overshoot is produced. For comparison, the system controlled by a PI plus high-pass filter active damping (HD) method [63, 66, 113] is also tested in two scenarios: One with the same parameters (k_p = 0.0484, k_i = 15.972) as those of the PDF controller, and the other with the same rise time (5.97 ms) as the latter by reducing the PI gains (k_p = 0.08, k_i = 0.52). Identical high-pass filter parameters are used in the PDF and PI systems. In the first scenario, the transi-

ent contains oscillation and strong overshoot (47%), while in the latter scenario, an overshoot of 9% exists and the settling time is about five times that of the PDF system (61.8 versus 12.8 ms). Moreover, the coupling between *d*- and *q*-axis currents in the PDF system is much milder than that in the PI systems. Similar to the simple PDF controller used for the ICF system, the PDF controller for the GCF system can achieve a well-damped transient response over a wide range of control gains, whereas the PI method can only reduce the overshoot by using small gains.

5.4.3 Performance at Low Sampling Frequency

It is known that the time delay may impose influence on the transient response [33, 105]. To evaluate the influence of a larger time delay on the PDF controller, the system with a lower sampling frequency (f_s = 6000 Hz, f_s / f_{res} = 4.567, f_{res} / f_s = 0.219) is examined. It can be deduced from (5.21) that ω_{hp} should be larger than $0.1177\omega_s$ to ensure $\omega_1 > \omega_{res}$. Therefore, $\omega_{hp} = 0.5\omega_s$ is chosen to achieve a robust damping [63]. Then ω_1 is obtained as $0.279\omega_s$ from (5.21). In this case k_{hp0} = 0.5489 and k_{hp1} = 0.392 are calculated from (5.22). k_{hp1} is smaller than k_{hp0}, contrary to the case with f_s = 15000 Hz. Hence k_{hp} can be set to k_{hp1} / 2. k_p and k_i are still tuned according to (5.27). With the designed PDF controller, GM = 6.18 dB and PM = 46.5°.

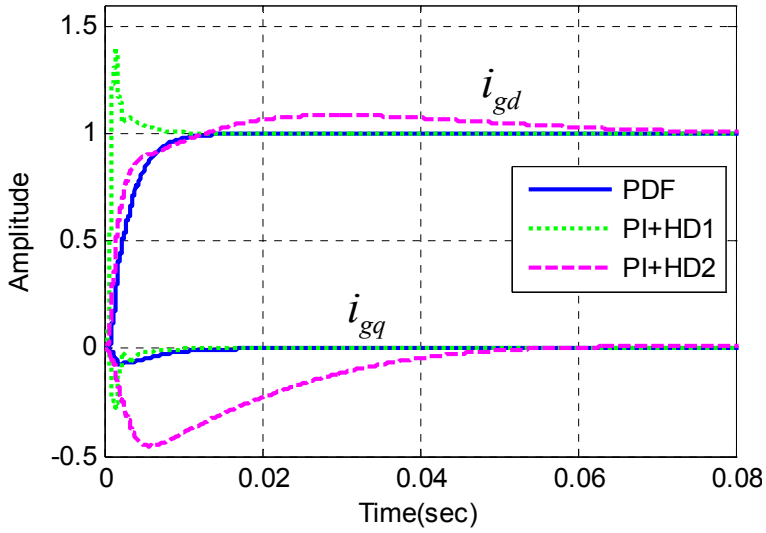

Figure 5.19: Step responses of the PDF system and PI plus high-pass filter active damping control system, with f_s = 6000 Hz.

Likewise, step responses of the PDF and PI plus high-pass filter active damping controlled systems are shown in Figure 5.19. As expected, the transient response of the PDF system is smooth without overshoot. The PI controlled systems, in contrast, exhibit large overshoot (40 and 8%) or a long settling time (60.2 versus 12.2 ms of the PDF system; $k_p = 0.012$ and $k_i = 0.78$). These results further verify the advantage of the PDF controller even at a low sampling frequency.

5.5 Experimental Results

5.5.1 PDF for Inverter Current Feedback System

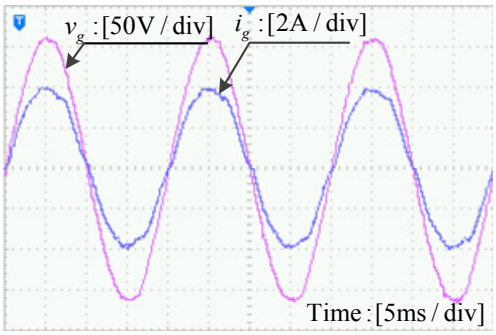

Figure 5.20: Steady-state one-phase grid voltage and current of the PDF controlled ICF system.

First, the steady-state response of the PDF control system with $i_d^* = 4$ A was performed. Figure 5.20 shows the steady-state one-phase grid voltage (THD ≈ 1.9%) and current (THD ≈ 2.6%). It illustrates that the grid current is in phase with grid voltage. Note that a same current quality would be obtained by the PI system when identical controller parameters are used because of the identical disturbance rejection ability.

The transient responses with i_d^* stepping from 1 to 4 A have been tested. With the parameters obtained before ($k_p = 0.134$, $K = 1400$), the output currents of the PDF and PI systems are shown in Figure 5.21 and 5.22, respectively. The settling time of the PI system is about 4 ms, longer than that of the PDF system (2.5 ms). Moreover,

the PI system contains great overshoots (56.7% in i_{id} and 66.7% in i_{gd}, slightly different from simulation results because of issues such as the minor parasitic resistors and the variation of circuit parameters) and oscillations, whereas the transient response of the PDF system is without overshoot or oscillation. Furthermore, the coupling effect in the PI system from the change of the *d*-axis current on the *q*-axis current is more dramatic than that in the PDF system.

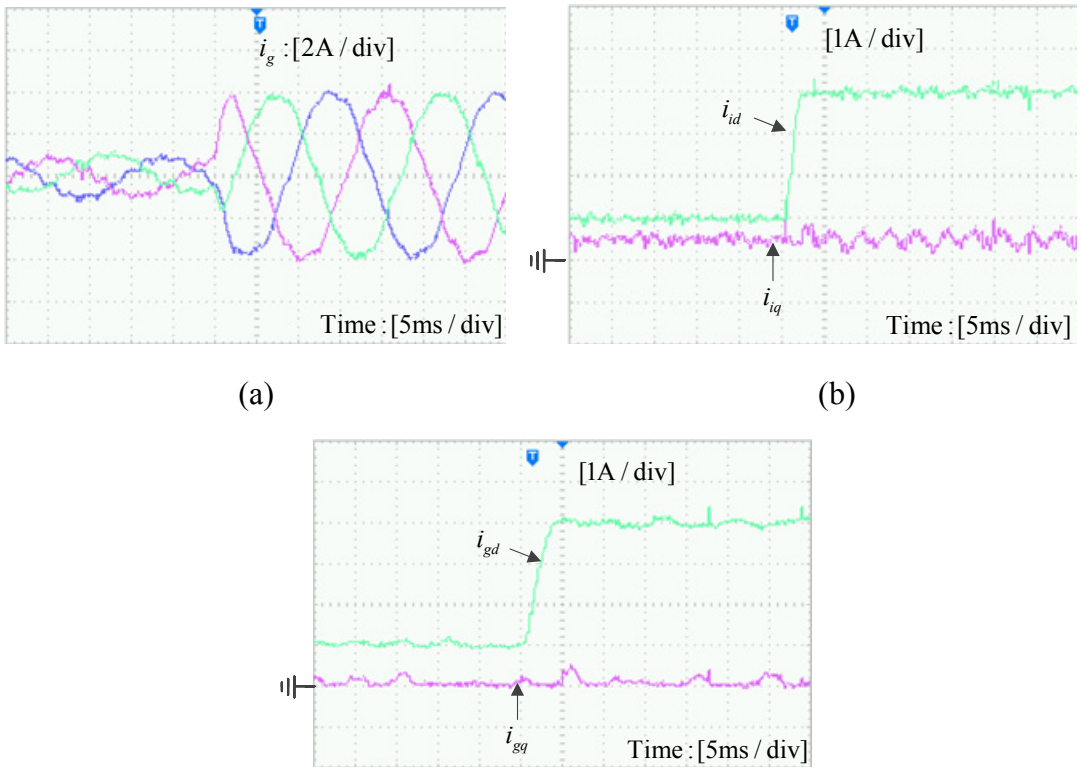

Figure 5.21: Transient response of PDF controlled ICF system. (a) Grid current. (b) *dq* inverter currents. (c) *dq* grid currents.

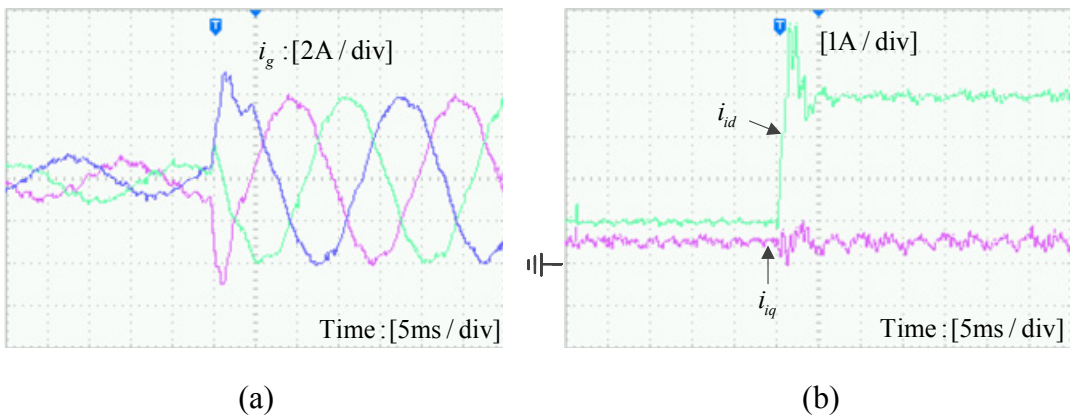

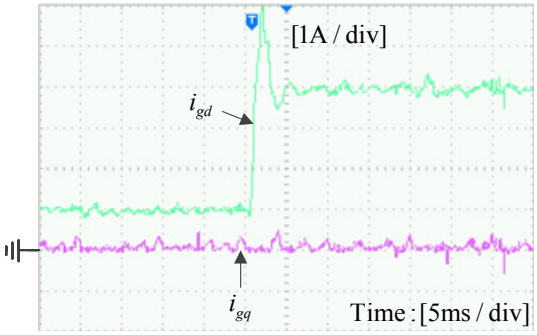

(c)

Figure 5.22: Transient response of PI controlled ICF system. (a) Grid current. (b) *dq* inverter currents. (c) *dq* grid currents.

When the PI controller is tuned to give a same rise time (1 ms) with the PDF controller, the transient response is shown in Figure 5.23. It can be seen that the settling time of the PI system is eight times that of the PDF system (20 versus 2.5 ms). In comparison to the simulation result in Figure 5.10, overshoot is damped out by parasitic resistors.

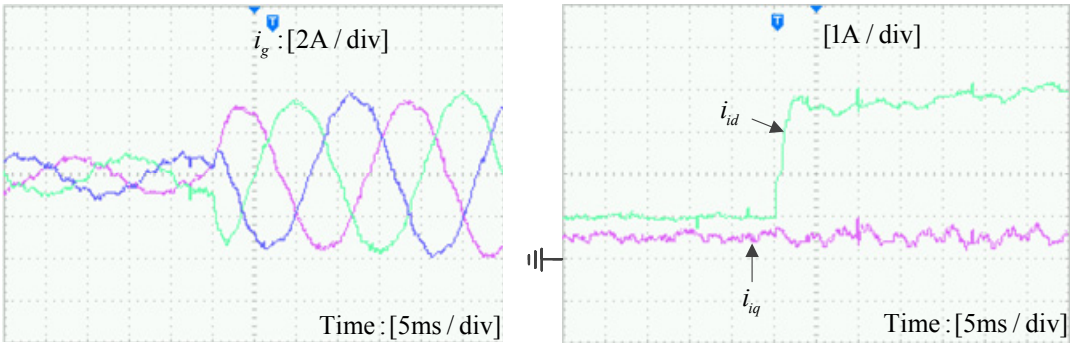

(a) (b)

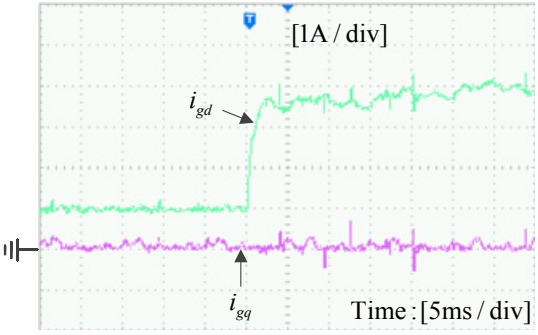

(c)

Figure 5.23: Transient response of PI controlled ICF system with the same rise time as the PDF system. (a) Grid current. (b) *dq* inverter currents. (c) *dq* grid currents.

5.5.2 PDF for Grid Current Feedback System

Figure 5.24 shows the steady-state response of one-phase grid voltage and current of the PDF system when i_{gd} = 4 A. It illustrates that the grid current, with a THD about 3.6%, is synchronized with the grid voltage. The grid voltage adds significant harmonic components to the grid current, but the THD meets the IEEE standard (THD < 5% [11, 26]). In order to mitigate the harmonics, harmonic resonant compensators can be added in the forward path or inner feedback path, but the transient response would be affected [22, 26].

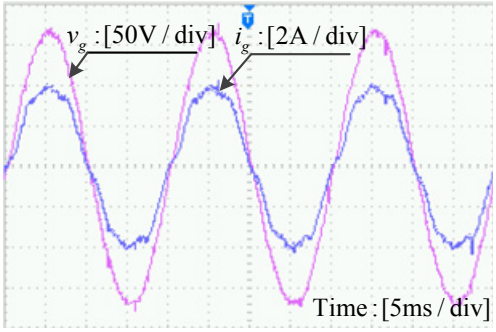

Figure 5.24: Steady-state one-phase grid voltage and current of the PDF controlled GCF system.

With f_s = 15000 Hz, the transient response of the PDF system with i_d^* stepping from 1 to 4 A is shown in Figure 5.25. The result indicates a stable operation due to the active damping introduced by the PDF controller. Moreover, there is no overshoot in the transient response. For comparison, the GCF system controlled by PI plus high-pass filter active damping was also examined. For the case with the same parameters as the PDF controller, the transient response of i_{gd} shown in Figure 5.26 illustrates a significant overshoot (46.7%), in a good agreement with the simulation result. For the one with the same rise time (6 ms) as the PDF system, the transient response in Figure 5.27 shows a much longer settling time (60 versus 12 ms). Moreover, the harmonic disturbance from the grid is much more dramatic (THD ≈ 10.1% for 1 A and 6.3% for 4 A) due to the lower disturbance rejection ability caused by smaller controller gains. Again, the overshoot is decreased in contrast with the simulation due to parasitic resistors.

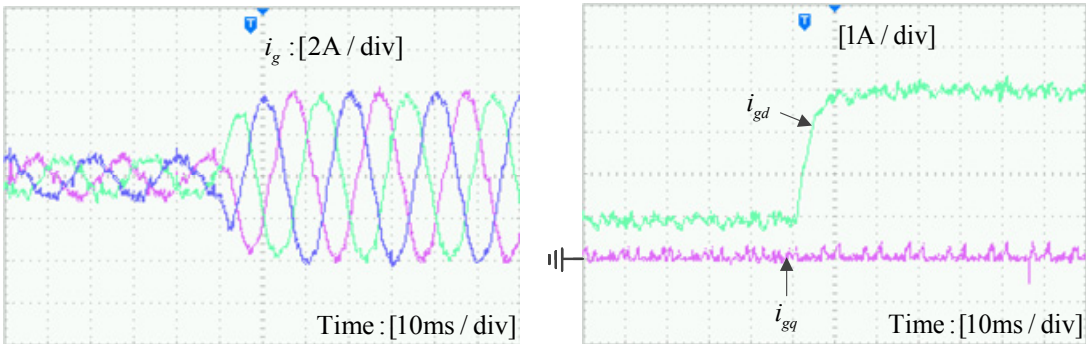

(a) (b)

Figure 5.25: Transient response of PDF controlled GCF system (f_s = 15000 Hz). (a) Grid current. (b) *dq* grid currents.

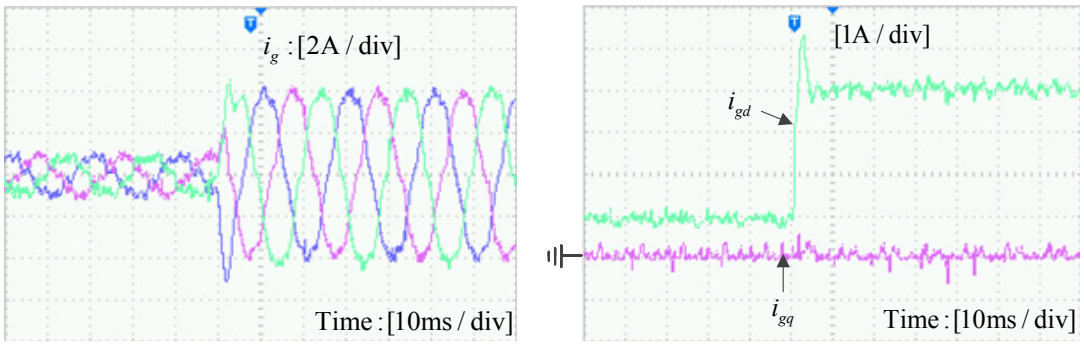

(a) (b)

Figure 5.26: Transient response of PI plus high-pass filter active damping controlled GCF system, with the same parameters as the PDF controller (f_s = 15000 Hz). (a) Grid current. (b) *dq* grid currents.

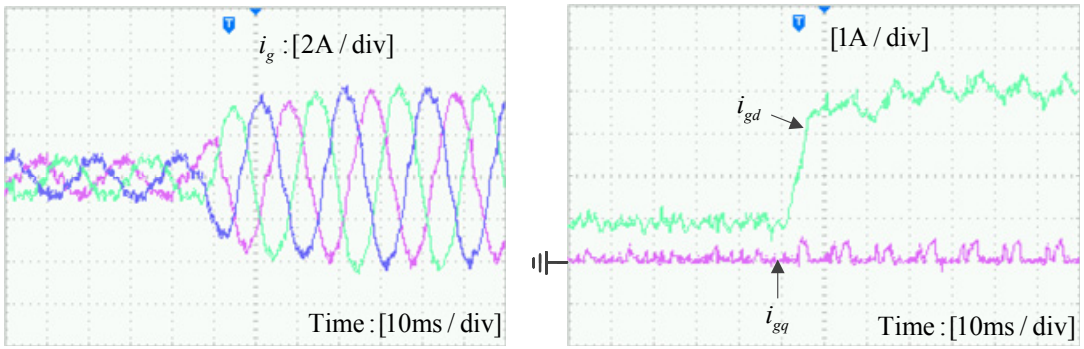

(a) (b)

Figure 5.27: Transient response of PI plus high-pass filter active damping controlled GCF system, with the same rise time as the PDF system (f_s = 15000 Hz). (a) Grid current. (b) *dq* grid currents.

For the case with f_s = 6000 Hz, the experimental transient responses corresponding to Figure 5.19 are shown in Figure 5.28. The transient response of the PDF system is smooth without overshoot. The PI controlled systems, however, exhibit a strong overshoot of 40% or a longer settling time (about 60 versus 13 ms of the PDF system) with high harmonic distortion. These results further confirm the advantage of the PDF controller.

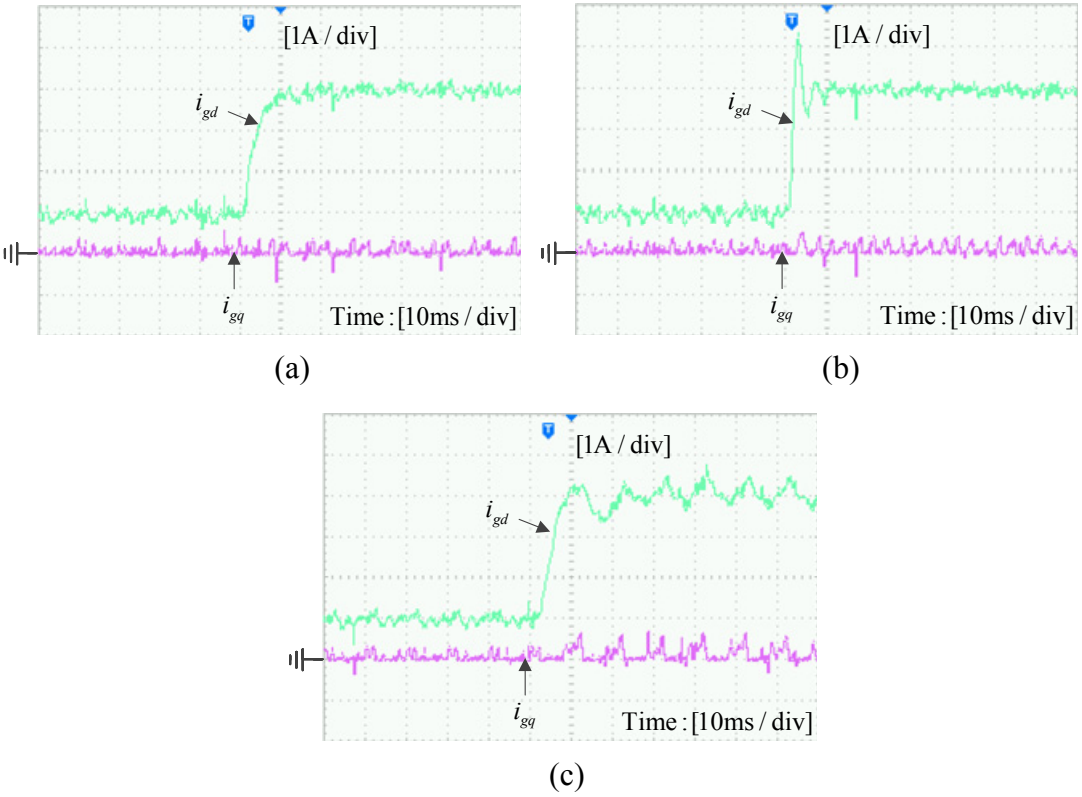

Figure 5.28: Transient responses of GCF systems with f_s = 6000 Hz. (a) PDF. (b) PI plus high-pass filter active damping with the same parameters as the PDF. (c) PI plus high-pass filter active damping with the same rise time as the PDF.

5.6 Conclusion

The PDF has been applied to the current control of three-phase grid-connected inverters with *LCL* filters, which significantly improves the transient response to a step change in the reference input via eliminating overshoot and oscillation. The complex vector method has been adopted for the modeling of the *LCL*-filtered system, in the continuous *s*-domain as well as in the discrete *z*-domain. Two PDF con-

trollers have been developed for an ICF system and a GCF system, respectively. For the ICF, a simple PDF controller with identical stability characteristics to that of the PI controller is developed. Compared with the PI controller which can only reduce the transient overshoot by decreasing the controller gains, the PDF controller completely eliminates the overshoot and oscillation over a wide range of controller parameters. For the GCF, a PDF controller with an additional second-order derivative implemented as a complex high-pass filter has been developed which provides an active damping. The stable condition for the controller parameters has been derived by means of Nyquist stability criterion. A design procedure has been presented that ensures adequate stability margins and satisfactory transient performance. Experimental tests have confirmed the significant performance improvement of the PDF controllers in comparison with the conventional PI control methods.

Chapter 6

Attenuation of Low-Order Current Harmonics in Three-Phase *LCL*-Filtered Grid-Connected Inverters

6.1 Introduction

Grid-connected inverters play a critical role in the quality of the power injected from the DPGSs into the power grid. The delivered grid current is required to have a low THD, which, according to many standards such as the IEEE Standard 15471, should be smaller than 5% (see more details in Table 1.1) [12, 38]. There are mainly two aspects that are involved in the THD: high frequency PWM switching harmonics, and low-order harmonics due to the distortion in grid voltage [26].

To mitigate the switching harmonics, *LCL* filters are adopted widely that exhibit wonderful attenuation ability [23, 71, 119]. As deduced in Chapters 3 and 4, the single-loop control with the GCF can provide damping if $f_s < 6f_{res}$. Nonetheless it is rarely adopted because the time delay is significant which weakens system stability [63, 71]. In contrast, the single-loop indirect control with ICF has been adopted in many works [23, 49, 71, 132], and the system can be made stable if $f_s > 6f_{res}$ [71, 72, 76]. Apart from the single-loop methods, multiloop-based active damping techniques, which include an inner damping loop with the feedback of other variables such as the inverter current, capacitor voltage, and capacitor current, can be used to stabilize the system [23, 58, 81]. In particular, the CCF damping is the most widely used one [58].

It has been found that a second-order derivative feedback of the grid current can produce active damping, still it is equivalent to a proportional feedback of the capacitor current [119].

As for the rejection of the low-order harmonics, there are basically two methods. The first one is the feed-forward of the grid voltage, especially the full feed-forward schemes [91, 130]. However, this method is sensitive to parameter variations and time delay, and multiple derivative terms are introduced which are difficult to implement [56]. The other method is utilizing selective resonant harmonic (RESH) compensators that provide an infinite harmonic impedance [25, 86]. This method has the merit of easy plug-in for the traditional PI and PR controllers and is thus widely used [75]. In this case, the control loop bandwidth needs to be designed carefully to cover the resonant frequencies, in order to avoid stability problems caused by the phase steps of the resonant terms [25].

Both of the damping methods and RESH compensation have been widely studied. However, most research works have focused on either of them; the interaction between them has been seldom researched [75]. Furthermore, in conventional current control methods, a PLL is generally required to generate the reference current [12, 51]. However, a simple PLL will create distorted reference signals which aggravate the harmonic distortion [51], while a sophisticated PLL can generate a harmonic free reference but increases the control complexity and computation load [53]. The PLL will also affect the output admittance and even trigger low-frequency instability [55, 56]. Castilla *et al.* [26, 49, 132] proposed a linear single-loop control scheme in which a PLL is not needed. Nonetheless, the harmonic mitigation in the grid current is unsatisfactory, because it is indirectly controlled by the inverter current.

In this chapter, a direct grid current control method is proposed for three-phase *LCL*-filtered grid-connected inverters, which generates the reference current directly from the grid voltage and effectively suppresses the grid current harmonic distortion. It will be demonstrated that the conventional current control methods are difficult to

achieve a satisfactory harmonic attenuation performance because of an indirect control and/or PLL. The interaction between active damping methods and RESH compensators is discussed, and it is found the ICF damping is superior to the CCF damping in improving system stability. A systematic design procedure is then proposed to optimize the control performance. Finally the improved harmonic attenuation ability of the proposed control method in comparison to conventional ones is verified by experimental results.

6.2 Conventional Current Control Methods for *LCL*-Filtered Grid-Connected Inverters

6.2.1 System Transfer Functions

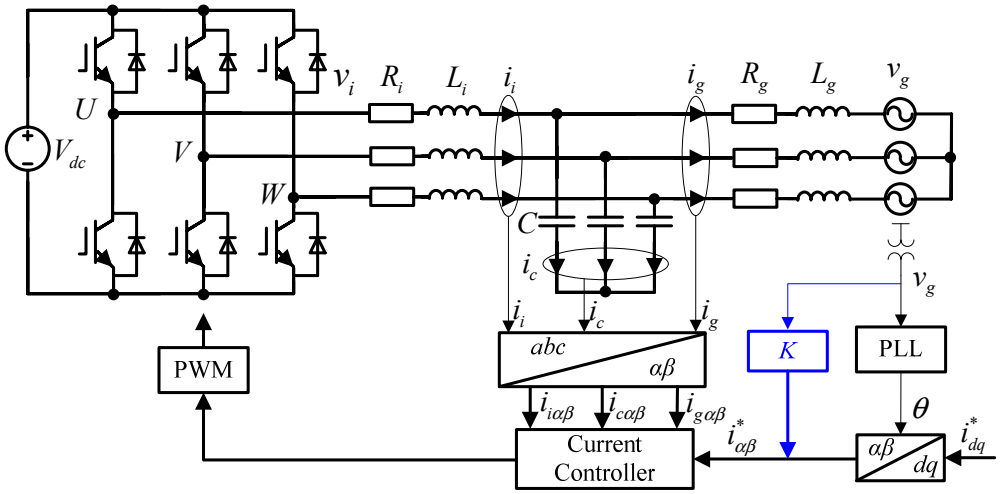

Figure 6.1: Current controlled three-phase *LCL*-filtered grid-connected inverter.

The circuit diagram of the three-phase *LCL*-filtered grid-connected inverter is re-drawn in Figure 6.1. The sampling frequency used in this chapter is f_s = 12 kHz. In this part, the parasitic resistors associated with the inductors are taken into consideration. Parameters of the circuit can be found in Table 2.2 and 3.2. The inverter current i_i, grid current i_g, and capacitor current i_c are usually sensed as the feedback variables, to form a single- or dual-loop current control system [76].

Defining $f_a = CL_iL_g$, $f_b = C(R_iL_g + L_iR_g)$, $f_c = CR_iR_g + L_i + L_g$, and $f_d = R_i + R_g$, the transfer functions from the inverter voltage v_i to i_i, i_g, and i_c are expressed as (6.1) – (6.3):

$$G_{i_i v_i}(s) = \frac{i_i(s)}{v_i(s)} = \frac{s^2 CL_g + sCR_g + 1}{s^3 f_a + s^2 f_b + s f_c + f_d} \tag{6.1}$$

$$G_{i_g v_i}(s) = \frac{i_g(s)}{v_i(s)} = \frac{1}{s^3 f_a + s^2 f_b + s f_c + f_d} \tag{6.2}$$

$$G_{i_c v_i}(s) = \frac{i_c(s)}{v_i(s)} = \frac{s^2 CL_g + sCR_g}{s^3 f_a + s^2 f_b + s f_c + f_d} \tag{6.3}$$

Considering the grid voltage v_g which may be distorted by low-order harmonics as the disturbance, the transfer functions from v_g to i_i, i_g, and i_c are given as (6.4) – (6.6):

$$G_{i_i v_g}(s) = \frac{i_i(s)}{v_g(s)} = \frac{-1}{s^3 f_a + s^2 f_b + s f_c + f_d} \tag{6.4}$$

$$G_{i_g v_g}(s) = \frac{i_g(s)}{v_g(s)} = -\frac{s^2 CL_i + sCR_i + 1}{s^3 f_a + s^2 f_b + s f_c + f_d} \tag{6.5}$$

$$G_{i_c v_g}(s) = \frac{i_c(s)}{v_g(s)} = \frac{s^2 CL_i + sCR_i}{s^3 f_a + s^2 f_b + s f_c + f_d} \tag{6.6}$$

In a closed-loop control system, the output i_g is given in (6.7) as a function of the reference current i^* and the disturbance v_g:

$$i_g = G_{cl}(s) i^* + G_{gd}(s) v_g \tag{6.7}$$

where $G_{cl}(s)$ is the closed-loop transfer function from the reference to grid current, and $G_{gd}(s)$ is the closed-loop transfer function from the grid voltage to grid current that reflects the disturbance rejection capability. In this chapter, the control is implemented in the stationary $\alpha\beta$ frame, thus single-phase analysis and design is used [12].

6.2.2 Conventional Current Controllers and Their Limitations

Conventionally, the synchronization of i_g to v_g through a PLL (see Figure 6.1) is

needed to obtain the unity PF, and the RESH compensators are in parallel with the PR regulator for the purpose of harmonic mitigation [75, 86]. As mentioned in previous chapters, there are two control methods that are widely applied to the *LCL*-filtered grid-connected inverter. The first one is single-loop indirect control with ICF [23, 119]. The second is dual-loop direct control with CCF active damping [58]. In this section, the limitations of these two methods on the harmonic attenuation will be identified and discussed.

6.2.2.1. Single-Loop Indirect Control

A single-loop controlled ICF system can utilize the inherent damping of the *LCL* filter and can be made stable if $f_s > 6f_{res}$ [71]. The control block diagram is shown in Figure 6.2(a). The PR regulator $G_{PR}(s)$ and RESH terms $G_{HC}(s)$ are expressed as:

$$G_{PR}(s) = k_p\left(1 + \frac{k_r s}{s^2 + \omega_n^2}\right), G_{HC}(s) = \sum_{n=5,7,11,13\ldots h} \frac{k_{rn} s}{s^2 + (n\omega_n)^2}. \tag{6.8}$$

The closed-loop transfer function from the grid voltage to inverter current and that to the grid current are obtained as

$$G_{gd1}(s) = \frac{i_i(s)}{v_g(s)} = \frac{G_{i_i v_g}(s)}{1 + G_c(s)G_d(s)k_{PWM}G_{i_i v_i}(s)} \tag{6.9}$$

and

$$G_{gd}(s) = \frac{i_g(s)}{v_g(s)} = G_{i_g v_g} - \frac{G_c(s)G_d(s)k_{PWM}G_{i_i v_g}(s)G_{i_g v_i}(s)}{1 + G_c(s)G_d(s)k_{PWM}G_{i_i v_i}(s)}, \tag{6.10}$$

respectively, where $G_c(s) = G_{PR}(s) + G_{HC}(s)$.

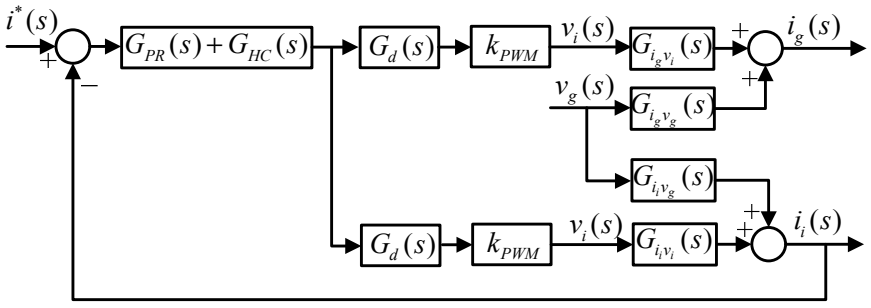

(a)

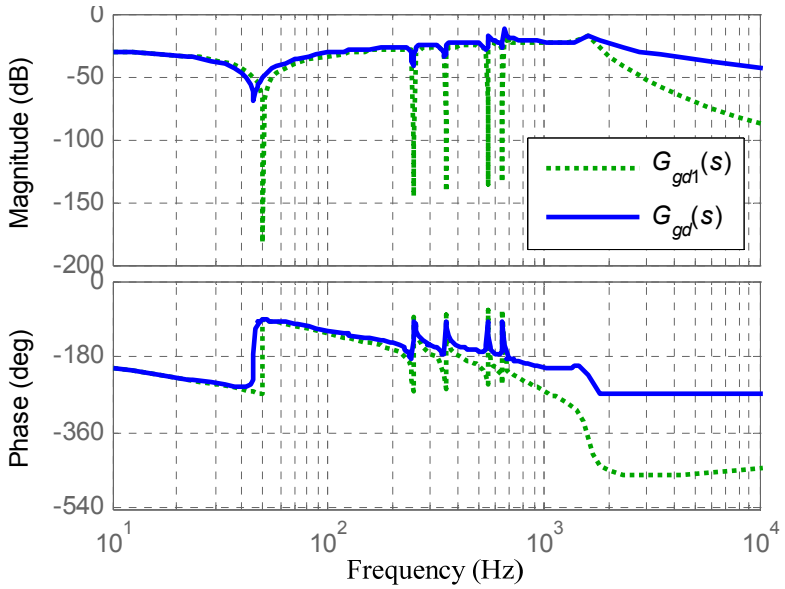

(b)

Figure 6.2: Single-loop indirect control with ICF. (a) Block diagram. (b) Bode diagrams of closed-loop transfer function from the grid voltage to inverter current i_i and that to the grid current i_g.

Taking n = 5, 7, 11, 13 for example, the Bode diagrams of (6.9) and (6.10) are shown in Figure 6.2(b). It can be seen the disturbance in the inverter current from the distorted grid voltage can be successfully suppressed, but the rejection in the grid current is unsatisfactory, because of the existence of the capacitor branch. Note that the disturbance rejection transfer functions of the linear single-loop indirect control scheme proposed in [26, 49, 132] are identical to (6.9) and (6.10). Therefore the scheme in these references is actually insufficient to mitigate the harmonic distortion in the grid current.

In view of the limitation of the indirect control method, a direct grid current control should be adopted for the purpose of harmonic attenuation. As deduced in Chapters 3 and 4, a single-loop GCF system can be made stable if $f_s < 6f_{res}$ [30, 71]. However, in this case the phase lag caused by the time delay is significant, making the insertion of RESH terms impossible. Instead, a dual-loop with active damping is generally needed for the direct control [133].

6.2.2.2. Dual-Loop Control with CCF Active Damping

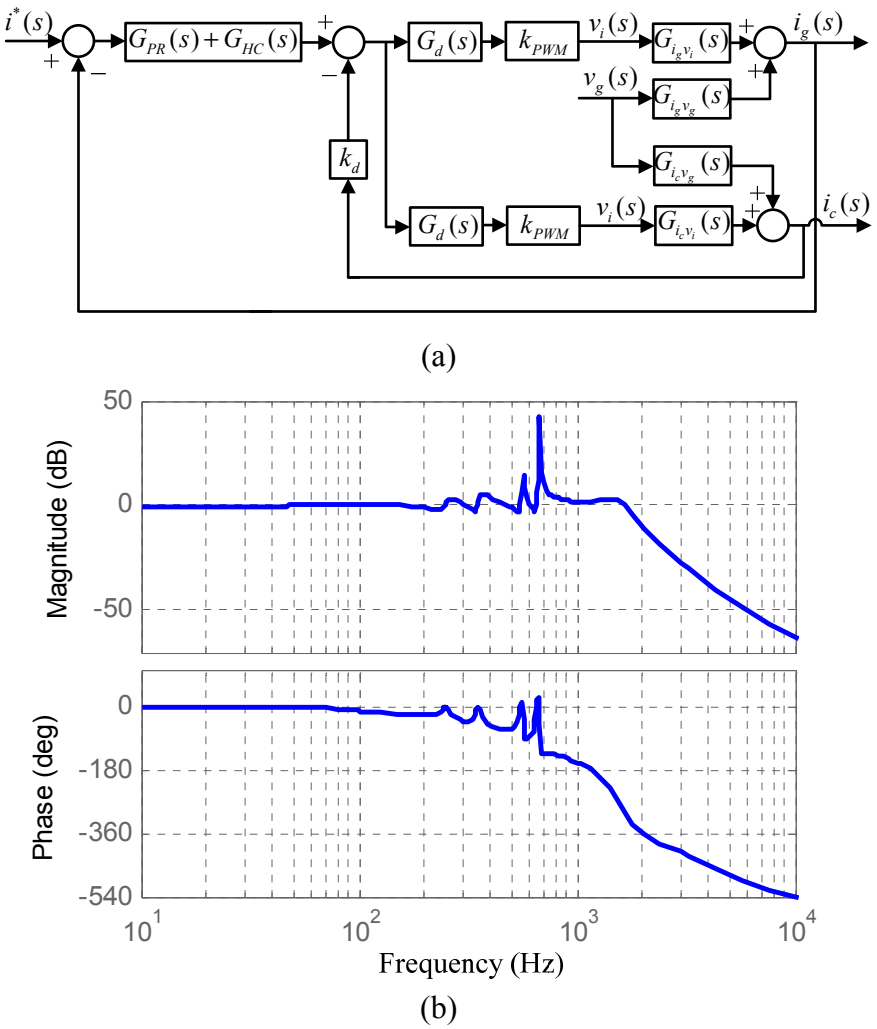

Figure 6.3: Dual-loop control with CCF active damping. (a) Block diagram. (b) Bode diagram of the closed-loop reference to grid current transfer function.

The block diagram is shown in Figure 6.3(a). A high disturbance rejection from $G_{gd}(s)$ is achieved as the grid current is directly controlled. But this is not the case for $G_{cl}(s)$ in (6.7), which is deduced as

$$G_{cl}(s)=\frac{G_c(s)G_d(s)k_{PWM}G_{i_g v_i}(s)}{1+k_d G_d(s)k_{PWM}G_{i_c v_i}(s)+G_c(s)G_d(s)k_{PWM}G_{i_g v_i}(s)}. \tag{6.11}$$

The Bode diagram of (6.11) is shown in Figure 6.3(b). It is apparent that the system can track the fundamental component, but also the harmonics which may exist in the reference input. Therefore, in order to get a high quality output, a harmonic free i^* should be provided. However, a simple PLL is unable to detect a harmonic free phase

signal, resulting in a distorted i^* [51]. A sophisticated PLL can avoid the phase distortion, but will dramatically increases the control complexity and computation load [53]. The limitations are also applicable to the cases with other damping variables such as the inverter current and capacitor voltage.

In brief, neither of the two conventional control methods is satisfactory for the harmonic attenuation in *LCL*-filtered grid-connected inverters. In the next section, an effective current control method will be proposed to address the problems.

6.3 Proposed Current Control Method

In this section, the proposed control method is introduced, which is able to effectively mitigate the harmonics and omits the use of PLL. Two active damping methods are compared, i.e., the CCF damping and ICF damping. It is found that the latter has the advantage in improving system stability when the resonant terms are used.

6.3.1 Proposed Control Method

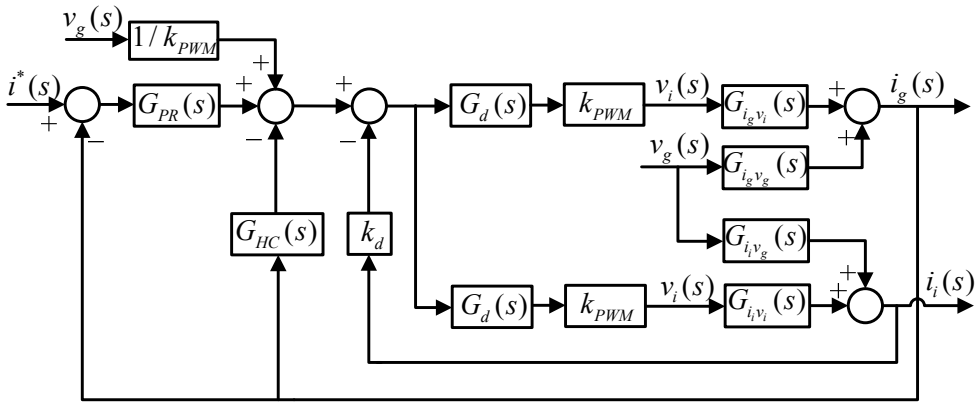

Figure 6.4: Block diagram of the proposed control system.

The block diagram of the proposed control system is shown in Figure 6.4. A proportional feed-forward of $v_g(s)$ is used to enhance the harmonic attenuation [130]. Active damping is achieved with the ICF. Different from the conventional controllers and the scheme in [26], the RESH compensators are in a separate inner-feedback path, while the PR regulator is not split, thus the merit of easy application for a PR control system is retained. The reference current is generated by proportioning the

grid voltage (see Figure 6.1), as given in (6.12), such that no PLL is needed for synchronization.

$$i^*(s) = Kv_g \tag{6.12}$$

The loop gain is obtained as

$$T(s) = \frac{(G_{PR}(s) + G_{HC}(s))G_d(s)k_{PWM}G_{i_g v_i}(s)}{1 + k_d G_d(s)k_{PWM}G_{i_i v_i}(s)}. \tag{6.13}$$

When the CCF active damping is used, the loop gain can be obtained by replacing $G_{i_i v_i}(s)$ with $G_{i_c v_i}(s)$, which is identical to that of the system in Figure 6.3(a).

To explain why the ICF damping is employed rather than the CCF, the two damping methods are compared here. Bode diagrams of the loop gains, with different controllers, are shown in Figure 6.5. As can be seen the resonant terms introduces abrupt magnitude ripples and ± 90° phase jumps at the resonant frequencies. Looking at the case without resonant terms (solid lines), if the magnitude is below 0 dB and simultaneously the phase is smaller than –90° at the resonant frequencies, the addition of a resonant term will bring in negative (–) or positive (+) crossings over –180° that may not be counteracted by each other, leading to stability problems [25, 75]. According to the Nyquist stability criterion, to avoid the stability problems when the resonant terms are inserted, at the resonant frequencies the magnitude should be above 0 dB or the phase be larger than –90°. It is interesting to note that, although the ICF decreases the magnitude to be below 0 dB, it increases the phase in low frequency range, which contributes to accommodate the resonant terms. By contrast, the CCF makes no phase improvement. This is because the capacitor can be ignored in low frequency range, making the CCF ineffective. The magnitude can be increased to be larger than 0 dB by using a larger k_p, but it leads to low stability margins and even instability [25]. Therefore the ICF is superior to the CCF in improving system stability.

The reason behind the phase increase introduced by the ICF can be intuitively explained using the virtual impedance method proposed in Chapter 4. As presented in

Section 4.3.1, in the low frequency range below f_s / 6 the ICF control equivalently adds a virtual impedance containing a positive resistor that is connected in series with the inverter side inductor. Meanwhile, in this range the capacitor can be neglected. As a result, the addition of the virtual resistor increases the phase angle.

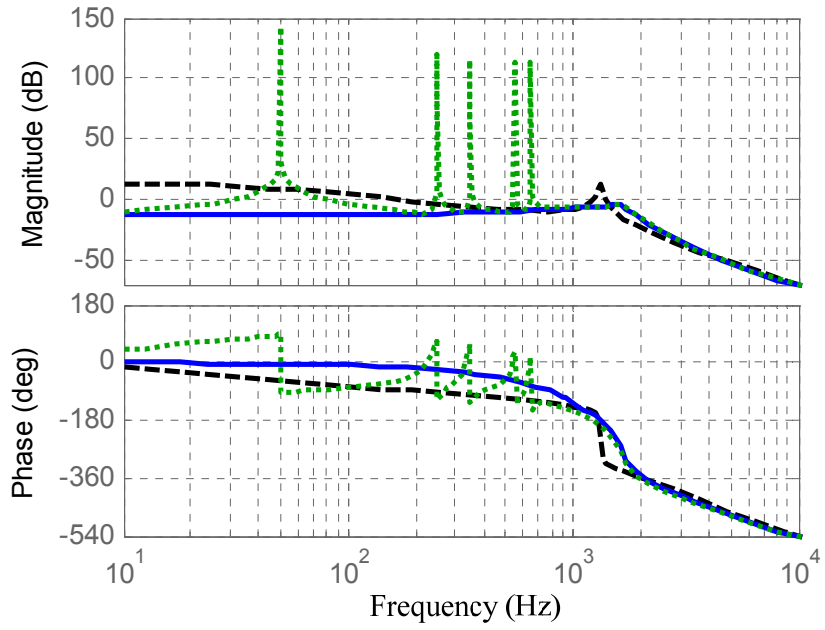

(a)

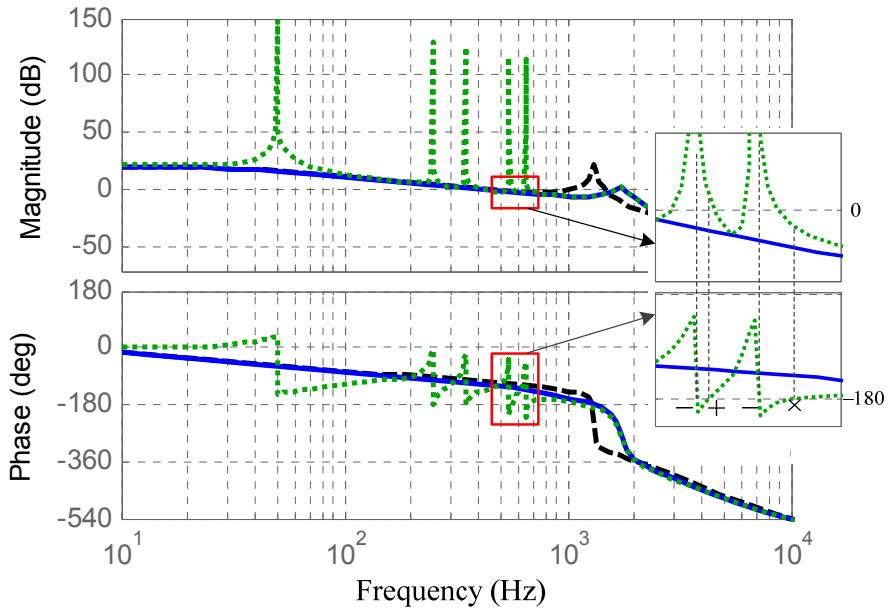

(b)

Figure 6.5: Bode diagrams of the loop gains with different active damping variables. (a) ICF. (b) CCF. (Dashed line: $k_d = 0$, k_p; solid line: $k_d \neq 0$, k_p; dotted line: $k_d \neq 0$, $G_{PR}(s) + G_{HC}(s)$.)

6.3.2 Discrete Model

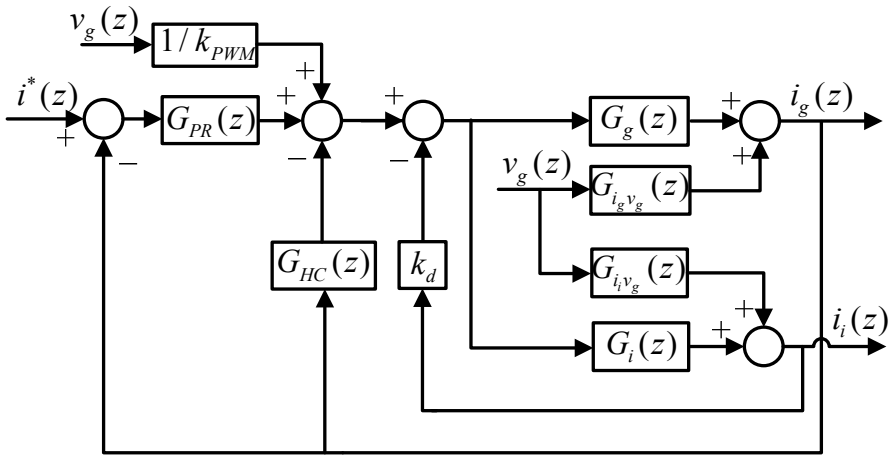

Figure 6.6: Block diagram of the digitally controlled grid-connected inverter.

To evaluate a digitally controlled system which contains unavoidable time delay, the discrete model should be gained. The proposed digital control system is shown in Figure 6.6, where $G_i(z) = Z\{e^{-sT_s} k_{PWM} G_{PWM}(s) G_{i_i v_i}(s)\}$ and $G_g(z) = Z\{e^{-sT_s} k_{PWM} G_{PWM}(s) G_{i_g v_i}(s)\}$. A detailed derivation for these discrete transfer functions with a processing time delay of $e^{-s\lambda T_s}$ $(0 < \lambda \leq 1)$ is provided in Appendix D. $G_{i_i v_g}(s)$ and $G_{i_g v_g}(s)$ are discretized to their discrete equivalents using the Tustin's method (2.17). The Tustin's method with pre-warping is used for the resonant terms in (6.8) to avoid frequency warping, by replacing 's' with

$$s = \frac{n\omega_n}{\tan(0.5 n\omega_n T_s)} \frac{z-1}{z+1}. \tag{6.14}$$

For instance, the RESH terms are discretized to:

$$\begin{aligned} G_{HC}(z) &= \sum_{n=5,7,11,13\ldots h} \left. \frac{k_r s}{s^2 + (n\omega_n)^2} \right|_{s=\frac{\omega}{\tan(\frac{\omega T_s}{2})}\frac{z-1}{z+1}} \\ &= \sum_{n=5,7,11,13\ldots h} \frac{k_r \tan(\frac{n\omega_n T_s}{2})(z^2-1)}{n\omega_n (z-1)^2 + n\omega_n \tan^2(\frac{n\omega_n T_s}{2})(z+1)^2} \end{aligned} \tag{6.15}$$

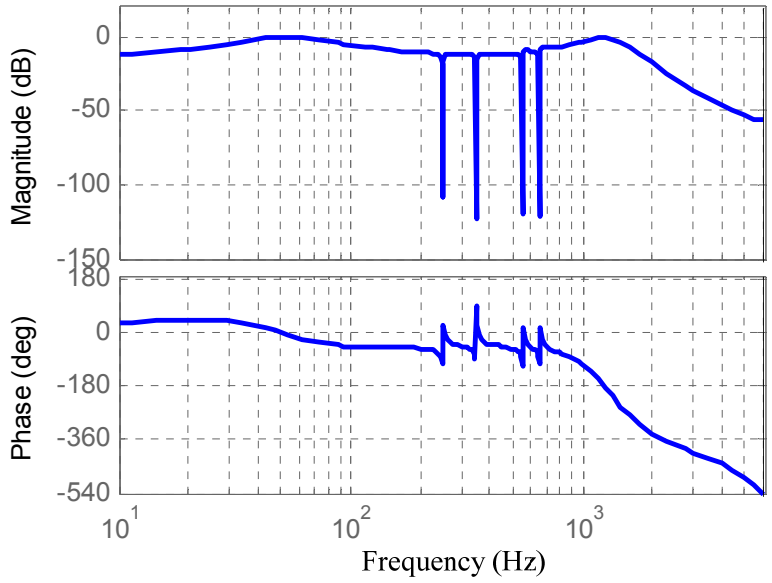

(a)

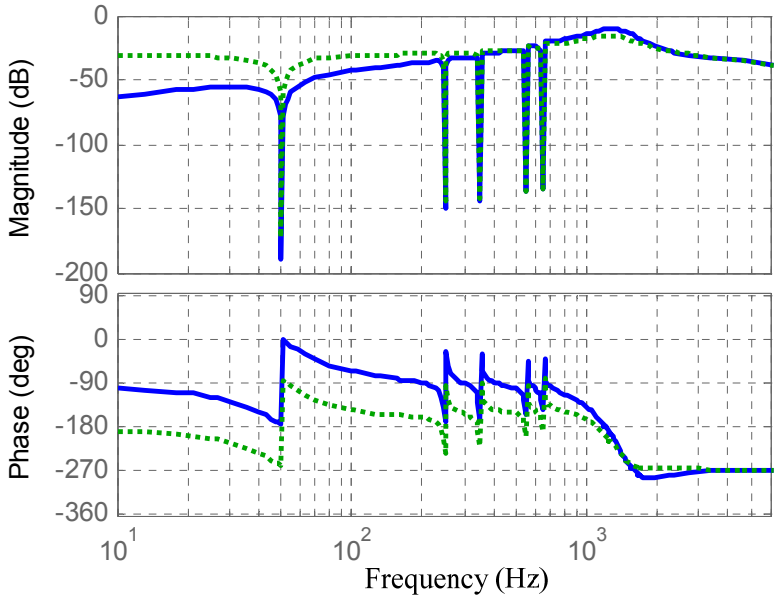

(b)

Figure 6.7: Bode diagrams of closed-loop transfer functions. (a) Reference to grid current transfer function. (b) Grid voltage to gird current transfer function (solid lines: with grid voltage feed-forward, dotted lines: without grid voltage feed-forward).

The following closed-loop transfer functions are then yielded:

$$G_{cl}(z) = \frac{G_{PR}(z)G_g(z)}{1 + k_d G_i(z) + (G_{PR}(z) + G_{HC}(z))G_g(z)} \tag{6.16}$$

$$G_{gd}(z) = \frac{G_g(z)/k_{PWM} - k_d G_{i_i v_g}(z)G_g(z) + (1 + k_d G_i(z))G_{i_g v_g}(z)}{1 + k_d G_i(z) + (G_{PR}(z) + G_{HC}(z))G_g(z)}. \tag{6.17}$$

The Bode diagrams of (6.16) and (6.17), with the optimized parameters in the next section, are shown in Figure 6.7. From Figure 6.7(a), it is apparent that the system can track the fundamental component accurately, with unity gain and zero phase deviation, while has great attenuation ability for the harmonics in $i^*(s)$ generated from (6.12). On the other hand, Figure 6.7(b) shows a strong rejection for the fundamental as well as harmonic components in the grid voltage (it can be seen that the feed-forward of the grid voltage improves the attenuation ability). Therefore the proposed control method has significant advantages over the conventional methods, and is able to produce clean output grid currents that are free from grid voltage harmonics. It is obvious that the method also allows the use of a simple PLL to obtain adjustable active and reactive power without distorting the output.

6.4 Controller Design

Several methods can be found in existing publications for multi-loop controller parameter tuning, but they all have obvious limitations. An interesting method was implemented by pole-zero cancellation in [102]. However, approximations were made on the pole-zero positions, leading the results to be potentially unreliable. A two-step approach was reported to first design the outer loop controller based on a simplified L-filter plant, then tune the inner loop based on open-loop transfer functions to maintain system stability [69]. In this method, since the damping performance is examined after the design of the outer loop controller, the system might be sensitive to filter resonances if the outer loop controller is not designed properly. In [78] the inner active damping loop was considered as a virtual impedance, but the design of the virtual impedance value is based on a trial-and-error method, thus is not explicit. A step-by-step controller design procedure was reported in [101], in which a few complicated equations have to be concerned.

To settle the limitations, an explicit and accurate discrete design method is proposed in this section. This method is able to achieve a proper damping performance, adequate GM and PM, as well as satisfactory PF angles.

6.4.1 Active Damping Loop

The system loop gain $T(z)$ in Figure 6.6 is yielded as

$$T(z) = \frac{(G_{PR}(z) + G_{HC}(z))G_g(z)}{1 + k_d G_i(z)}. \tag{6.18}$$

When the outer controller is disregarded, i.e., only considering the closed active damping loop, the Bode diagram and pole-zero map of $T(z)$ with a serial values of k_d are shown in Figure 6.8(a) and (b), respectively. As can be seen, when $k_d = 0$ a resonance exists at ω_{res}. The resonance is damped when k_d increases because of the positive virtual resistor it introduces. When an excessively large k_d is adopted, however, the equivalent resistor at the virtual resonance frequency is negative such that no damping is achieved (i.e., the virtual resonance frequency is beyond the critical frequency f_s / 6, see Section 4.3.1.2). This results in a non-minimum phase behavior as shown in Figure 6.8(a), which should be avoided for the sake of overall system stability [75, 109]. The stable boundary of k_d can be obtained using (4.7). This gives a value of 0.195, which is confirmed in Figure 6.8(b).

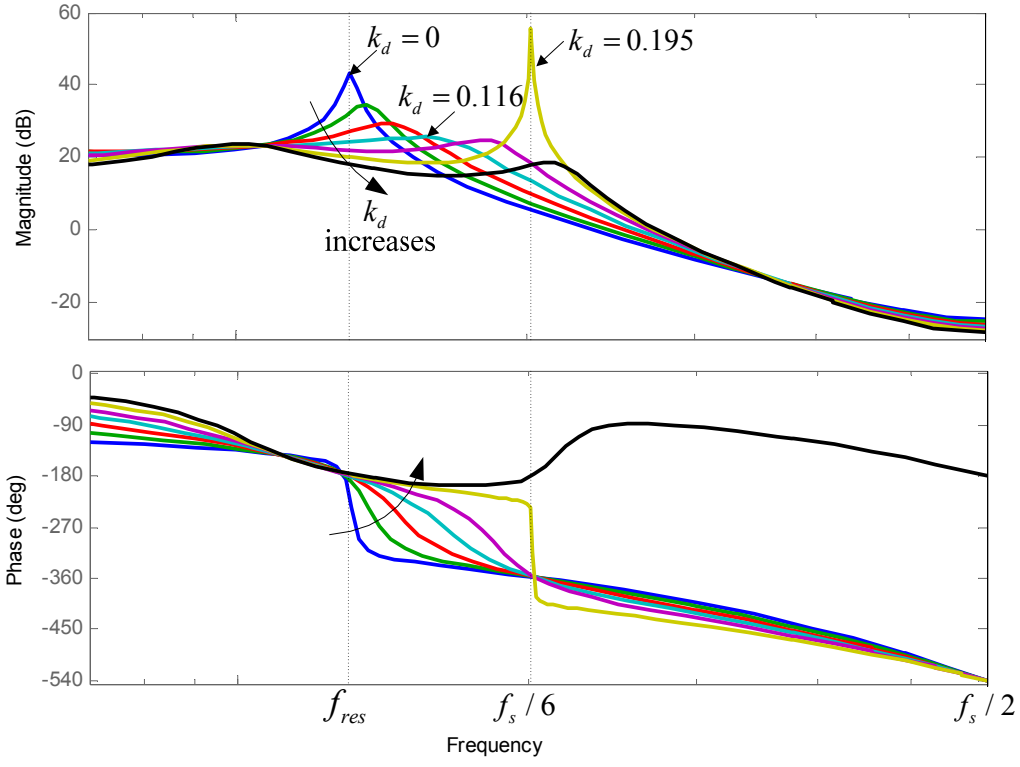

(a)

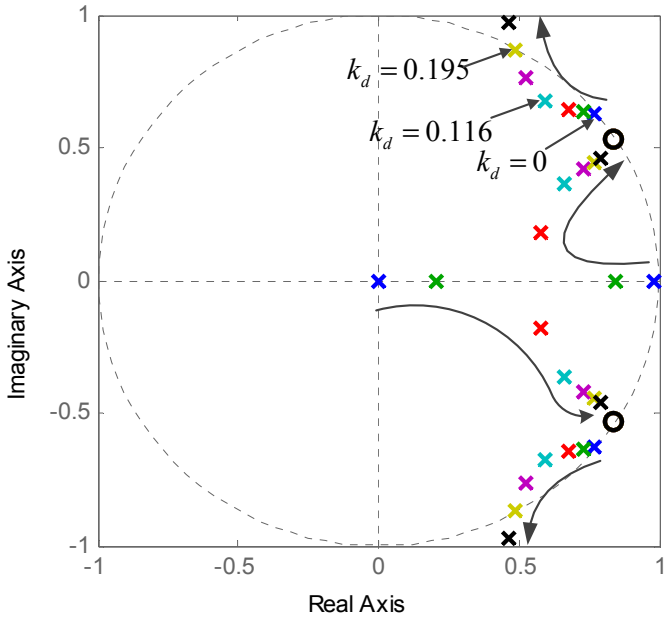

(b)

Figure 6.8: Closed inner active damping loop. (a) Bode diagram. (b) Pole-Zero map.

In this case, an optimized value k_d = 0.116 is used, by which a good active damping is achieved as demonstrated in Figure 6.8(a). At the same time, from the pole-zero map it can be observed that the dominant poles are farthest from the unit circle boundary, thus the fastest response in the inner loop is obtained.

6.4.2 Proportional Gain

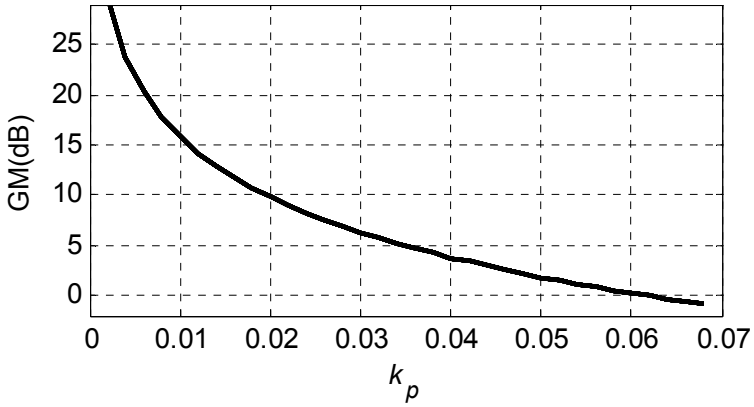

Figure 6.9: Relationship between GM and k_p.

The resonant terms only influence the frequency response around the resonant frequencies [25, 49]. As can be seen from Figure 6.5(a), the resonant terms have a

negligible impact at the –180° crossover frequency. Therefore the proportional gain k_p is the key parameter that affects the GM. The curve of GM in terms of k_p is shown in Figure 6.9. A low value yields a high GM but slow transient response, $k_p = 0.031$ is chosen that gives a GM of 6 dB.

6.4.3 Fundamental Resonant Term

According to the requirements for inverters, the PF should generally be in the range $0.999 \leq \cos \varphi \leq 1$, where φ is the PF angle which should fall into [–2.6°, 2.6°] [49]. In particular, there would be a grid frequency deviation of ±1Hz. Hence the PF angle range should be fulfilled when the grid frequency varies from 49 Hz to 51 Hz.

Since i^* is generated directly from v_g by (6.12), φ is the inverse of the phase of $G_{cl}(z)$ (see Figure 6.7(a)). Therefore the fundamental resonant term should be tuned to ensure a satisfactory φ. The relationships between φ and k_r at 49 Hz and 51 Hz are shown in Figure 6.10. As clearly illustrated, k_r should be larger than 1095, but a too great value would trigger instability. In this case a compromised $k_r = 1200$ is used.

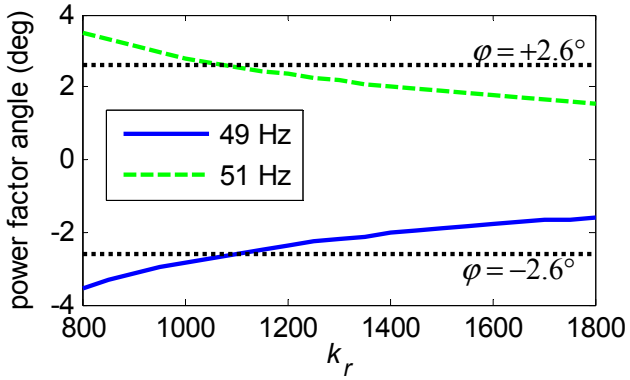

Figure 6.10: PF angle in terms of k_r.

6.4.4 RESH Terms

Finally, the RESH compensators are designed. Assuming identical gains k_{rn} are used, then k_{rn} and the highest harmonic order h are to be set. To avoid any –180° crossing around the resonant frequencies, the phase of the loop gain without $G_{HC}(z)$ at the h-order frequency should be larger than –90°. The phase crosses over –90° at 673 Hz, therefore $h = 13$. On the other hand, with the RESH compensators the mag-

nitude crosses over 0 dB around the harmonic frequencies, hence it is $G_{HC}(z)$ that affects the PM. The relationship between PM and k_{rn} is presented in Figure 6.11, from which $k_{rn} = 9.3$ is chosen that gives PM = 40.2°.

It has been considered that the GM is determined by k_p. However, the plots in Figure 6.5 show that the resonant terms affect both the magnitude and phase responses. The influence on the GM should therefore be examined. Taking $k_r = 4k_{rn} / k_p$ for example, the 3D-plot describing the GM as a function of k_p and k_r is shown in Figure 6.12. This figure reveals that the GM is mainly decided by k_p, while is slightly changed with the addition of the resonant terms. Therefore, the tuning of the proportional gain k_p in Section 6.4.2 is reasonable.

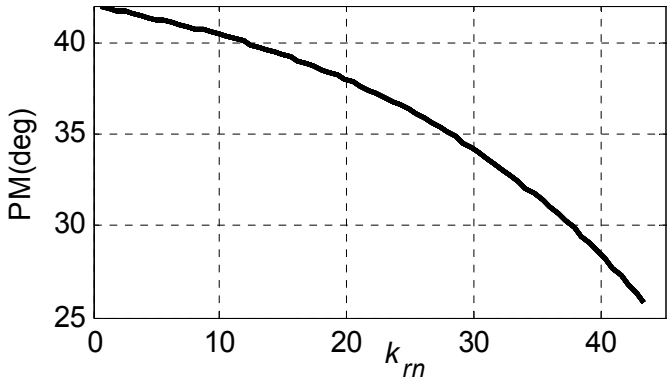

Figure 6.11: PM as a function of k_{rn}.

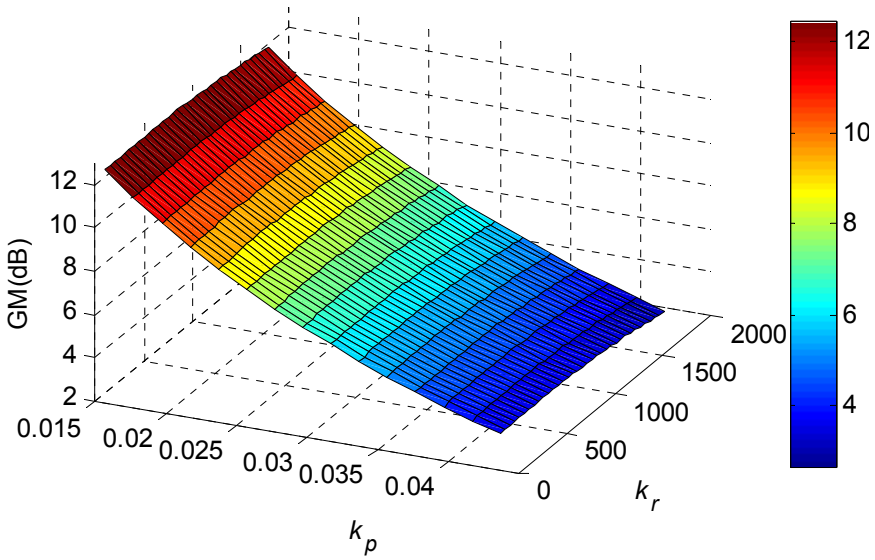

Figure 6.12: GM as a function of k_p and k_r.

Table 6.1: Parameters of the designed controller

Symbol	Quantity	Value
k_p	The proportional gain	0.031
k_d	Active damping proportional gain	0.116
k_r	Fundamental resonant gain	1200
n	Order of harmonics to be compensated	5,7,11,13
k_{rn}	Harmonics resonant controllers gain	9.3
f_s	Sampling and switching frequency	12 kHz

With the parameters obtained previously, as summarized in Table 6.1, GM is 5.9 dB which slightly deviates from the value with k_p only, and the PM is 40.2°. The phases of $G_{cl}(z)$ at 49 Hz and 51 Hz are 2.19° and –2.22°, respectively. The design procedure is therefore validated.

6.5 Experimental Results

The distorted grid voltage is simulated using a programmable AC source Omicron CMC 156, with a THD of 5.47%, as shown in Figure. 6.13. The magnitudes of fifth, seventh, eleventh, thirteenth harmonics with respect to the fundamental component are 4%, 3%, 2%, 1%, and the phases are 30°, 0°, 60°, 0°, respectively.

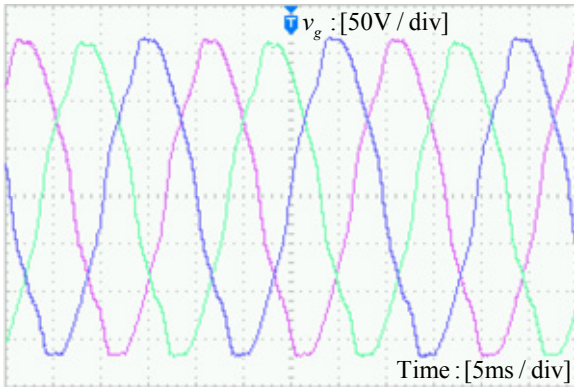

Figure 6.13: The distorted grid voltage from programmable AC source.

Firstly, the conventional methods are tested. The *d*-axis currents are set to 4 A. For the single-loop indirect control, a SRF-PLL [51] with a DSOGI based frequency locked loop [53] is used to generate a harmonic free reference, the *q*-axis current is

set to $\omega_n CV_g$ [71]. The output grid current is shown in Figure 6.14(a). The current is distorted with a high THD of 7.67%, due to the low disturbance rejection ability in (6.10). For the dual-loop control with CCF active damping, a SRF-PLL is used, and the q-axis current is set to 0. The result is shown in Figure 6.14(b), with a THD of 6.81% caused by the distorted reference. Moreover, the significant current ripples reveal the marginal stability of the CCF active damping. Therefore, the limitations of the conventional methods on the harmonic attenuation are verified.

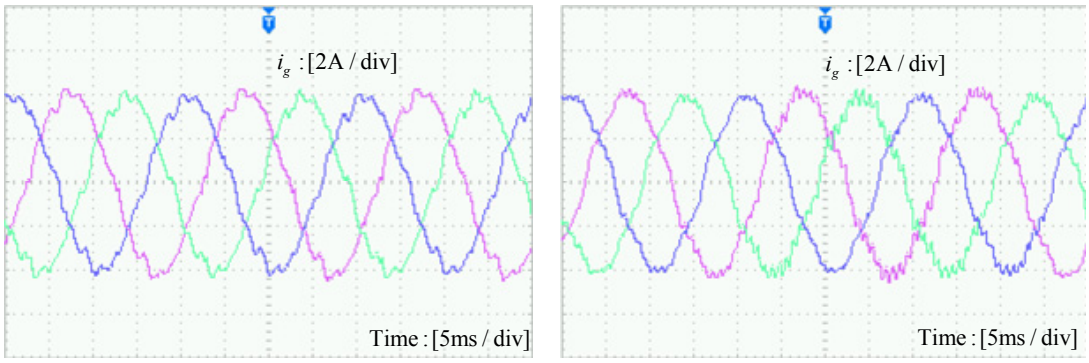

(a) (b)

Figure 6.14: Output grid current of conventional control methods. (a) Single-loop indirect control with ICF. (b) Dual-loop control with CCF active damping.

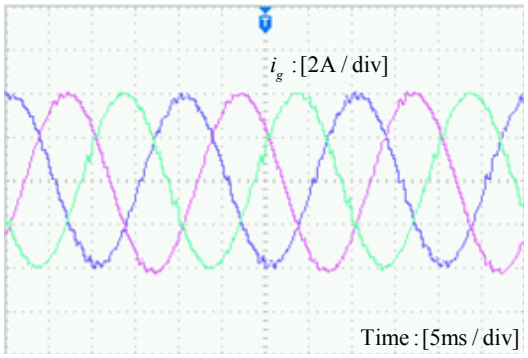

Figure 6.15: Experimental grid current of the proposed current control method.

Then the performances of the proposed control method are examined. The scaling factor K in (6.12) is set to 0.0258 to get a current amplitude of 4 A. The grid current is shown in Figure 6.15, with a low THD of 0.88%, which verifies the improved harmonic distortion attenuation ability. Also, the enhanced system stability due to

ICF damping is confirmed. Single-phase grid voltage and grid current when the fundamental frequency is set to 50 Hz, 49 Hz, and 51 Hz are presented in Figure 6.16(a) – (c), respectively. For 50Hz, the grid current is well synchronized with the grid voltage. For 49 Hz and 51 Hz, the PF angles are about –2° and 1°, respectively, both are within the restriction of ± 2.6°. The expected performances are therefore achieved.

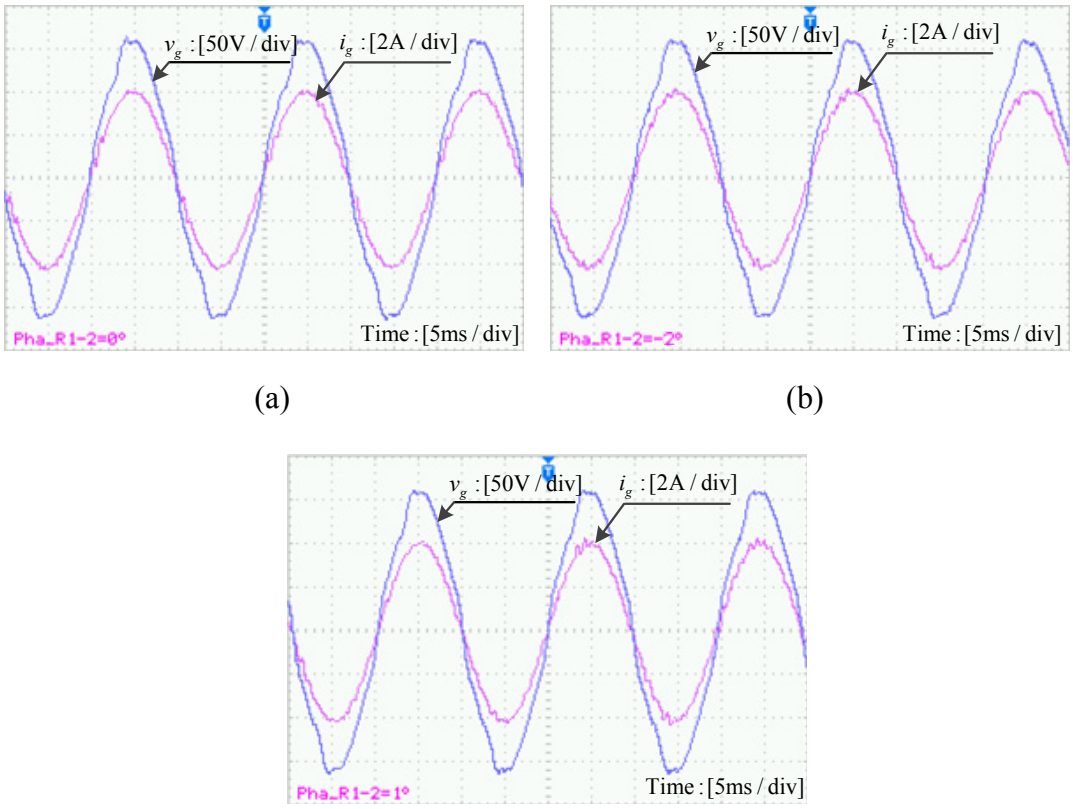

Figure 6.16: Experimental single-phase grid voltage and grid current when the fundamental grid frequency varies. (a) 50 Hz. (b) 49 Hz. (c) 51 Hz.

The experimental results are obtained under a significantly distorted grid condition with a THD of 5.47%. When the grid voltage is with a lower THD, the grid-current generated from the conventional two methods would meet the requirement. The proposed method, however, is able to produce a higher quality output with reduced control complexity.

6.6 Conclusion

This chapter has proposed a novel current control method that omits the use of PLL and effectively mitigates low-order current harmonics in three-phase *LCL*-filtered grid-connected inverters. Grid synchronization is achieved by generating the reference current directly from the grid voltage instead of by PLL. The RESH compensators are in the inner-feedback path rather than in parallel with the PR controller. Direct grid current control is achieved with the ICF active damping, which has been proved to be superior to the widely used CCF active damping in improving system stability when the RESH terms are inserted. A controller design procedure has been presented that guarantees adequate stability margins and ensures satisfactory PFs when the grid frequency varies. In comparison with conventional single- or dual-loop control methods which have been found to be unsatisfactory in attenuating the low-order harmonic distortion, the proposed strategy is able to obtain a much higher power quality and reduce the control complexity and computation burden. Results have been verified by experiment.

It has been found that both the single-loop ICF and GCF control methods are not suitable for harmonic attenuation in the grid current. This is because the RESH compensators significantly affect the frequency response in low frequency ranges, which would degrade harmonic mitigation and lead to stability problems. In contrast, the single-loop methods in the previous chapters only employ a PI or PDF controller without RESH compensators. Therefore, the finding does not downgrade the importance of the stability analysis for the single-loop control methods carried out previously.

Chapter 7

Conclusions and Future Work

7.1 Conclusions

The work in this thesis focused on the current control of grid-connected inverters in microgrids in terms of system stability, transient performance, grid synchronization, and power quality. A number of limitations and problems in existing work have been tackled by performing comprehensive system stability analyses and proposing novel current control methods.

The stability of single-loop controlled grid-connected inverters with *LCL* filters has, for the first time, found to be delay-dependent. The stable ranges of time delay for the ICF and GCF loop have been derived, in the continuous *s*-domain and also in the discrete *z*-domain. The optimal range of time delay has also been discussed. It has been shown that in the optimal range, the existence of a time delay weakens the stability of the ICF loop, whereas a proper time delay is required for the GCF loop. To improve system stability, a LP based time delay reduction method is proposed for the ICF, while a proper time delay is added to the GCF. Moreover, a simple PI controller design method has been presented, by which adequate stability margins can be guaranteed. The delay-dependent stability study has explained why different conclusions on the stability of ICF and GCF systems were drawn in different previous studies, i.e., the time delay in these cases falls into different ranges. The procedure can be extended to analyze the influence of time delay on the stability of *LCL*-filtered grid-connected inverters controlled by other methods including active damping.

Then the *LCL* resonance damping mechanism of three different control methods has been investigated, including the single-loop methods and a dual-loop with CCF active damping. The virtual impedances of these control methods have been identified. It has been shown that the virtual impedance achieves a potential damping to the *LCL* resonance. Based on the fact that a positive virtual resistance at the virtual resonance frequency is required for system stability, the requirement on the sampling frequency has been obtained for the single-loop control methods, and different cases of the dual-loop control method have been discussed. Furthermore, the gain boundaries of these controllers have been deduced. The damping investigation inspires a simple approach by means of virtual impedance to analyze system stability and predict controller gain boundaries, which facilitates the design of control loops. In comparison with classical stability analysis tools such as the Nyquist stability criterion and root locus, the proposed approach is much more intuitive.

Regarding the transient performance, the PDF current control has been applied to three-phase *LCL*-filtered grid-connected inverters, as an advantageous strategy over PI control in the SRF, to improve the transient response to a step change in the reference input via eliminating overshoot and oscillation. The complex vector method has been adopted for the modeling of the *LCL*-filtered system. Two PDF controllers have been developed for an ICF system and a GCF system, respectively. For the ICF, a simple PDF controller with identical stability characteristics to that of the PI controller is designed. Compared with the PI controller which can only reduce the transient overshoot by decreasing the controller gains, the PDF controller completely eliminates the overshoot and oscillation over a wide range of controller parameters. For the GCF, a PDF controller with an additional second-order derivative implemented as a complex high-pass filter has been developed, which provides active damping with only one feedback signal. A controller design procedure has been presented that ensures adequate stability margins and satisfactory transient performance.

As for the grid synchronization and power quality issues, a novel current control method has been proposed that omits the use of PLL and effectively mitigates low-order current harmonics in three-phase *LCL*-filtered grid-connected inverters. Grid synchronization is achieved by generating the reference current directly from the grid voltage instead of by PLL. The RESH compensators are in a separate inner-feedback path rather than in parallel with the PR controller. Direct grid current control is achieved with an ICF active damping, which has been proved to be superior to the widely used CCF active damping in improving system stability when the RESH terms are inserted. A controller design procedure has been presented that guarantees adequate stability margins and ensures satisfactory PFs when the grid frequency varies. In comparison with conventional single- or dual-loop control methods which have been found to be unsatisfactory in attenuating the harmonic distortion, the proposed strategy is able to obtain a much higher power quality and reduce the control complexity and computation burden.

The validity of the stability analyses and the proposed control methods has been verified by simulation and experiment.

In the thesis, several current control methods have been studied, which can be basically classified into two types: without or with active damping. The control without active damping includes the single-loop ICF and GCF, and also the PDF for ICF. The control with active damping includes the dual-loop approach with an inner ICF or CCF damping loop, and also the PDF for GCF. The control without active damping is very simple, but the stability is delay-dependent, which means the systems are only stable in certain sampling frequency ranges. By contrast, the control with active damping is more complicated in structure and design, but the systems can be made stable under different conditions. Furthermore, active damping methods improve the harmonic attenuation capability for the grid current. To sum up, these current control methods can be employed according to different requirements.

7.2 Future Work

Based on the research achievements, various issues can be taken care of in the future work.

At present active damping techniques for the *LCL* resonance is a hot research subject. The active damping strategies involved in this thesis include multiloop-based inner inverter current and capacitor current proportional feedback damping, and single-loop with the GCF through a high-pass filter. Apart from these feedback variables, the capacitor voltage can be sensed to form an inner damping loop using different feedback strategies such as lead-lag networks [40, 72, 81]. Filter-based active damping methods are also widely researched [79]. Recently, numerous new and interesting damping methods, mainly multiloop-based, have been reported [63, 64, 121]. Therefore, the existing active damping methods can be reviewed and compared. Furthermore, the virtual impedance method could be applied to investigate the damping effect of the various methods and thus to give an explicit overview and comparison.

As introduced in Chapter 5, in the SRF the cross-coupling between *d*- and *q*-axis currents of the *LCL* system is complicated, which will affect the transient response and even cause stability problems. The coupling has not been completely eliminated in the work. Several attempts have been made by different researchers to cancel the coupling, but the result is unsatisfactory or the method is rather complicated [41, 45, 92, 93]. Considering the fact that the complex vector models have taken the coupling into consideration, complex vector based method would be effective to achieve the target. The complex vector modeling and control method for the *LCL*-filtered grid-connected inverter has been introduced in the thesis. Based on the achievement, a complex vector method could be developed to eliminate the cross-coupling.

In the thesis, the grid voltage is considered as balanced. However, grid faults usually give rise to the appearance of unbalanced grid voltages. The unbalanced condition may bring in negative effects like introducing uncontrolled oscillations in the active and reactive power delivered to the grid. According to the grid requirements,

the DPGSs should have a fault ride-through capability against short grid disturbances. This is achieved by proper control of the grid-connected inverters. The PDF control method and the proposed harmonic attenuation method could be applied and tested under non-ideal conditions to see whether they can improve the fault ride-through capability. Furthermore, novel strategies for instantaneous active and reactive power control are promising in enhancing the fault ride-through capability, for example those can obtain different power and current characteristics according to different requirements.

References

[1] Renewable Energy Policy Network for the 21st Century, "Renewables 2015 Global Status Report, " Paris, France, 2015.

[2] International Energy Agency, "World Energy Outlook 2015", 2015.

[3] M. B. Jebli and S. B. Youssef, "Output, renewable and non-renewable energy consumption and international trade: Evidence from a panel of 69 countries," *Renew. Energy,* vol. 83, pp. 799–808, 2015.

[4] S. Chowdhury, S. P. Chowdhury, and P. Crossley, *Microgrids and Active Distribution Networks*. London, U.K.: Inst. Eng. Technol., 2009.

[5] N. W. A. Lidula and A. D. Rajapakse, "Microgrids research: A review of experimental microgrids and test systems," *Renew. Sustain. Energy Rev.*, vol. 15, no. 1, pp. 186–202, Jan. 2011.

[6] J. Rocabert, A. Luna, F. Blaabjerg, P. Rodriguez, "Control of power converters in AC microgrids," *IEEE Trans. Power Electron.*, vol. 27, no. 11, pp. 4734–4749, Nov. 2012.

[7] R. Teodorescu, M. Liserre, and R. Rodriguez, *Grid Converters for Photovoltaic and Wind Power Systems*. Hoboken, NJ: Wiley, 2010.

[8] F. Blaabjerg, Z. Chen, and S. B. Kjaer, "Power electronics as efficient interface in dispersed power generation systems," *IEEE Trans. Power Electron.*, vol. 19, no. 5, pp. 1184r1194, Sep. 2004.

[9] N. Hatziargyriou, H. Asano, R. Iravani, and C. Marnay, "Microgrids," *IEEE Power Energy Mag.*, vol. 5, no. 4, pp. 78–94, Jul./Aug. 2007.

[10] L. Ran, J. R. Bumby, and P. J. Tavner, "Use of turbine inertia for power smoothing of wind turbines with a DFIG," in *Proc. 11th Int. Conf. Harmon.*

Quality Power, Sep. 2004, vol. 63, pp. 106–111.

[11] A. Timbus, M. Liserre, R. Teodorescu, P. Rodriguez, and F. Blaabjerg, "Evaluation of current controllers for distributed power generation systems," *IEEE Trans. Power Electron.*, vol. 24, no. 3, pp. 654–664, Mar. 2009.

[12] F. Blaabjerg, R. Teodorescu, M. Liserre, and A. V. Timbus, "Overview of control and grid synchronization for distributed power generation systems," *IEEE Trans. Ind. Electron.*, vol. 53, no. 5, pp. 1398–1409, Oct. 2006.

[13] D. Xiang, L. Ran, P. Tavner, and S. Yang, "Control of a doubly fed induction generator in a wind turbine during grid fault ride-through," *IEEE Trans. Energy Convers.*, vol. 21, no. 3, pp. 652–662, Sep. 2006.

[14] C. H. Ng, M. A. Parker, L. Ran, P. J. Tavner, J. R. Bumby, and E. Spooner, "A multilevel modular converter for a large, light weight wind turbine generator," *IEEE Trans. Power Electron.*, vol. 23, no. 3, pp. 1062–1074, May 2008.

[15] T. Esram and P. L. Chapman, "Comparison of photovoltaic array maximum power point tracking techniques," *IEEE Trans. Energy Convers.*, vol. 22, no. 2, pp. 439–449, Jun. 2007.

[16] A. Ahmed, L. Ran, S. Moon, and J. H. Park, "A fast PV power tracking control algorithm with reduced power mode," *IEEE Trans. Energy Convers.*, vol. 28, no. 3, pp. 1–11, Aug. 2013.

[17] J. M. Guerrero, J. C. Vásquez, J. Matas, M. Castilla, and L. G. de Vicuña, "Control strategy for flexible microgrids based on parallel line-interactive UPS systems," *IEEE Trans. Ind. Electron.*, vol. 56, no. 3, pp. 726–735, Aug. 2009.

[18] M. A. Perez, S. Bernet, J. Rodriguez, S. Kouro, and R. Lizana, "Circuit topologies, modeling, control schemes, and applications of modular multilevel converters," *IEEE Trans. Power Electron.*, vol. 30, no. 1, pp. 4–14, Jan. 2015.

[19] J. Rodriguez, S. Bernet, B. Wu, J. O. Pontt, and S. Kouro, "Multilevel voltage-source-converter topologies for industrial medium-voltage drives," *IEEE Trans. Ind. Electron.*, vol. 54, no. 6, pp. 2930–2945, Dec. 2007.

[20] G. F. Franklin, J. D. Powell, and A. Emami-Naeini, *Feedback control of dynamic systems*: Upper Saddle River, N.J. ; Pearson Education, 2010. 6th ed., 2010.

[21] D. Pan, X. Ruan, C. Bao, W. Li, and X. Wang, "Capacitor-current-feedback active damping with reduced computation delay for improving robustness of LCL-type grid-connected inverter," *IEEE Trans. Power Electron.*, vol. 29, no. 7, pp. 3414–3427, Jul. 2014.

[22] A. Vidal, F. D. Freijedo, A. G. Yepes, P. Fernandez-Comesana, J. Malvar, Ó. Lopez*, et al.*, "Assessment and optimization of the transient response of proportional-resonant current controllers for distributed power generation systems," *IEEE Trans. Ind. Electron*., vol. 60, no. 4, pp. 1367–1383, Apr. 2013.

[23] X. Zhang, J. W. Spencer, and J. M. Guerrero, "Small-signal modeling of digitally controlled grid-connected inverters with LCL filters," *IEEE Trans. Ind. Electron.*, vol. 60, no. 9, pp. 3752–3765, Sep. 2013.

[24] Y. Tang, P. C. Loh, P. Wang, F. H. Choo, and F. Gao, "Exploring inherent damping characteristic of LCL-filters for three-phase grid-connected voltage source inverters," *IEEE Trans. Power Electron.*, vol. 27, no. 3, pp. 1433–1443, Mar. 2012.

[25] M. Liserre, R. Teodorescu, and F. Blaabjerg, "Stability of photovoltaic and wind turbine grid-connected inverters for a large set of grid impedance values," *IEEE Trans. Power Electron.*, vol. 21, no. 1, pp. 263–272, Jan. 2006.

[26] M. Castilla, J. Miret, A. Camacho, J. Matas, and L. G. de Vicuna, "Reduction of current harmonic distortion in three-phase grid-connected photovoltaic inverters

via resonant current control," *IEEE Trans. Ind. Electron.*, vol. 60, no. 4, pp. 1464–1472, Apr. 2013.

[27] A. Kahrobaeian and Y. Ibrahim, "Robust single-loop direct current control of LCL-filtered converter-based DG units in grid-connected and autonomous microgrid modes," *IEEE Trans. Power Electron.,* vol. 29, no. 10, pp. 5605–5619, Oct. 2014.

[28] R. Teodorescu, F. Blaabjerg, M. Liserre, and A. Dell'Aquila, "A stable three-phase LCL-filter based active rectifier without damping," in *Proc. IEEE Ind. Appl. Soc. Annu. Meeting*, 2003, pp. 1552–1557.

[29] J. Yin, S. Duan, and B. Liu, "Stability analysis of grid-connected inverter with LCL filter adopting a digital single-loop controller with inherent damping characteristic," *IEEE Trans. Ind. Inform*., vol. 9, no. 2, pp. 1104–1112, May 2013.

[30] S. G. Parker, B. P. McGrath, and D. G. Holmes, "Regions of active damping control for LCL filters," *IEEE Trans. Ind. Appl.*, vol. 50, pp. 424–432, Jan./Feb. 2014.

[31] R. Li, B. Liu, S. Duan, J. Yin, and X. Jiang, "Analysis of delay effects in single-loop controlled grid-connected inverter with LCL filter," in *Proc. IEEE Appl. Power Electron. Conf*., 2013, pp. 329–333.

[32] C. Zou, B. Liu, S. Duan, and R. Li, "Influence of delay on system stability and delay optimization of grid-connected inverters with LCL filter," *IEEE Trans. Ind. Inform*., vol. 10, no. 3, pp. 1775–1784, Aug. 2014.

[33] J. Dannehl, F. W. Fuchs, and P. B. Thøgersen, "PI state space current control of grid-connected PWM converters with LCL filters," *IEEE Trans. Power Electron.,* vol. 25, no. 9, pp. 2320–2330, Sep. 2010.

[34] J. Dannehl, C. Wessels, and F. W. Fuchs, “Limitations of voltage-oriented PI current control of grid-connected PWM rectifiers with LCL filters,” *IEEE Trans. Ind. Electron.*, vol. 56, no. 2, pp. 380–388, Feb. 2009.

[35] F. D. Freijedo, A. Vidal, A. G. Yepes, J. M. Guerrero, O. Lopez, J. Malvar*, et al.*, “Tuning of synchronous-frame PI current controllers in grid-connected converters operating at a low sampling rate by MIMO root locus,” *IEEE Trans. Ind. Electron.,* vol. 62, no. 8, pp. 5006–5017, Aug. 2015.

[36] A. G. Yepes, A. Vidal, J. Malvar, O. Lopez, and J. Doval-Gandoy, “Tuning method aimed at optimized settling time and overshoot for synchronous proportional-integral current control in electric machines,” *IEEE Trans. Power Electron.*, vol. 29, no. 6, pp. 3041–3054, Jun. 2014.

[37] A. G. Yepes, A. Vidal, F. D. Freijedo, J. Malvar, O. Lopez, and J. Doval-Gandoy, “Transient response evaluation of resonant controllers for AC drives,” in *Proc. IEEE Energy Convers. Congr. Expo.*, Sep. 2012, pp. 471–478.

[38] T. S. Basso and R. DeBlasio, “IEEE 1547 series of standards: Interconnection issues,” *IEEE Trans. Power Electron.,* vol. 19, no. 5, pp. 1159–1162, Sep. 2004.

[39] D. G. Holmes, T. A. Lipo, B. P. McGrath, and W. Y. Kong, “Optimized design of stationary frame three phase ac current regulators,” *IEEE Trans. Power Electron.*, vol. 24, no. 11, pp. 2417–2426, Nov. 2009.

[40] R. Peña Alzola, M. Liserre, F. Blaabjerg, R. Sebastian, J. Dannehl, and F. W. Fuchs, “Systematic design of the lead-lag network method for active damping in LCL-filter based three phase converters,” *IEEE Trans. Ind. Inf.*, vol. 10, no. 1, pp. 43–52, Feb. 2014.

[41] E. Wu and P. Lehn, “Digital current control of a voltage source converter with active damping of LCL resonance,” *IEEE Trans. Power Electron.*, vol. 21, no. 5, pp. 1364–1373, Sep. 2006.

[42] B. Bahrani, M. Vasiladiotis, and A. Rufer, “High-order vector control of grid-connected voltage-source converters with LCL-filters,” *IEEE Trans. Ind. Electron.*, vol. 61, no. 6, pp. 2767–2775, Jun. 2014.

[43] X. Bao, F. Zhuo, Y. Tian, and P. Tan, “Simplified feedback linearization control of three-phase photovoltaic inverter with an LCL filter,” *IEEE Trans. Power Electron.,* vol. 28, no. 6, pp. 2739–2752, Jun. 2013.

[44] S. A. Khajehoddin and P. K. Jain, “A control design approach for three-phase grid-connected renewable energy resources,” *IEEE Trans. Sustain. Energy*, vol. 2, no. 4, pp. 423–432, Oct. 2011.

[45] X. Fu, S. Li, and I. Jaithwa, “Implement optimal vector control for LCL-filter-based grid-connected converters by using recurrent neural networks,” *IEEE Trans. Ind. Electron.*, vol. 62, no. 7, pp. 4443–4454, Jul. 2015.

[46] S. Eren, M. Pahlevaninezhad, A. Bakhshai, and P. K. Jain, “Composite nonlinear feedback control and stability analysis of a grid-connected voltage source inverter with LCL filter,” *IEEE Trans. Ind. Electron.*, vol. 60, no. 11, pp. 5059–5074, Nov. 2013.

[47] J. Scoltock, T. Geyer, and U. K. Madawala, “A model predictive direct current control strategy with predictive references for MV grid-connected converters with LCL-filters,” *IEEE Trans. Power Electron.,* vol. 30, no. 10, pp. 5926–5937, Oct. 2015.

[48] X. Zhang, Y. Wang, C. Yu, L. Guo, and R. Cao, “Hysteresis model predictive control for high-power grid-connected inverters with output LCL-filter,” *IEEE Trans. Ind. Electron.,* vol. 63, no. 1, pp. 246–256, Jan. 2016.

[49] M. Castilla, J. Miret, J. Matas, L. G. de Vicuña, and J. M. Guerrero, “Control design guidelines for single-phase grid-connected photovoltaic inverters with damped resonant harmonic compensators,” *IEEE Trans. Ind. Electron.*, vol. 56,

no. 11, pp. 4492–4501, Nov. 2009.

[50] A. Timbus, R. Teodorescu, F. Blaabjerg, and M. Liserre, “Synchronization methods for three phase distributed power generation systems. An overview and evaluation,” in *Proc. IEEE 36th PESC*, Jun. 2005, pp. 2474–2481.

[51] S.-K. Chung, “Phase-locked loop for grid-connected three-phase power conversion systems,” in *Proc. Inst. Elect. Eng.-Electron. Power Appl.*, vol. 147, no. 3, pp. 213–219, May 2000.

[52] P. Rodriguez, J. Pou, J. Bergas, J. I. Candela, R. P. Burgos, and D. Boroyevich, “Decoupled double synchronous reference frame PLL for power converter control,” *IEEE Trans. Power Electron.*, vol. 22, no. 2, pp. 584–592, Mar. 2007.

[53] P. Rodriguez, A. Luna, I. Candela, R. Mujal, R. Teodorescu, and F. Blaabjerg, “Multiresonant frequency-locked loop for grid synchronization of power converters under distorted grid conditions,” *IEEE Trans. Ind. Electron.*, vol. 58, no. 1, pp. 127–138, Jan. 2011.

[54] M. Reyes, P. Rodriguez, S. Vazquez, A. Luna, R. Teodorescu, and J. Carrasco, “Enhanced decoupled double synchronous reference frame current controller for unbalanced grid-voltage conditions,” *IEEE Trans. Power Electron.*, vol. 27, no. 9, pp. 3934–3943, Sep. 2012.

[55] X. Wang, Y. Li, F. Blaabjerg, and P. C. Loh, “Virtual-impedance-based control for voltage-source and current-source converters,” *IEEE Trans. Power Electron.,* vol. 30, no. 12, pp. 7019–7037, Dec. 2015.

[56] X. Wu, X. Li, X. Yuan, and Y. Geng, “Grid harmonics suppression scheme for LCL-type grid-connected inverters based on output admittance revision,” *IEEE Trans. Sustain. Energy*, vol. 6, no. 2, pp. 411–421, Apr. 2015.

[57] C. Lascu, L. Asiminoaei, I. Boldea, and F. Blaabjerg, “Frequency response analysis of current controllers for selective harmonic compensation in active

power filters," *IEEE Trans. Ind. Electron.*, vol. 56, no. 2, pp. 337–347, Feb. 2009.

[58] E. Twining and D. G. Holmes, "Grid current regulation of a three-phase voltage source inverter with an LCL input filter," *IEEE Trans. Power Electron.*, vol. 18, no. 3, pp. 888–895, May 2003.

[59] M. Liserre, R. Teodorescu, and F. Blaabjerg, "Multiple harmonics control for three-phase grid converter systems with the use of PI-RES current controller in a rotating frame," *IEEE Trans. Power Electron.*, vol. 21, no. 3, pp. 836–840, May. 2006.

[60] A. Kulkarni and V. John, "Mitigation of lower order harmonics in a grid-connected single-phase PV inverter," *IEEE Trans. Power Electron.*, vol. 28, no. 11, pp. 5024–5037, Nov. 2013.

[61] A. Vidal, A.G. Yepes, F. D. Freijedo, O. Lopez, J. Malvar, F. Baneira, and J. Doval-Gandoy, "A method for identification of the equivalent inductance and resistance in the plant model of current-controlled grid-tied converters," *IEEE Trans. Power Electron.*, vol. 30, no. 12, pp. 7245–7261, Dec. 2015.

[62] M. Liserre, F. Blaabjerg, and S. Hansen, "Design and control of an LCL-filter-based three-phase active rectifier," *IEEE Trans. Ind. Appl.*, vol. 41, no. 5, pp. 1281–1291, Sep./Oct. 2005.

[63] X. Wang, F. Blaabjerg, and P. C. Loh, "Grid-current-feedback active damping for LCL resonance in grid-connected voltage-source converters," *IEEE Trans. Power Electron.,* vol. 31, no. 1, pp. 213–223, Jan. 2016.

[64] R. N. Beres, X. Wang, F. Blaabjerg, M. Liserre, and C. L. Bak, "Optimal design of high-order passive-damped filters for grid-connected applications," *IEEE Trans. Power Electron.,* vol. 31, no. 3, pp. 2083–2098, Mar. 2016.

[65] M. Zabaleta, E. Burguete, D. Madariaga, I. Zubimendi, M. Zubiaga, and I. Larrazabal, “LCL grid filter design of a multimegawatt medium-voltage converter for offshore wind turbine using SHEPWM modulation,” *IEEE Trans. Power Electron.,* vol. 31, no. 3, pp. 1993–2001, Mar. 2016.

[66] J. Xu, S. Xie, and T. Tang, “Active damping-based control for grid-connected LCL-filtered inverter with injected grid current feedback Only,” *IEEE Trans. Ind. Electron.*, vol. 61, no. 9, pp. 4746–4758, Sep. 2014.

[67] L. Harnefors, A. G. Yepes, A. Vidal, and J. Doval-Gandoy, “Passivity-based stabilization of resonant current controllers with consideration of time delay,” *IEEE Trans. Power Electron.*, vol. 29, no. 12, pp. 6260–6263, Dec. 2014.

[68] R. Pena-Alzola, M. Liserre, F. Blaabjerg, R. Sebastián, J. Dannehl, and F. W. Fuchs, “Analysis of the passive damping losses in LCL-filter based grid converters,” *IEEE Trans. Power Electron.*, vol. 28, no. 6, pp. 2642–2646, Jun. 2013.

[69] M. H. Bierhoff and F. W. Fuchs, “Active damping for three-phase PWM rectifiers with high-order line-side filters,” *IEEE Trans. Ind. Electron.*, vol. 56, no. 2, pp. 371–379, Feb. 2009.

[70] M. Xue, Y. Zhang, Y. Kang, Y. Yi, S. Li, and F. Liu, “Full feedforward of grid voltage for discrete state feedback controlled grid-connected inverter with LCL filter,” *IEEE Trans. Power Electron.*, vol. 27, no. 10, pp. 4234–4247, Oct. 2012.

[71] J. Wang, J. D. Yan, L. Jiang, and J. Zou, “Delay-dependent stability of single-loop controlled grid-connected inverters with LCL filters,” *IEEE Trans. Power Electron.,* vol. 31, no. 1, pp. 743–757, Jan. 2016.

[72] L. Harnefors, A. G. Yepes, A. Vidal, and J. Doval-Gandoy, “Passivity-based controller design of grid-connected VSCs for prevention of electrical resonance instability*,” IEEE Trans. Ind. Electron.*, vol. 62, no. 2, pp. 702–710, Feb. 2015.

[73] S. Buso and P. Mattavelli, *Digital Control in Power Electronics*. San Rafael, CA: Morgan & Claypool, 2006.

[74] D. M. Van de Sype, K. De Gussemé, F. M. L. L. De Belie, A. P. Van den Bossche, and J. A. Melkebeek, "Small-signal z-domain analysis of digitally controlled converters," *IEEE Trans. Power Electron.*, vol. 21, no. 2, pp. 470–478, Mar. 2006.

[75] X. Wang, F. Blaabjerg, and P. Loh, "Virtual RC damping of LCL-filtered voltage source converters with extended selective harmonic Compensation," *IEEE Trans. Power Electron,* vol. 30, no. 9, pp. 4726–4737, Sep. 2015.

[76] J. Wang and J. D. Yan, "Using virtual impedance to analyze the stability of LCL-filtered grid-connected inverters," in *Proc. IEEE Int. Conf. Ind. Technol.,* Seville, Spain, Mar. 17-19, 2015, pp. 1220–1225.

[77] D. Pan, X. Ruan, C. Bao, W. Li, and X. Wang, "Optimized controller design for LCL-type grid-connected inverter to achieve high robustness against grid-impedance variation," *IEEE Trans. Ind. Electron.*, vol. 62, no. 3, pp. 1537–1547, Mar. 2015.

[78] J. He and Y. W. Li, "Generalized closed-loop control schemes with embedded virtual impedances for voltage source converters with LC or LCL filters," *IEEE Trans. Power Electron.*, vol. 27, no. 4, pp. 1850–1861, Apr. 2012.

[79] J. Dannehl, M. Liserre, and F. W. Fuchs, "Filter-based active damping of voltage source converters with LCL filter," *IEEE Trans. Ind. Electron.,* vol. 58, no. 8, pp. 3623–3633, Aug. 2011.

[80] M. Liserre, A. Dell'Aquila, and F. Blaabjerg, "Genetic algorithm-based design of the active damping for an LCL-filter three-phase active rectifier,"*IEEE Trans. Power Electron.*, vol. 19, no. 1, pp. 76–86, Jan. 2004.

[81] Z. Xin, P. C. Loh, X. Wang, F. Blaabjerg, and Y. Tang, “Highly accurate derivatives for LCL-filtered grid converter with capacitor voltage active damping,” *IEEE Trans. Power Electron.,* vol. 31, no. 5, pp. 3612–3625, May 2016.

[82] O. Vodyakho and C. Mi, “Three-level inverter-based shunt active power filter in three-phase three-wire and four-wire systems,” *IEEE Trans. Power Electron.*, vol. 24, no. 5, pp. 1350–1363, May 2009.

[83] D. Jovcic, L. Zhang, and M. Hajian, “LCL VSC converter for high-power applications,” *IEEE Trans. Power Del.*, vol. 28, no. 1, pp. 137–144, Jan. 2013.

[84] N. Flourentzou, V. G. Agelidis, and G. D. Demetriades, “VSC-based HVDC power transmission systems: An overview,” *IEEE Trans. Power Electron.*, vol. 24, no. 3, pp. 592–602, Mar. 2009.

[85] P. Rodriguez, A. V. Timbus, R. Teodorescu, M. Liserre, and F. Blaabjerg, “Flexible active power control of distributed power generation systems during grid faults,” *IEEE Trans. Ind. Electron.*, vol. 54, no. 5, pp. 2583–2592, Oct. 2007.

[86] D. N. Zmood and D. G. Holmes, “Stationary frame current regulation of PWM inverters with zero steady-state error,” *IEEE Trans. Power Electron.*,vol. 18, no. 3, pp. 814–822, May 2003.

[87] D. Zmood, D. Holmes, and G. Bode, “Frequency domain analysis of threephase linear current regulators,” *IEEE Trans. Ind. Appl.*, vol. 37, no. 2, pp. 601–610, Mar. 2001.

[88] M. P. Kazmierkowski and L. Malesani, “Current control techniques for three-phase voltage-source PWM converters: A survey,” *IEEE Trans. Ind. Electron.*, vol. 45, no. 5, pp. 691–703, Oct. 1998.

[89] H. Akagi, Y. Kanazawa, and A. Nabae, “Instantaneous reactive power compensators comprising switching devices without energy storage components,” *IEEE Trans. Ind. Applicat.*, vol. IA-20, no. 3, pp. 625–630, May/Jun. 1984.

[90] R. S. Herrera, P. Salmeron, and K. Hyosung, “Instantaneous reactive power theory applied to active power filter compensation: Different approaches, assessment, and experimental results,” *IEEE Trans. Ind. Electron.*, vol. 55, no. 1, pp. 184–196, Jan. 2008.

[91] W. Li, X. Ruan, D. Pan, and X. Wang, “Full-feedforward schemes of grid voltages for a three-phase LCL-type grid-connected inverter,” *IEEE Trans. Ind. Electron.*, vol. 60, no. 6, pp. 2237–2250, Jun. 2013.

[92] J. Shi, J. Shen, B. Qu, and Z. Tan, “High-performance complex controller for high-power converters with low pulse ratios,” in *Proc. IEEE 9th Int. Conf. Power Electron. ECCE Asia,* 2015, pp. 2180–2187.

[93] K. Qu, T. Ye, J. Zhao, and X. Chen, “A feedforward compensation based decoupling control strategy for grid-connected inverter with LCL filter,” in *Proc. IEEE 9th Int. Conf. Power Electron. ECCE Asia,* 2015, pp. 2463–2468.

[94] N. He, J. Zhang, Y. Zhu, G. Shen, and D. Xu, “Weighted average current control in three-phase grid inverter with LCL filter,” *IEEE Trans. Power Electron.*, vol. 28, no. 6, pp. 2785–2797, Jun. 2013.

[95] H. Kim, M. Degner, J. Guerrero, F. Briz, and R. Lorenz, “Discrete-time current regulator design for AC machine drives*,” IEEE Trans. Ind. Appl.*, vol. 46, no. 4, pp. 1425–1435, Jul./Aug. 2010.

[96] B.-H. Bae and S.-K. Sul, “A compensation method for time delay of full digital synchronous frame current regulator of PWM AC drives,” *IEEE Trans. Ind. Appl.*, vol. 39, no. 3, pp. 802–810, May/Jun. 2003.

[97] J.-S. Yim, S.-K. Sul, B.-H. Bae, N. Patel, and S. Hiti, “Modified current control schemes for high-performance permanent-magnet AC drives with low sampling to operating frequency ratio,” *IEEE Trans. Ind. Appl.*, vol. 45, no. 2, pp. 763–771, Mar./Apr. 2009.

[98] D. G. Holmes and T. L. Lip, *Pulse Width Modulation for Power Converters: Principles and Practice.* New York: Wiley, 2003.

[99] Y. Ren and J. Fang, “Current-sensing resistor design to include current derivative in PWM H-bridge unipolar switching power amplifiers for magnetic Bearings,” *IEEE Trans. Ind. Electron.,* vol. 59, no. 12, pp. 4590–4600, Nov. 2012.

[100] A. Mullane, G. Lightbody, and R. Yacamini, “Wind-turbine fault ridethrough enhancement,” *IEEE Trans. Power Syst.*, vol. 20, no. 4, pp. 1929–1937, Nov. 2005.

[101] C. Bao, X. Ruan, X. Wang, W. Li, D. Pan, and K. Weng, “Step-by-step controller design for LCL-type grid-connected inverter with capacitor-current-feedback active-damping,” *IEEE Trans. Power Electron.,* vol. 29, no. 3, pp. 1239–1253, Mar. 2014.

[102] F. Liu, Y. Zhou, S. Duan, J. Yin, B. Liu, and F. Liu, “Parameter design of a two-current-loop controller used in a grid-connected inverter system with LCL filter,” *IEEE Trans. Ind. Electron.*, vol. 56, no. 11, pp. 4483–4491, Nov. 2009.

[103] V. Miskovic, V. Blasko, T. Jahns, A. Smith, and C. Romenesko, “Observer based active damping of LCL resonance in grid connected voltage source converters,” *IEEE Trans. Ind. Appl.*, vol. 50, no. 6, pp. 3977–3985, Nov./Dec. 2014.

[104] J. Dannehl, F. W. Fuchs, S. Hansen, and P. B. Thøgersen, “Investigation of active damping approaches for PI-based current control of grid-connected

pulse width modulation converters with LCL filters," *IEEE Trans. Ind. Appl*., vol. 46, no. 4, pp. 1509–1517, Jul./Aug. 2010.

[105] S. Bibian and H. Jin, "Time delay compensation of digital control for DC switchmode power supplies using prediction techniques," *IEEE Trans. Power Electron.,* vol. 15, no. 5, pp. 835–842, Sep. 2000.

[106] T. Nussbaumer, M. L. Heidwein, G. Gong, S. D. Round, and J. W. Kolar, "Comparison of prediction techniques to compensate time delays caused by digital control of a three-phase buck-type PWM rectifier system," *IEEE Trans. Ind. Electron.*, vol. 55, no. 2, pp. 791–799, Feb. 2008.

[107] P. Mattavelli, F. Polo, F. Dal Lago, and S. Saggini, "Analysis of control-delay reduction for the improvement of UPS voltage-loop bandwidth," *IEEE Trans. Ind. Electron.*, vol. 55, no. 8, pp. 2903–2911, Aug. 2008.

[108] I. J. Gabe, V. F. Montagner, and H. Pinheiro, "Design and implementation of a robust current controller for VSI connected to the grid through an LCL filter," *IEEE Trans. Power Electron*., vol. 24, no. 6, pp. 1444–1452, Jun. 2009.

[109] D. Yang, X. Ruan, and H. Wu, "A real-time computation method with dual sampling modes to improve the current control performance of the LCL-type grid-connected inverter," *IEEE Trans. Ind. Electron.*, vol. 62, no. 7, pp. 4563–4572, Jul. 2015.

[110] Y. Tang, P. C. Loh, P. Wang, F. H. Choo, F. Gao, and F. Blaabjerg, "Generalized design of high performance shunt active power filter with output LCL filter," *IEEE Trans. Ind. Electron.*, vol. 59, no. 3, pp. 1443–1452, Mar. 2012.

[111] Y. He, H. S. Chung, C. N. Ho, and W. Wu, "Use of boundary control with second-order switching surface to reduce the system order for deadbeat controller in grid-connected inverter," *IEEE Trans. Power Electron*., vol. 31, no. 3, pp. 2638–2653, Mar. 2016.

[112] F. Briz, M. W. Degner, and R. D. Lorenz, “Analysis and design of current regulators using complex vectors,” *IEEE Trans. Ind. Appl.*, vol. 36, no. 3, pp. 817–825, May/Jun. 2000.

[113] M. Hanif, V. Khadkikar, W. Xiao, and J. L. Kirtley, “Two degrees of freedom active damping technique for LCL filter-based grid connected PV systems,” *IEEE Trans. Ind. Electron.*, vol. 61, pp. 2795–2803, Jun. 2014.

[114] R. M. Phelan, *Automatic Control Systems*. Ithaca, NY, USA: Cornell Univ. Press, 1977.

[115] W. Phipps, R. Duke, and M. J. Harrison, “A proposal for a new generation power converter with pseudo-derivative control,” presented at the *Int. Telecommunications Energy Conf.*, Providence RI, USA, 2006, pp. 1–5.

[116] D. Y. Ohm, “Analysis of PID and PDF compensators for motion control systems,” in *Proc. IEEE Conf. Rec. Ind. Appl. Soc. Annu. Meet.*, Oct. 1994, vol. 3, pp. 1923–1929.

[117] S. Gataric and N.R. Garrigan, “Modeling and design of three-phase systems using complex transfer functions”, in *Proc. IEEE Power Electron. Spec. Conf.*, vol. 2, Jun./Jul. 1999, pp. 691–697.

[118] L. Harnefors, “Modeling of three-phase dynamic systems using complex transfer functions and transfer matrices”, *IEEE Trans. Ind. Electron.*, vol. 54, no. 4, pp. 2239–2248, Aug. 2007.

[119] J. Wang, J. Yan, and L. Jiang, “Pseudo-derivative-feedback current control for three-phase grid-connected inverters with LCL filters,” *IEEE Trans. Power Electron.*, vol. 31, no. 5, pp. 3898–3912, May. 2016.

[120] R. Teodorescu and F. Blaabjerg, “Flexible control of small wind turbines with grid failure detection operating in stand-alone and gridconnected modes,” *IEEE Trans. Power Electron.*, vol. 19, no. 5, pp. 1323–1332, Sep. 2004.

[121] C. A. Busada, S. Gomez Jorge, and J. A. Solsona, “Full-state feedback equivalent controller for active damping in LCL-filtered grid-connected inverters using a reduced number of sensors,” *IEEE Trans. Ind. Electron.,* vol. 62, no. 10, pp. 5993–6002, Oct. 2015.

[122] J. Holtz, “The representation of AC machine dynamics by complex signal flow graphs,” *IEEE Trans. Ind. Electron.,* vol. 42, no. 3, pp. 263–271, Jun. 1995.

[123] L. Harnefors, X. Wang, A. G. Yepes, and F. Blaabjerg, “Passivity-based stability assessment of grid-connected VSCs—An overview,” *IEEE J. Emerg. Sel. Topics Power Electron.,* vol. 4, no. 1, pp. 116–125, Mar. 2016.

[124] J. Holtz and N. Oikonomou, “Fast dynamic control of medium voltage drives operating at very low switching frequency—An Overview,” *IEEE Trans. Ind. Electron.*, vol. 55, no. 3, pp. 1005–1013, Mar. 2008.

[125] N. Hoffmann, F. W. Fuchs, M. Kazmierkowski, and D. Schroder, “Digital current control in a rotating reference frame - Part I: System modeling and the discrete time-domain current controller with improved decoupling capabilities,” *IEEE Trans. Power Electron.,* vol. 31, no. 7, pp. 5290–5305, Jul. 2016.

[126] J. Kukkola, M. Hinkkanen, and K. Zenger, “Observer-based state-space current controller for a grid converter equipped with an LCL filter: Analytical method for direct discrete-time design,” *IEEE Trans. Ind. Appl.,* vol. 51, no. 5, pp. 4079–4090, Sep./Oct. 2015.

[127] C. Ramos, A. Martins, and A. Carvalho, “Complex state-space current controller for grid-connected converters with an LCL filter,” in *Proc. 35th Annu. IEEE Conf. Ind. Electron. Soc. (IECON’09)*, Porto, Portugal, Nov. 2009, pp. 296–301.

[128] L. Harnefors, L. Zhang, and M. Bongiorno, "Frequency-domain passivity-based current controller design," *IET Power Electron.*, vol. 1, no. 4, pp. 455–465, Dec. 2008.

[129] F. Tang, J. Xinmin, Z. Xiao, and T. Yibin, "Stability analysis on parallel of LCL-filter-based grid-connected converters in MW-level direct-drive wind generation using complex vector," presented at the *Int. Conf. Electrical Machines Systems*, Beijing, China, Aug. 2011, pp. 1–6.

[130] X. Wang, X. Ruan, S. Liu, and C. K. Tse, "Full feedforward of grid voltage for grid-connected inverter with LCL filter to suppress current distortion due to grid voltage harmonics," *IEEE Trans. Power Electron.*, vol. 25, no. 12, pp. 3119–3127, Dec. 2010.

[131] A. G. Yepes, F. D. Freijedo, J. Doval-Gandoy, O. Lopez, J. Malvar, and P. Fernandez-Comesana, "Effects of discretization methods on the performance of resonant controllers," *IEEE Trans. Power Electron.*, vol. 25, no. 7, pp. 1692–1712, Jul. 2010.

[132] M. Castilla, J. Miret, J. Matas, L. García de Vicuña, and J. M. Guerrero, "Linear current control scheme with series resonant harmonic compensator for single-phase grid-connected photovoltaic inverters," *IEEE Trans. Ind. Electron.,* vol. 55, no. 7, pp. 2724–2733, Jul. 2008.

[133] Y. Jia, J. Zhao, and X. Fu, "Direct grid current control of LCL-filtered grid-connected inverter mitigating grid voltage disturbance," *IEEE Trans. Power Electron.*, vol. 29, no. 3, pp. 1532–1541, Mar. 2014.

Appendix A

A Derivation Example of the Stable Ranges of Time Delay in the Discrete *z*-Domain

This is a derivation example of the stable ranges of time delay in Chapter 3.

For the GCF, $G_g(z)$ in (3.17) can be written as

$$G_g(z) = \frac{k_{PWM}}{(L_i + L_g)\omega_{res}} \frac{z^3 a + z^2 b + zc + d}{z^{\ell}(z^3 - z^2 e + ze - 1)}, \tag{A.1}$$

with $a = m\theta - \sin m\theta$, $b = (1-m)\theta - \sin(1-m)\theta + 2\sin m\theta - 2m\theta\cos\theta$, $c = m\theta - 2(1-m)\theta\cos\theta - \sin m\theta + 2\sin(1-m)\theta$, $d = (1-m)\theta - \sin(1-m)\theta$, $e = 2\cos\theta + 1$, and $\theta = \omega_{res}T_s$ ($\theta < \pi$). With $G_c(s) = k_p$, the denominator of the closed-loop transfer function (3.19) is denoted as

$$D(z) = z^{\ell+3} - z^{\ell+2}e + z^{\ell+1}e - z^{\ell} + z^3 Ka + z^2 Kb + zKc + Kd, \tag{A.2}$$

where $K = \frac{k_p k_{PWM}}{(L_i + L_g)\omega_{res}}$.

Taking $\ell = 1$ and $0 \le m < 1$, i.e., $0 < \lambda$ ($\lambda = \ell - m$) ≤ 1 for example, in this case $D(z) = z^4 + (Ka - e)z^3 + (Kb + e)z^2 + (Kc - 1)z + Kd$. Using the w-transform $z = (w+1)/(w-1)$, $D(w)$ can be expressed as

$$D(w) = D(z)\Big|_{z=\frac{w+1}{w-1}} = \frac{Aw^4 + Bw^3 + Cw^2 + Dw + E}{(w-1)^4}, \tag{A.3}$$

with $A = K(a + b + c + d)$, $B = 2(3 + Ka - Kc - 2Kd - e)$, $C = 2(3 - Kb + 3Kd - e)$, $D = 2(1 - Ka + Kc - 2Kd + e)$, $E = 2 - Ka + Kb - Kc + Kd + 2e$. Defining $e_1 = 1 + e = 2(1 + \cos\theta)$, $e_2 = 3 - e = 2(1 - \cos\theta)$, $K_1 = K(a - c - 2d)$, $K_2 = K(-b + 3d)$, $K_3 = K(-a + c - 2d)$, and $K_4 = K(-a + b - c + d)$, we have:

$$A = K\theta e_2, B = 2(e_2 + K_1), C = 2(e_2 + K_2), D = 2(e_1 + K_3), E = 2e_1 + K_4. \tag{A.4}$$

Note that $0 < \theta < \pi$, $e_1 > 0$ and $e_2 > 0$ are obtained, hence $A > 0$, $B > 0$, $C > 0$, $D > 0$, and $E > 0$.

To ensure system stability, all of the roots of the characteristic equation $Aw^4 + Bw^3 + Cw^2 + Dw + E = 0$ should be in the LPH, this can be evaluated using the

Routh's stability criterion. The Routh array of $Aw^4 + Bw^3 + Cw^2 + Dw + E = 0$ is given as:

$$\begin{array}{lll} w^4: & A & C & E \\ w^3: & B & D & \\ w^2: & \dfrac{BC-AD}{B} & E & \\ w^1: & D-\dfrac{B^2E}{BC-AD} & & \\ w^0: & E & & \end{array}$$

$A > 0$, $B > 0$, and $E > 0$ have been satisfied. To ensure stability $BC - AD > 0$ and $BCD - AD^2 - B^2E > 0$ are also required, i.e.,

$$\begin{cases} 2(e_2 + K_1)(e_2 + K_2) > K\theta e_2(e_1 + K_3) \\ 2(e_2 + K_1)(e_2 + K_2)(e_1 + K_3) > K\theta e_2(e_1 + K_3)^2 + (e_2 + K_1)^2(2e_1 + K_4) \end{cases} \tag{A.5}$$

Note that K_1, K_2, K_3, and K_4 all contain a factor of K, the first inequality can be fulfilled using an infinitely small K (i.e., by setting an infinitely small k_p). The second inequality can be simplified to (A.6) below when an infinitely small K is used so that the second-order and third-order terms for K can be eliminated.

$$(2K_3 - K_4)e_2 + 2(K_2 - K_1)e_1 > K\theta e_1^2 \tag{A.6}$$

Eliminating K in (A.6) gives

$$(-a-b+3c-5d)(3-e) + 2(-a-b+c+5d)(1+e) > \theta(1+e)^2, \tag{A.7}$$

which can be converted to

$$\begin{array}{c} \sin[(2-m)\theta] < \sin[(1-m)\theta] \\ \Rightarrow \sin[(\lambda+1)\omega_{res}T_s] < \sin(\lambda\omega_{res}T_s). \end{array} \tag{A.8}$$

Finally, because $\omega_{res}T_s < \pi$ and in this GCF example $0 < \lambda \leq 1$, the following stable range of time delay is obtained

$$\frac{\pi}{2\omega_{res}} < (\lambda + \frac{1}{2})T_s < (\lambda + \frac{1}{2})\frac{\pi}{\omega_{res}}, (0 < \lambda \leq 1). \tag{A.9}$$

Appendix B

Transformation between Discrete Complex Transfer Functions in Stationary Frame and SRF

This is a derivation of the relationship between discrete complex transfer functions in the stationary frame and SRF in Chapter 5.

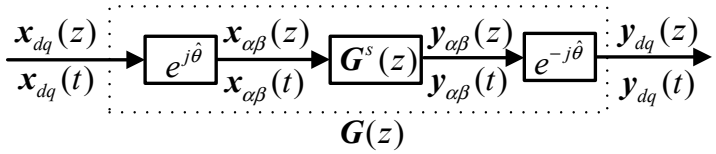

Figure B.1: Signal transmission diagram.

The diagram of signal transmission in the stationary frame and SRF is shown in Figure B.1, where $\boldsymbol{x}$ is the input signal and $\boldsymbol{y}$ the output. $\boldsymbol{G}^s(z)$ and $\boldsymbol{G}(z)$ are discrete complex transfer functions in the stationary frame and SRF, respectively, i.e., $\boldsymbol{G}^s(z) = \boldsymbol{y}_{\alpha\beta}(z) / \boldsymbol{x}_{\alpha\beta}(z)$ and $\boldsymbol{G}(z) = \boldsymbol{y}_{dq}(z) / \boldsymbol{x}_{dq}(z)$.

The sequence $\boldsymbol{y}_{\alpha\beta}(t)$ can be written as

$$\boldsymbol{y}_{\alpha\beta}(t) = \sum_{k=0}^{+\infty} \left[y_\alpha(kT_s) + jy_\beta(kT_s) \right] \delta(t - kT_s) . \tag{B.1}$$

Its Laplace transform expression is

$$\boldsymbol{y}_{\alpha\beta}(s) = \sum_{k=0}^{+\infty} \left[y_\alpha(kT_s) + jy_\beta(kT_s) \right] e^{-skT_s} . \tag{B.2}$$

Using $z = e^{sT_s}$, $\boldsymbol{y}_{\alpha\beta}(z)$ can be yielded as

$$\boldsymbol{y}_{\alpha\beta}(z) = \sum_{k=0}^{+\infty} \left[y_\alpha(kT_s) + jy_\beta(kT_s) \right] z^{-k} . \tag{B.3}$$

According to the Laplace transform in the stationary frame and SRF, i.e., $L\left(\boldsymbol{f}_{dq}(t)\right) = L\left(\boldsymbol{f}_{\alpha\beta}(t)e^{-j\hat{\theta}}\right) = \boldsymbol{f}_{\alpha\beta}(s+j\omega_n)$ [117, 118], we have

$$\begin{aligned}\boldsymbol{y}_{dq}(s) &= L\left(\boldsymbol{y}_{dq}(t)\right) = L\left(\boldsymbol{y}_{\alpha\beta}(t)e^{-j\hat{\theta}}\right) = \boldsymbol{y}_{\alpha\beta}(s+j\omega_n) \\ &= \sum_{k=0}^{+\infty}\left[y_\alpha(kT_s) + jy_\beta(kT_s)\right]e^{-(s+j\omega_n)kT_s}\end{aligned} \tag{B.4}$$

Hence, $\boldsymbol{y}_{dq}(z)$ is yielded as

$$\begin{aligned}\boldsymbol{y}_{dq}(z) &= \sum_{k=0}^{+\infty}\left[y_\alpha(kT_s) + jy_\beta(kT_s)\right]z^{-k}e^{-j\omega_n kT_s} \\ &= \sum_{k=0}^{+\infty}\left[y_\alpha(kT_s) + jy_\beta(kT_s)\right]\left(ze^{j\omega_n T_s}\right)^{-k} \\ &= \boldsymbol{y}_{\alpha\beta}(ze^{j\omega_n T_s})\end{aligned} \tag{B.5}$$

Likewise, the z-transform of the input signals in the two frames results in $\boldsymbol{x}_{dq}(z) = \boldsymbol{x}_{\alpha\beta}(ze^{j\omega_n T_s})$. Therefore, the transformation between discrete complex transfer functions in the stationary frame and SRF is given as:

$$\boldsymbol{G}(z) = \boldsymbol{G}^s(ze^{j\omega_n T_s}) \tag{B.6}$$

Appendix C

Derivation of Different Forms for the *z*-Domain Complex Vector Plant Model in the SRF

This is a derivation of different forms for the discrete SRF complex vector model in Chapter 5.

$$\boldsymbol{G}_g(z)=\frac{k_{PWM}}{(L_i+L_g)ze^{j\omega_n T_s}}\left(\frac{T_s}{ze^{j\omega_n T_s}-1}-\frac{\sin\omega_{res}T_s}{\omega_{res}}\frac{ze^{j\omega_n T_s}-1}{z^2e^{j2\omega_n T_s}-2ze^{j\omega_n T_s}\cos\omega_{res}T_s+1}\right)$$

$$=\frac{k_{PWM}T_s}{(L_i+L_g)ze^{j\varphi}}\left[\frac{1}{ze^{j\varphi}-1}-\frac{\sin\theta}{\theta}\frac{ze^{j\varphi}-1}{(ze^{j\varphi}-e^{j\theta})(ze^{j\varphi}-e^{-j\theta})}\right]$$

$$=\frac{k_{PWM}T_se^{-j\varphi}}{(L_i+L_g)z}\left[\frac{e^{-j\varphi}}{z-e^{-j\varphi}}-\frac{\sin\theta}{\theta}\frac{ze^{-j\varphi}-e^{-j2\varphi}}{(z-e^{j(\theta-\varphi)})(z-e^{-j(\theta+\varphi)})}\right]$$

$$=\frac{k_{PWM}T_se^{-j\varphi}}{(L_i+L_g)z}\left\{\frac{e^{-j\varphi}(z-e^{j\varphi})}{z^2-2z\cos\varphi+1}-\frac{\sin\theta}{\theta}\frac{(ze^{-j\varphi}-e^{-j2\varphi})(z-e^{-j(\theta-\varphi)})(z-e^{j(\theta+\varphi)})}{[z^2-2z\cos(\theta-\varphi)+1][z^2-2z\cos(\theta+\varphi)+1]}\right\}$$

$$=\frac{k_{PWM}T_se^{-j\varphi}}{(L_i+L_g)z}\left\{\frac{e^{-j\varphi}(z-e^{j\varphi})}{z^2-2z\cos\varphi+1}-\right.$$

$$\left.\frac{\sin\theta}{\theta}\frac{z^3e^{-j\varphi}-z^2(2\cos\theta+e^{-j2\varphi})+z(e^{j\varphi}+e^{j(\theta-\varphi)}+e^{-j(\theta+\varphi)})-1}{[z^2-2z\cos(\theta-\varphi)+1][z^2-2z\cos(\theta+\varphi)+1]}\right\}$$

$$=\frac{k_{PWM}T_s}{(L_i+L_g)z}\left\{\frac{(ze^{-j2\varphi}-e^{-j\varphi})}{z^2-2z\cos\varphi+1}-\right.$$

$$\left.\frac{\sin\theta}{\theta}\frac{z^3e^{-j2\varphi}-z^2(2\cos\theta e^{-j\varphi}+e^{-j3\varphi})+z(1+2e^{-j2\varphi}\cos\theta)-e^{-j\varphi}}{[z^2-2z\cos(\theta-\varphi)+1][z^2-2z\cos(\theta+\varphi)+1]}\right\}$$

$$=\frac{k_{PWM}T_s}{(L_i+L_g)z}\left\{\frac{z\cos2\varphi-\cos\varphi}{z^2-2z\cos\varphi+1}-\right.$$

$$\left.\frac{\sin\theta}{\theta}\frac{z^3\cos2\varphi-z^2(2\cos\theta\cos\varphi+\cos3\varphi)+z(1+2\cos2\varphi\cos\theta)-\cos\varphi}{[z^2-2z\cos(\theta-\varphi)+1][z^2-2z\cos(\theta+\varphi)+1]}\right\}$$

$$+j\frac{k_{PWM}T_s}{(L_i+L_g)z}\left\{\frac{-z\sin2\varphi+\sin\varphi}{z^2-2z\cos\varphi+1}-\right.$$

$$\left.\frac{\sin\theta}{\theta}\frac{-z^3\sin2\varphi+z^2(2\cos\theta\sin\varphi+\sin3\varphi)-z2\sin2\varphi\cos\theta+\sin\varphi}{[z^2-2z\cos(\theta-\varphi)+1][z^2-2z\cos(\theta+\varphi)+1]}\right\}$$

Alternatively, $\boldsymbol{G}_g(z)$ can be expressed as:

$$\boldsymbol{G}_g(z) = \frac{k_{PWM}}{(L_i + L_g)ze^{j\varphi}}\left[\frac{T_s}{ze^{j\varphi}-1} - \frac{\sin\theta}{\omega_{res}}\frac{ze^{j\varphi}-1}{(ze^{j\varphi}-e^{j\theta})(ze^{j\varphi}-e^{-j\theta})}\right]$$

$$= \frac{k_{PWM}}{z(L_i + L_g)\omega_{res}e^{j\varphi}}\left[\frac{\theta}{ze^{j\varphi}-1} - \frac{\sin\theta(ze^{j\varphi}-1)}{(ze^{j\varphi}-e^{j\theta})(ze^{j\varphi}-e^{-j\theta})}\right]$$

$$= \frac{k_{PWM}e^{-j\varphi}}{z(L_i + L_g)\omega_{res}}\left[\frac{\theta(ze^{j\varphi}-e^{j\theta})(ze^{j\varphi}-e^{-j\theta}) - \sin\theta(ze^{j\varphi}-1)^2}{(ze^{j\varphi}-1)(ze^{j\varphi}-e^{j\theta})(ze^{j\varphi}-e^{-j\theta})}\right]$$

$$= \frac{k_{PWM}}{z(L_i + L_g)\omega_{res}}\left\{\frac{z^2(\theta e^{j\varphi} - \sin\theta e^{j\varphi}) + z(2\sin\theta - 2\theta\cos\theta) + (\theta - \sin\theta)e^{-j\varphi}}{z^3e^{j3\varphi} - z^2[e^{j(2\varphi-\theta)} + e^{j(2\varphi+\theta)} + e^{j2\varphi}] + z[e^{j\varphi} + e^{j(\varphi-\theta)} + e^{j(\varphi+\theta)}] - 1}\right\}$$

$$= \frac{N_{gr} + jN_{gi}}{D_{gr} + jD_{gi}}$$

$$D_{gr} = z^4\cos 3\varphi - z^3\cos 2\varphi(2\cos\theta + 1) + z^2\cos\varphi(1 + 2\cos\theta) - z,$$

$$D_{gi} = z^4\sin 3\varphi - z^3\sin 2\varphi(2\cos\theta + 1) + z^2\sin\varphi(1 + 2\cos\theta),$$

$$N_{gr} = \frac{k_{PWM}}{(L_i + L_g)\omega_{res}}\left[z^2(\theta - \sin\theta)\cos\varphi + z(2\sin\theta - 2\theta\cos\theta) + (\theta - \sin\theta)\cos\varphi\right],$$

$$N_{gi} = \frac{k_{PWM}\sin\varphi(\theta - \sin\theta)}{(L_i + L_g)\omega_{res}}(z^2 - 1)$$

Appendix D

Derivation of Discrete Plant Transfer Functions

This derivation aims to obtain the discrete plant transfer functions in Chapter 6, for the case with a processing time delay of $e^{-s\lambda T_s}$ ($0 < \lambda \le 1$).

Defining the following terms:

$$\begin{cases} f_Q = \sqrt{(2f_b^3 - 9f_af_bf_c + 27f_a^2f_d)^2 - 4(f_b^2 - 3f_af_c)^3}, \\ f_C = \sqrt[3]{\dfrac{1}{2}(f_Q + 2f_b^3 - 9f_af_bf_c + 27f_a^2f_d)}, \\ a = \dfrac{f_b}{3f_a} + \dfrac{f_C}{3f_a} + \dfrac{f_b^2 - 3f_af_c}{3f_af_C}, \\ b = \dfrac{f_b}{3f_a} - \dfrac{(1+j\sqrt{3})f_C}{6f_a} - \dfrac{(1-j\sqrt{3})(f_b^2 - 3f_af_c)}{6f_af_C}, \\ c = \dfrac{f_b}{3f_a} - \dfrac{(1-j\sqrt{3})f_C}{6f_a} - \dfrac{(1+j\sqrt{3})(f_b^2 - 3f_af_c)}{6f_af_C}, \end{cases} \tag{D.1}$$

The transfer function $G_{i_iv_i}(s)$ can be split to

$$\begin{aligned} G_{i_iv_i}(s) &= \frac{A_i}{s+a} + \frac{B_i}{s+b} + \frac{C_i}{s+c} \\ &\begin{cases} A_i = \dfrac{a^2L_gC - aC(R_d + R_g) + 1}{(a-b)(a-c)f_a}, \\ B_i = \dfrac{b^2L_gC - bC(R_d + R_g) + 1}{(b-a)(b-c)f_a}, \\ C_i = \dfrac{c^2L_gC - cC(R_d + R_g) + 1}{(c-b)(c-a)f_a}. \end{cases} \end{aligned} \tag{D.2}$$

With the processing time delay $e^{-s\lambda T_s}$, the z-domain transfer function $G_i(z)$ is yielded as

$$\begin{aligned} G_i(z) &= Z\left\{e^{-s\lambda T_s}k_{PWM}G_{PWM}(s)G_{i_iv_i}(s)\right\} = k_{PWM}\frac{z-1}{z}Z\left\{\frac{e^{-s\lambda T_s}G_{i_iv_i}(s)}{s}\right\} \\ &= k_{PWM}\frac{z-1}{z}Z\left\{\frac{e^{-s\lambda T_s}}{s}\left(\frac{A_i}{s+a} + \frac{B_i}{s+b} + \frac{C_i}{s+c}\right)\right\} \end{aligned} \tag{D.3}$$

Equation (D.3) can be deduced using the following property [23, 74]

$$Z\left\{\frac{e^{-s\lambda T_s}}{s}\frac{A_i}{s+a}\right\}=\frac{A_i\left[z-e^{-aT_s}-(z-1)e^{-a(1-\lambda)T_s}\right]}{a(z-1)(z-e^{-aT_s})}$$
$$\Rightarrow k_{PWM}\frac{z-1}{z}Z\left\{\frac{e^{-s\lambda T_s}}{s}\frac{A_i}{s+a}\right\}=\frac{k_{PWM}}{z}A_i\frac{A_1z+A_2}{z-e^{-aT_s}} \tag{D.4}$$

where $A_1=\frac{1-e^{-a(1-\lambda)T_s}}{a}, A_2=\frac{e^{-a(1-\lambda)T_s}-e^{-aT_s}}{a}$.

Likewise, defining $B_1=\frac{1-e^{-b(1-\lambda)T_s}}{b}, B_2=\frac{e^{-b(1-\lambda)T_s}-e^{-bT_s}}{b}, C_1=\frac{1-e^{-c(1-\lambda)T_s}}{c}, C_2=\frac{e^{-c(1-\lambda)T_s}-e^{-cT_s}}{c}$, and $D_3=-e^{-aT_s}-e^{-bT_s}-e^{-cT_s}, D_3=-e^{-(a+b)T_s}-e^{-(b+c)T_s}-e^{-(a+c)T_s}, D_1=-e^{-(a+b+c)T_s}$, $G_i(z)$ is derived as

$$G_i(z)=\frac{k_{PWM}(N_{i3}z^3+N_{i2}z^2+N_{i1}z+N_{i0})}{z^4+D_3z^3+D_2z^2+D_1z}, \tag{D.5}$$

with $N_{i3}=A_iA_1+B_iB_1+C_iC_1, N_{i2}=A_i[A_2-A_1(e^{-bT_s}+e^{-cT_s})]+B_i[B_2-B_1(e^{-aT_s}+e^{-bT_s})]+C_i[C_2-C_1(e^{-aT_s}+e^{-bT_s})]$, $N_{i1}=A_i[A_1e^{-(b+c)T_s}-A_2(e^{-bT_s}+e^{-cT_s})]+B_i[B_1e^{-(a+c)T_s}-B_2(e^{-aT_s}+e^{-cT_s})]+C_i[C_1e^{-(a+b)T_s}-C_2(e^{-aT_s}+e^{-bT_s})], N_{i0}=A_iA_2e^{-(b+c)T_s}+B_iB_2e^{-(a+c)T_s}+C_iC_2e^{-(a+b)T_s}$.

Similarly, the transfer function $G_{i_gv_i}(s)$ can be split to

$$G_{i_iv_i}(s)=\frac{A_g}{s+a}+\frac{B_g}{s+b}+\frac{C_g}{s+c}, \tag{D.6}$$

with $A_g=\frac{1-aCR_d}{(a-b)(a-c)f_a}, B_g=\frac{1-bCR_d}{(b-a)(b-c)f_a}, C_g=\frac{1-cCR_d}{(c-b)(c-a)f_a}$.

Then the discrete transfer function $G_g(z)$ can be deduced as

$$G_g(z)=\frac{k_{PWM}(N_{g3}z^3+N_{g2}z^2+N_{g1}z+N_{g0})}{z^4+D_3z^3+D_2z^2+D_1z} \tag{D.7}$$

$N_{g3}=A_gA_1+B_gB_1+C_gC_1, N_{g2}=A_g[A_2-A_1(e^{-bT_s}+e^{-cT_s})]+B_g[B_2-B_1(e^{-aT_s}+e^{-bT_s})]+C_g[C_2-C_1(e^{-aT_s}+e^{-bT_s})]$, $N_{g1}=A_g[A_1e^{-(b+c)T_s}-A_2(e^{-bT_s}+e^{-cT_s})]+B_g[B_1e^{-(a+c)T_s}-B_2($

$e^{-aT_s} + e^{-cT_s})] + C_g[C_1 e^{-(a+b)T_s} - C_2(e^{-aT_s} + e^{-bT_s})], N_{g0} = A_g A_2 e^{-(b+c)T_s} + B_g B_2 e^{-(a+c)T_s} + C_g C_2$

$e^{-(a+b)T_s}$.

The transfer function $G_{i_c v_i}(s)$ can be split to

$$G_{i_c v_i}(s) = \frac{A_c}{s+a} + \frac{B_c}{s+b} + \frac{C_c}{s+c}, \tag{D.8}$$

with $A_c = \frac{a^2 CL_g - aCR_g}{(a-b)(a-c)f_a}, B_c = \frac{b^2 CL_g - bCR_g}{(b-a)(b-c)f_a}, C_c = \frac{c^2 CL_g - cCR_g}{(c-b)(c-a)f_a}$. Likewise, the discrete transfer function $G_C(z)$ can be written as

$$G_C(z) = \frac{K_{PWM}(N_{c3} z^3 + N_{c2} z^2 + N_{c1} z + N_{c0})}{z^4 + D_3 z^3 + D_2 z^2 + D_1 z}, \tag{D.9}$$

$N_{c3} = A_c A_1 + B_c B_1 + C_c C_1, N_{c2} = A_c[A_2 - A_1(e^{-bT_s} + e^{-cT_s})] + B_c[B_2 - B_1(e^{-aT_s} + e^{-bT_s})]$ +

$C_c[C_2 - C_1(e^{-aT_s} + e^{-bT_s})]$, $N_{c1} = A_c[A_1 e^{-(b+c)T_s} - A_2(e^{-bT_s} + e^{-cT_s})] + B_c[B_1 e^{-(a+c)T_s} - B_2($

$e^{-aT_s} + e^{-cT_s})] + C_c[C_1 e^{-(a+b)T_s} - C_2(e^{-aT_s} + e^{-bT_s})], N_{c0} = A_c A_2 e^{-(b+c)T_s} + B_c B_2 e^{-(a+c)T_s} + C_c C_2$

$e^{-(a+b)T_s}$.